MASTER

IDO-19313

ADDITIONAL ANALYSIS OF THE SL-1 EXCURSION

Final Report of Progress July through October 1962

November 21, 1962

Flight Propulsion Laboratory Department
General Electric Company
Idaho Falls, Idaho

UNITED STATES ATOMIC ENERGY COMMISSION • DIVISION OF TECHNICAL INFORMATION

DISCLAIMER

Other issues of this report bear the number TM-62-11-707.

This report has been reproduced directly from the best available copy.

Printed in USA. Price $2.75. Available from the Office of Technical Services, Department of Commerce, Washington 25, D. C.

USAEC Division of Technical Information Extension, Oak Ridge, Tennessee

IDO-19313
REACTOR TECHNOLOGY

ADDITIONAL ANALYSIS OF THE SL-1 EXCURSION

FINAL REPORT OF PROGRESS
JULY THROUGH OCTOBER 1962

SL-1 Project
Idaho Test Station
General Electric Company

November 21, 1962

United States Atomic Energy Commission Contract No. AT (10-1) 1095

TABLE OF CONTENTS

Table of Contents (Con't) | Page No.

ACKNOWLEDGEMENTS

Although it would be impossible to give credit to all the individuals whose efforts contributed to this report, it seems appropriate to identify some who were particularly instrumental in its completion.

Editor:	JF Kunze
Laboratories:	GG Plastino FL Sims TA Linn AJ Lovell RJ Park
Analysis:	JF Kunze RW Hyndman
Explosive Model Tests:	VA DeLiso
Design Recommendations:	EF Thurston

C. L. Storrs, Manager
SL-1 Project

INDEX OF ILLUSTRATIONS

Index of Illustrations (Con't) Page No.

Index of Illustrations (Cont'd) | Page No.

LIST OF TABLES

PREFACE

This report describes the work done from July through October, 1962, under two extensions of the SL-1 recovery contract. The objectives of this work were, first, to obtain significant scientific data pertaining to reactor excursions, and in particular the SL-1 excursion; second, to extend the analysis of reactor transient behavior so as to obtain an improved understanding of the thermal and mechanical processes that take place during and following a reactor excursion; and third, to obtain chemical, metallurgical, and nuclear data relative to the pre-accident performance of the SL-1, which had completed many hours of testing.

In consideration of the fact that this was the last opportunity to obtain samples of the SL-1 power plant easily, if at all, many detailed laboratory investigations were made, exceeding the requirements of the immediate analysis. The results are given in Section I, and their significance is discussed briefly in Section II. Section III consists of an attempt to construct a mathematical model of reactor excursions, based partly upon fundamental thermodynamic and nuclear considerations, although necessarily utilizing several empirical results as well. This model has been applied to SPERT and BORAX excursions with some success. Section IV summarizes the recommendations concerning reactor design and operation which have arisen from the SL-1 accident and its analysis.

I. LABORATORY INVESTIGATIONS

1. Pressure Vessel Studies

1.1 Integrated Flux Profile

The SL-1 pressure vessel was fabricated from SA-212, Grade B Firebox Quality steel which was clad on the inner surface with Type 304 stainless steel. During the incident investigation the vessel was separated into two major sections by a complete horizontal cut made just above the active core region.

The circumferential cut is shown in Figure I-1; however, in the drawing the lower portion of the pressure vessel has been rotated to show the metallurgical sample locations with respect to the welds. The activation samples are not shown in their correct circumferential locations, but the longitudinal positions are shown as they were measured.

The upper section of the pressure vessel was sampled at 12 inch intervals which started 9 inches below the top of the flange. The sampling, which resulted in 9 separate samples of each type material, was accomplished through the use of two drills. The larger drill was used to counter-drill the hole to obtain a "clean" sample of the metal for activation analysis. The wall and clad samples were taken from opposite positions at the same elevation. The radiation level of the upper section ranged between 300 mr/hr to 700 mr/hr at contact.

Obtaining the samples from the lower section of the pressure vessel was more difficult since the radiation level was in the order of 5 R/hr at 5 feet. It was believed that the high radiation level was mainly related to severe contamination; however, decontamination methods had little effect in reducing the radiation. Since personnel exposure was of prime concern and the drilling process for sampling was quite lengthy, it was decided to cut a 2 inch wide vertical strip the length of the lower section. This piece was decontaminated more easily because of the reduction in size and lead shielding applied to reduce the radiation exposure while drilling.

The samples from the lower section of the pressure vessel were obtained in the same manner as they had been from the upper section with the exception that they were taken at 6 inch intervals.

Samples of the carbon steel and stainless steel were examined to determine which prominent photopeaks and their related isotopes could be used in the activation analysis. This work resulted in the choice of Mn^{54} for fast neutron activation and Co^{60} for slow neutron activation for carbon steel and stainless steel, respectively. Elemental analyses were performed to determine the percentage of iron and cobalt. These analyses showed 97.89±0.90% iron in the carbon steel and 0.13±0.013% Co in the 304 type stainless steel.

The activation analysis for each section of the pressure vessel was accomplished by application of gamma scanning techniques and radiochemical separations. The carbon steel and stainless steel samples were handled separately since gamma scanning required identical composition of material and sample geometry. The drilling samples were dissolved in HCl and HNO_3 and taken up to 25 ml volumes in flasks (Figure I-2). The samples of a given type were then counted at a distance of 10 cm from a NaI(Tl) 3"x3" crystal using a multi-channel analyzer system. One of the samples of each group was chosen as a standard and counted a number of times to obtain a standard deviation for the counting process.

The counting process related to the solution samples did not require corrections for efficiency, nuclear decay scheme or absorber losses since only data relative to the standard sample was being obtained. Each sample and its related data were handled in the same manner which included counting, computing the area under the photopeak and converting to a desirable unit for comparative purposes. The unit chosen was cpm/gram, count per minute per gram of drilling. The counting results were normalized to the standard sample with its average cpm/gm unit chosen as 1.0. The gamma scanning data are presented in Tables I-I and I-II.

Following the gamma scanning process, radiochemical separations were performed for Mn and Co on standard samples. The separations were made to give an ideal geometry for a known amount of material which allowed a quantitative disintegration rate to be obtained. The separations were done in duplicate in order to check the separation process. These results produced the following absolute disintegration per minute per gram drilling values:

$Co^{60} = 6.57 \times 10^4$ dpm/gm at 1042, 8-21-62
$= 6.53 \times 10^4$ dpm/gm at 1129, 8-21-62
$Mn^{54} = 3.41 \times 10^3$ dpm/gm at 1057, 8-21-62
$= 3.34 \times 10^3$ dpm/gm at 1505, 8-21-62

The final step in the pressure vessel activation analysis included the conversion of the dpm/gm values at count time to fast and slow integrated nvt values through the application of the following equation.

$$\Phi T = \frac{(D)(m)(T)}{V\Sigma(1-e^{-\lambda T})e^{-\lambda t}} \qquad (1)$$

where

D = dpm/gm of drilling at count time
m = mass of sample
T = exposure time
V = sample volume
Σ = macroscopic cross-section
λ = decay constant
t = decay time

For the 314 day Mn^{54} and 5.3 year Co^{60} equation (1) takes on the following form:

$$\Phi T = \frac{(D)(m)(T)}{V\Sigma\lambda T e^{-\lambda t}} = \frac{(D)(m)}{V\Sigma\lambda e^{-\lambda t}} \qquad (2)$$

for each operating period short compared to the half life.

The decay time for Mn^{54} was obtained by dividing the SL-1 operating history into seven major operating periods and decaying from the midpoint of the count time back to the midpoint of each operating period. These data are presented in Table I-III and Figure I-3. The decay time used for Co^{60} was the midpoint of the entire SL-1 operation.

After the nvt was calculated for the standard samples, the integrated flux profile was obtained by taking the product of the standard nvt value and the normalized gamma scanning data. These results are tabulated in Tables I-I and I-II and presented in Figure I-4, SL-1 Pressure Vessel Activation Profile.

1.2 Metallographic Analysis

1.2.1 Wall Material

Samples were taken from the pressure vessel as shown by Figure I-1. The ITS samples were decontaminated, then radiographed. After radiographing the samples were cut into tensile, bend and metallography samples as shown in Figures I-5, I-6 and I-7. See Appendix A for explanation of identification of samples. The radiography and test results of the various specimens cut from the ITS samples follow.

1.2.2 Radiography

In general the welds at the midsection of the pressure vessel appeared to be sound. Sample ITS-46 and sample ITS-47, see Figure I-1, were radiographed. Radiographs of these samples were made and no discontinuities were detected. In the sample from the "T" weld at the top of the vessel, ITS-45, evidence of transverse cracks and some porosity is easily discernible as shown by the radiograph in Figure I-8. The bend test sample, sectioned from sample ITS-45, as shown in Figure I-5, had surface cracks. The radiograph of this bend specimen and the two tensile specimens is shown in Figure I-9. It should be noted that these cracks were internal and became surface cracks only after the bend specimen was cut from the sample.

1.2.3 Metallography

The general structure of the carbon steel and stainless steel adjacent to the weld heat-affected zones appears to be about the same for the various samples. Figure I-10 is a macrograph taken from sample ITS-45 showing structure of the carbon steel base material and severe transverse cracks in the heat-affected zone.

The cracks seen in the radiographs of sample ITS-45, were of special interest. These cracks were in a heat-affected zone caused by the welding of stainless steel to the carbon steel plate. The heat-affected zone is shown in cross-section indicated by an arrow in Figure I-11a. The collinear grain structure of the heat-affected zone is shown in Figure I-11b. This type of structure is more likely to crack than a more random structure, in a direction perpendicular to the grain boundaries.

The vessel had expanded from a circumference of 14.14 feet to 15.18 feet at the location of the upper circumferential weld during the incident. The expansion accounts for a 7% elongation. The amount of elongation was apparently enough to crack the vessel in the heat-affected zone of the circumferential weld.

1.2.4 Weld Study

The metallographic weld samples taken from the pressure vessel sample, as indicated in Figures I-5, I-6 and I-7, were polished and macro etched for examination. The macrophotographs of these sections are shown in Figures I-12 and I-13. There is minimal evidence of gas porosity, and in general the welds show excellent fusion to the parent materials.

Bend tests were made on samples taken across the welds as indicated in Figures I-5, I-6 and I-7. The bend test specimens were cut from the carbon steel portion of the vessel as 3/8" by 1-1/2" by 8" bars. These bars were radiographed before testing and found to be sound except for specimens 4B45 and 1B49 which were cracked. The radiograph in Figure I-9 shows cracks in specimen 4B45. The cracks appearing on the surface toward the stainless steel clad are shown in Figure I-15. The other specimens, 1B46, 1B47, 1B48, 1B49 and 4B47, withstood the bend test. Figure I-16 is a photograph showing some of the test specimens after testing. It required 7810 to 10800 pounds of force to bend the sound samples, whereas it required 7500 pounds of force to break sample 4B45.

1.2.5 Tensile and Hardness Properties

The tensile specimen blank removed from the ITS pressure vessel sample, as indicated in Figures I-5, I-6 and I-7, was machined into tensile specimens in conformance to NRL specifications (gauge length 1-3/4" x 1/4" dia.).

The specimens were measured and hardness tests taken on the shoulder before they were pulled, using a Riehle tensile test machine.

The data obtained from the hardness and tensile tests are tabulated in Table I-IV. There are two factors which would increase the hardness, yield strength, and tensile strength but decrease the elongation. One is radiation damage, which should be relatively low in the pressure vessel even in the highest activation area; and the other is cold work of the vessel during the excursion.

Examination of the vessel has shown there was considerable distortion of the vessel attributed to the incident. The estimated amount of cold work in the specimens caused by the distortion of the vessel is indicated in Table I-IV. The property variations correlate very well with these estimates.

1.3.1 Flange Studs

The flange studs on the pressure vessel were bent outward during the incident when the flange tilted. Figure I-17 shows the bends on seven of the studs when removed from the vessel flange.

Four of the studs were cut into tensile and metallographic samples. Two tensile specimens were taken from each of the four studs with their centers near the shoulder of the reduced area away from the bend. The hardness was taken on the tensile specimen shoulder and they were pulled to obtain the tensile data with the Riehle tensile machine. The results of the hardness test and tensile test are tabulated in Table I-V.

The hardness and tensile results indicate the studs had relatively constant properties with a tensile strength range from 130 to 140 K psi. The specifications for Type A-193-B-14 call for 125 to 145 K psi min.

2. Core and Related Studies

2.1 Fission Product Analysis

The purpose of the fission product analysis of the debris from the bottom of the reactor pressure vessel was to obtain inventory data which would allow the determination of fission product release related to the SL-1 incident.

Since a considerable amount of work had been done earlier on debris samples during the uranium analysis, it was believed that the remaining solution samples which were available could be used for fission product analyses. It was necessary to dilute these samples in order to obtain activities which were sufficiently low to allow counting by the multi-channel analyzer system. All of the samples were prepared in vials of the same size to give a constant geometry for counting. Since each sample was to be analyzed for Ce^{144}, Cs^{137}, $Zr^{95}Nb^{95}$ and Sr^{90} it was believed that the application of gamma scanning techniques would provide the results with the least difficulty. The solution samples were counted and the relative* data in terms of counts per minute per gram of debris for each isotope of interest was obtained for each sample. One of the samples was chosen as the standard and radiochemical separations were performed in order to obtain absolute disintegration rates. Since the solution sample relative data were all normalized to that of the standard sample it was possible to convert all of the data to absolute values through application of the standard sample separation data. These results are presented in Table I-VII.

Since the final inventory results were dependent upon knowledge of the total amount of each type fission product produced in the SL-1, a control sample was obtained. This sample was taken from Element 14, Plate E-31, at a position 18 inches from the top of the element. The choice of this sample was based upon the existence of information related to the neutron flux and the small variation in the location of the peak flux during operation. From these and other analytical data it was possible to calculate the amounts of fission products present and to compare with the empirical data obtained. See Table I-VI.

During the aforementioned portion of the study, insufficient consideration was given the insoluble residue and the related fission product retention. The debris had been subjected to acid dissolution during the uranium inventory and following the filtering process the insoluble residue was discarded. There did exist, therefore, a question as to what portion of the fission products was actually discarded since the residue samples were very radioactive (5-25 R/hr at 1 foot for a 5 gm sample).

Because of the need for a greater recovery of fission products it was believed that a fusion of the debris into a soluble compound would produce the desired results. Laboratory experiments were set up to determine which fusion process, if any, would work most satisfactorily with the type of debris present. Potassium pyrosulfate, sodium carbonate and sodium hydroxide compounds were each tried as the flux in the fusion process. The latter proved to be the most successful and is described in Appendix B.

* It was impossible to determine an absolute disintegration rate from the geometry of the vials which contained the solutions.

Following the laboratory test, a furnace and the necessary equipment for the work were set up in the Hot Cell Area as the fusion process was to be applied to extremely "hot" samples which required shielding for the reduction of personnel exposures. Six samples were subjected to the sodium hydroxide fusion and they included one sample of coarse screening material, one sample of medium screening material and four samples of fine screening material.

After the fusions were completed, the samples were dissolved in dilute hydrochloric acid. These samples were then handled in the same manner as were the solution samples from the uranium inventory, i.e., the solutions of known dilution were prepared in vials and counted using the reproducible geometry. Then, radiochemical separations were performed on the solution chosen as the standard to give samples of ideal geometry and allow absolute determinations to be made.

The gamma-ray spectra obtained from counting the vials revealed anomalous results since the only fission product present in significant amounts was Cs-137. A study of the techniques associated with the handling of the samples during the fusion process led to the conclusion that the results had been affected by the temperature either through volatilization into the atmosphere and/or migration into the platinum crucible. Figure I-18 is a complex spectrum of fission products from the solution samples and Figure I-19 is a spectrum of a fusion sample which shows a decided decontamination effect.

Strontium separations were performed on each of the fusion samples and these data showed considerable variation which was originally believed to be due to sampling techniques. The agreement between duplicate separations performed on the same solution, however, did not provide the uniformity required.

The results obtained from ICPP analyses are presented in Table I-VIII. The ICPP results indicate very good agreement with the fuel analysis made at the ITS Laboratory; however, the ITS uranium results were obtained through numerous analyses since sampling introduced obvious and severe variations in the results from single samples. It is believed that the results of all "spot" sampling for fission products in the debris would be subject to the same considerable "scatter."

It is therefore felt that the Cs-137 results listed in Table I-VI are correct for the set of samples involved. It is known that fission products were lost when the insoluble residue was discarded and that possibly some of Cs-137 atoms were lost in the fusion process. It is concluded, therefore, that the number of Cs-137 atoms present in the debris, 1-3-61, was not less than $2.89 \times 10^{22} \pm 20\%$, which is the average of the total debris results of Table I-VII, based on the ITS data only. This represents 571±114 curies of Cs-137.

2.2 Alpha-Alumina Studies

During the final phase of the SL-1 investigation, additional analyses were performed on the debris from the reactor pressure vessel to quantitatively determine the amount of alpha-alumina, α-Al_2O_3, present in the fine grade of debris screening ($<$ 12 mesh). Earlier work related to this study included the examination of the insoluble residue following acid dissolution; however, the most recent work was performed on a composite sample without the removal of the soluble portion.

The composite sample of fines weighing 113.3338 grams was obtained from several containers in the Radioactive Materials Laboratory. The radiation level associated with this sample was greater than 25 R/hr at 1 foot; however, manual methods were required to perform the subsequent screening process. A lead brick shield was constructed and the sample poured into the series of sieves which included 20 mesh, 80 mesh and 200 mesh screens. The sample was shaken and each grade of screening weighed. Table I-IX is a presentation of the screening data. These data compare favorably with those obtained previously and it is believed that the anomalies that are present are due to the presence of soluble solids of varying sizes, which were not present in the samples reported in IDO-19311.

Following the screening process, X-ray powder samples were prepared from the two finest grades of screenings. Since difficulty was encountered in the sample preparation process, this study was not completed. Additional sample material was not available, thereby eliminating a repeat analysis. See Final Report of SL-1 Recovery Operation, May 1961 Thru July 1962, TM 62-7-704, IDO-19311, Page III-76.

2.3 Flux Wire Analysis

During the final phase of the SL-1 investigation six identifiable flux wires were dismantled and counted. These flux wires brought the total number of recovered pellets to 395 for an 83% recovery. A number of unidentified pieces of flux wires were discarded because there was no possible means to associate them with a particular location. Results, supplemental to those in IDO-19311, are tabulated in Appendix E. Table I-XVI and Figure III-3 give the overall flux profile of the excursion, and Figure I-42 shows profiles along some of the wires.

2.4 Fuel Studies

2.4.1. Chemistry

The SL-1 core was fueled with U-Al alloy fuel clad with X8001 Al-alloy. Final uranium content of fabricated plates was about 8.0 wt % with some variation from plate to plate. U^{235} enrichment was 93.%. Analysis of a new fuel sample is shown in Table I-X.

Several samples were taken from post-incident fuel elements selected from one quadrant of the core. These samples were taken adjacent to metallographic and physical test samples, Figure I-20, to allow correlation of fuel depletion with metallurgical analysis. Core location of sampled elements is shown in Figure I-21. See Appendix A for description of sampling procedure and sample designation.

Total uranium content and isotopic composition of samples are shown in Table I-X. Fuel burnup profiles as a function of axial distance from the top of the fuel element are shown in Figures I-22 through I-24. An obvious discrepancy in U^{235}/U^{238} ratio and the % burnup can be seen in sample FC47-3, and should be regarded as a poor sample. This point was not used in plotting the burnup profile for fuel element #47.

2.4.2 Metallurgy

Metallography and tensile blanks, as indicated in Figure I-20, were used for examination. Metallography specimens were mounted in pairs to give one longitudinal and one transverse specimen in each mount. The specimens were mounted by hand loading with the remote specimen mounting press.

Metallography

The metallographic specimen sets were taken to the HCA for polishing with the remote automet equipment. The specimens were photographed through the periscope then etched with 0.5% HF for examination on the remotized metallograph.

Zone Unaffected by Heat

Photograph through the periscope typical of all specimen sets outside of the heat-affected zone is shown by Figure I-25. The long specimen is the longitudinal and the short specimen is the transverse section. The structure of the meat from specimens out of the heat-affected zone is the same as the structure of unirradiated meat. Typical photomicrographs are shown in Figure I-26.

Heat-Affected Zone

There are three temperature (temperature reached during incident) zones within the meat in the heat-affected portion of the fuel plates. These zones can be seen in Figure I-27, which shows the high temperature zone in the center, the intermediate temperature zones next to the center, and the lower temperature zones on the outside next to the cladding.

The temperature zones are apparent on a macro scale. Figure I-28 shows a macrophotograph of the specimens taken 7" down on a plate from fuel element cartridge 52. The longitudinal specimen has only a fine dark line through the center. This area of the meat had reached the intermediate temperature zone. The structure at the center of this sample is shown at 500x in Figure I-29a, with the structure away from the center shown in Figure I-29b. The macrophotograph of specimen from fuel element cartridge 6 at 4" from the top, shows this intermediate temperature zone as it disappears on the longitudinal section, Figure I-30. The series of photomicrographs, Figures I-30a and I-30b, show the structure change as a traverse is made down the longitudinal specimen into the intermediate zone.

The three temperature zones were observed on one other specimen set besides the one shown in Figure I-28 from fuel element 52 at 7" from the top. This specimen set was from fuel element 47 at 15" from the top in the maximum heat-affected area. Macrophotograph of the specimens is shown in Figure I-32. The structure at the center of the fuel plate meat is shown in Figure I-35a. This figure with I-33a and I-33b represents a traverse across the heat-affected portion of the fuel plate meat. The meat outside the intermediate temperature zone has the same structure as the meat of specimens outside the heat-affected zone, Figure I-35b.

The remainder of the specimen sets taken from within what was observed to be a heat-affected zone, as indicated on the drawing of the specimen locations, had all the fuel plate meat in the high temperature zone, Figure I-36.

It is apparent that some of the clad has melted and is alloyed with the meat in the high temperature zone. In some places melt beads were observed to run out between the fuel plates. One of these melt beads, sectioned, is shown in Figure I-37.

There is close agreement between metallographic examination and the observed heat-affected zone, as seen through the periscope of the RML. Thus, by observing that the first phase change in Al-17% U is at 640° C, it appears that for the fuel plates examined the core temperature was 640° C or greater in the coarse shaded areas as shown on the drawing of fuel specimen locations, Figure I-20.

Examination of clad corrosion showed the corrosion to be fairly uniform at 2.5 to 3.5 mils thick, Figures I-38a and I-38b.

2.4.3 Tensile and Hardness

Tensile specimen blanks were obtained from the fuel plates as shown by Figure I-20. These blanks were then punched into tensile specimens using a special tensile specimen punch. The details on this fixture are included in Appendix A.

The hardness was taken on each end of the tensile specimen tabs before they were tested in the Tinius-Olsen tensile test machine. The hardness and tensile test data are summarized below:

Sample No.	Rockwell 15T	UTS	YS	Percent Elongation
Control	31	134,850	81,563	18.4
Control	31	134,850	79,388	18.4
Control	31	143,550	71,775	16.9
FT39-3	50-45	165,953	130,500	5.1
FT39-25	44-38	174,000	156,600	5.1
FT60-3-A	--	160,950	115,275	5.1
FT60-3-B	45-45	170,955	147,900	8.8
FT60-3-C	40-37	170,085	134,850	4.4
FT60-10	55-42	188,355	174,000	2.9
FT60-18-A	39-42	197,490	178,350	3.1
FT60-18-B	52-43	184,875	--	3.7
FT6-3	45-55	170,085	147,900	2.2
FT47-3-A	41-51	168,345	121,800	8.8
FT47-3-C	31-42	165,300	128,325	3.7

There is, as expected, a marked difference in the hardness and tensile properties from unirradiated to irradiated specimens. The yield strength has almost doubled. The percent elongation is about a third in most cases. Attempts to correlate the variations in properties within the irradiated specimens with radiation exposure showed very little correlation.

2.4.4 Density

The density of fuel sample is dependent on the heat-affected area from which the sample is taken. This is apparent by comparing the densities as summarized below with the position of the tensile samples in Figure I-20.

Sample	Density	Relative Heat Damage
F4	2.888	None - Control Sample
F6	2.902	None - Control Sample
F8	2.898	None - Control Sample
FT52-2	2.880	Outside heat-affected area
FT39-2	2.746	One end inside heat-affected zone
FT39-25	2.662	All inside heat-affected zone
FT60-3	2.914	Outside heat-affected zone
FT60-10	2.905	Outside heat-affected zone
FT60-18	2.921	Outside heat-affected zone
FT6-3	2.767	One end inside heat-affected zone
FT47-3	2.704	Outside heat-affected zone
FT47-12	2.737	One half inside heat-affected zone
FT47-18	2.681	All inside heat-affected zone

2.5 Boron Studies

2.5.1 X-Ray Diffraction

The boron-aluminum poison strips from the SL-1 core were covered with a tenacious corrosion film. This film appeared hard, brittle and black. Samples of the film were taken for X-ray powder pattern identification. The material was shown to be alpha-basic aluminum oxide. The pattern indicated no other oxides in the film, which indicates only a single corrosion product on the poison plates.

2.5.2 Chemistry

The boron poison plates in the SL-1 reactor consisted of strips, either full or half fuel element length, spot welded to the edges of fuel elements to provide a source of burnable poison. These strips were made of elemental boron and X8001 aluminum alloy. The composition of new poison plate material was 0.423±0.016 wt. % boron, enriched to 92.94± 0.22% B^{10}.

Subsequent to dismantling the core, selected samples of boron-aluminum strips were taken from one quadrant of the reactor. These were analyzed for wt. % boron, and boron isotopic composition for correlation with physical appearance and metallographic examination. The analyses are shown in Table I-XI. The reference numbers correspond to the sample locations shown on the plate diagrams in Figure I-39. See Appendix A for description and identification of samples. Figures I-40 and I-41 show the axial B^{10} burnup as a function of distance from the upper end of the plate.

The corrosion and deterioration of the poison plates can be seen to be related directly to the B^{10} depletion.

The core locations of poison strips from which samples were selected are shown in Figure I-21.

2.5.3 Macro Examination

Metallographic samples were taken from four boron poison strips, Figure I-39. The strips chosen were from the low flux through the peak flux zones.

Boron strip #11 was still intact with only slight deterioration on the edge 17" from the top. Longitudinal and transverse samples were cut 3-1/2" from the top, 16" from the top and 2" from the bottom. These samples are shown mounted in Figures I-43, I-44 and I45. There is very little deterioration in the sample taken near the top but the deterioration is pronounced in the higher neutron area.

There were only four samples taken from strip #6. The mounted samples are shown in Figures I-46 and I-47. The first two samples were taken from a non-deteriorated area near the top, while the second two samples were taken from the deteriorated edge.

Only two samples were taken from strips #32 and #22. These were taken from the bottom deteriorated edge, Figures I-48 and I-49.

The lamination type of deterioration is evident on all the samples from the deteriorated edge, Figures I-47, I-48 and I-49, as well as the samples from strip #11 taken from the area of highest flux, Figures I-44 and I-45. This lamination was observed before the samples were cut from the strips as shown by Figure I-50.

It is apparent that deterioration is related to flux. Comparing the samples taken from the various strips with the boron burnup, Figure I-40 and I-41, it appears samples from areas with less than 30% burnup have no apparent deterioration, whereas samples with more than 56% burnup are deteriorated.

2.5.4 Micro Examination

The samples were polished for metallographic examination using the remotized automet equipment in the HCA. After polishing, the samples were etched with 0.5% HF, then examined on the remote metallograph.

There are three areas on each sample which were of interest:

1. There was edge corrosion on all samples which ranged from 2-1/2 mil. to 3-1/2 mil. thick, Figures I-51a and I-51b. The Bakelite in which the samples are mounted caused the corrosion film to crack as it cooled. The edge corrosion film appears to have two shades - one a lighter gray than the other. X-ray diffraction has shown there to be only one corrosion product, α $Al_2O(OH)_2$. The light gray portion of the corrosion film next to the Bakelite mounting is apparently the corrosion product from the clad (remains of the extrusion envelope), where the darker gray is corrosion product from bulk plate.

2. There is a second corrosion area in samples from the higher flux zones which is similar in appearance to the darker gray portion of the edge corrosion film but is internal. The edge corrosion film and the internal corrosion are shown in Figures I-51, I-52 and I-53a. X-ray diffraction shows this corrosion product to be the same as the edge. This internal corrosion appears to form as laminations along the rolling axis of the strip. This corrosion only appears in the samples which show laminar deterioration in a macrophotograph. The amount of internal corrosion is related to the flux the sample has seen, but the exact corrosion mechanism has not been determined.

3. The third area of interest in the boron poison strip is the bulk area not affected by internal edge corrosion. There is little or no difference in the appearance of the bulk uncorroded areas from samples with low neutron exposure and samples with peak neutron exposure. The uncorroded area, Figure I-53b, in a high radiation zone has structurally the same appearance as the unirradiated sample. There could be some difference around the boron inclusion, but high enough magnification to determine a difference was not obtainable without going to electron microscopic examination.

2.5.5 Tensile

The tensile properties of the boron poison strips are summarized below.

Sample No.	UTS psi	YS psi	% Elongation
BT6-3-A	25,355	25,116	--
BT11-3-A	25,355	24,518	--
BT11-3-B	25,953	24,279	03.0
Control	25,355	18,777	02.2
Control	31,694	17,581	02.2

There were not enough specimens tested to statistically determine the amount of variation of the tensile strength relative to the integrated neutron flux. From the number of samples tested it appears there is very little change noted in the tensile properties between the unirradiated and irradiated specimens. However, the yield strength of the irradiated test samples appears to have increased by about 30%.

2.5.6 Density

The density of the boron strip seems to have a fairly wide range in both unirradiated and irradiated specimens. The density for four control samples and four irradiated samples is as follows:

Control Samples

Specimen No.	Density
B1	2.743
B3	2.732
B5	2.720
B8	2.738
Irradiated	
BT11-3	2.729
BT6-3	2.729
BT32-3	2.688
BT22-3	2.722

The density of the irradiated samples, with the exception of sample B5, is consistently lower.

2.6 Cadmium Control Rods

2.6.1 Chemistry

Four samples were taken from the center control rod for Cd isotopic composition determination. The samples were taken from one of the cruciform blades (7-4)* adjacent to samples obtained for physical test and metallography, Figure I-54. See Appendix A for description and identification of samples.

Because of special treatment required for the determination of Cd isotopes, the samples were analyzed at the Oak Ridge National Laboratories. Table I-XII shows the isotopic analysis and indicates Cd% burnup (Cd^{113} depletion). Analysis of normal cadmium is included for reference.

A burnup of Cd (% depletion) vs. distance along the control rod blade is shown in Figure I-55.

2.6.2 Metallurgy

Specimens were removed from the cadmium blades, as indicated in Figure I-54. See Appendix A for description and identification of samples.

* Blade 7-4 was located between fuel element #7 and fuel element #4.

Samples were mounted in the RML and transferred to the HCA for metallographic preparation. Typical specimens are shown by Figures I-56, I-57 and I-58, which show an edge weld, spot weld and longitudinal section respectively.

The structure of the cadmium varied from sample to sample. There was some evidence of grain growth. The existence or non-existence of twins seems to follow no set pattern. Figures I-59a and I-59b show the difference between these two structures. It should be noted that the cadmium, as examined, was probably cold worked, not only during recovery operation but during handling and mounting. Figure I-60 shows some of the distortion which apparently occurred during the incident.

The variation in structure in relation to the cadmium metal away from the edge and the metal adjacent to the edge weld is shown in Figure I-61. There was evidence that melting had occurred during the welding at the cadmium edge next to the weld. A sample from an unirradiated blade was examined. The sample sections are shown in Figures I-62, I-63 and I-64. The edge next to the weld had melted. There was no evidence of cadmium present in the weld by emission spectrography analysis. Other things of interest were found. The blade* during sectioning was found to be full of water. Considerable corrosion attack was evident in the cadmium and on the aluminum cladding. Only one of the four spot welds was holding.

The blades examined in the RML were also noted to have very few spot welds holding. It was first thought this had been caused by the incident, but the indication is that many of the spot welds may have been very weak to start with. The cross section of a spot weld from the unirradiated blade is shown in Figure I-64. Fusion of the clad alloy appears in good condition.

Many of the edge welds of the post-incident blades were either cracked or split open. See Figures I-65b and I-66.

The existence of water between the clad material of the cadmium blades could contribute to rapid steam formation resulting in swelling of the blades. There would be high stresses at the stress riser, Figures I-56 and I-67, when one plate tended to shift past the other as the blade buckled. The existence of poor spot welds would not help reduce this shifting of one plate past the other. That such a shifting of plates took place is indicated by Figure I-60.

The existence of water in between the aluminum clad material would contribute to the corrosion observed on the cadmium blades and the clad material. The amount of surface corrosion observed on the interior surfaces of the blades is not considered severe enough to have affected the nuclear characteristic of the control rods.

* This blade was the one used in the storage pool as a mockup model to determine ramp-rod withdrawal rates.

Tensile

Tensile specimen blanks were taken from the cadmium blades as shown in Figure I-54. The blanks were used to obtain the density then punched into tensile specimens with a special tensile punch unit. See Appendix A. The data obtained from the tensile specimens are shown in Table I-XIII.

There is a marked decrease in ductility in the irradiation specimens compared to the control specimens. The ductility is still fair even in the severest case (12%). The specimens showed no definite yield point but more of a continuous yielding.

The specimens were noted to have a fairly severe corrosion coating which flaked off during the tensile test.

Density

The density of the cadmium varies widely even in the control samples as shown by the following summary:

Density of Cadmium Tensile Specimen*

Specimen No.	Density	Relative Exposure
5L	8.630	Control sample
4T	8.621	Control sample
3L	8.598	Control sample
1L	8.622	Control sample
2T	8.616	Control sample
C9T - 6	8.62	Low flux zone
C9T - 12	8.38	Intermediate flux zone
C9T - 33	8.26	High flux zone
C9T - 22	8.20	High flux zone

The irradiated samples from the high flux areas have low densities. This is evident when comparing the density of the irradiated samples with their location in #9 blade, as shown by Figure I-54.

2.7 Aluminum Shroud

2.7.1 Metallography

Specimens were taken from the aluminum shrouds as shown by Figure I-68. Samples of the shroud material generally were obtained by cutting transverse strips with an abrasive wheel, using water coolant, and then cutting the smaller samples from these strips with an air-powered shear. See Appendix A for description and identification of samples.

* This blade was the one used in the storage pool as a mockup model to determine ramp rod-withdrawal rates.

Metallography specimens were mounted in the RML and prepared for examination in the HCA. Typical specimens are shown in Figures I-69 and I-70. The specimen set in Figure I-69 represents longitudinal section (long specimen) and transverse specimen (short specimen). Figure I-70 shows the weld cross section where one weld has failed.

The cause of weld failure is apparent by examining the weld section of Figure I-70 after etching and shown in Figure I-71. There is lack of penetration in both the weld which failed, Figure I-71a, and the one which did not fail, Figure I-71b. This condition is not present in all the shroud welds, but many of the welds lacked adequate penetration. Figure I-72 shows the inside of a weld seam where both poor and good penetration exists. Weld failures were caused by weakness at the weld due to lack of adequate weld penetration.

The general structure and corrosion depth of both longitudinal and transverse specimens is shown in Figure 73a. The weld structure and corrosion at interface of unfused weld joint is shown in Figure 73b.

2.7.2 Tensile and Hardness

The tensile specimen blanks were obtained from the aluminum shroud, as shown in Figure I-68. The blanks were used to determine the density and then punched into tensile specimens with the tensile punch unit.

The hardness was determined using the tensile specimen tabs before the specimens were tested on the Tinius-Olsen tensile test machine. The hardness and tensile data are tabulated in Table I-XIV. The data are varied, but even in the extreme case the material still has good ductility and reasonable strength. There is little, if any, correlation between radiation exposure and apparent property. The cold work during the incident would be the prime contributing factor to the variations observed in the physical properties.

2.7.3 The density of shroud tensile specimens is very constant as shown below:

Specimen No.	Density
S9T- 4	2.72
S9T-27	2.72
S9T-60	2.73
S9T-40	2.72
S1T-46	2.73

There has been no observed indication of damage to the shroud material other than in the seam welds.

3. Miscellaneous Analysis

3.1 Shield Plug Flange Studs

Six studs were removed from shield plug #8 nozzle flange. The studs, after being decontaminated, were machined into tensile and metallography specimens. The tensile specimens were made to the NRL square end tensile specimen specifications.

The hardness was obtained on the square shoulder of the tensile specimens before they were tested. The hardness measurements, along with the tensile test measurements from the six specimens, is summarized in Table I-XV.

The results from the hardness and tensile tests indicate the studs were uniform in strength and apparently were not severely cold worked during the incident, though the last four to five threads were stripped off, Figure I-74. The lack of severe cold work is indicated by the 13 to 16% elongation and 57 to 64% reduction in area. Highly cold worked ferritic steel of this tensile strength range (136 to 160 K psi) would show much lower elongation and reduction in area.

The microstructure in the studs shows some general deformation but not severe. The structure near the sheared threads shows slightly more deformation than the rest of the cross section. The thread had fractured with very little deformation. The fractured edge of the threads could not be observed because of the heavy attack of chemicals used in decontamination of the studs.

3.2 Model Explosive Tests

The tests conducted on a 1/4 scale model of the SL-1 pressure vessel at Aberdeen Proving Ground and reported in IDO-19311 did not yield all the experimental information desired. It was felt that these tests could provide significant corroboration of the theoretical analysis of the water hammer effect during the incident.

The Aberdeen tests succeeded in showing that a 1/2-pound charge of Pentolite in the scale model, equivalent to a 32-pound charge in the full scale SL-1, released sufficient energy to create the water hammer effect observed from the incident. The continuation of these tests at the Idaho Test Station was aimed at determining the water and plug velocities, the height to which the vessel would rise, and the deformation to the vessel resulting from the high pressure. The tests were recorded with a high speed motion picture camera.

Test I - Open top vessel incident water level, 1/2 pound Pentolite charge.

Results: All the water above the charge was ejected and the bottom of vessel was blown away. The water velocity was measured to be 225 ± 25 feet/sec as it left the vessel. See Figure I-80.

Test II - Head in place, incident water level, 1/2-pound charge of Pentolite.

Results: Despite the fact that the vessel wall around the charge was protected by a mockup of the thermal shield and a sponge rubber lining, the charge still blew open the vessel wall just above the thermal shield, Figure I-81. The broken wall imbedded itself into the dirt of the hole in which the vessel was placed and limited the rise of the vessel to about 4 inches (equivalent to 16 inches for the full scale SL-1). Much of the effectiveness of the generated pressure for producing a water hammer effect was lost through the broken wall. Nevertheless, the shield plug nozzles did burst, Figure I-82, though the reduced water hammer pressure was insufficient to collapse the rod guide tubes. The shield plugs were ejected with a velocity of 70±10 ft/sec.

TABLE I-I

Carbon Steel Gamma Scanning Data

Mn^{54} Fast nvt

Date	Time	Sample Number	Count Time Minutes	0.82 Mev Area	Sample Weight Grams	cpm/gm at Ct.	(1) cpm/gm	$N_x = \frac{(cpm/gm)x^{(1)}}{(cpm/gm)std}$	nvt (2)
		CS- 1							
8-14-62	1551	CS- 2	999.9	15332	2.2756	4.50	4.43	0.2074	8.42×10^{13}
	1336	CS- 3	120	2390	1.5075	8.96	8.82	0.4129	1.68×10^{14}
	1133	CS- 4	120	3985	1.9457	11.20	11.02	0.5159	2.09
	0923	CS- 5	120	6647	2.8799	12.90	12.70	0.5946	2.41
8-10-62	1425	CS- 6	90	6227	1.9521	22.13	21.58	1.0084	
	1555		600	40925		21.62	21.08	0.9850	
8-11-62	0155			41020		21.72	21.24	0.9925	
	1155			41404		22.03	21.55	1.0070	
	2155			41211		21.87	21.32	0.9963	
8-12-62	0755			41242		21.93	21.49	1.0042	
	1755			41384		22.03	21.55	1.0070	
		Standard Sample Results					21.40 Ave.	1.000±.009	4.06×10^{14} (3)
8-13-62	1024	CS- 7	120	20430	1.2788	82.89	81.23	3.80	1.54×10^{15}
8-15-62	0906	CS- 8	60	46984	1.5270	342.50	338	15.8	6.41
8-13-62	1529	CS- 9	30	120858	1.2814	3145	3104	145.3	5.90×10^{16}
9-21-62	1015	CS-10	5	74233	0.5556	26700	28526	1335	5.42×10^{17}
	1025	CS-11	3	102772	0.7261	47200	50427	2361	9.59
	1031	CS-12	2	135935	0.9486	71700	76603	3586	1.46×10^{18}
	1035	CS-13	2	150933	0.9432	80000	85470	4001	1.62
	1040	CS-14	3	107716	0.6578	54600	58340	2731	1.11
	1045	CS-15	5	76384	0.5581	27400	29274	1371	5.57×10^{17}
	1110	CS-16	10	27054	0.4229	6400	6838	320	1.30
	1125	CS-17	30	37805	0.5107	2470	2639	124	5.03×10^{16}
	1250	CS-18	60	28935	0.5123	941	1005	47.1	1.91
	1511	CS-19	60	12632	0.2866	735	785	36.8	1.49
9-24-62	0843	CS-20	240	57296	0.4259	561	606	28.4	1.15
	1614	CS-21	240	82702	0.6393	539	582	27.2	1.10
	1247	CS-22	180	59496	0.6321	523	565	26.5	1.08
	1551	CS-23	240	94265	0.7441	528	570	26.7	1.08

(1) All relative cpm/gm data corrected to 8-21-62, which is the date the radiochemical separations were performed.

(2) nvt = $(N)_x(nvt)_{std}$, and provides the absolute integrated flux at 1-3-61.

(3) This nvt of standard is corrected back to 1-3-61 from 8-21-62.

TABLE I-II

Stainless Steel Gamma Scanning Data

Co^{60} Thermal nvt

Date	Time	Sample Number	Count Time Minutes	1.33 Mev Area	Sample Weight Grams	cpm/gm	$\frac{(cpm/gm)_x}{(cpm/gm)_{std}}$	nvt
8-2-62	0918	SS- 1	120	1478	0.3745	32.8	0.1100	7.42×10^{14}
	1120	SS- 2	120	3592	0.3848	65.0	0.2179	1.48×10^{15}
	1326	SS- 3	120	5513	0.3067	127.2	0.4264	2.89×10^{15}
	1530	SS- 4	240	26930	0.5545	186.8	0.6262	4.25×10^{15}
8-3-62	0920	SS- 5	120	13524	0.3406	299.8	1.0050	
	1257		120	13454		297.1	0.9960	
	1500		999.9	111490		299.2	1.0030	
8-4-62	0700		999.9	110644		297.7	0.9980	
	2300		999.9	112269		298.6	1.0010	
8-5-62	1500		999.9	111183		297.4	0.9970	
	Standard Results					298.3) Ave.	1000±.0036	6.75×10^{15}
8-6-62	1051	SS- 6	120	57606	0.6941	676.0	2.2662	1.54×10^{16}
	1255	SS- 7	60	68153	0.5460	2061.7	6.912	4.69×10^{16}
	1404	SS- 8	60	167963	0.5451	5116.1	17.151	1.16×10^{17}
	1507	SS- 9	20	389172	0.6665	29196	97.9	6.64×10^{17}
9-25-62	0836	SS-10	2	72061	0.3391	1.06×10^{5}	355	2.41×10^{18}
	0847	SS-11	5	441907	0.4234	2.09×10^{5}	701	4.75×10^{18}
	0854	SS-12	5	510019	0.3282	3.11×10^{5}	1043	7.07×10^{18}
	0902	SS-13	5	685837	0.3699	3.71×10^{5}	1244	8.43×10^{18}
	0910	SS-14	3	568039	0.7542	2.51×10^{5}	841	5.71×10^{18}
	0930	SS-15	1	40495	0.3389	1.20×10^{5}	402	2.73×10^{18}
	0933	SS-16	5	73319	0.3857	3.80×10^{4}	127	8.61×10^{17}
	0941	SS-17	10	63095	0.4255	1.48×10^{4}	49.6	3.36×10^{17}
	1146	SS-18	30	110472	0.3774	9.76×10^{3}	32.7	2.22×10^{17}
	1319	SS-19	30	66487	0.3270	6.78×10^{3}	22.7	1.54×10^{17}
	1355	SS-20	30	57449	0.4289	4.46×10^{3}	15.0	1.02×10^{17}
	1436	SS-21	180	185040	0.2802	3.67×10^{3}	12.3	8.34×10^{16}
	1508	SS-22	60	40980	0.1846	3.70×10^{3}	12.4	8.40×10^{16}
	1610	SS-23	30	18120	0.1711	3.53×10^{3}	11.8	8.00×10^{16}

TABLE I-III

Mn^{54} Decay Data

Group	$\phi T)_n$	$\phi T)_n / \phi T)_{ave}$	Decay Time (Days)	$e^{-\lambda t_n}$	$\frac{\phi T)_n}{\phi T)_{ave}} e^{-\lambda t_n}$
1	70	0.526	1313	0.055	0.0289
2	130	0.977	1157	0.078	0.0762
3	120	0.902	1035	0.101	0.0911
4	45	0.338	974	0.117	0.0395
5	220	1.654	873	0.145	0.240
6	90	0.677	767	0.183	0.124
7	250	1.880	659	0.252	0.474
					Σ 1.0737

$$\phi T = \frac{930}{133} \frac{Dm}{V \Sigma \lambda \sum_{n=1}^{7} \frac{\phi T)_n}{\phi T)_{AVE}} e^{-\lambda t_n}}$$

$$= 4.02 \times 10^{14} \text{ nvt}^{**}$$

** This is the integrated fast flux computed from the standard sample analysis.

TABLE I-IV

Hardness and Tensile Data from Pressure Vessel Tensile Specimens

Sample Number	Fast Neutron Activation nvt	Hardness 30N	Hardness B	Yield* Strength (S_y)psi	Tensile Strength (S_u)psi	Percent Elongation	Percent Reduction in Area	Direction	Estimated Cold Work % Elongation
1-45	8.4×10^{13}	32	B90	82400	85000	11	49	H	7.5
2-45	8.4×10^{13}	32	B90	80800	85200	11	47	H	
6-45	8.4×10^{13}	30	B89	73000	84000	15	56	H	
7-45	8.4×10^{13}	31	B90	71900	83300	14	54	H	
8-45	8.4×10^{13}	31	B91	78300	83500	12	43	H	
9-45	8.4×10^{13}	31	B90	77100	83500	13	54	H	
5-46	2.4×10^{14}	22	B81	47300	71300	28	57	H	0.0
6-46	2.4×10^{14}	21	B81	45700	69700	27	59	H	
2-46	2.4×10^{14}	23	B83	49700	71000	21	57	V	
4-46	2.4×10^{14}	21	B80	45500	70300	26	58	V	
2-47	1.5×10^{15}	30	B84	49100	72100	21	55	V	1.13
3-47	1.5×10^{15}	22	B83	Not shown	72600	26	60	V	1.13
1T50	1.8×10^{16}	33	B93	81000	90200	13	49	-	Unknown
2T50	1.8×10^{16}	32	B93	81000	90800	14	47	-	Unknown
2-48A	5.6×10^{17}	25	54	58100	73400	24	61	V	1.9
2-48B	5.6×10^{17}	23	54	55700	73500	23	61	V	
3-48A	5.6×10^{17}	26	53	55000	72700	22	58	V	
3-48B	5.6×10^{17}	23	53	55400	72100	22	61	V	
4-48A	5.6×10^{17}	24	56	59500	73200	21	63	H	
4-48B	5.6×10^{17}	22	53	61300	74100	21	64	H	
5-48A	5.6×10^{17}	24	53	55300	71500	22	62	H	
5-48B	5.6×10^{17}	24	55	57300	72500	22	64	H	
2-49A	1.9×10^{16}	25	53	49300	78200	27	61	V	
2-49B	1.9×10^{16}	27	54	49800	80600				
3-49A	1.9×10^{16}	24	56	50500	81000	26	56	V	
3-49B	1.9×10^{16}	23	52	53700	72300	24	61	V	
4-49A	1.9×10^{16}	22	52	53000	72300	22	61	H	
4-49B	1.9×10^{16}	22	51	56600	71800	25	62	H	
5-49A	1.9×10^{16}	22	52	54800	71600	21	62	H	
5-49B	1.9×10^{16}	23	52	46700	79300	30	59	H	

* 0.2% offset

TABLE I-V

Hardness and Tensile Data from Pressure Vessel Flange Studs

Sample Number	Rockwell Hardness 30N	C	Yield Strength psi	Tensile Strength psi	Elong. %	% Red. in Area
G-1	51	C27	118K	132K	15	64
G-2	43	C30	114K	130K	14	66
H-1	51	C32	134K	148K	13	59
H-2	51	C32	133K	146K	14	60
J-1	53	C33	--	144K	13	58
J-2	52	C32	135K	148K	14	59
I	52	C32	122K	138K	15	60

TABLE I-VI

Fuel Punching Fission Product Analysis

Punching Weight = 0.5501 gm
Total Uranium = 4.14%
U^{235} Enrichment = 90.69%
U^{235} Burnup = 10.87% *
Uranium Weight = 2.28×10^{-2} gm
U^{235} Weight = 2.07×10^{-2}
U-235 Burnup = 2.25×10^{-3}

$$Cs^{137} \text{ atoms produced} = \frac{(6.023 \times 10^{23})(2.25 \times 10^{-3})(6.15 \times 10^{-2})}{2.35 \times 10^{2}}$$

$$= 3.55 \times 10^{17} \quad (1)$$

$$Cs^{137} \text{ atoms produced} = 2.39 \times 10^{17} \quad (2)$$

(1) Calculated using empirically obtained parameters.
(2) Derived from counting solution sample of punching; see sample 25 Table I-VI.

* Using flux wire data obtained in August, 1960, before the incident (C. W. Luke, unpublished data) a burnup of 10% is calculated for this region, the same as the isotopic analysis result.

TABLE I-VII

Debris Fission Product Inventory Study

Uranium Inventory Debris Solution Samples

Sample	Sample Size	Count Date	Time	$Cs^{137})_R$ (1)	N(2)	$Cs^{137})_A$ (3)	Debris Weight	dpm	# of Cs^{137} Atoms (7) 1-3-61
56	Fine	8-23-62	1450	3.55×10^{7}	0.15	4.53×10^{9}	3.447×10^{4}	1.57×10^{14}	
59	Fine	8-23-62	1304	1.05×10^{8}	0.44	1.33×10^{10}	3.447×10^{4}	4.67×10^{14}	
								Ave. 3.17×10^{14}	7.22×10^{21}
39	Medium	8-23-62	1313	6.21×10^{8}	2.63	7.94×10^{10}	1.31×10^{4}	1.05×10^{15}	
62	Medium	8-23-62	1457	7.57×10^{7}	0.32	9.66×10^{9}	1.31×10^{4}	1.27×10^{14}	
								Ave. 5.89×10^{14}	1.34×10^{22}
40	Coarse	8-23-62	1355	1.15×10^{9}	4.87	1.47×10^{11}	4.54×10^{3}	6.70×10^{14}	
								Ave. 6.70×10^{14}	1.53×10^{22}
14)std.	Punching	8-17-62	1322	2.36×10^{8}	1.0±.0189	3.02×10^{10} (4)	--	Total in Debris(6)	3.59×10^{22}
25)control	Punching	8-21-62	1527	1.49×10^{8}	0.633	1.91×10^{10}	--	1.05×10^{10}	2.39×10^{17}

Total Debris Fusion Samples

Sample	Sample Size	Count Date	Time	$Cs^{137})_R$ (1)	N(2)	$Cs^{137})_A$ (3)	Debris Weight	dpm	# of Cs^{137} Atoms (7) 1-3-61
1F	Fine	9-25-62	1437	1.23×10^{10}	0.728	2.82×10^{10}	3.447×10^{4}	9.82×10^{14}	
2F	Fine		1445	8.64×10^{9}	0.511	1.98×10^{10}	3.447×10^{4}	6.84×10^{14}	
3F	Fine		1455	5.15×10^{9}	0.305	1.18×10^{10}	3.447×10^{4}	4.11×10^{14}	
4F	Fine		1503	4.52×10^{9}	0.267	1.04×10^{10}	3.447×10^{4}	3.59×10^{14}	
								Ave. 6.11×10^{14}	1.39×10^{22}
M	Medium	9-25-62	1356	5.7×10^{9}	0.337	1.31×10^{10}	1.31×10^{4}	1.72×10^{14}	
								Ave. 1.72×10^{14}	3.92×10^{21}
C)std.	Coarse	9-25-62	0908	1.69×10^{10}	1.0±.005	3.88×10^{10} (5)	4.54×10^{3}	1.76×10^{14}	
	(See notes)							Ave. 1.76×10^{14}	4.01×10^{21}
									Total(6) 2.18×10^{22}

TABLE I-VII (Continued)

Debris Fission Product Inventory Study

(1) Relative cpm/gm values at count time

(2) $N = (\text{cpm/gm})\text{sample} / (\text{cpm/gm})_{\text{standard}}$ at count time.

(3) Absolute dpm/gm values; $Cs^{137} = N_{\text{sample}} \times$ standard value. These data are corrected back to 1-3-61.

(4) Duplicate separations performed; $Cs^{137} = 2.91\times10^{10} \pm 3\%$, giving $Cs^{137} = 3.02\times10^{10}$ dpm/gm, 1-3-61.

(5) Duplicate separations performed; $Cs^{137} = 3.73\times10^{10} \pm 2.5\%$, 9-28-62, giving $Cs^{137} = 3.88\times10^{10}$ dpm/gm, 1-3-61.

(6) $\sum$ of number of atoms of Cs^{137} in fine, medium and coarse debris.

(7) $\frac{\text{dpm}}{\lambda}$ = # atoms; $\lambda = \frac{.693}{t\ 1/2} = 4.39\times10^{8}\ \text{min}^{-1}$

TABLE I-VIII

ICPP* Debris Analysis Results

Batch	Volume (Liters)	Uranium (grams)	Curies					
			Cs^{137}	Ce^{144}	Sr^{90}	$ZrNb^{95}$	Cs^{134}	Ru^{106}
1	425	235	121.6	482.4	67.8	8.8	8.6	54.4
2	250	265.8	63.2	250	78.4	5.2	5.1	24.6
3	300	216.3	55.5	223	56.2	5.2	4.5	25.1
4	346	258.1	62.3	275.9	49.6	6.0	5.5	35.7
5	391	202.1	57.6	202.9	42.5	4.0	4.7	19.2
Total	1712	1177.3	360.2	1433.9	294.5	29.2	28.4	159.0
Total in Core (from 930 MwD of operation)			3050	15000	3070			400

* Idaho Chemical Processing Plant; Private communication from A. L. Ayers, Phillips Petroleum Company

TABLE I-IX

Debris Screening Data

Sample Size (Mesh)	Screened Sample Weight (Grams)	Weight Percent	Visual Identification
<12->20	74.5026	65.74	lead shot, sand
<20->80	25.405	22.46	sand
<80->200	9.0889	8.02	fine grit
<200	4.2918	3.79	fine powder

TABLE I-X

SL-1 Uranium Fuel Analysis

Ref. No.	Fuel Element No.	Plate No.	Sample Distance from Top of Fuel Element	Total U Wt % U	Isotopic Composition (%) U^{234}	U^{235}	U^{236}	U^{238}	U^{235} Depletion % Burnup
(Unused)	29	E-316	New Fuel	7.98±0.07	0.95	93.13	0.32	5.60	--
FC6-2	6	E-165	2 in.	7.90±0.15	0.94	92.59	0.77	5.70	2.32
FC6-4	6	E-165	4 in.	7.54±0.14	0.95	92.36	0.90	5.79	4.10
FC6-6	6	E-165	6 in.	3.92±0.07	0.97	91.30	1.74	5.99	8.37
FC39-1	39	E-516	1 in.	8.33±0.15	0.95	92.57	0.77	5.71	2.50
FC39-14	39	E-516	14 in.	4.91±0.08	1.02	90.38	2.48	6.12	11.16
FC39-24	39	E-516	24 in.	4.68±0.08	1.03	89.88	2.83	6.26	13.66
FC39-M	39	E-516	10 in. (molten pc)	10.60.0.16	1.01	90.78	2.19	6.02	9.32
FC47-3	47	E-604	3 in.	8.00±0.15	0.98	90.34	0.75	7.93	31.47 *
FC47-10	47	E-604	10 in.	7.15±0.14	1.02	91.04	1.97	5.79	8.31
FC47-16	47	E-604	16 in.	5.46±0.11	1.03	90.30	2.54	6.13	11.40
FC47-25	47	E-604	25 in.	7.63±0.15	1.01	91.22	1.79	5.98	8.31
FC52-1	52	E-689	1 in.	7.63±0.15	0.97	92.49	0.82	5.72	2.73
FC52-7	52	E-689	7 in.	1.95±0.05	1.02	90.05	2.26	6.67	18.82
FC52-16	52	E-673	16 in.	5.45±0.11	1.02	89.68	2.98	6.32	14.67
FC52-26	52	E-673	26 in.	4.54±0.08	1.04	90.68	2.08	6.20	12.06
FC60-3	60	E-781	3 in.	7.45±0.14	0.97	92.37	0.91	5.75	3.44
FC60-9	60	E-781	9 in.	7.31±0.14	0.98	91.73	1.40	5.89	6.35
FC60-17	60	E-781	17 in.	7.29±0.14	1.00	91.17	1.83	6.00	8.61
FC60-26	60	E-781	26 in.	7.35±0.14	0.99	91.93	1.23	5.85	5.52
--	14	E-131	18 in.	4.14±0.08	1.01	90.69	2.11	6.12	10.87

*Questionable result - Incompatible with sample location.

TABLE I-XI

SL-1 Al-B Poison Strips

Specimen Ref. & Location No.	Total Boron Wt.% B.	Boron Enrichment Wt.% B^{10}	B^{10} Depletion % Burnup
New Al-B Strip	0.423±0.016	92.94±0.22	--
BC6-1	0.41±.01	87.8	45.8
BC6-7	0.31±.01	88.4	42.6
BC6-15	0.22±.01	83.7	61.3
BC11-1	0.33±.01	88.4	42.6
BC11-7	0.19±.01	88.3	43.2
BC11-12	0.21±.03	81.5	66.8
BC11-18	0.20±.01	85.0	57.3
BC11-25	0.35±.01	86.4	52.2
BC22-1	0.34±.01	86.5	51.7
BC22-9	0.20±.02	80.4	69.1
BC32-1	0.37±.01	79.4	70.9
BC32-11	0.23±.02	71.8	80.8

TABLE I-XII

SL-1 #9 Control Rod Cadmium Composition* (Blade 7-4)

Specimen Ref. & Location No.	%Cd^{106}	%Cd^{108}	%Cd^{110}	%Cd^{111}	%Cd^{112}	%Cd^{113}	%Cd^{114}	%Cd^{116}	Cd % Burnup
Normal Cadmium	1.18±.02	0.84±.02	12.31±.05	12.79±.05	24.10±.10	12.30±.05	28.91±.10	7.58±.05	--
C9C-1	1.19	0.84	12.38	12.77	24.10	12.19	28.94	7.60	0.90
C9C-8	1.20	0.85	12.36	12.74	24.14	12.44	29.01	7.57	--
C9C-18	1.12	0.79	12.28	12.91	24.07	12.12	28.93	7.79	1.34
C9C-32	1.14	0.81	12.34	12.81	24.19	11.22	29.98	7.51	9.12

* Analysis performed at Oak Ridge National Laboratories - private communication from John Sites.

TABLE I-XIII

Tensile Data - Cadmium Blades

Sample No.	Ultimate Tensile Strength psi	% Elongation
Control	6270	80
Control	8025	-
Control	9823	83
Control	6395	82
Control	6479	81
C9T-6-A	7315	34
C9T-6-B	7231	29
C9T-12-A	6340	26
C9T-12-B	6897	24
C9T-12-C	5225	26
C9T-12-D	4598	32
C9T-33-A	7398	34
C9T-33-B	7231	15
C9T-33-C	4932	50
C9T-33-D	5099	21
C9T-22-A	7315	28
C9T-19-A	4932	27
C7T-14-A	6479	12
C7T-14-B	5350	19
C7T-26-A	6395	19
C7T-26-B	4890	16

TABLE I-XIV

Hardness and Tensile Data - Aluminum Shroud

Sample Number	Sample	Rockwell Hardness 15T	Tensile Strength (psi)	Yield Strength (psi)	% Elongation
5C	S9T-4	44-51	13675	9400	39.7
6A	S9T-27	--	13440	9750	33.8
6B	S9T-27	50-44	13776	6384	45.0
6C	S9T-27	46-56	12936	8736	39.0
7A	S9T-60	--	13440	7812	41.2
7B	S9T-60	51-45	12768	10100	19.8
7C	S9T-60	41-46	13776	10200	33.8
7D	S9T-60	41-48	13440	11100	23.5
8C	S9T-40	43-52	12432	9750	19.6
8D	S9T-40	58-62	13440	9408	41.2
10B	S1T-27	45-55	12936	8736	--
11A	S1T-46	56-58	13944	9744	30.9
11B	S1T-46	51-38	13507	10730	16.9
12A	S1T-60	50-61	12936	8736	35.3
16A	S7T-4		12768	9408	30.1
16B	S7T-4		13608	8736	35.3
17A	S7T-28		12852	8988	35.3
17B	S7T-28		13608	8064	40.4
18A	S7T-50		12936	8904	40.0
19A	S7T-60		12768	7560	40.4
19B	S7T-60		13608	9072	41.9
20A-1	S6T-2		12852	7392	40.4
20A-2	S6T-2		12768	7476	39.0
20B	S6T-2		13776	8736	39.0
21A	S6T-59		12969	10248	34.5
21B	S6T-59		13776	9072	40.4
22A	S6T-46		13020	10584	31.6
22B	S6T-46		13356	7560	33.1

TABLE I-XV

Hardness and Tensile Data from #8 Shield Plug Flange Studs

Sample Number	Rockwell Hardness 30N	C	Yield Strength (S_y)psi	Tensile Strength (S_u) psi	Elong. %	% Red in Area
A-1	52	31	127 K	143 K	13	62
B-1	52	31	121 K	136 K	15	64
C-1	50	32	119 K	136 K	16	64
D-1	52	30	132 K	146 K	13	60
E-1	53	32	131 K	146 K	15	61
F-1	56	33	148 K	160 K	13	57

TABLE I-XVI

Total Energy Density Profile in SL-1

Mw-sec/Kg U-235*	Element - Inches of Reactor in Specified Range
27-28	6.0
26-27	10.8
25-26	7.4
24-25	6.8
23-24	22.4
22-23	27.2
21-22	20.8
20-21	17.2
19-20	16.0
18-19	16.4
17-18	15.2
16-17	17.2
15-16	38.8
14-15	31.6
13-14	41.6
12-13	47.6
11-12	56.0
10-11	39.6
8-10	134.0
6-8	231.2
4-6	171.2
Less than 4	58.8
Total	1033.8

*Total energy density is normalized to average burnup condition throughout reactor.

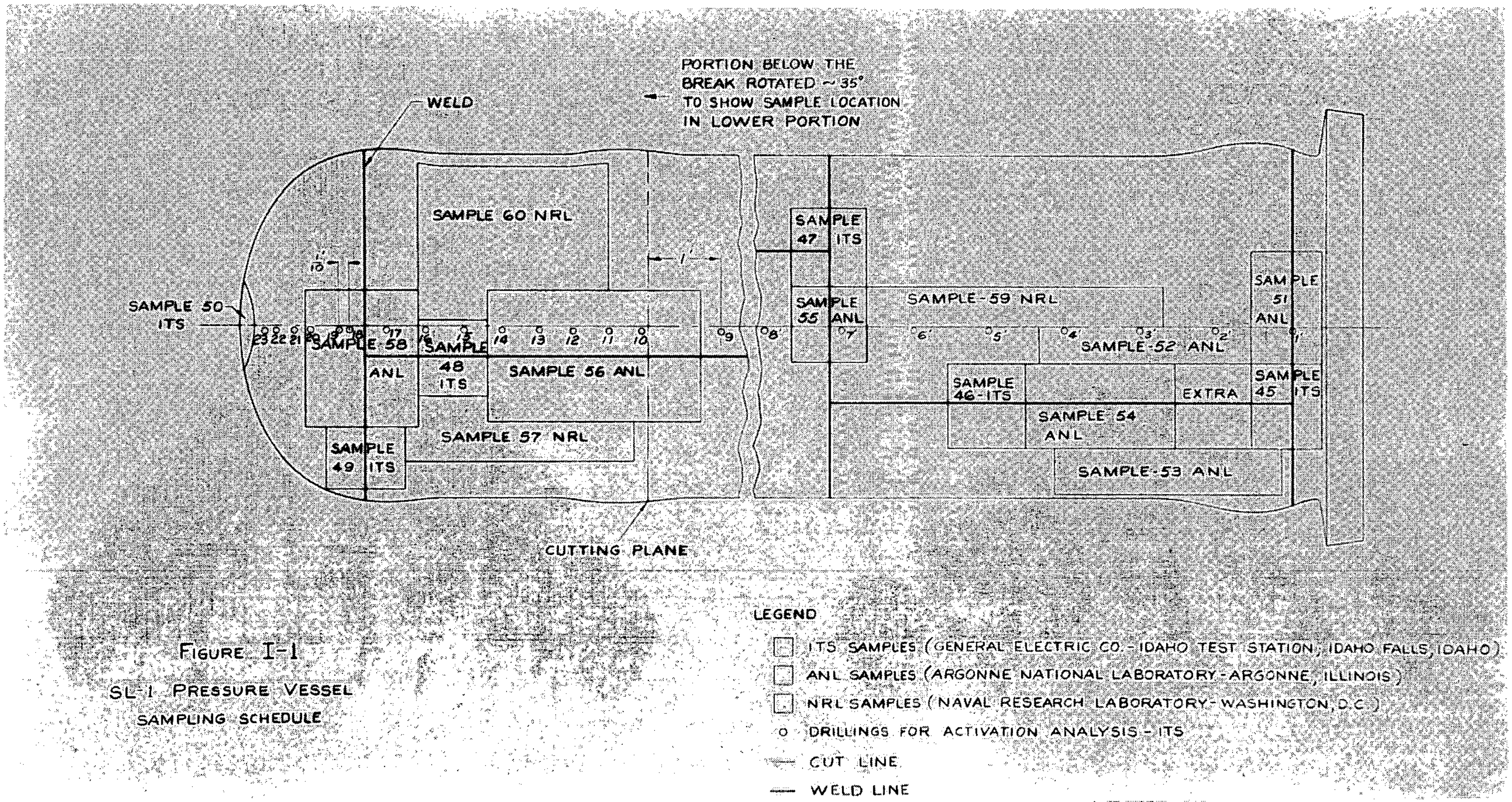

FIGURE I-1
SL-1 PRESSURE VESSEL
SAMPLING SCHEDULE

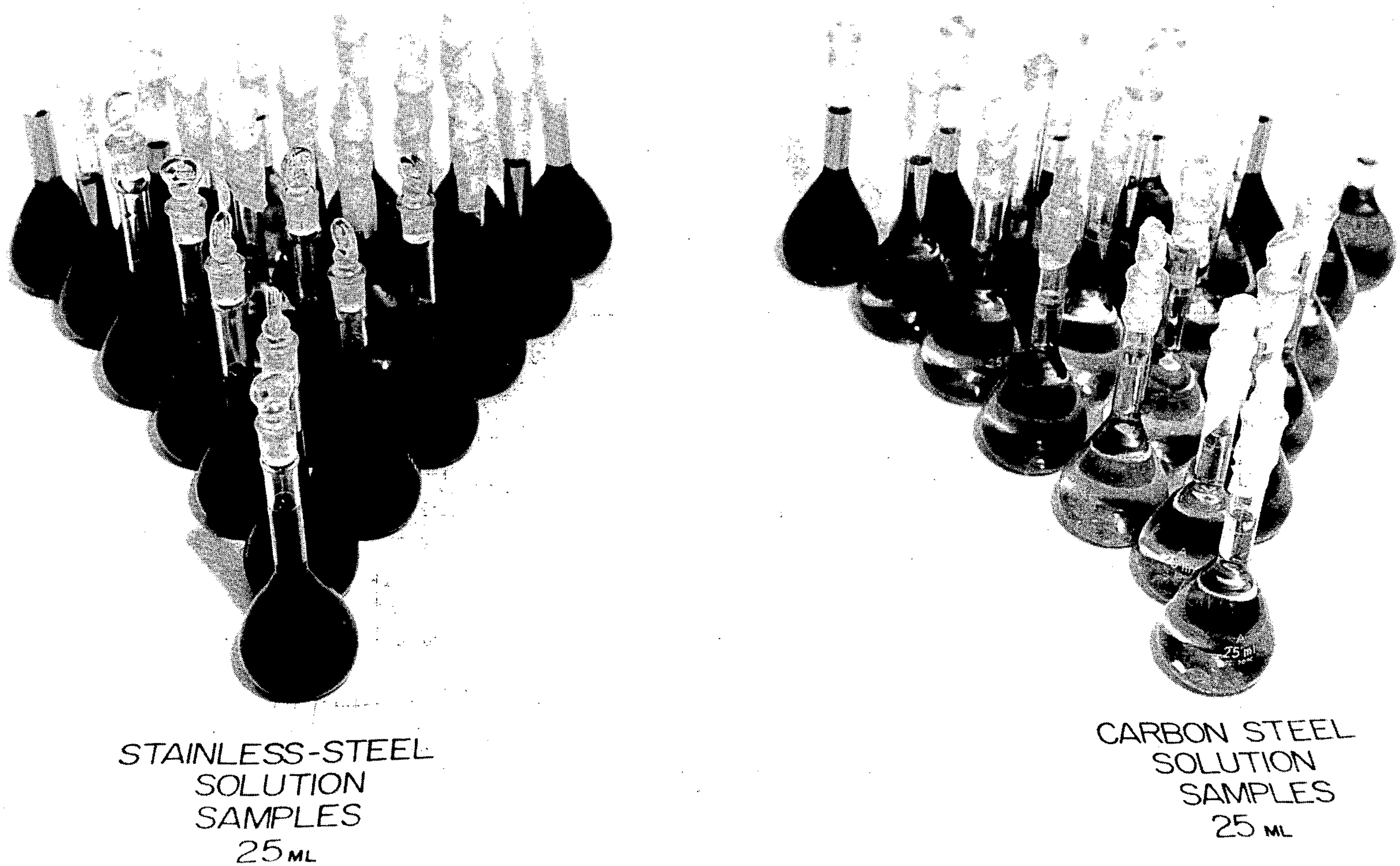

U-5183-2

Figure I-2, Solutions Contained in the Flask Geometry Used to Determine Relative Activation of Pressure Vessel Samples.

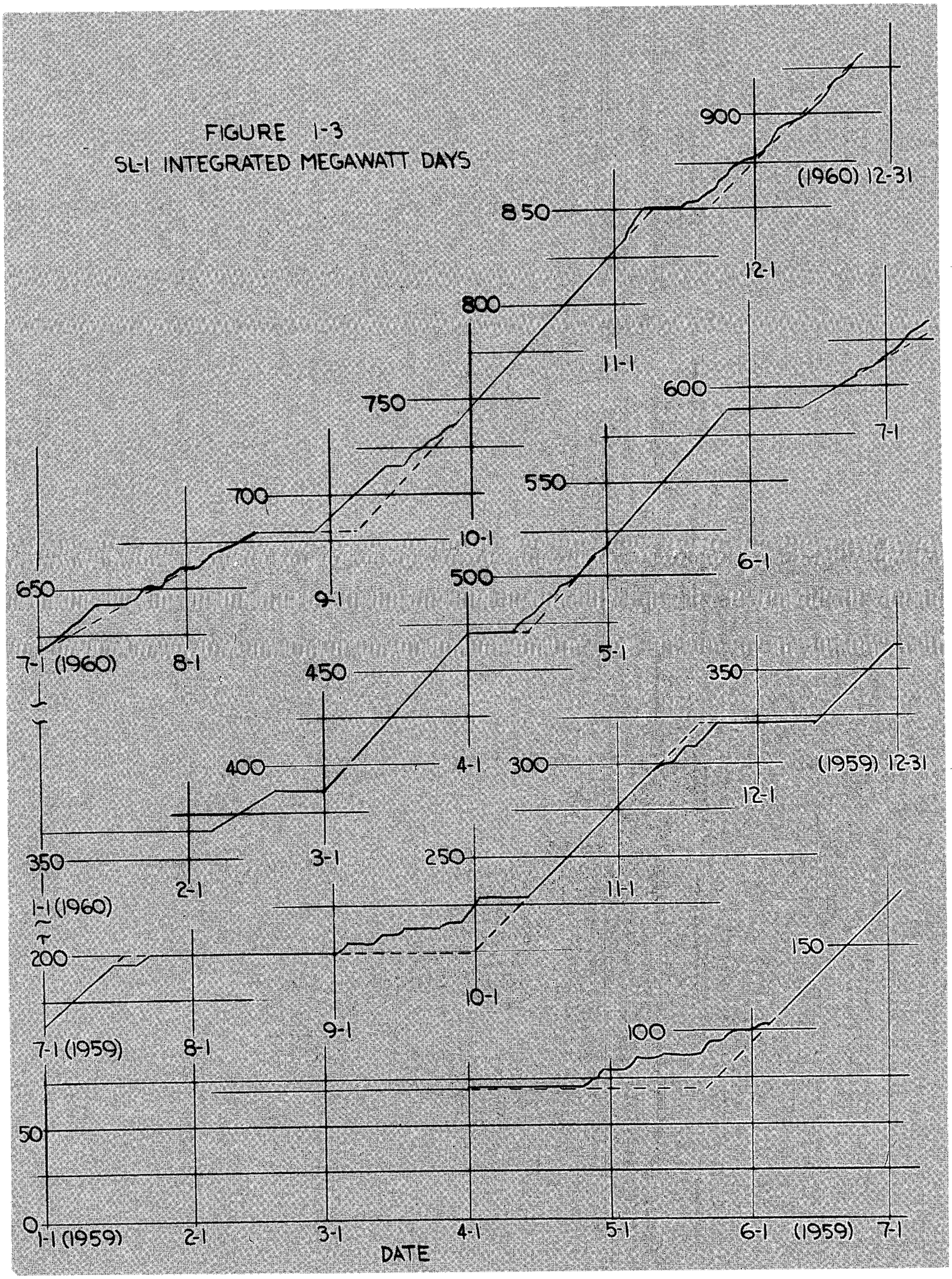

FIGURE 1-3
SL-1 INTEGRATED MEGAWATT DAYS

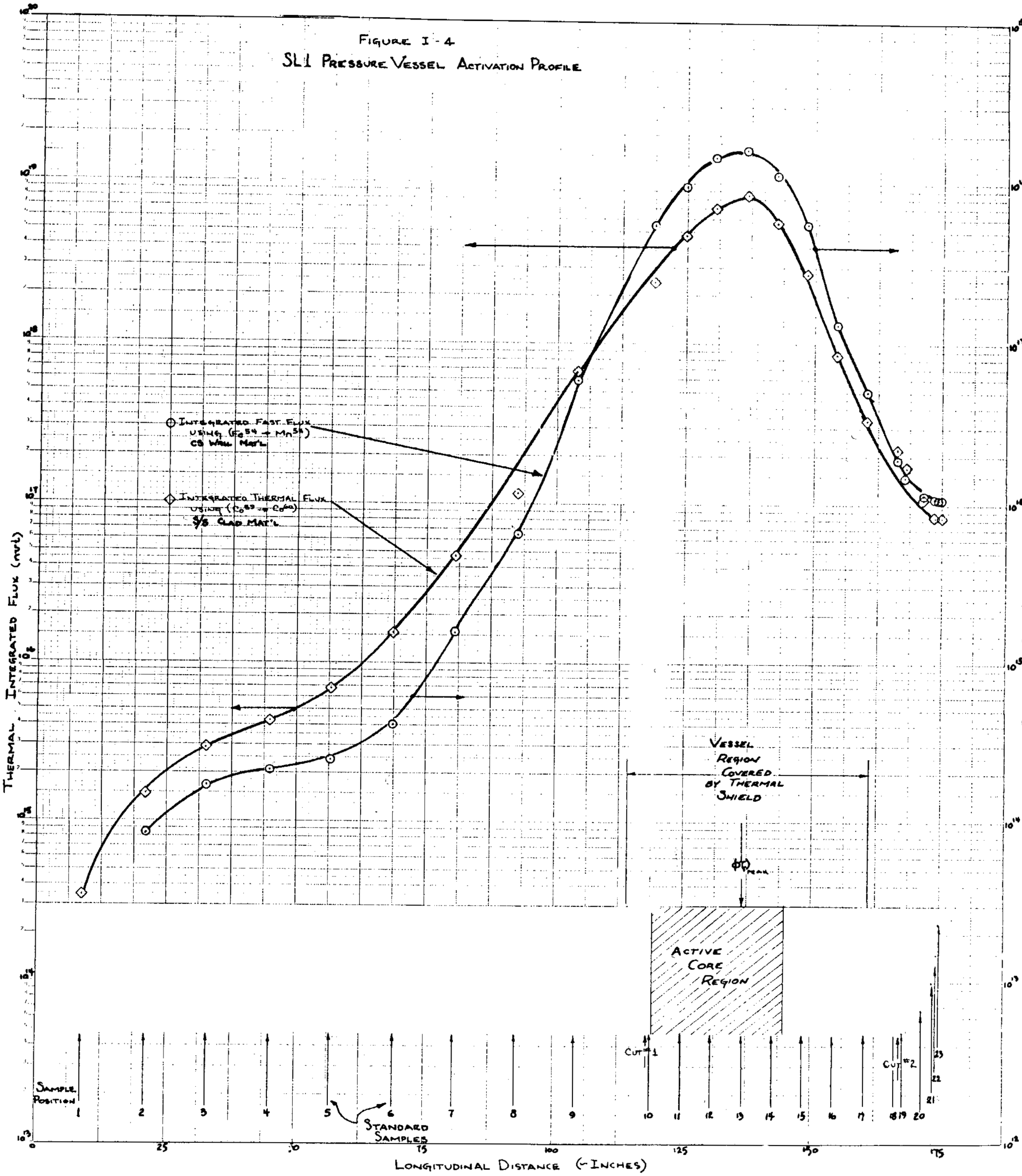

Figure I-4
SL1 Pressure Vessel Activation Profile
Integrated Fast Flux using (Fe^{54} → Mn^{54}) CS Wall Mat'l
Integrated Thermal Flux using (Co^{59} → Co^{60}) S/S Clad Mat'l
Vessel Region Covered by Thermal Shield
Active Core Region
Sample Position
Standard Samples
Cut #1
Cut #2
Thermal Integrated Flux (nvt)
Fast Integrated Flux (nvt)
Longitudinal Distance (~Inches)

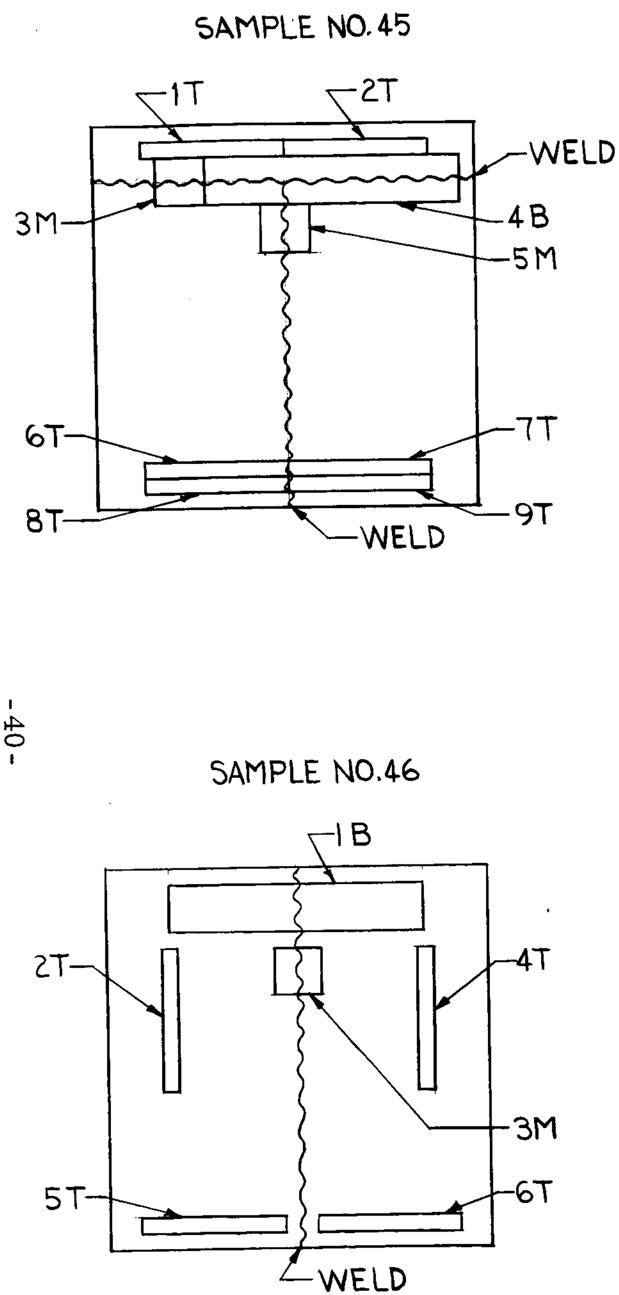

FIG. NO. I-5
PRESSURE VESSEL
SPECIMEN LOCATION

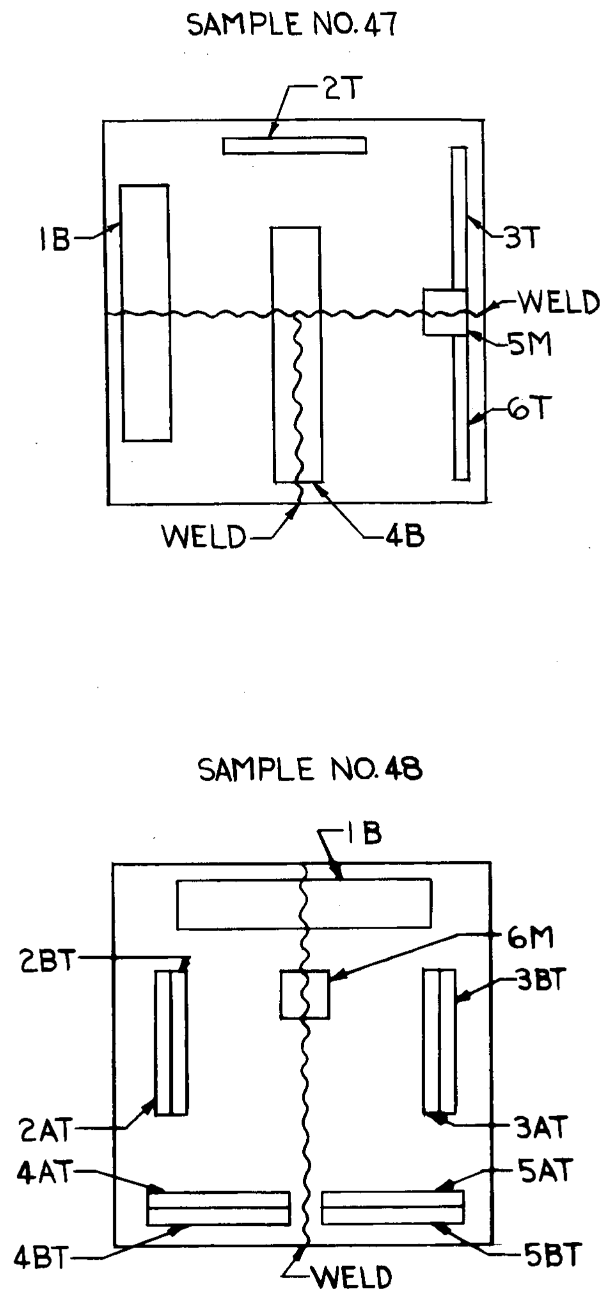

FIG. NO. I-6
PRESSURE VESSEL
SPECIMEN LOCATION

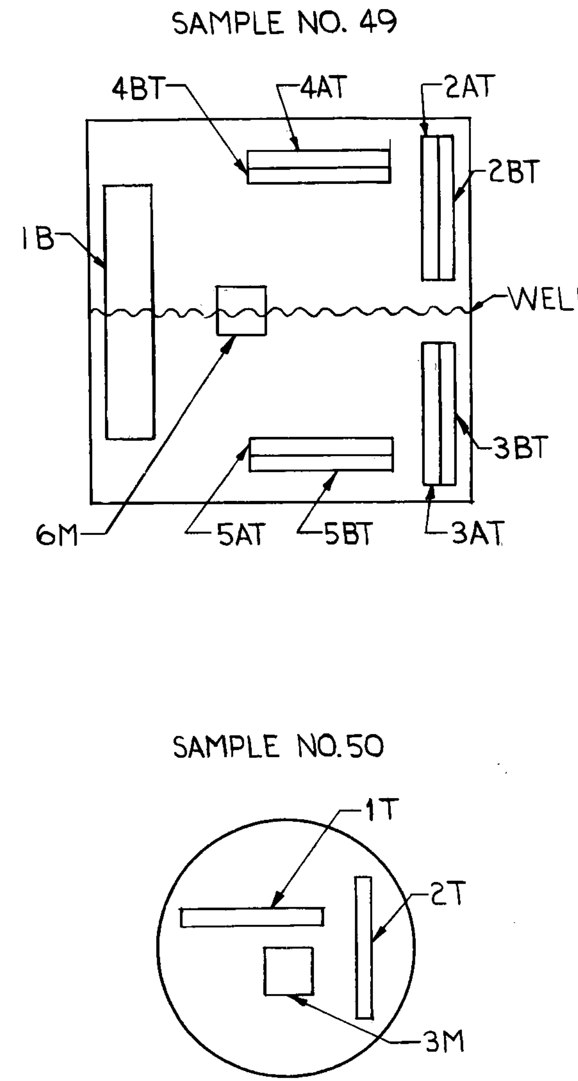

FIG. NO. I-7
PRESSURE VESSEL
SPECIMEN LOCATION

U-5182-2-a

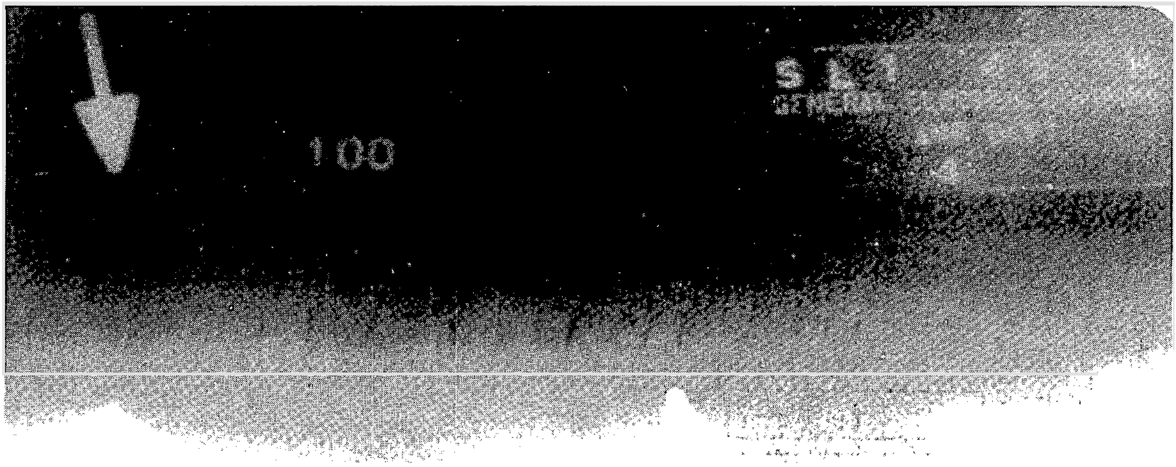

Figure I-8, Radiograph of Transverse Cracks in Weld from Sample ITS-45.

U-5182-2-b

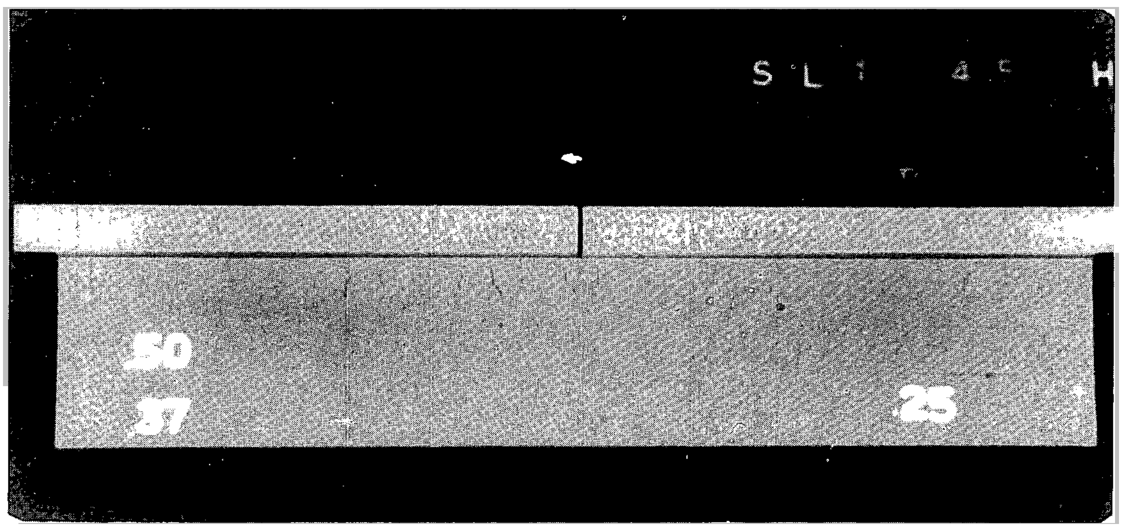

Figure I-9, Radiograph of Transverse Cracks in Bend Specimen Obtained from Sample ITS-45.

U-5093-45B

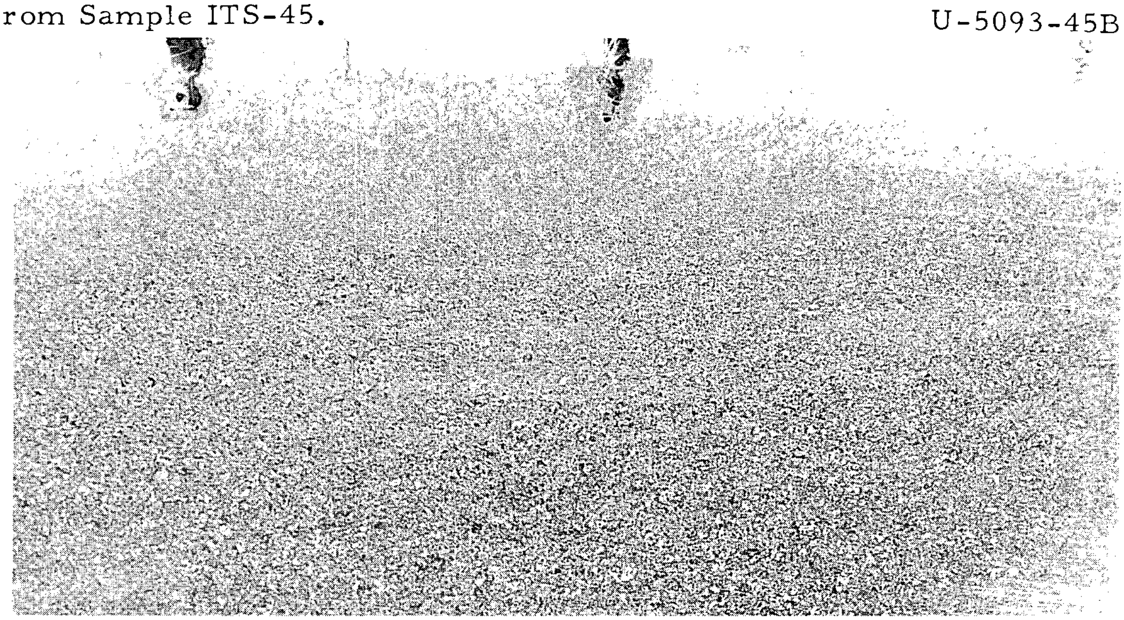

Figure I-10, Macrophotograph Showing Cracks and Structure of Heat-Affected Weld Zone.

Figure I-11a, Macrophotograph of the Circumferential Weld at Upper End of Pressure Vessel. Arrow indicates heat-affected zone where crack was formed.

U-5093-5C

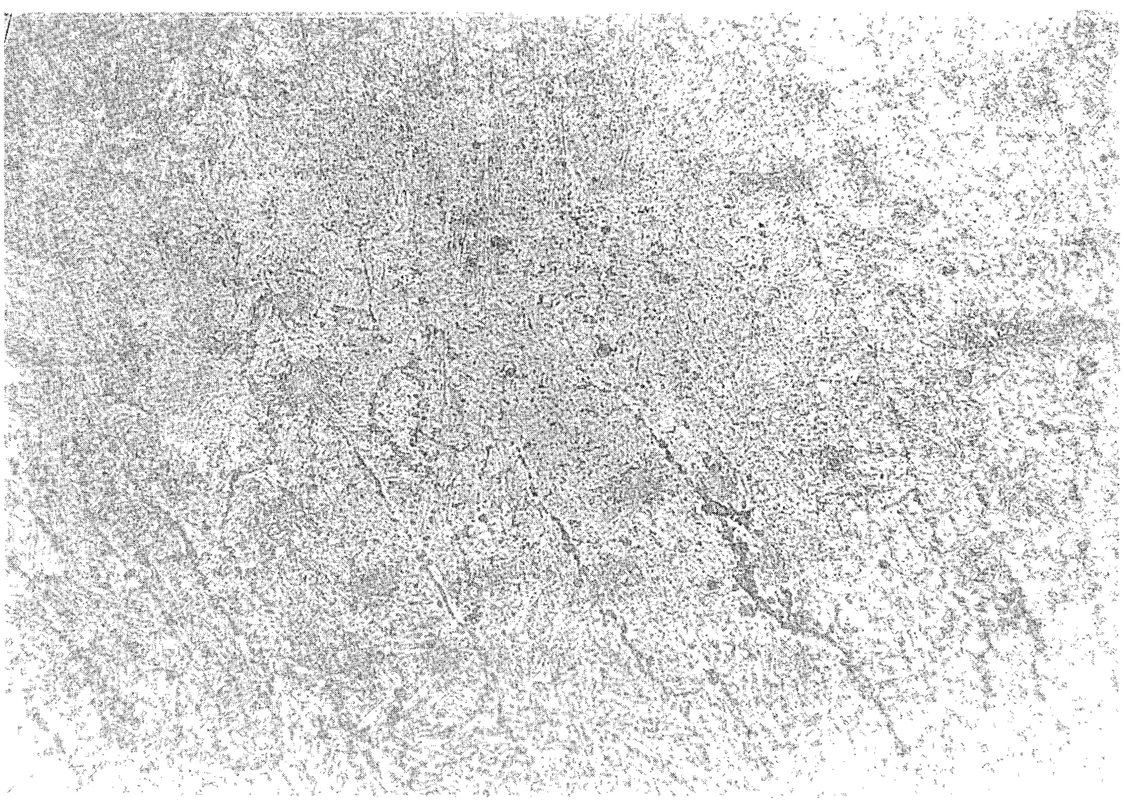

Figure I-11b, Photomicrograph of Heat-Affected Zone Showing Collinear Grain Structure.

U-5093-5M45A

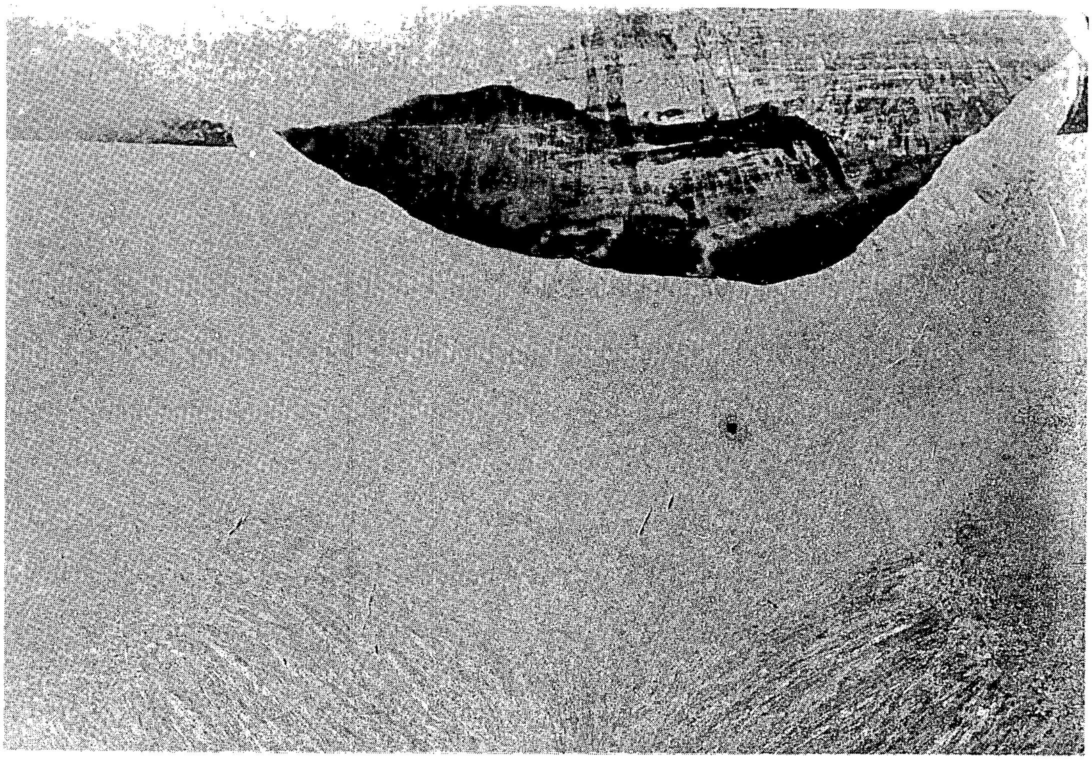

Figure I-12a, Macrophotograph of Vertical Weld of Specimen 5M45A.

U-5093-3M46A

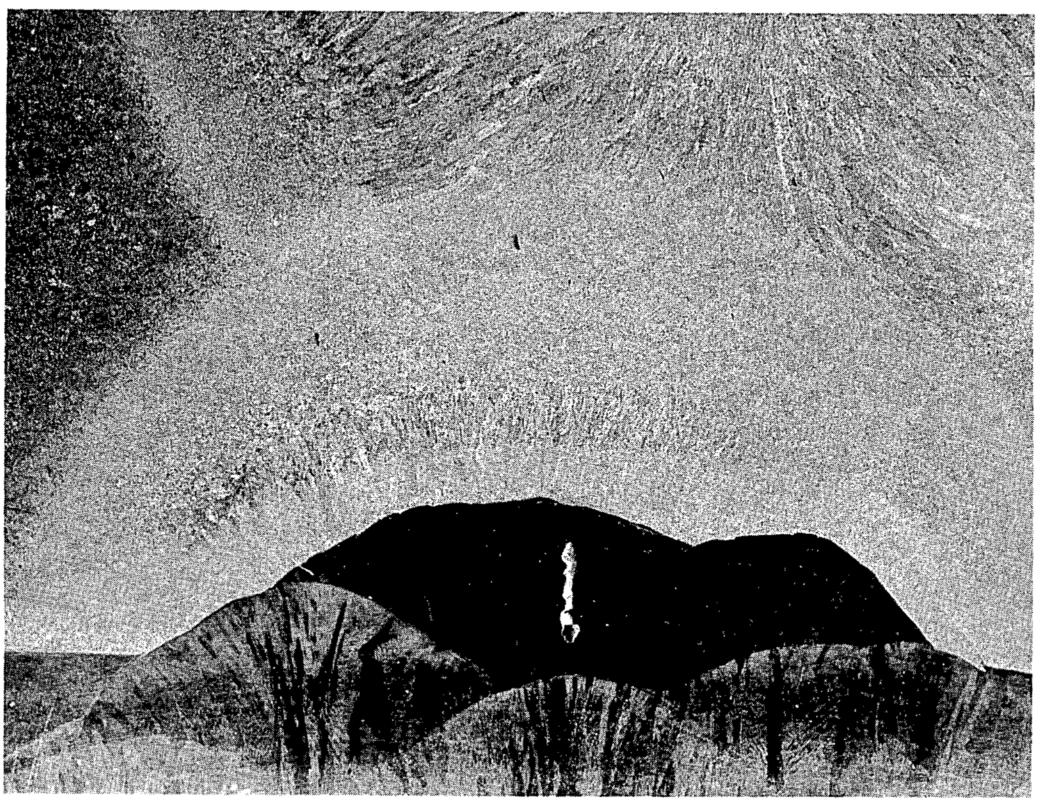

Figure I-12b, Macrophotograph of Vertical Weld of Specimen 3M46A.

U-5093-5M47A

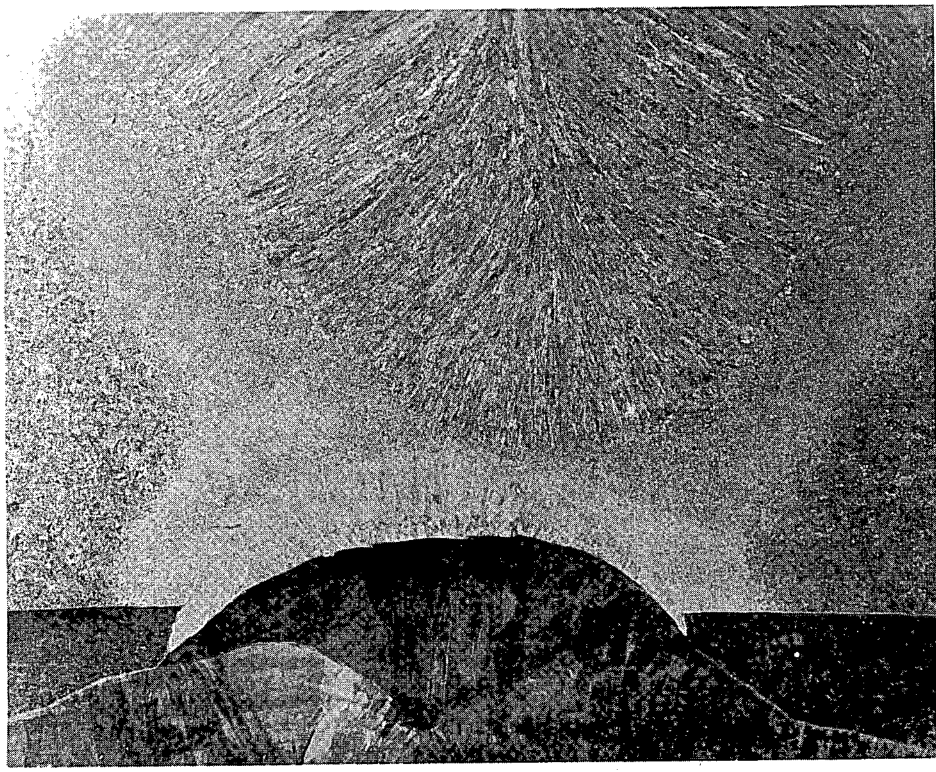

Figure I-13a, Macrophotograph of the Horizontal Weld of Specimen 5M47A.

U-5093-49A

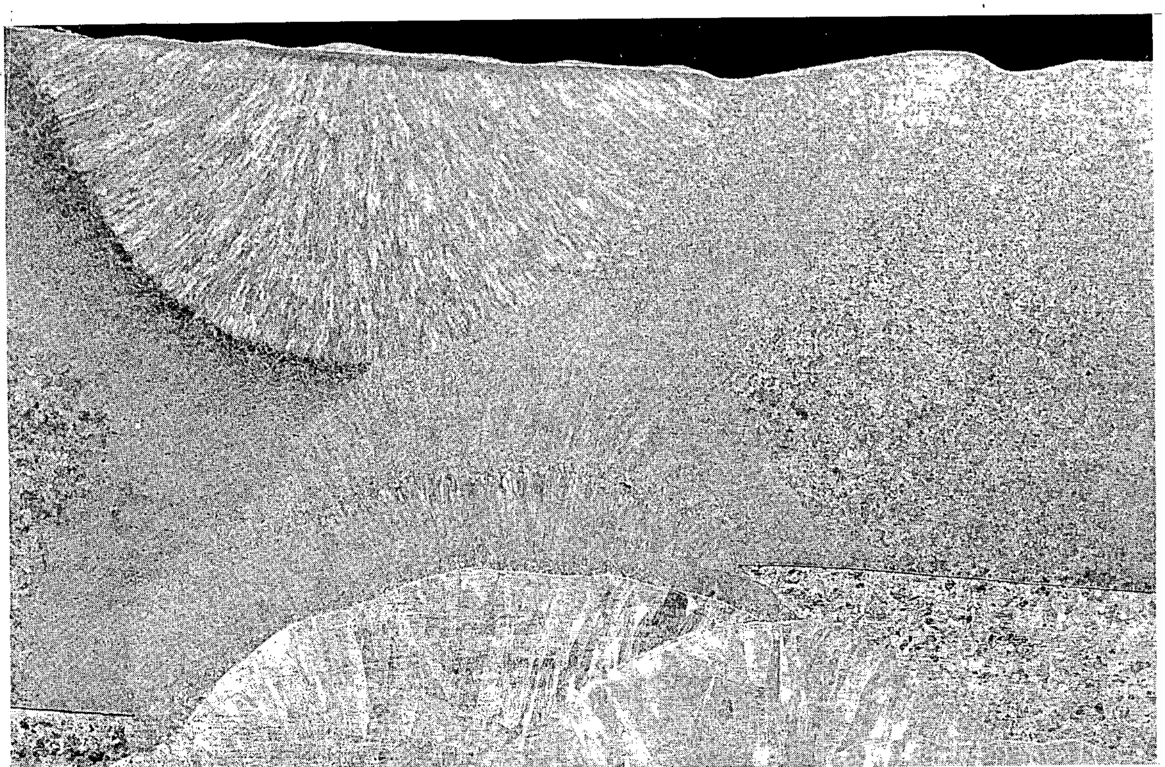

Figure I-13b, Macrophotograph of the Horizontal Weld of Specimen 6M49.

U-5181-1

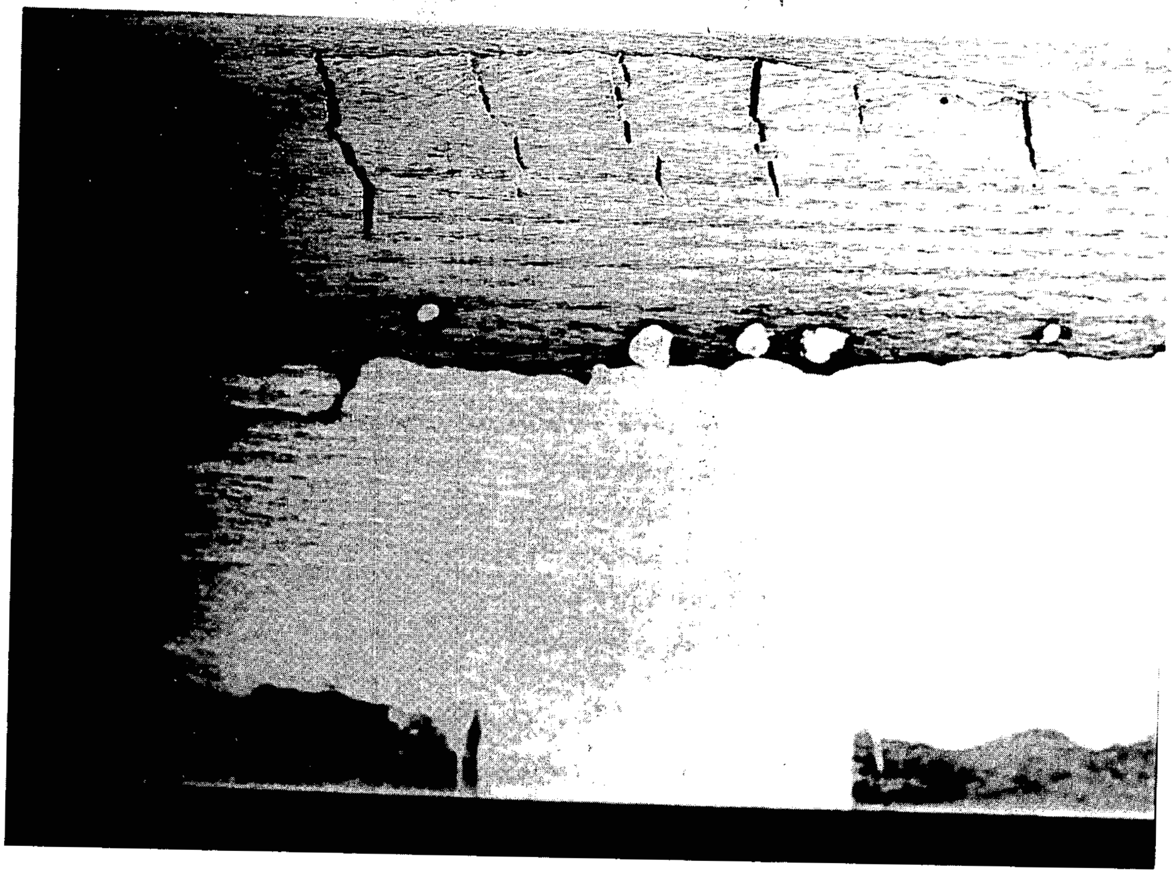

Figure I-14, Pressure Vessel Bend Test Specimen 4B45

U-5181-3

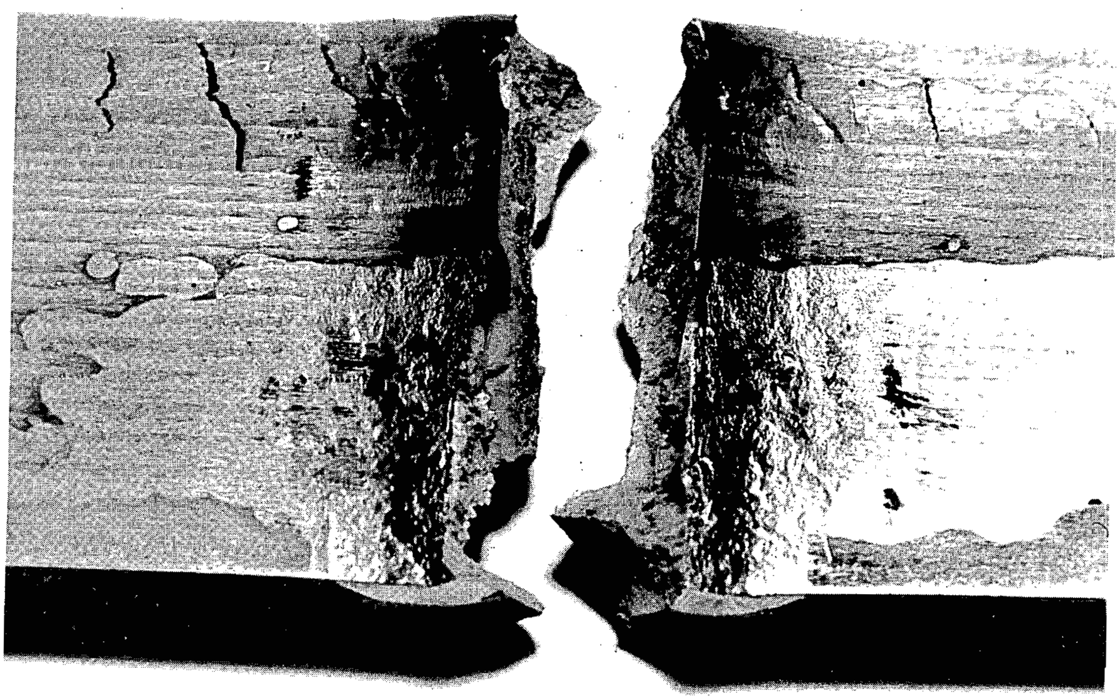

Figure I-15, Bend Test Specimen 4B45 After Testing.

U-5181-2

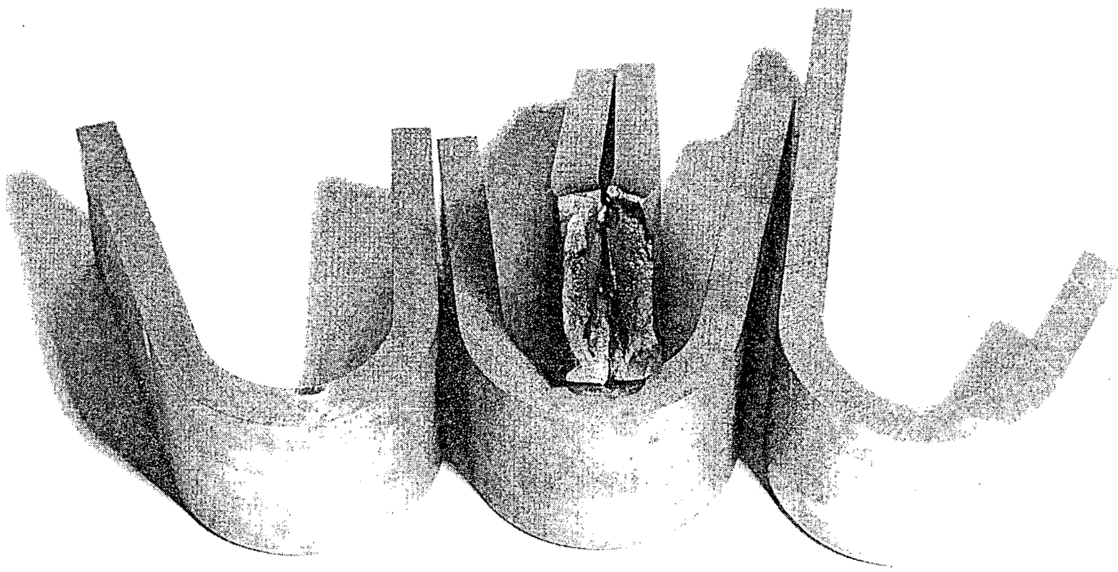

Figure I-16, Bend Test Specimens After Testing

U-5172-1

Figure I-17, Pressure Vessel Flange Studs Showing Deformation.

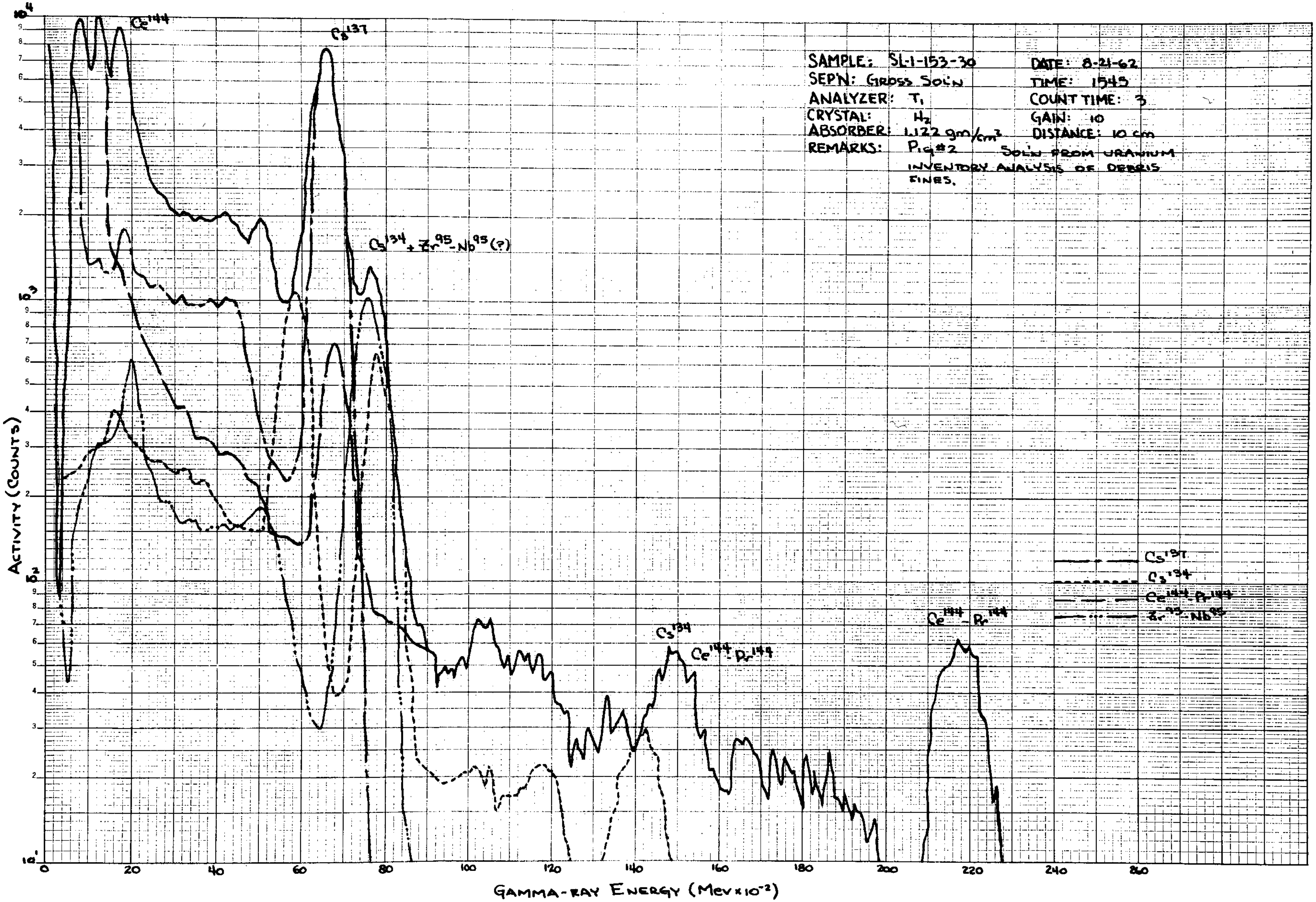
SAMPLE: SL-1-153-30
SEP'N: GROSS SOL'N
ANALYZER: T1
CRYSTAL: H2
ABSORBER: 1.122 gm/cm3
REMARKS: Pig #2 SOL'N FROM URANIUM INVENTORY ANALYSIS OF DEBRIS FINES.
DATE: 8-21-62
TIME: 1545
COUNT TIME: 3
GAIN: 10
DISTANCE: 10 cm
Ce144
Cs137
Cs134 + Zr95-Nb95 (?)
Cs134
Ce144-Pr144
Ce144-Pr144
Cs137
Cs134
Ce144-Pr144
Zr95-Nb95
ACTIVITY (COUNTS)
GAMMA-RAY ENERGY (Mev x 10-2)

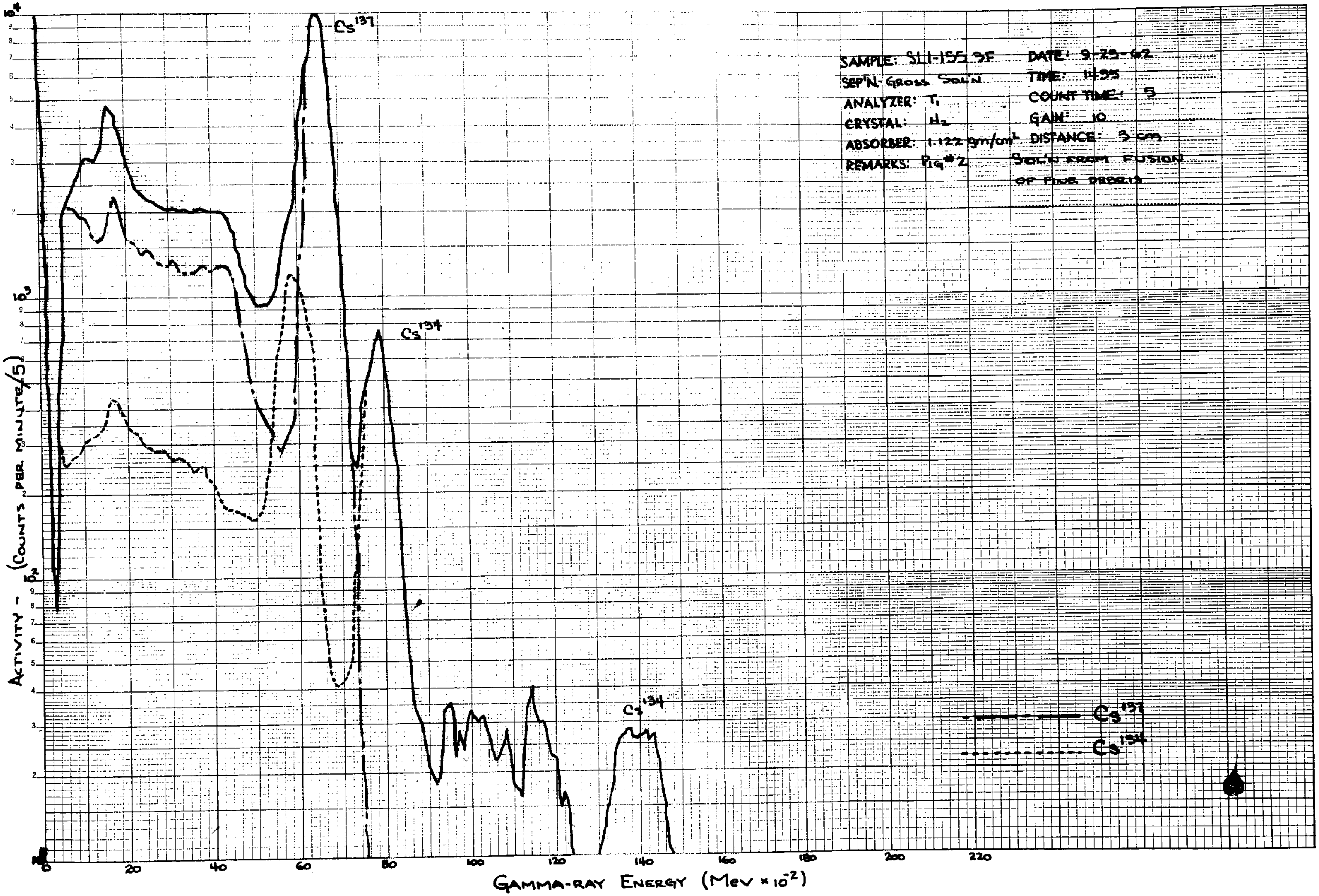
SAMPLE: SLI-155 9F
DATE: 9-29-62
SEP'N: GROSS SOL'N
TIME: 1435
ANALYZER: T_1
COUNT TIME: 5
CRYSTAL: H_2
GAIN: 10
ABSORBER: 1.122 gm/cm²
DISTANCE: 3 cm
REMARKS: Pig #2
SOL'N FROM FUSION OF FINE DEBRIS
Cs137
Cs134
Cs134
Cs137
Cs134
ACTIVITY - (COUNTS PER MINUTE/5)
GAMMA-RAY ENERGY (MeV × 10⁻²)
0
20
40
60
80
100
120
140
160
180
200
220

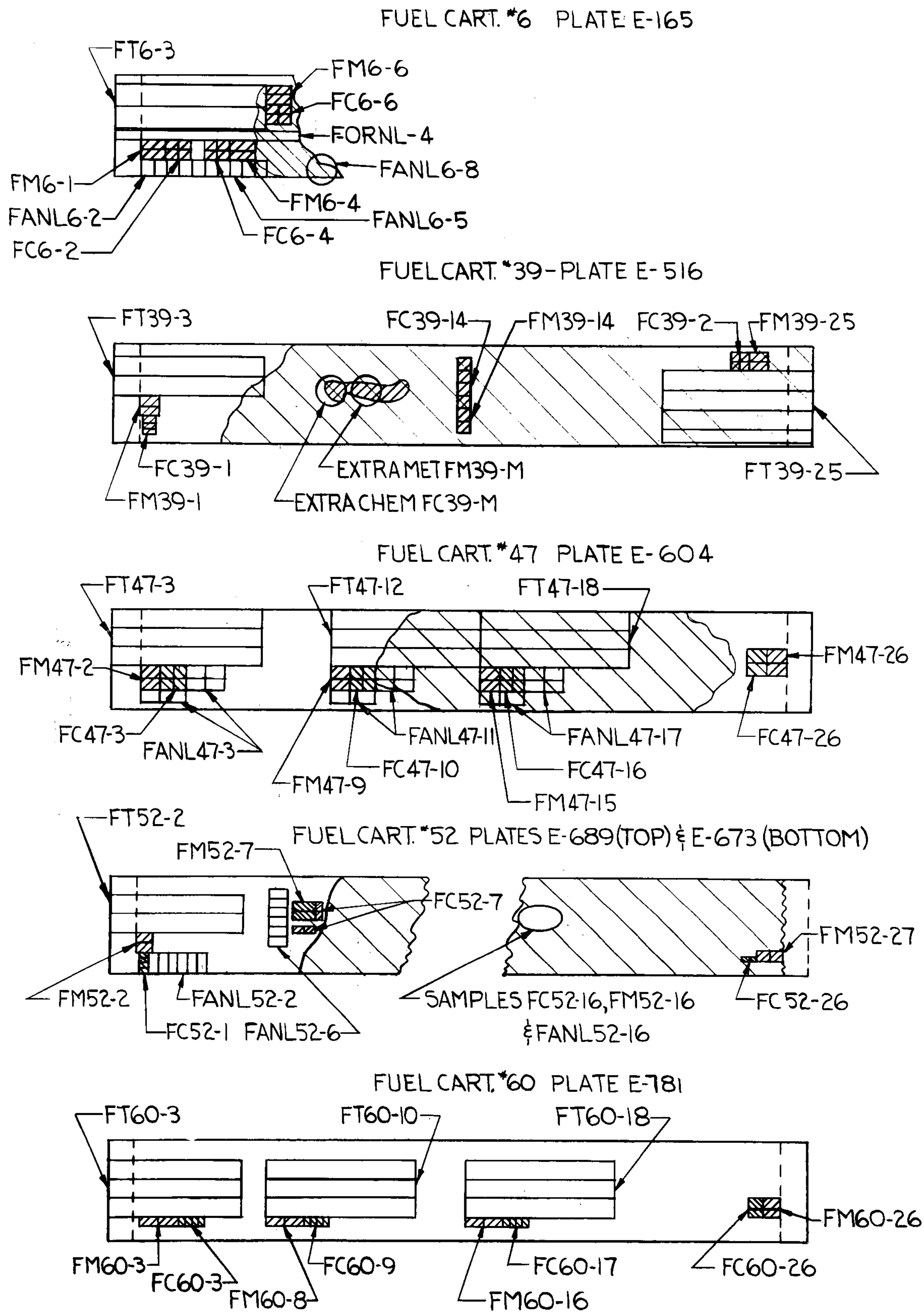

FIG. NO. I-20
FUEL CARTRIDGE
SPECIMEN LOCATION

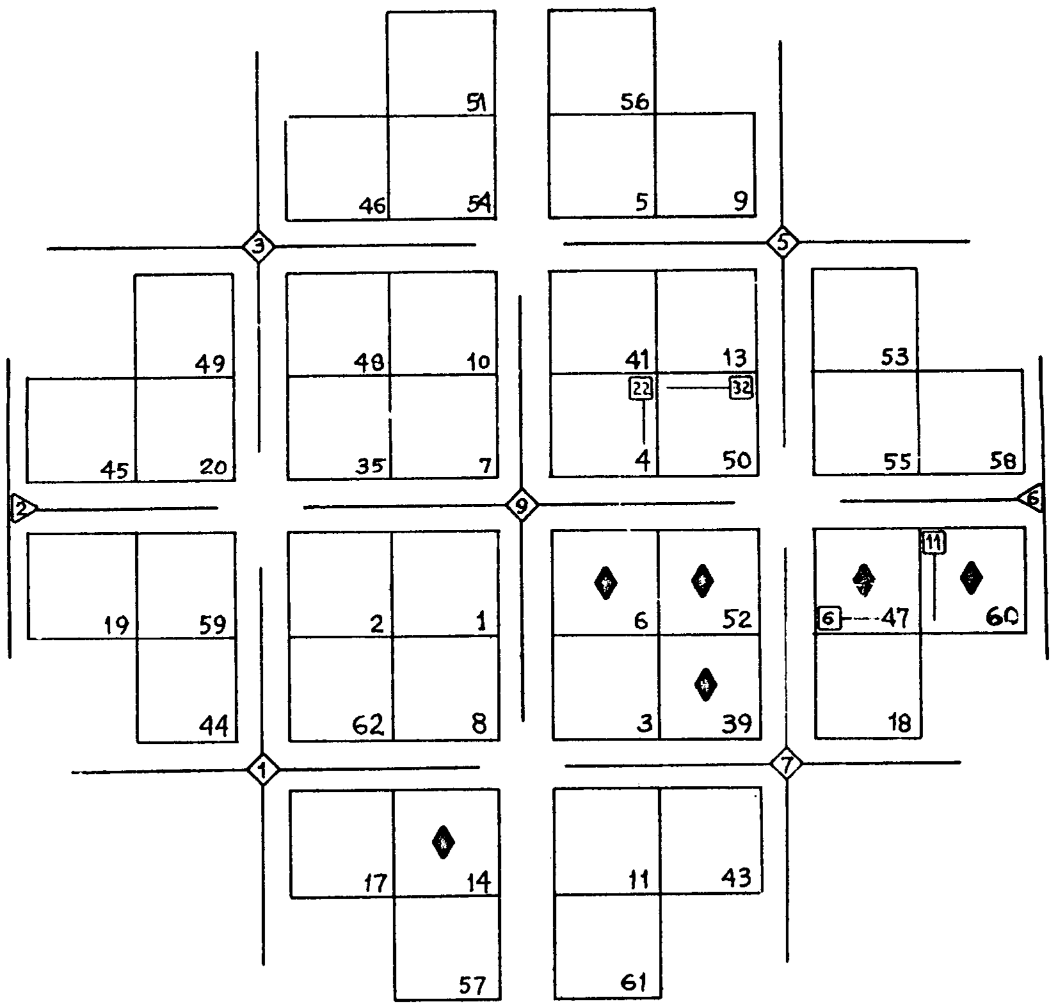

Figure I-21, Schematic diagram of elements sampled for fuel burnup.

Samples taken from elements marked ◆.

Core location of boron poison plate samples

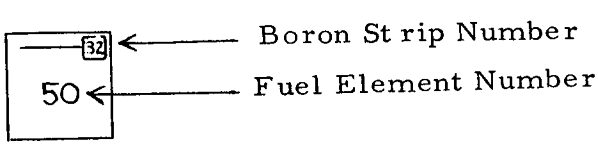

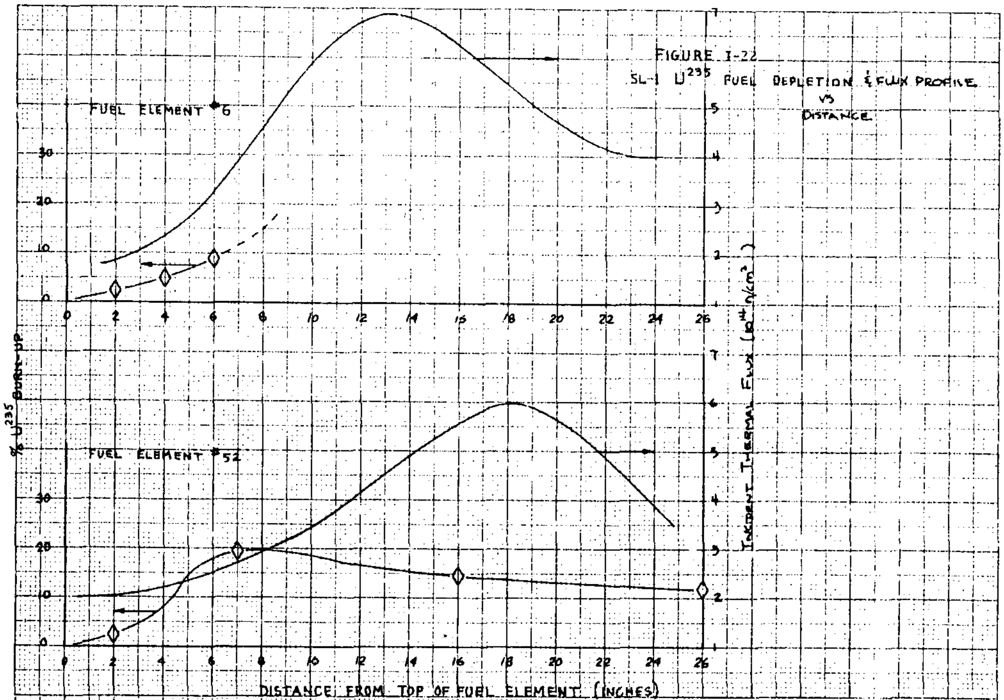

FIGURE I-22
SL-1 U^{235} FUEL DEPLETION & FLUX PROFILE VS DISTANCE

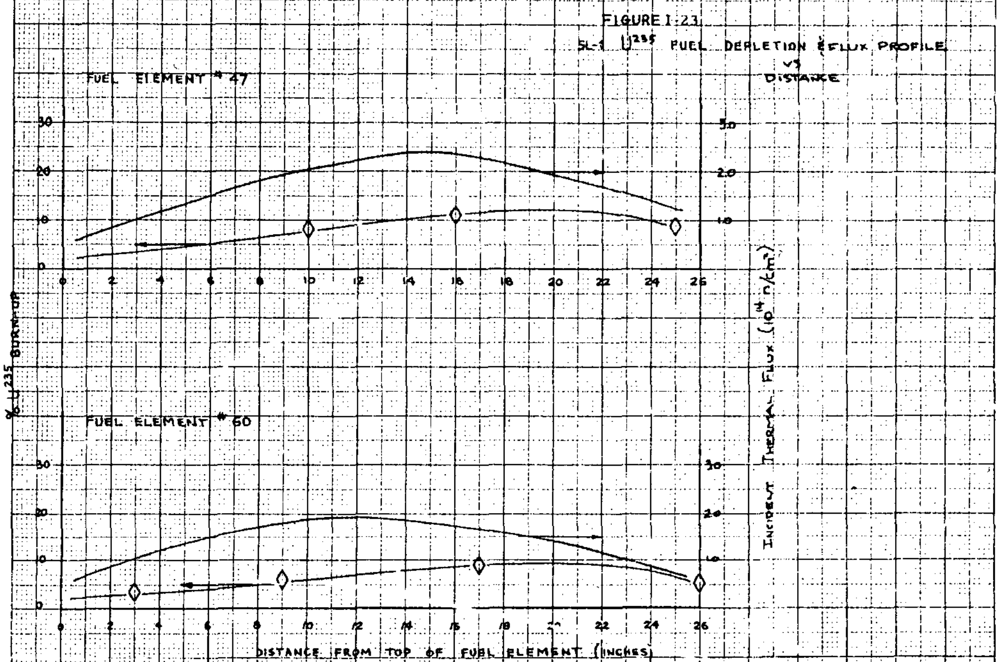

FIGURE I-23
SL-1 U^{235} FUEL DEPLETION & FLUX PROFILE VS DISTANCE

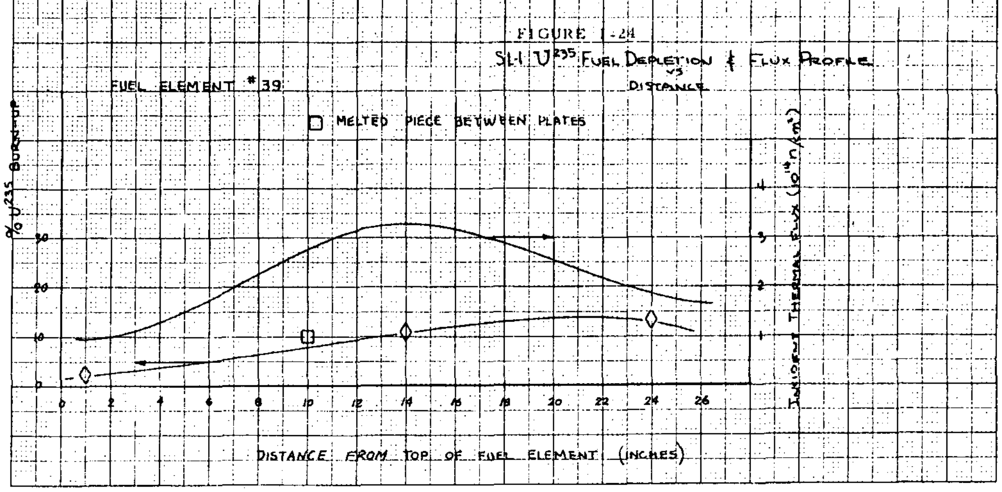

FIGURE I-24
SL-1 U^{235} FUEL DEPLETION & FLUX PROFILE VS DISTANCE

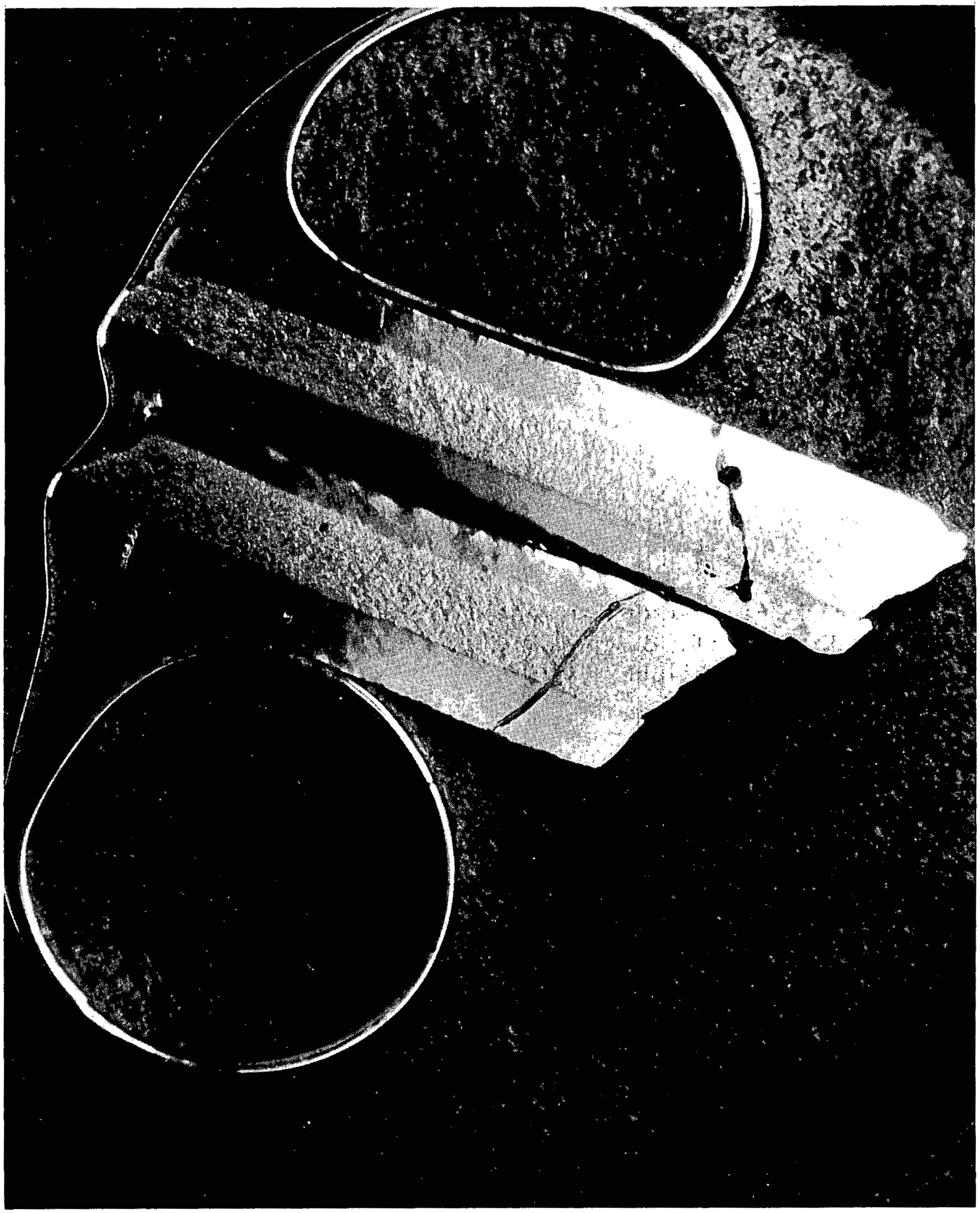

Figure I-25, Longitudinal and Transverse Specimen, Fuel Element 60, Plate E-781, 16 Inches from Top of Element.

U-5175-407A

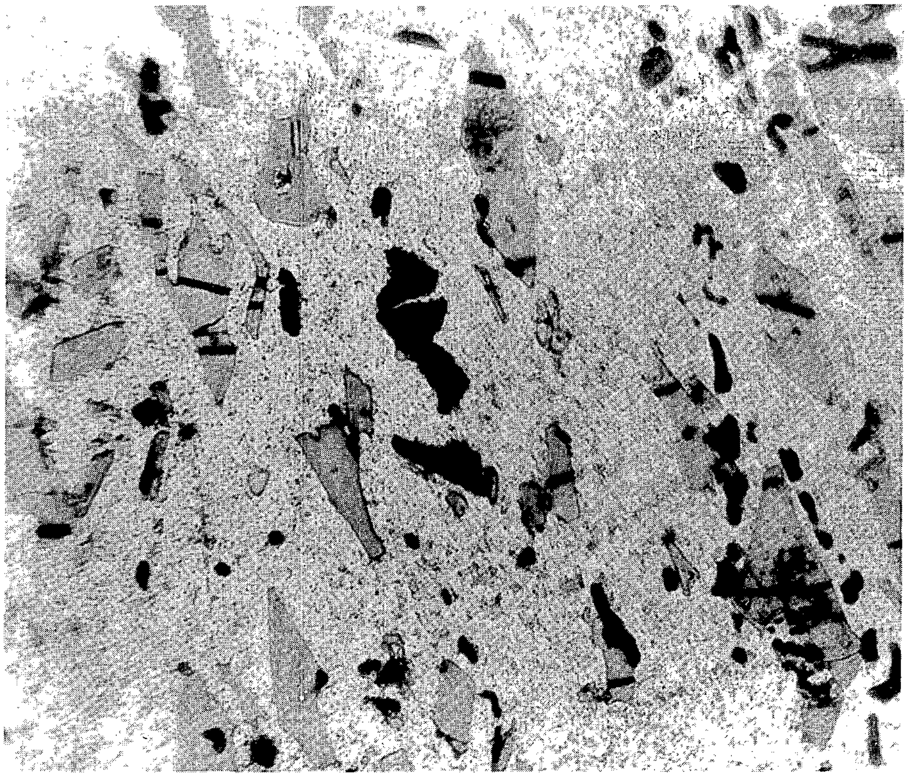

Figure I-26a, Photomicrograph (1000x) of Fuel Matrix, Fuel Element 60, Below Top Dead Edge, Longitudinal View. 0.5%HF etch.

U-5175-410A

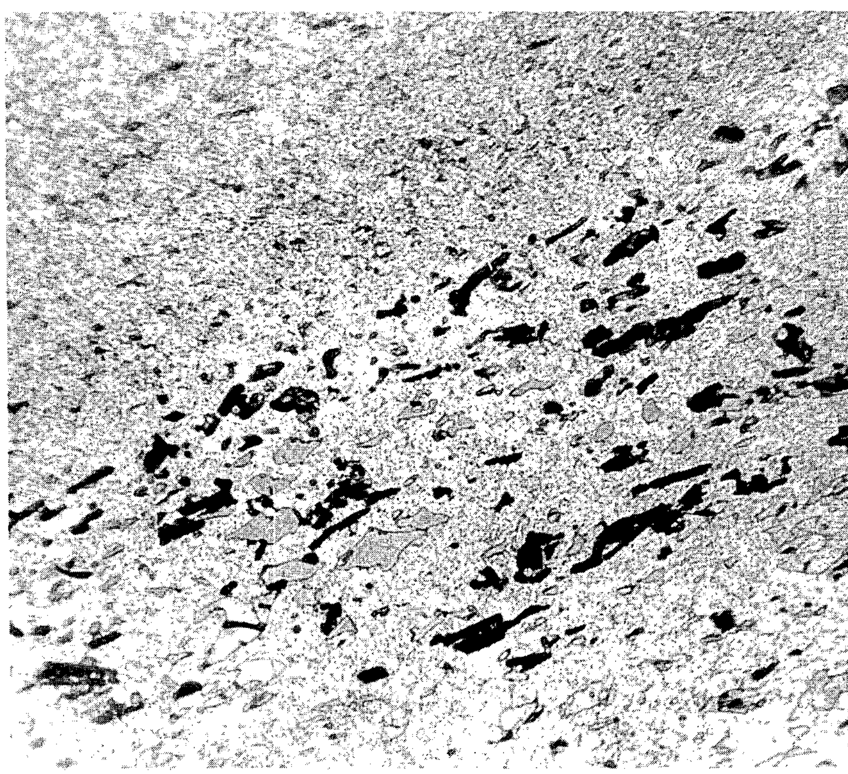

Figure I-26b, Photomicrograph (500x) of Fuel Matrix and Clad at Interface, Fuel Element 52, Just Below Top Dead Edge. Transverse View. 0.5% HF etch.

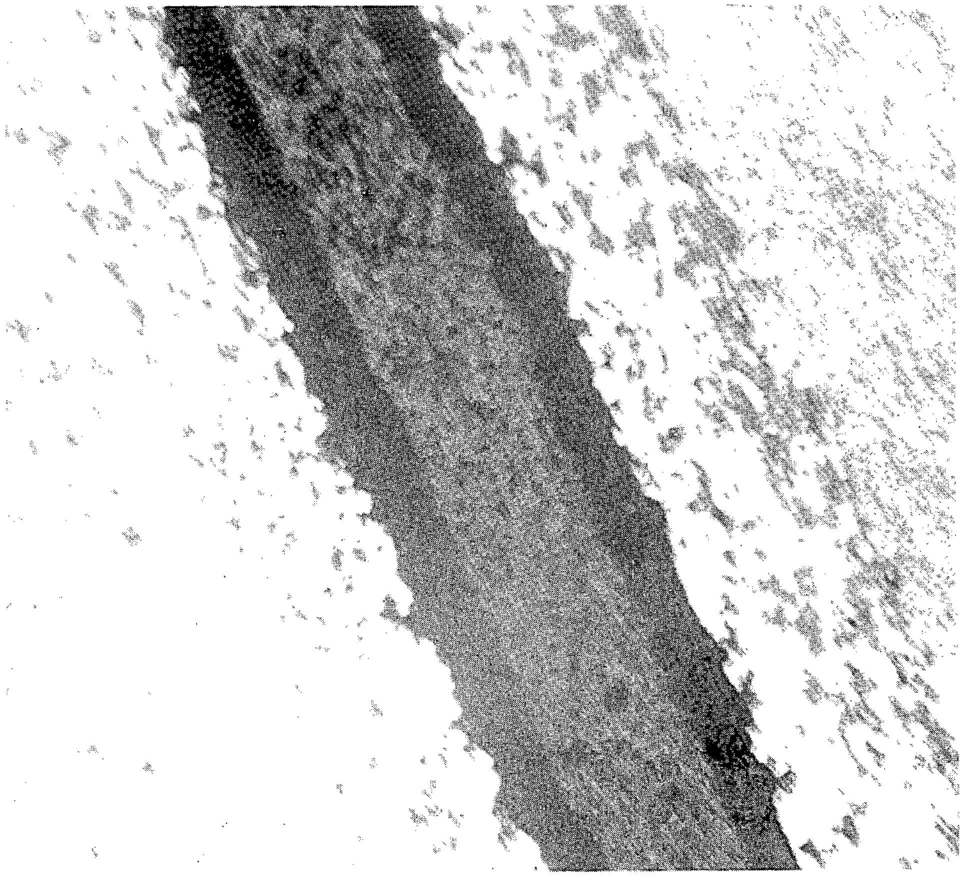

Figure I-27, Longitudinal Cross-Section View of Fuel Element 47, 9 Inches Below Top of Plate and Adjacent to Visibly Observed Heat-Affected Zone. (70x). 0.05%HF etch.

U-5174-14

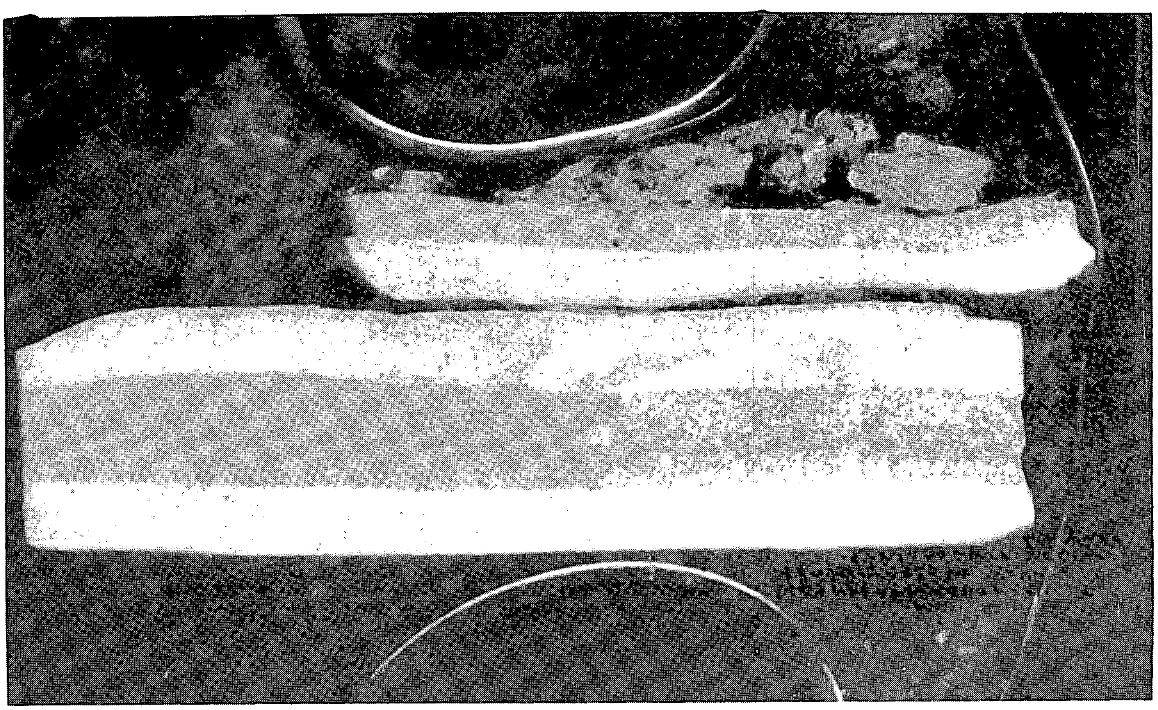

Figure I-28, Mounted Specimen from Fuel Element 52, 7 Inches from Top of Plate (5x).

U-5175-408A

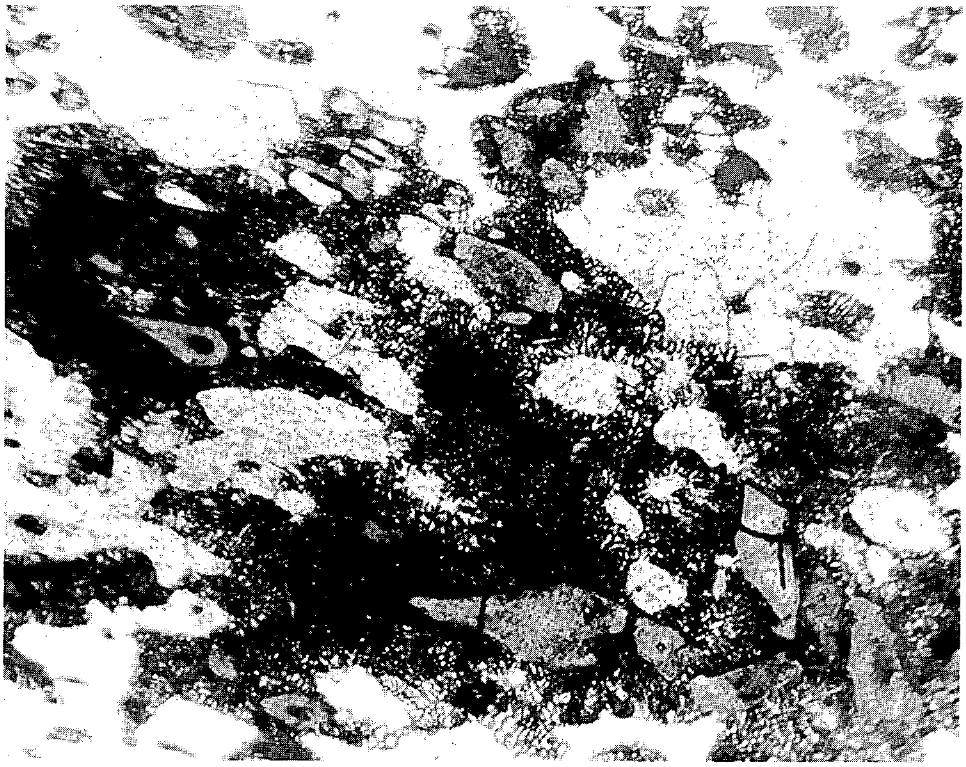

Figure I-29a, Longitudinal View (500x) Fuel Element 52, 7 Inches from Top of Plate. Fuel Matrix Centerline. 0.5% HF etch.

U-5175-408B

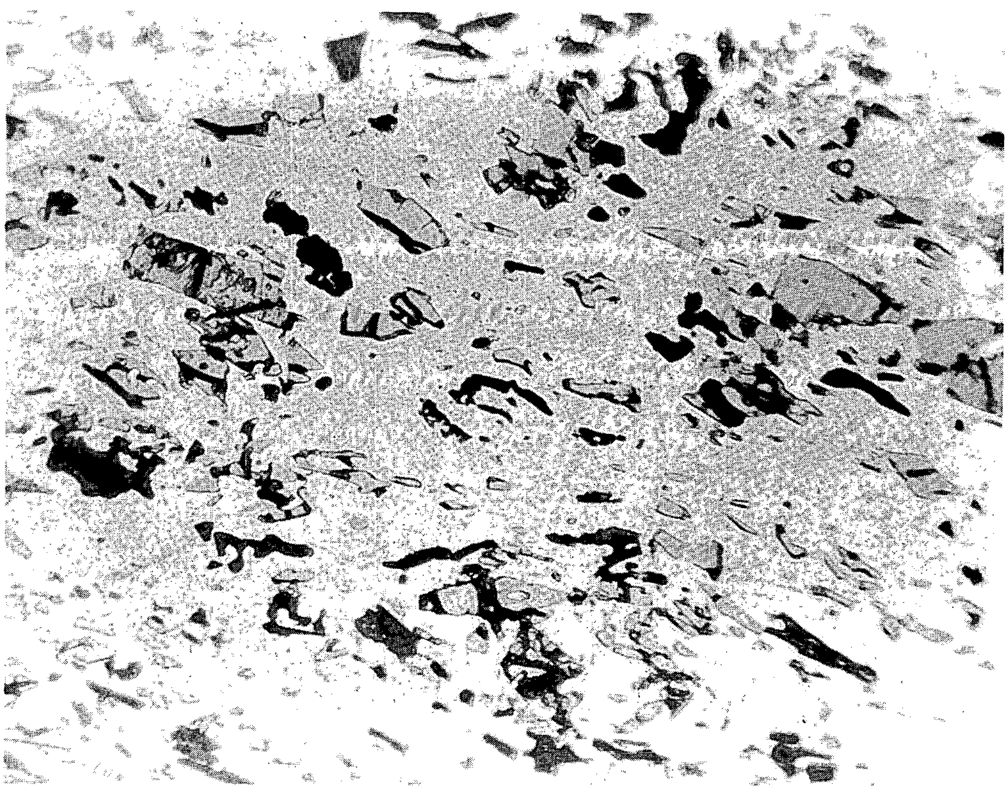

Figure I-29b, Longitudinal View (500x) Fuel Element 52, 7 Inches from Top of Plate, Adjacent Zone to Center of Fuel Matrix.

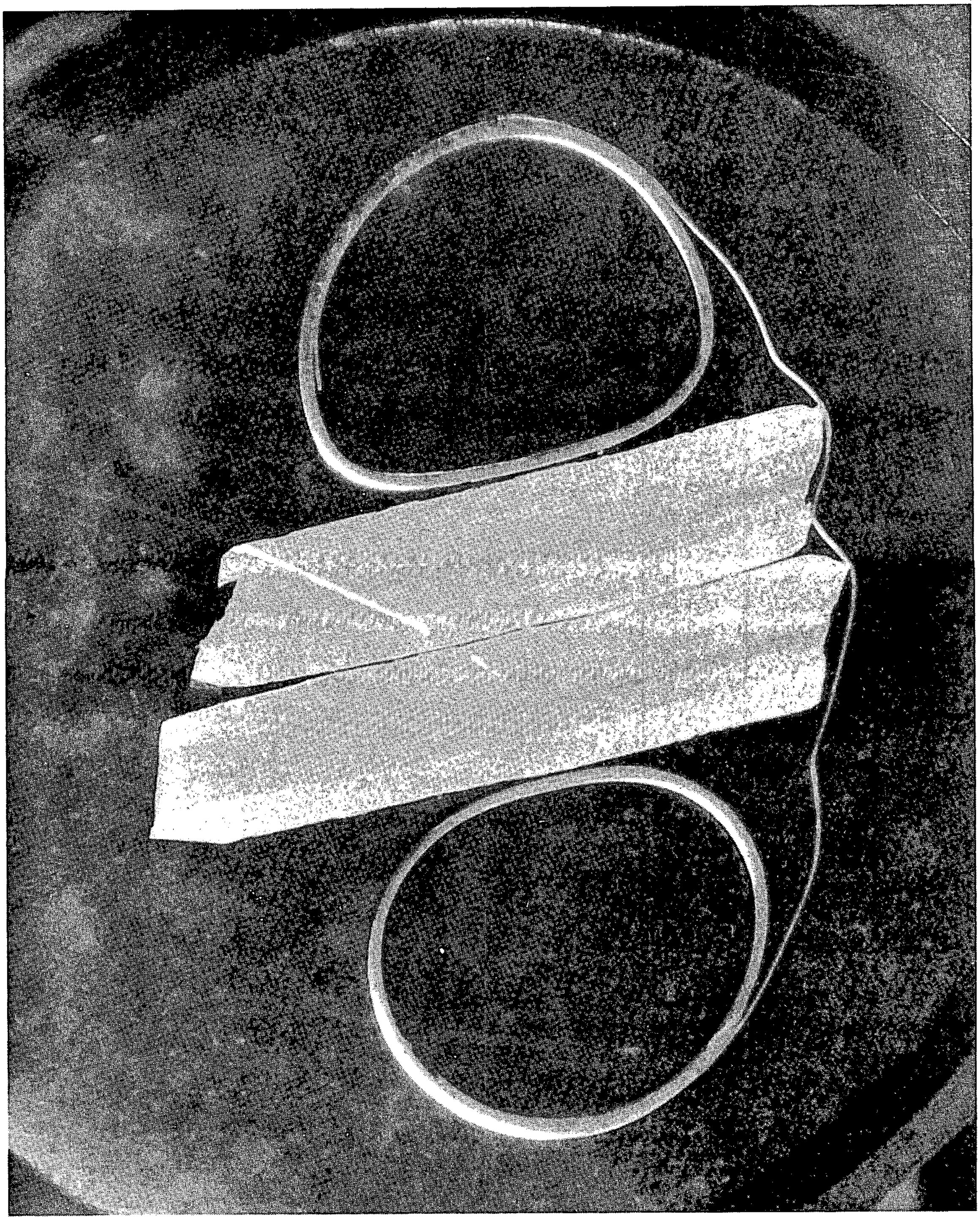

Figure I-30, Specimen Set Taken 4 Inches from Top of Plate. Fuel Element 6.

U-5175-426A

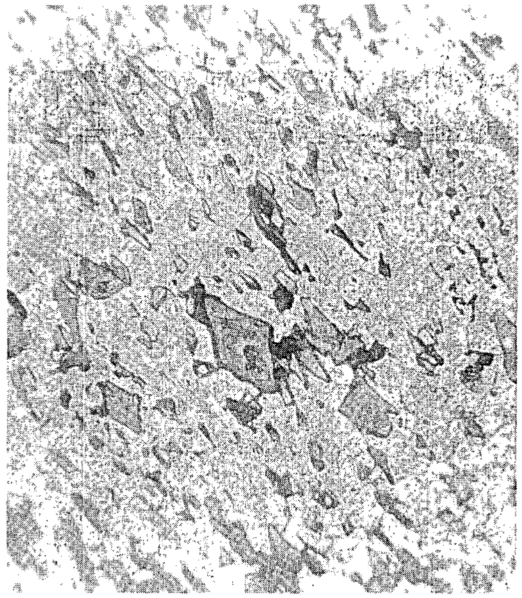

Figure I-31a, Longitudinal View (200x) in Center of Matrix Just Outside of Intermediate Temperature Zone. Fuel Element 6, 4 Inches from Top of Plate. 0.5% HF etch.

U-5175-426B

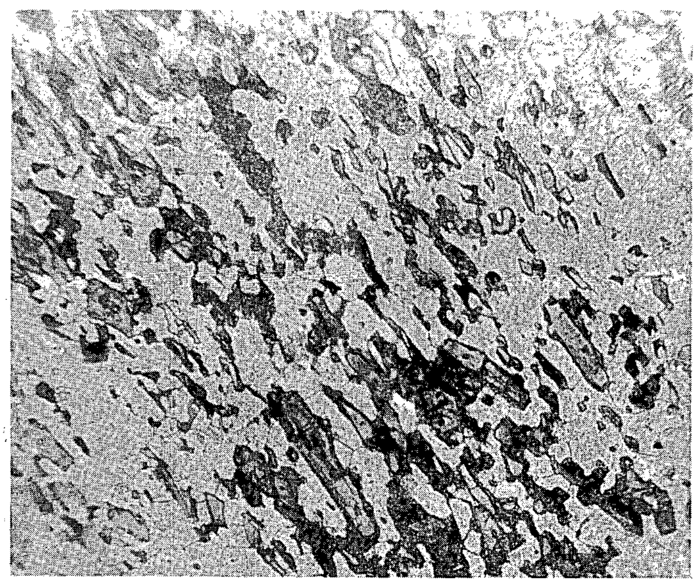

Figure I-31b, Longitudinal View (200x) in Center of Matrix in the Intermediate Temperature Zone. Fuel Element 6, 4 Inches from Top of Plate. 0.5% HF etch.

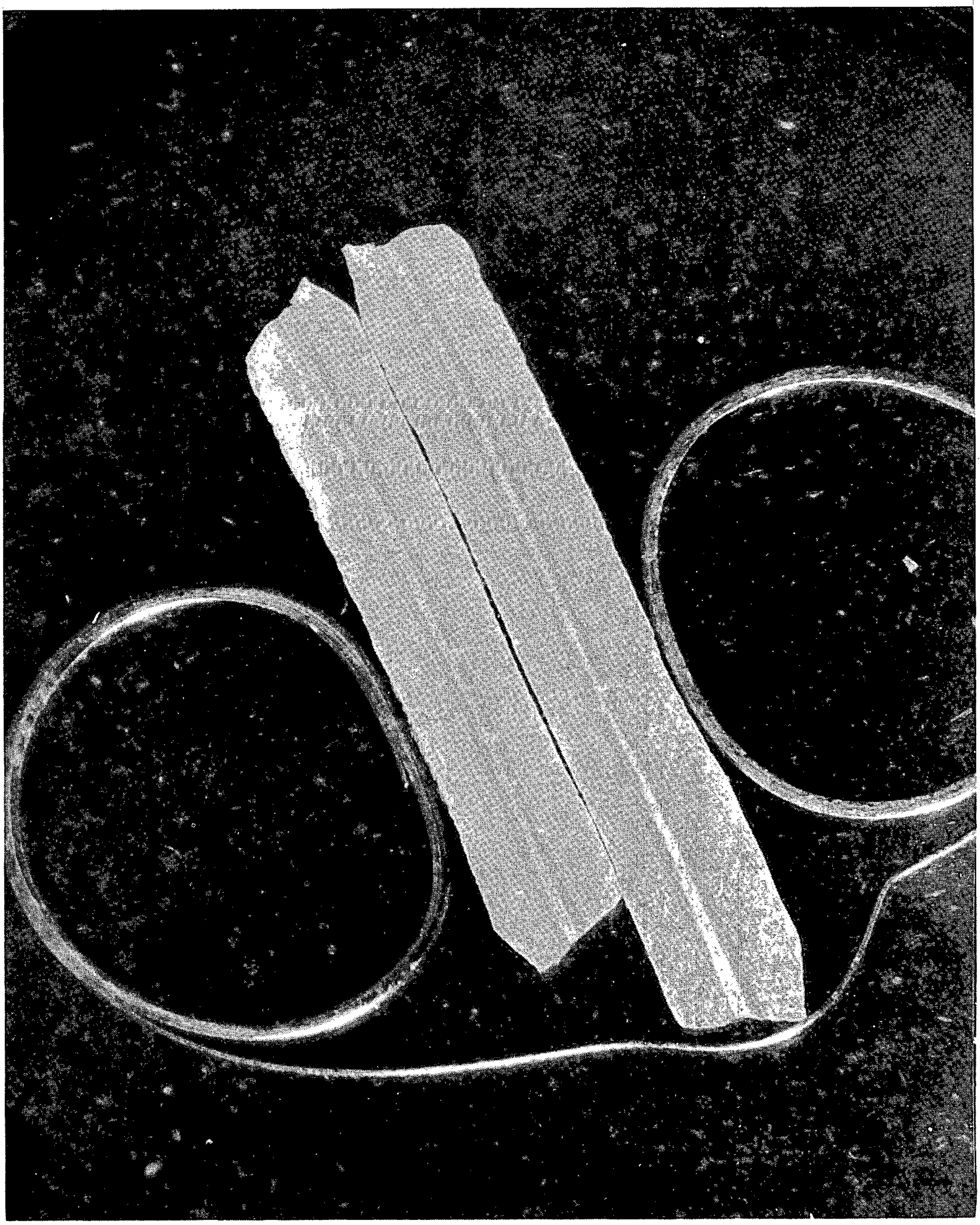

Figure I-32, Specimen Set from Fuel Element 47, 15 Inches from Top of Plate Showing Temperature Zones.

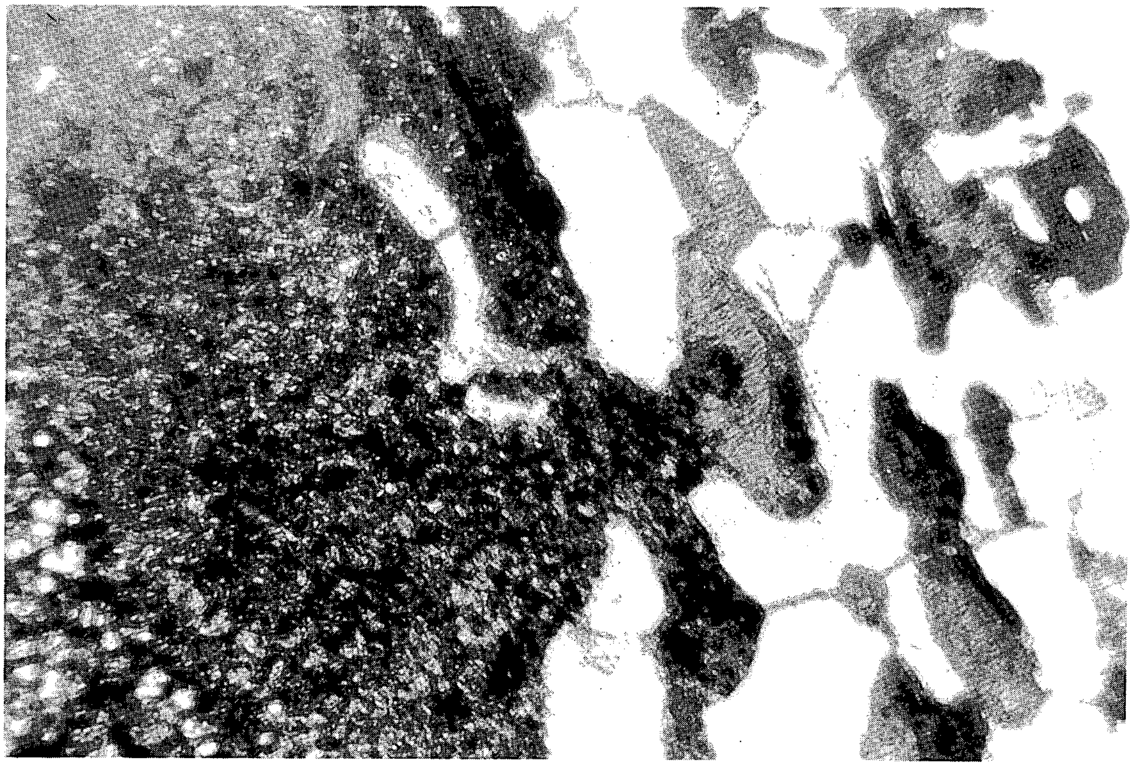

Figure I-33a, Photomicrograph (1000x) at Edge of Heat-Affected Zone. Fuel Element 47, 9 Inches from Top of Plate. 0.5% HF etch.

U-5175-424J

Figure I-33b, Photomicrograph at Side Opposite of Zone Shown in Figure I-33a.

U-5175-424G

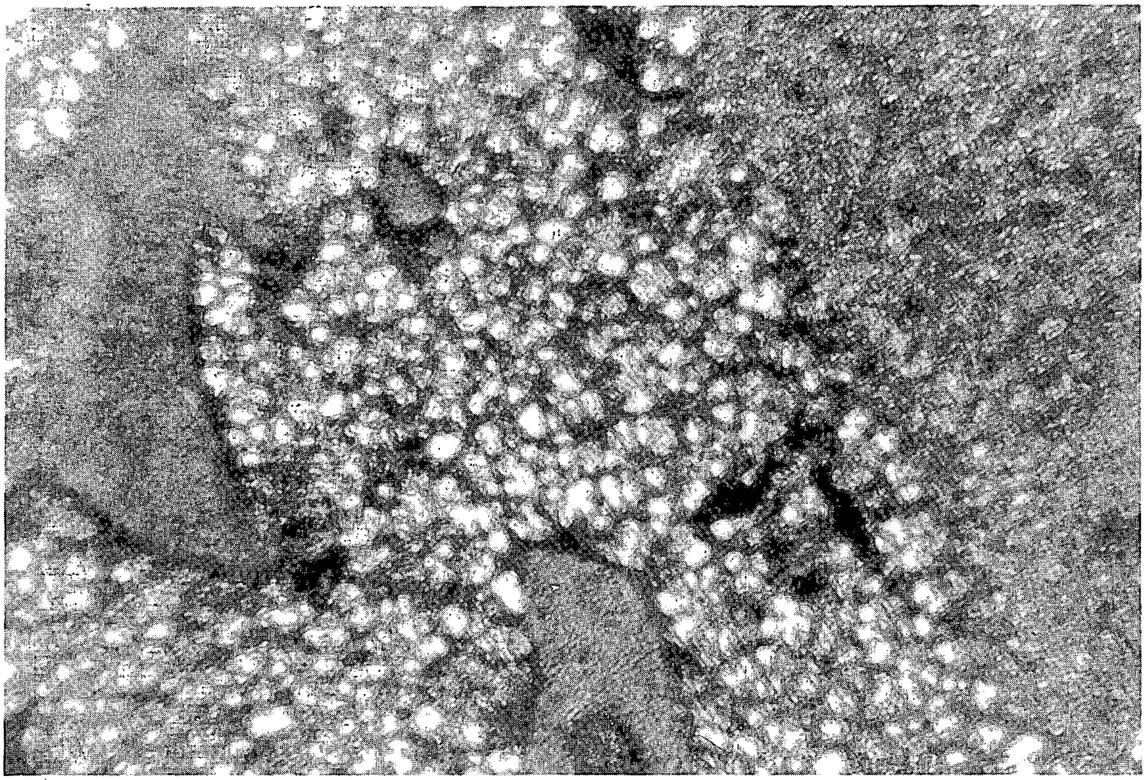

Figure I-34a, Same as Figure I-33a but at High and Intermediate Zone Interface.

U-5175-424I

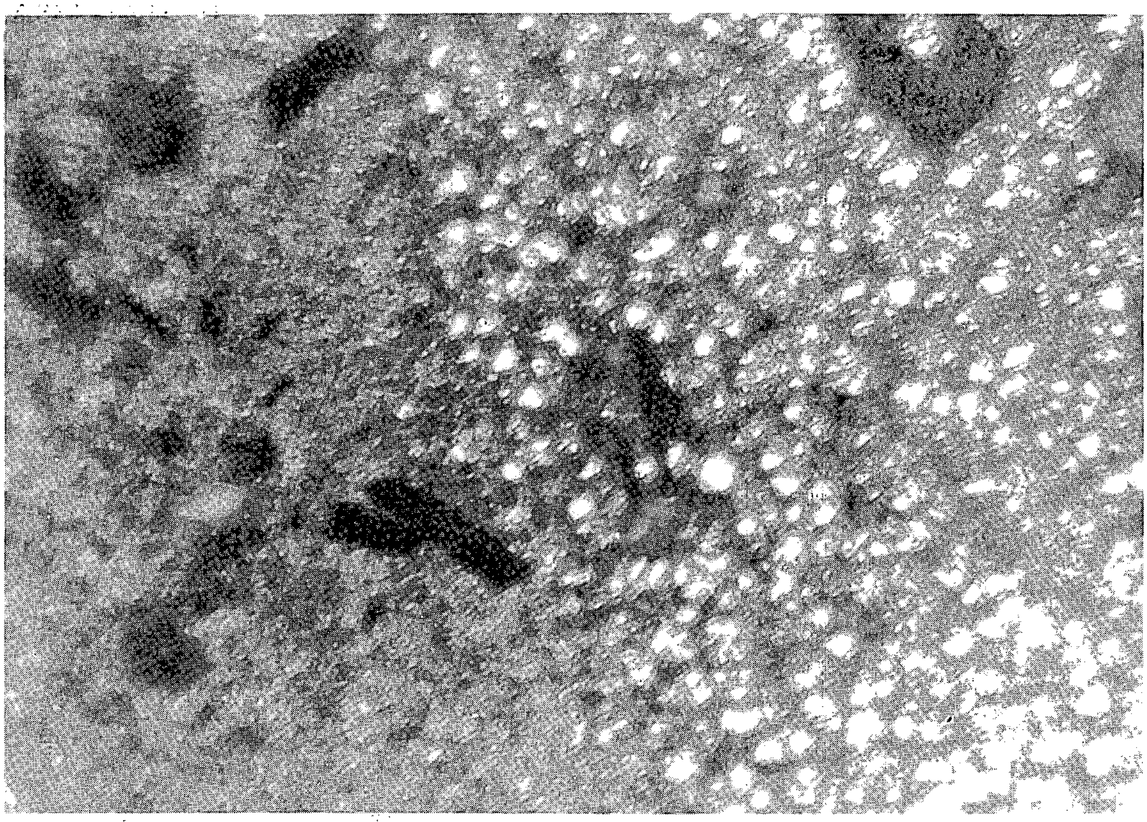

Figure I-34b, Same as Figure I-34a, Other Side of Center.

U-5175-424H

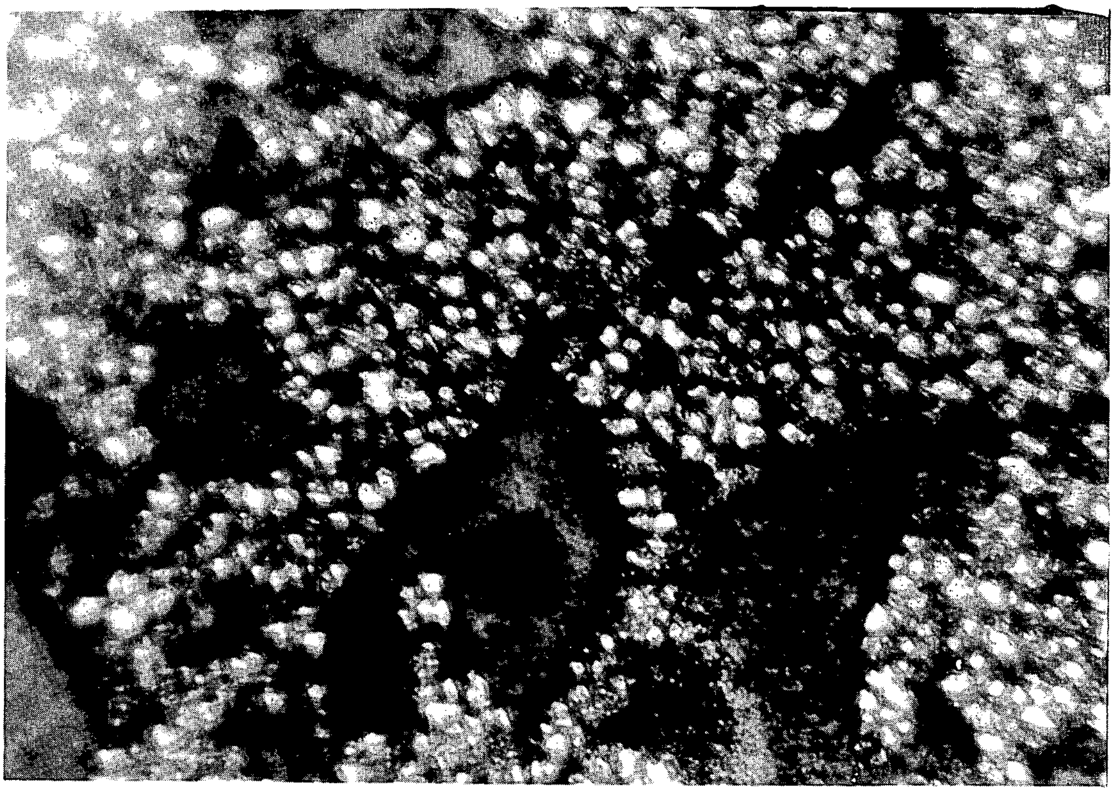

Figure I-35a, High Temperature Zone in Fuel Matrix. See Figure I-33a.

U-5175-438A

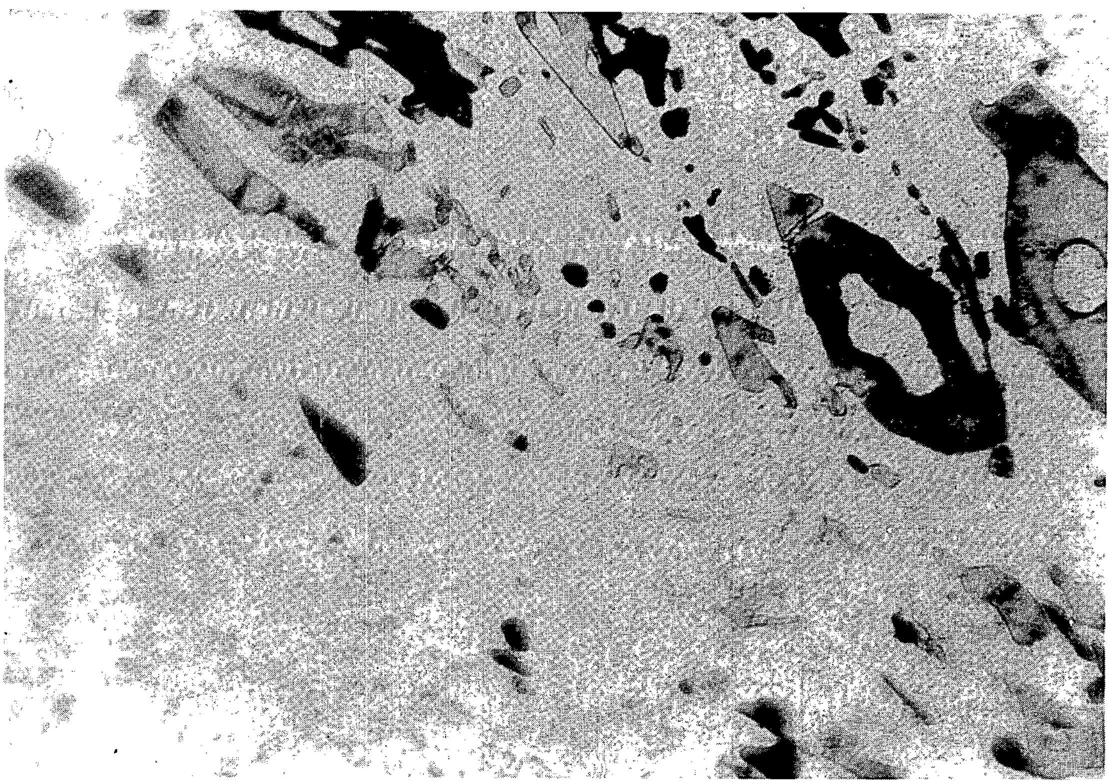

Figure I-35b, Fuel Element 47, 15 Inches from Top. Fuel Matrix Near Clad at 1000x Transverse Section. 0.5% HF etch.

U-5174-7

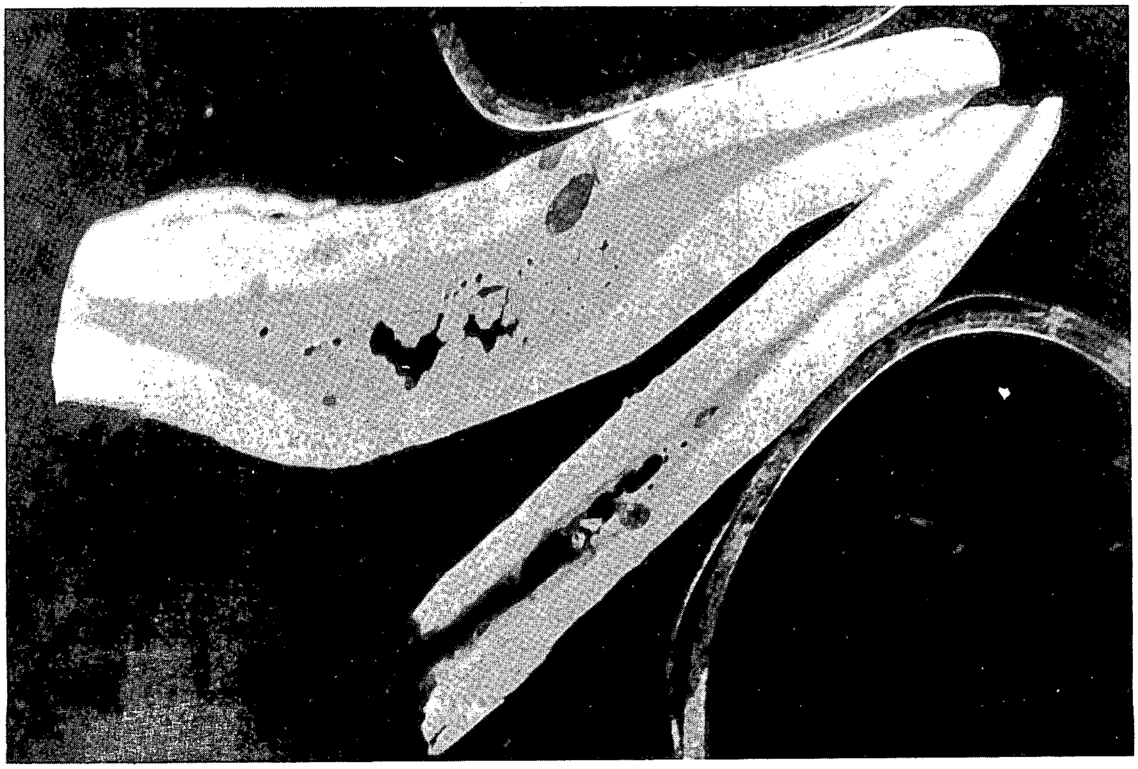

Figure I-36, Specimen Set from Fuel Element 52, 27 Inches from Top of Plate.

U-5174-8

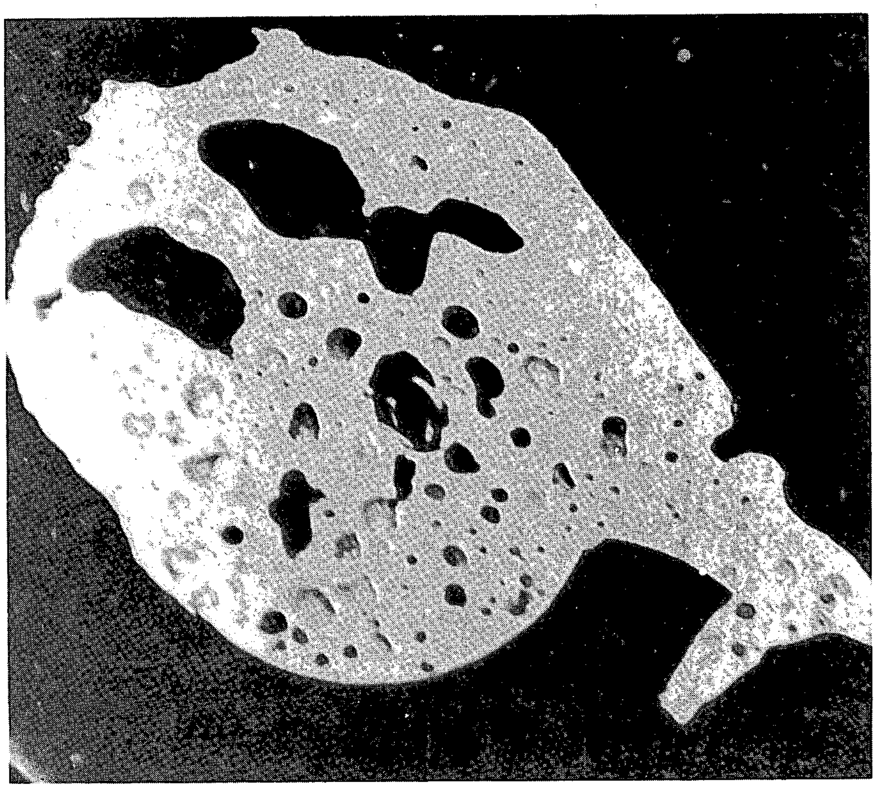

Figure I-37, Melted Bead from Fuel Element 39, 9 Inches from Top of Plate.

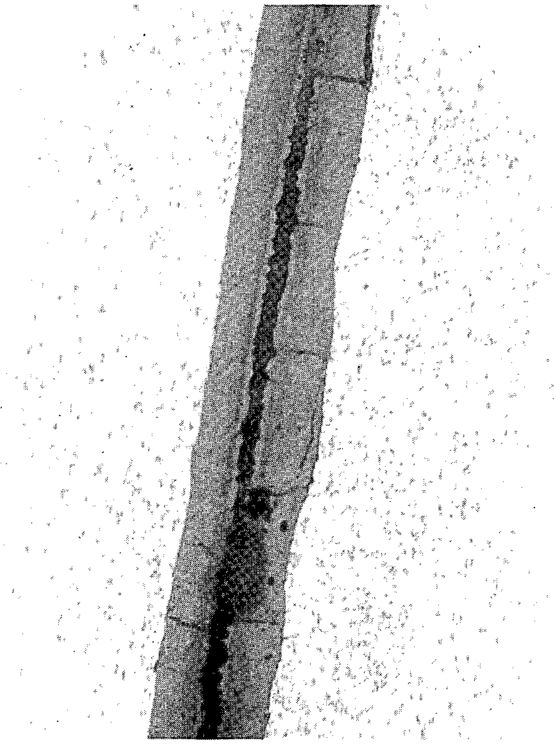

Figure I-38a, Corrosion on Edge of Longitudinal and Transverse Section from Fuel Element 47, 26 Inches from Top of Plate. 200x. 0.05% HF etch.

U-5175-422A

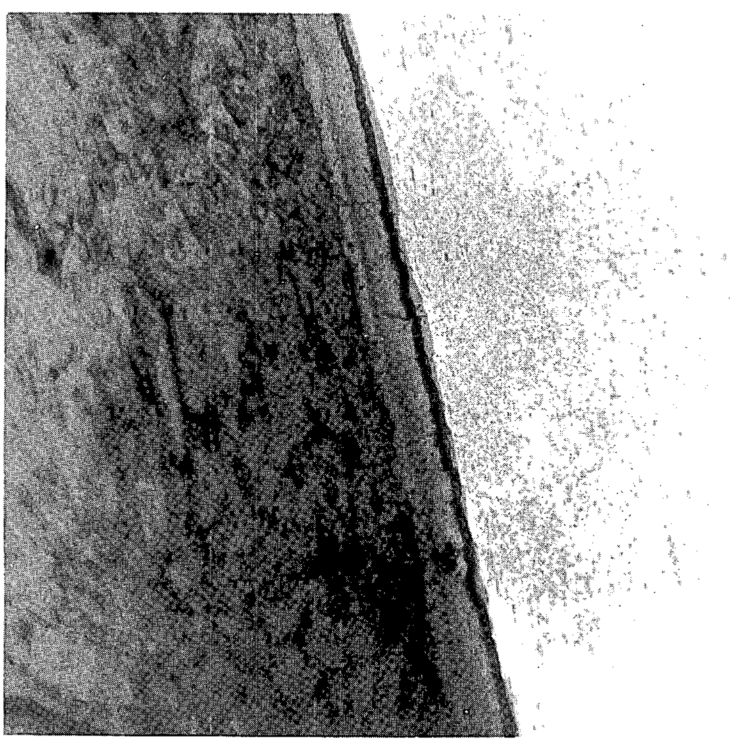

Figure I-38b, Corrosion on Edge of Longitudinal Section, Fuel Element 60, 3 Inches from Top of Plate. 200x. 0.5% HF etch.

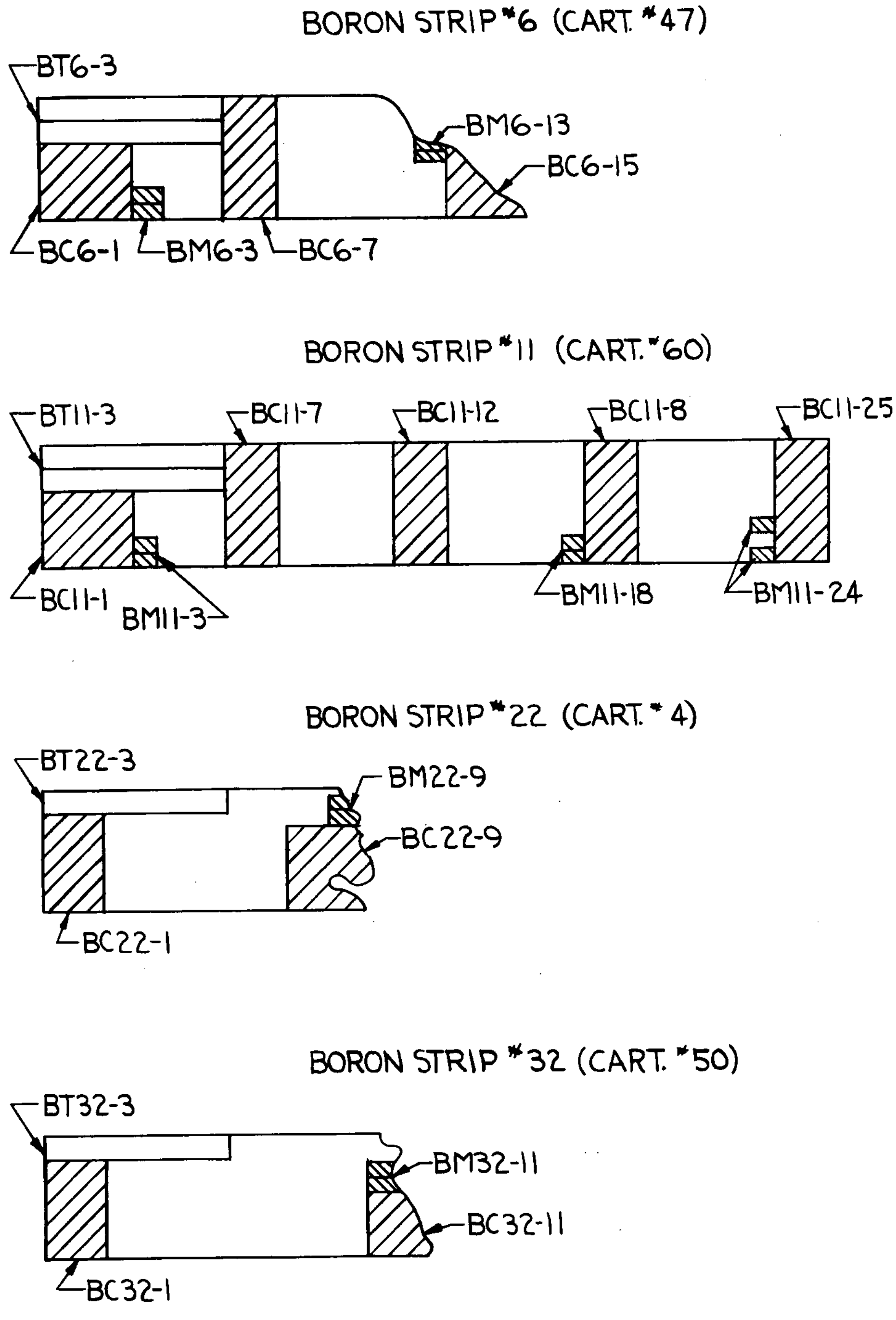

FIG. NO. I-39
SL-1 BORON STRIP
SPECIMEN LOCATION

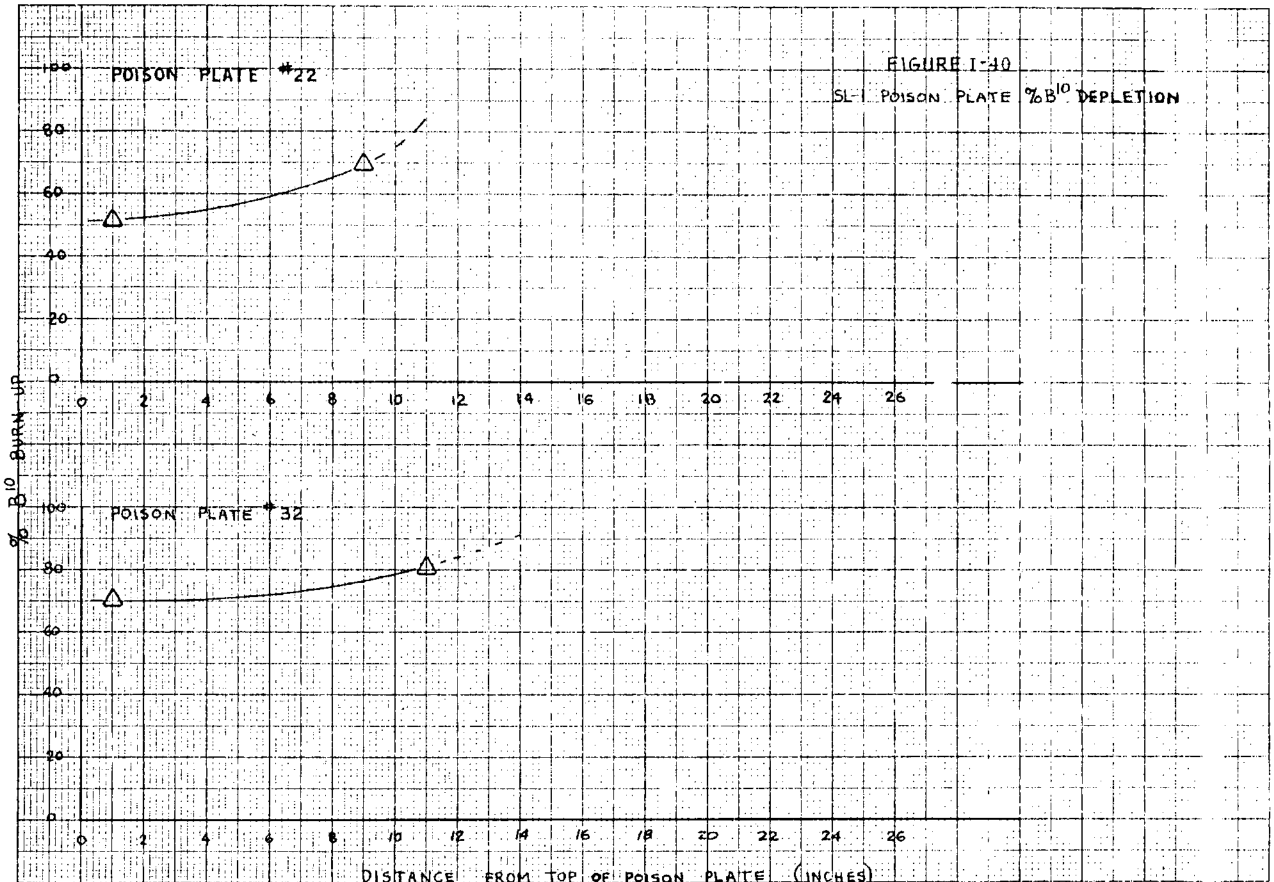

FIGURE I-10
SL-1 POISON PLATE % B^{10} DEPLETION

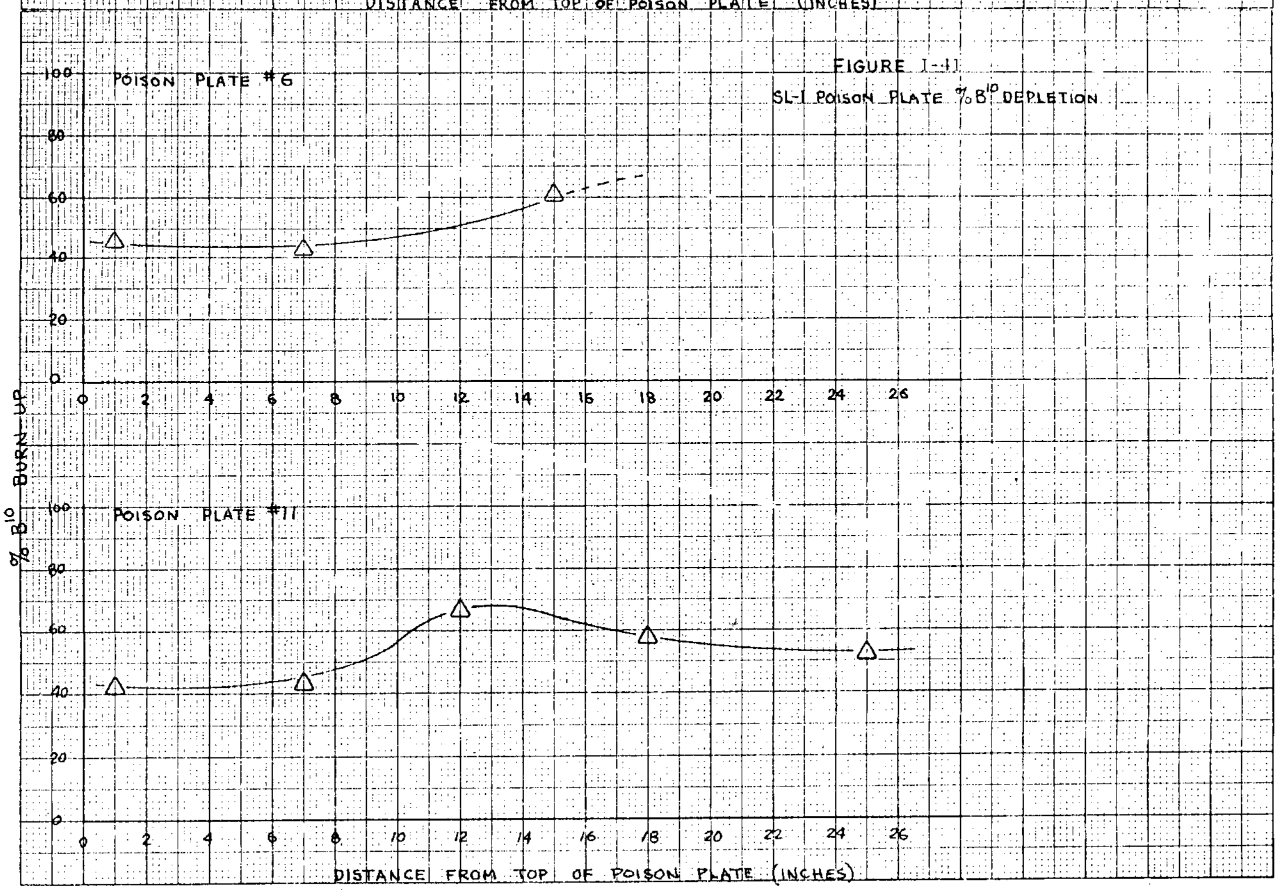

FIGURE I-11
SL-1 POISON PLATE % B^{10} DEPLETION

Figure I-42 Typical Longitudinal Flux Profiles Obtained From Co-Al Flux Wires

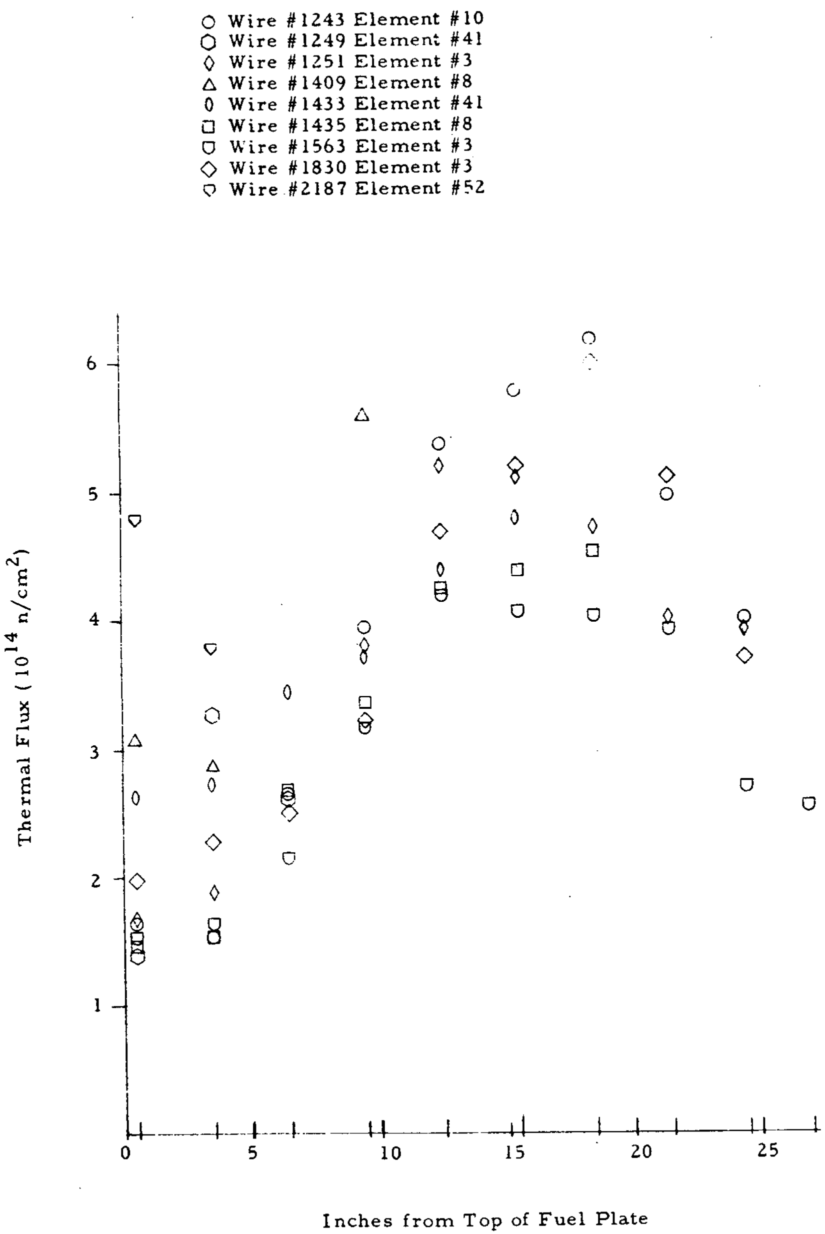

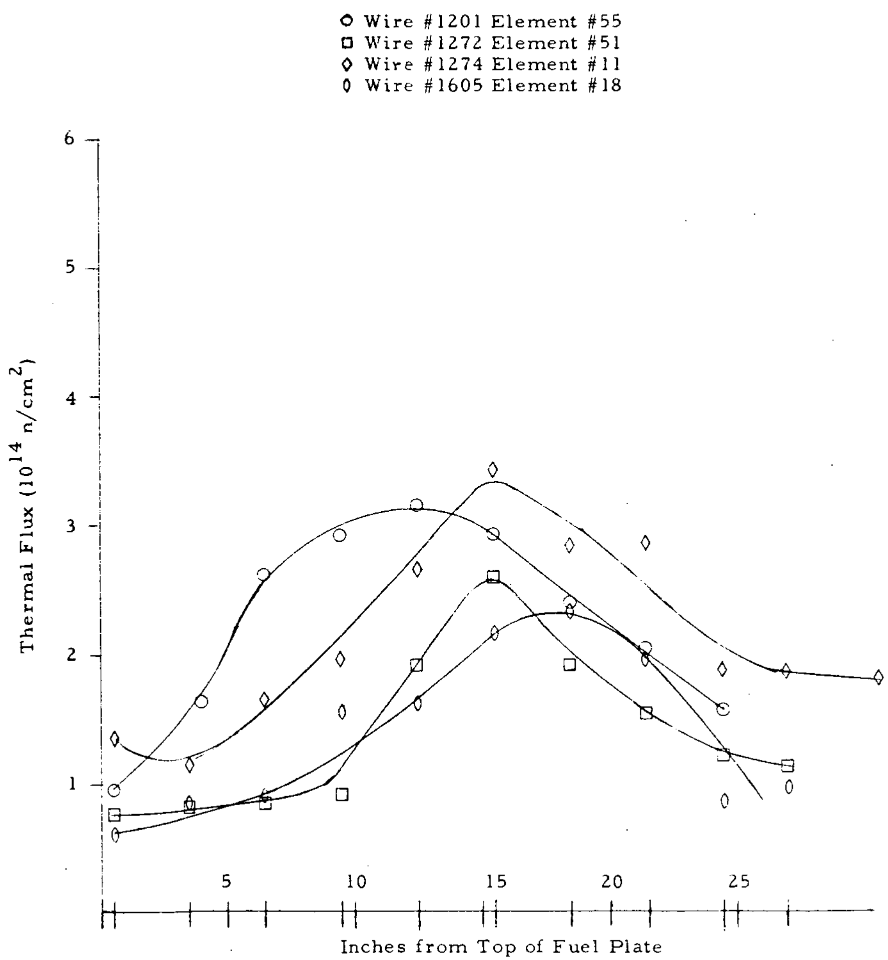

U-5174-10

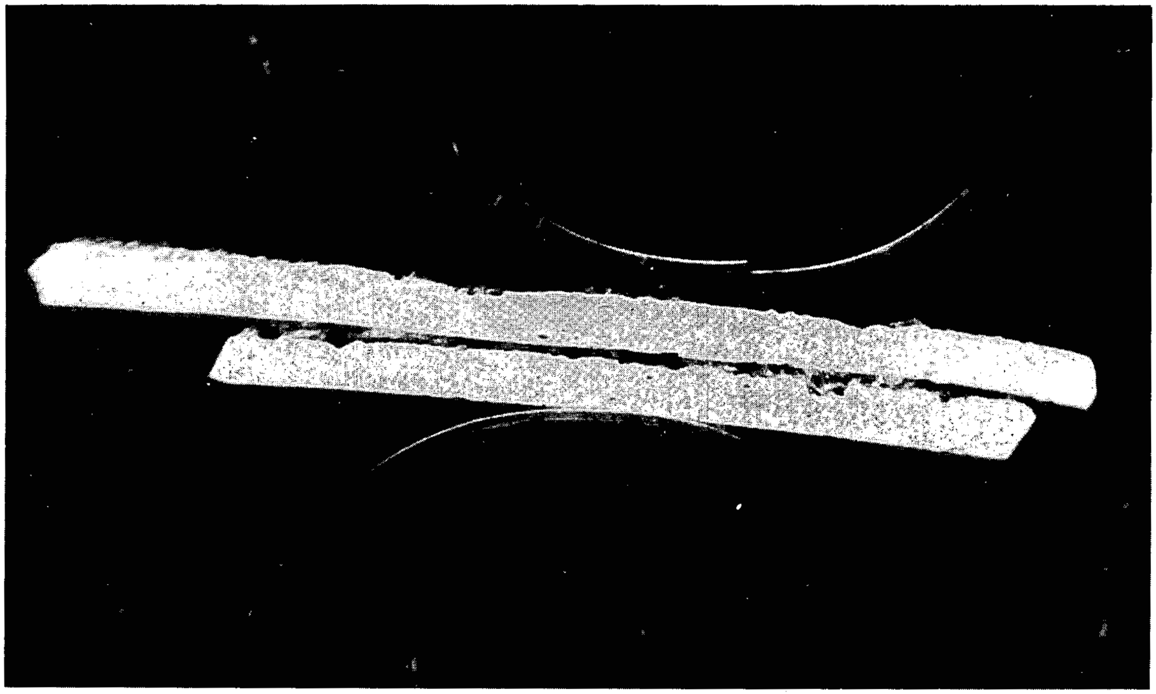

Figure I-43, Metallographic Samples #412 from Boron Strip #11, Fuel Element 60, Taken 3-1/2 Inches from the Top in a Non-Deteriorated Area.

U-5174-5

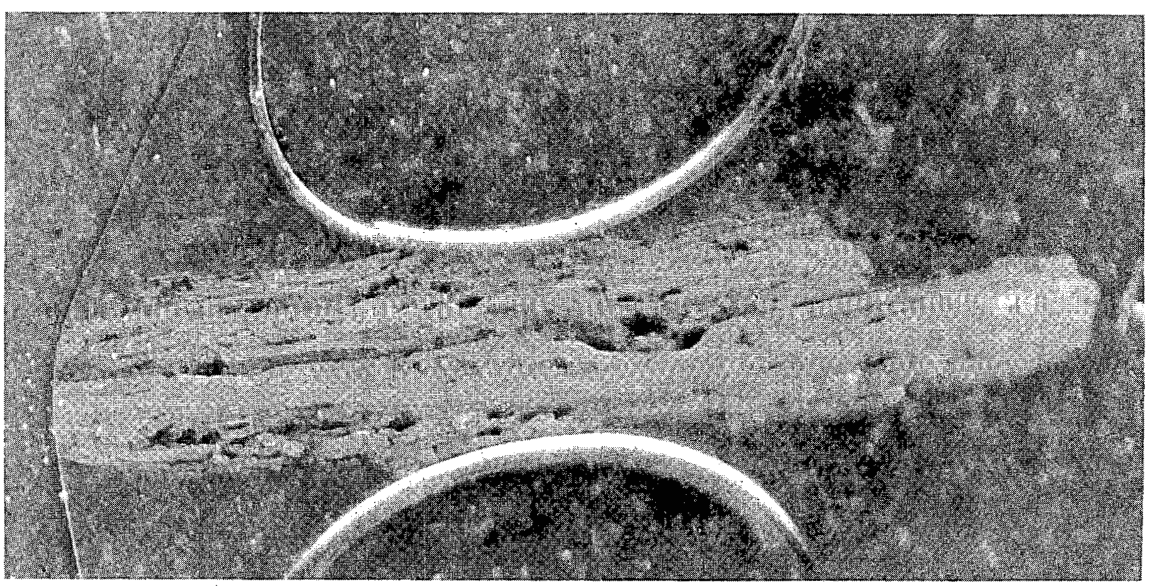

Figure I-44, Metallographic Samples #411 from Boron Strip #11, Fuel Element 60, Taken 16 Inches from the Top in a Badly Deteriorated Area.

U-5174-16

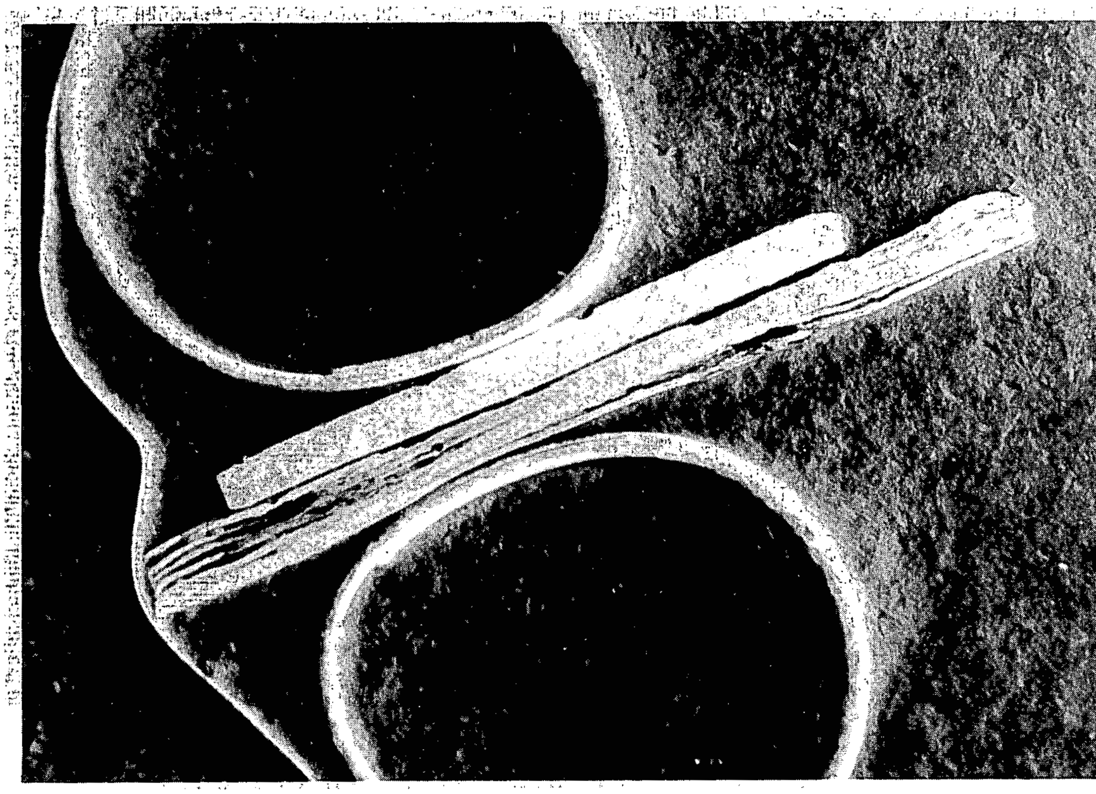

Figure I-45, Metallographic Samples #413 from Boron Strip #11, Fuel Element 60, Taken 2 Inches from the Bottom in a Partially Deteriorated Area.

U-5174-2

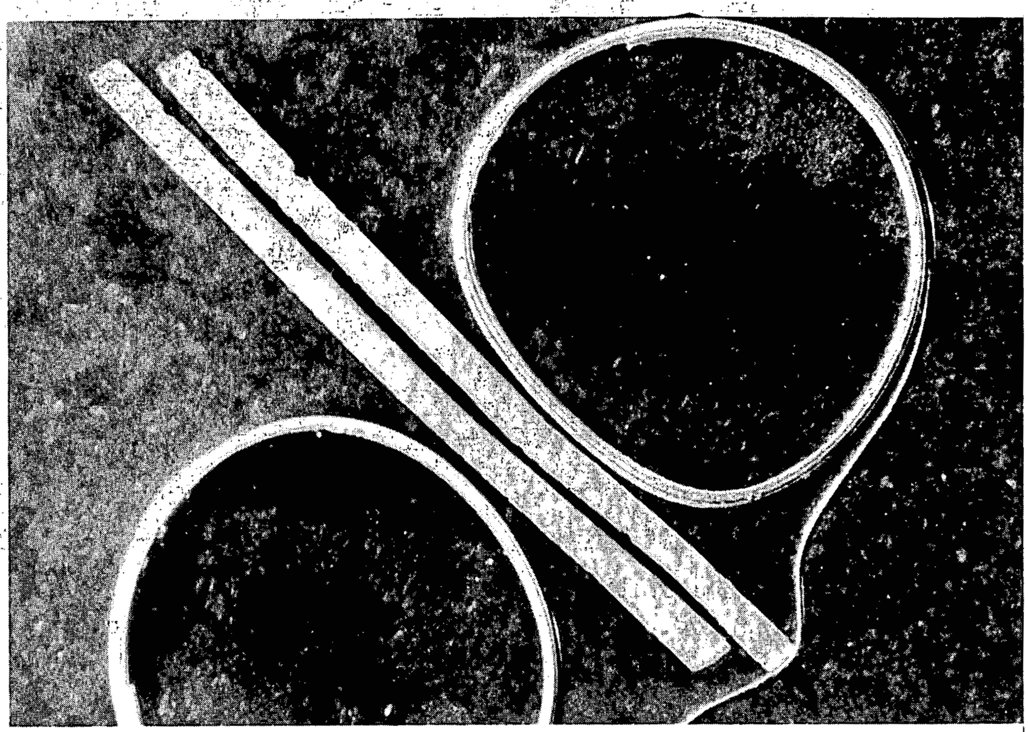

Figure I-46, Metallographic Samples #415 from Boron Strip #6, Fuel Element 47, Taken 3 Inches from the Top in a Non-Deteriorated Area.

U-5174-3

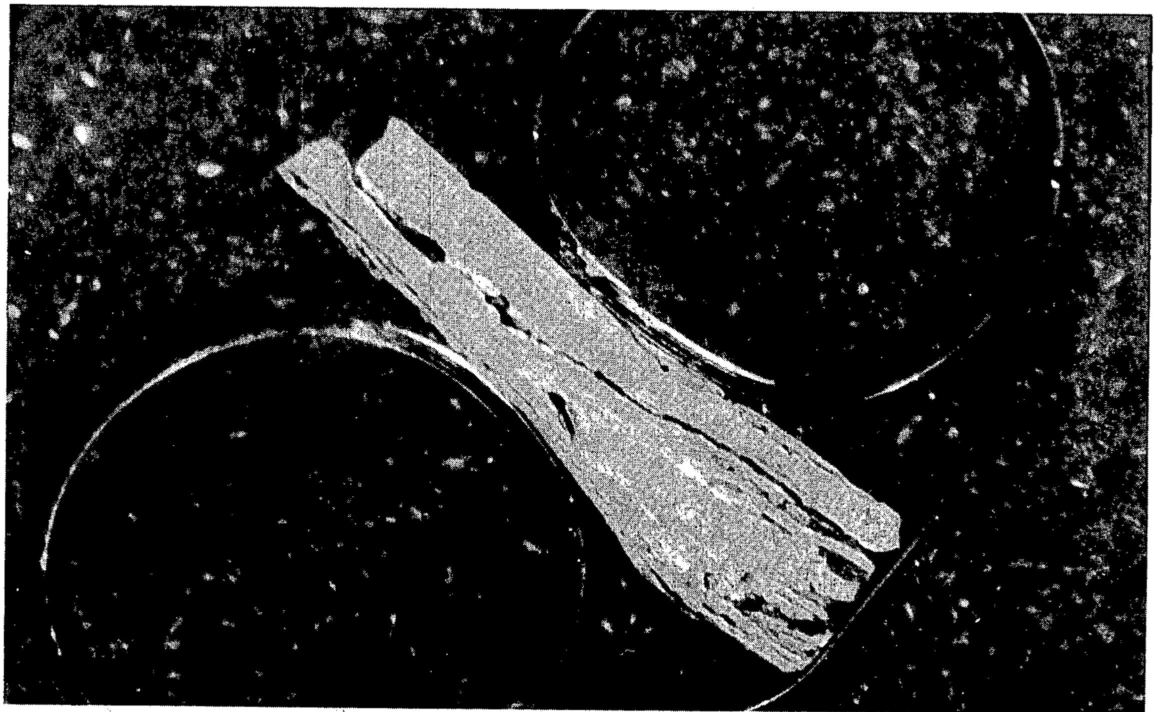

Figure I-47, Metallographic Samples #417 from Boron Strip #6, Fuel Element 47, Taken 13 Inches from the Top in a Highly Deteriorated Area.

U-5174-6

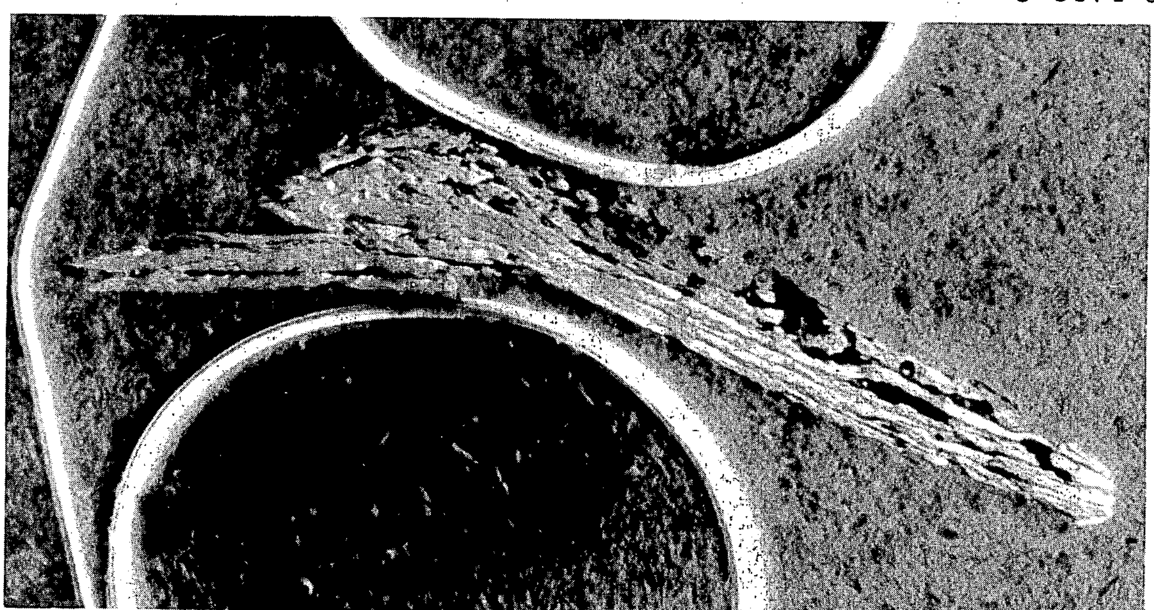

Figure I-48, Metallographic Samples #418 from Boron Strip #32, Fuel Element 50, Taken 11 Inches from the Top on the Highly Deteriorated Edge.

U-5174-4

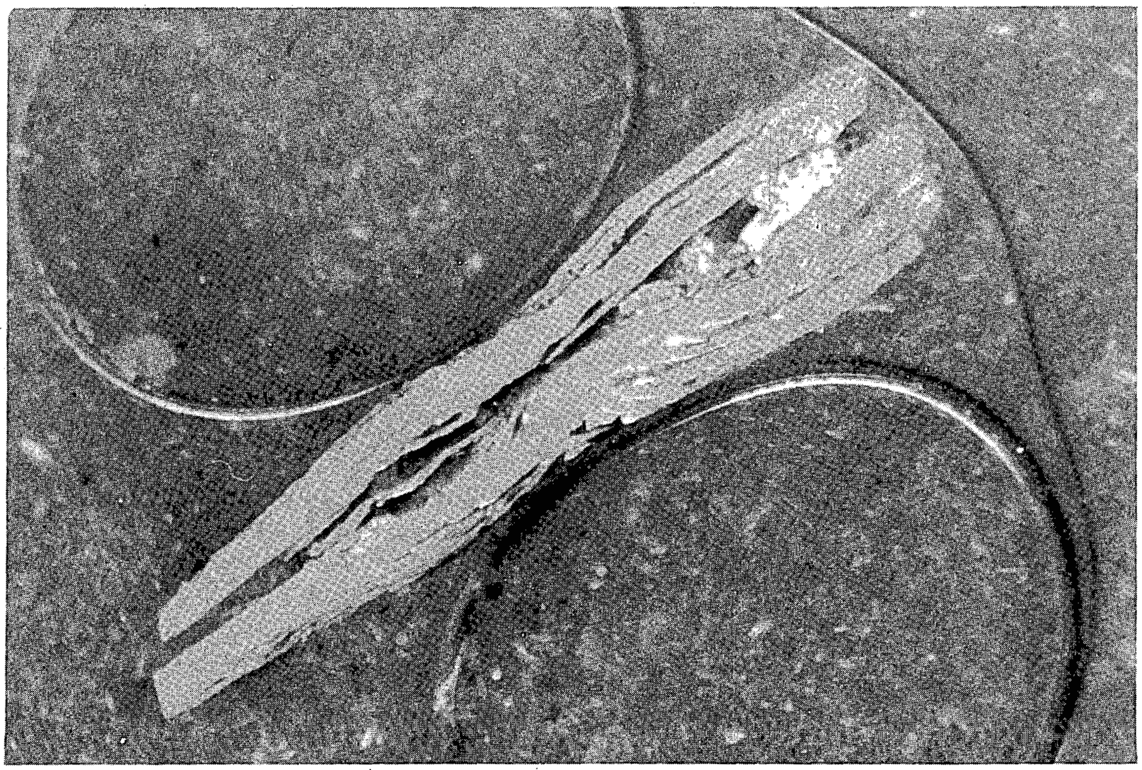

Figure I-49, Metallographic Samples #427 from Boron Strip #22, Fuel Element 22, Taken 9 Inches from Top on the Deteriorated Edge.

U-5001-385

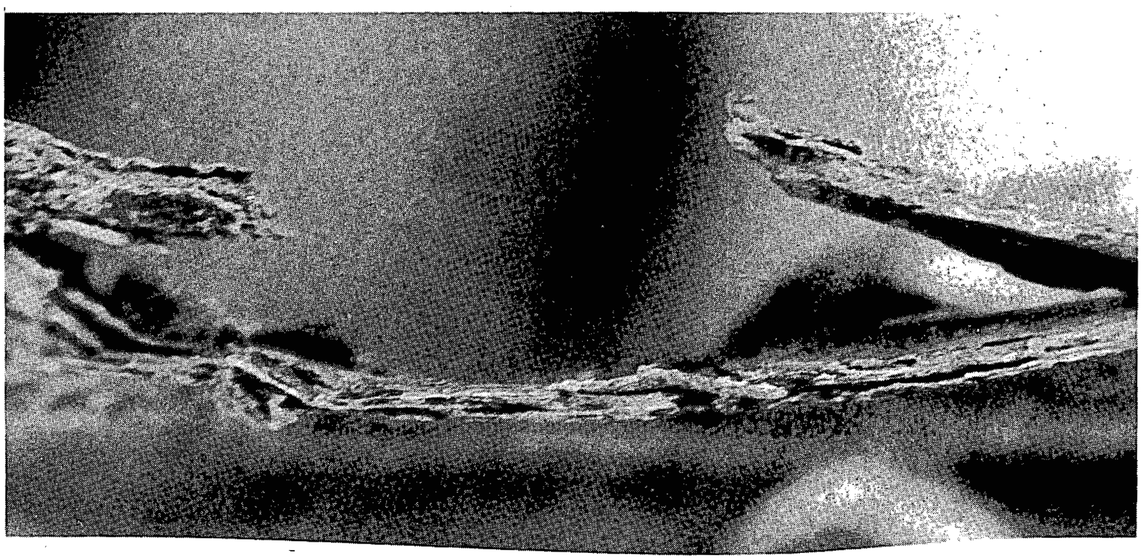

Figure I-50, Edge View of Boron Strip #24, Fuel Element 57, Showing Deteriorated Edges.

U-5175-415A

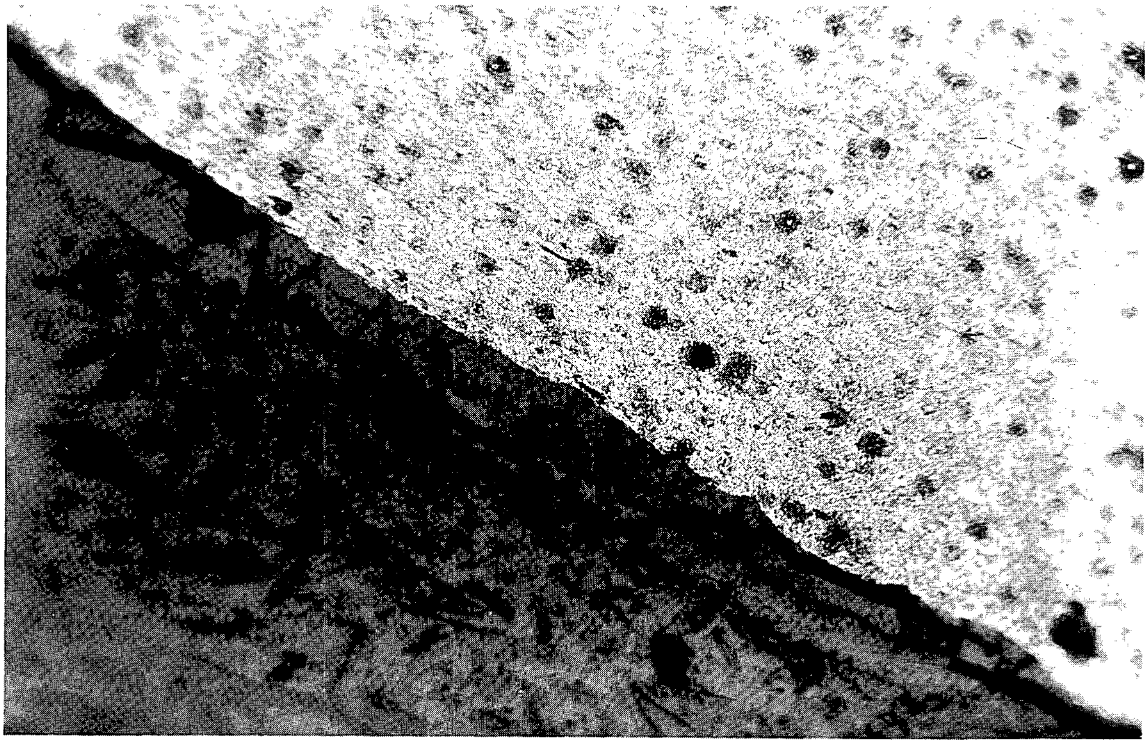

Figure I-51a, Corrosion on Edge of Boron Strip #6, Fuel Element 47, at 3 Inches from the Top Longitudinal Section. 300x. 0.05% HF etch.

U-5175-418B

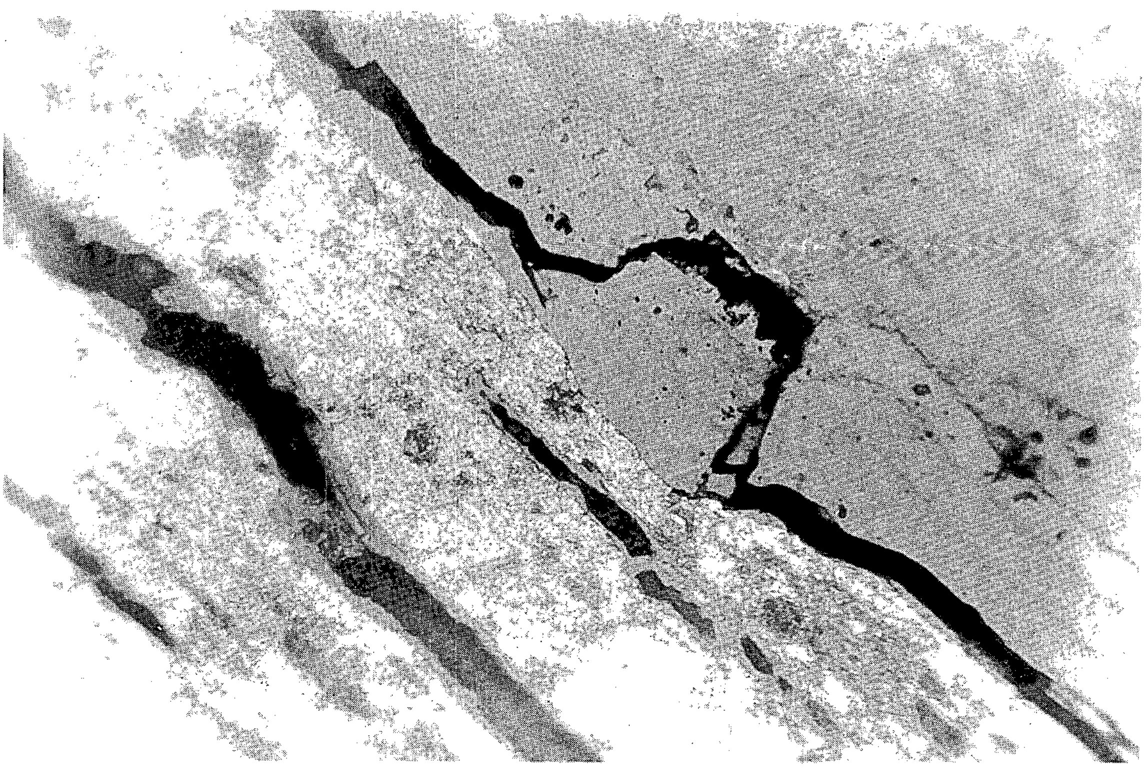

Figure I-51b, Edge and Internal Corrosion on Boron Strip #32, Fuel Element 50, 11 Inches from the Top in Maximum Deteriorated Area. 500x. 0.5% HF etch.

U-5175-418F

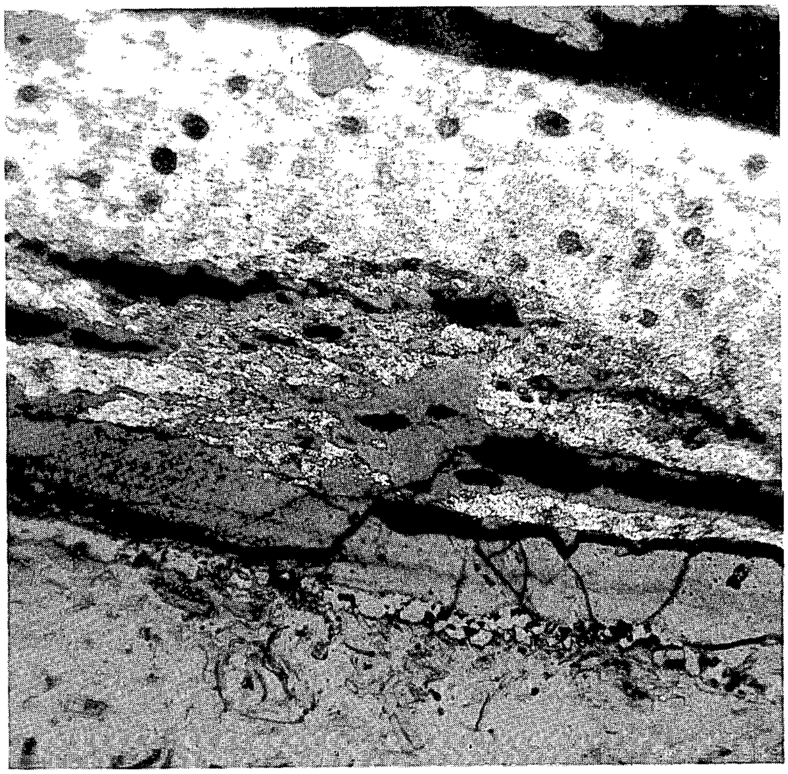

Figure I-52a, Edge and Internal Corrosion on Boron Strip #32, Fuel Element 50, 11 Inches from the Top. 300x. 0.5% HF etch.

U-5175-417C

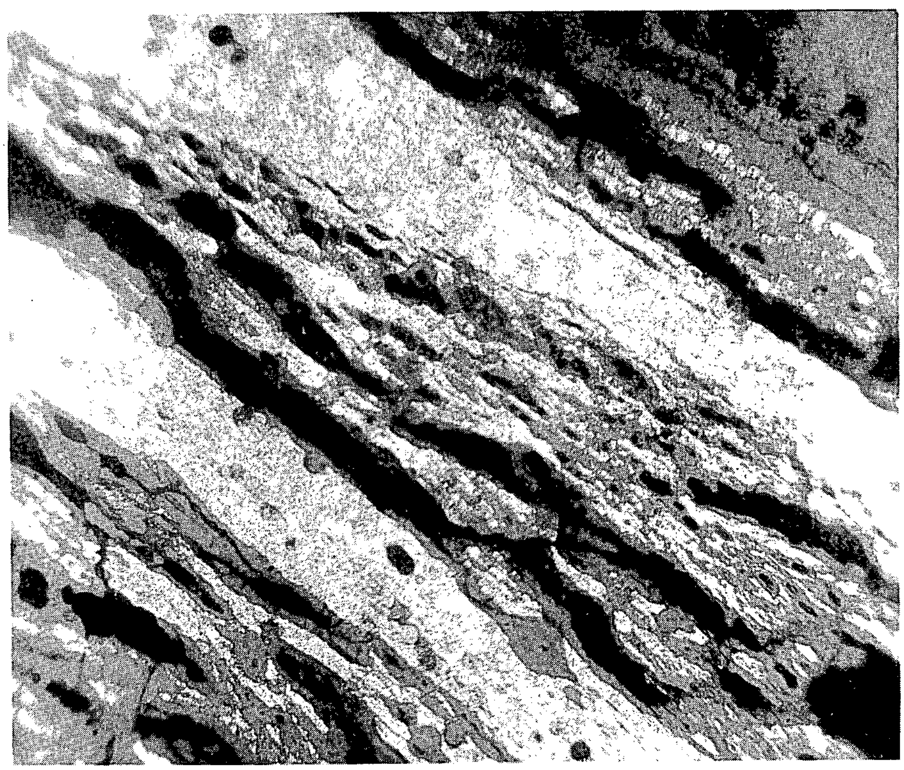

Figure I-52b, Edge and Internal Corrosion on Boron Strip #6, Fuel Element 47, 13 Inches from the Top in Maximum Deteriorated Area. 200x Longitudinal Section. 0.5% HF etch.

U-5175-411A

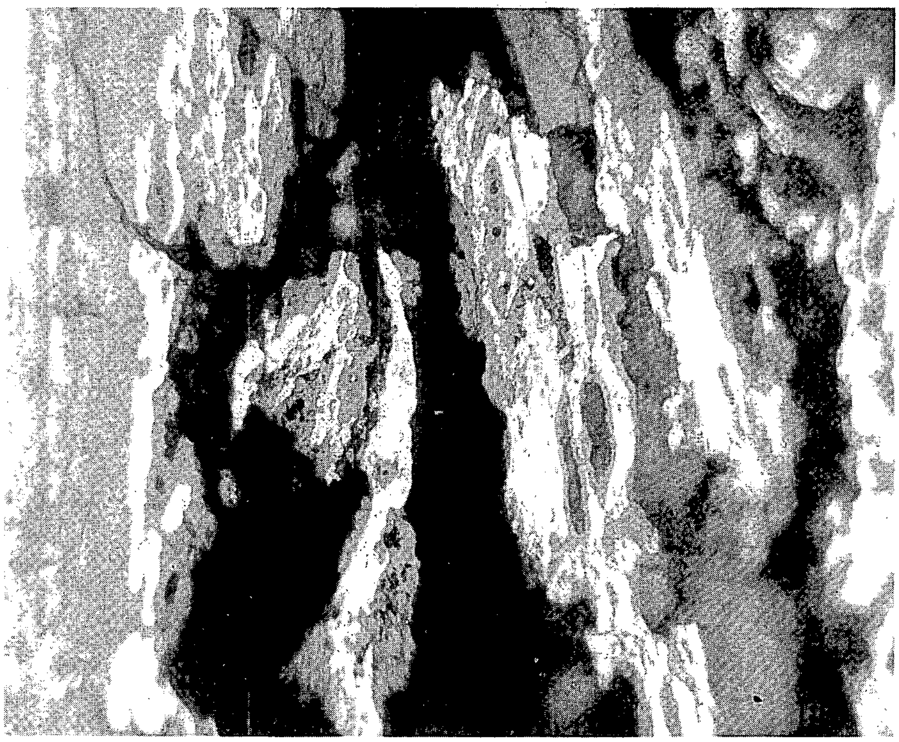

Figure I-53a, Edge on Internal Corrosion on Boron Strip #11, Fuel Element 60, 14 Inches from the Top in Highly Deteriorated Zone. 200x Longitudinal Section. 0.5% HF etch.

U-5175-413C

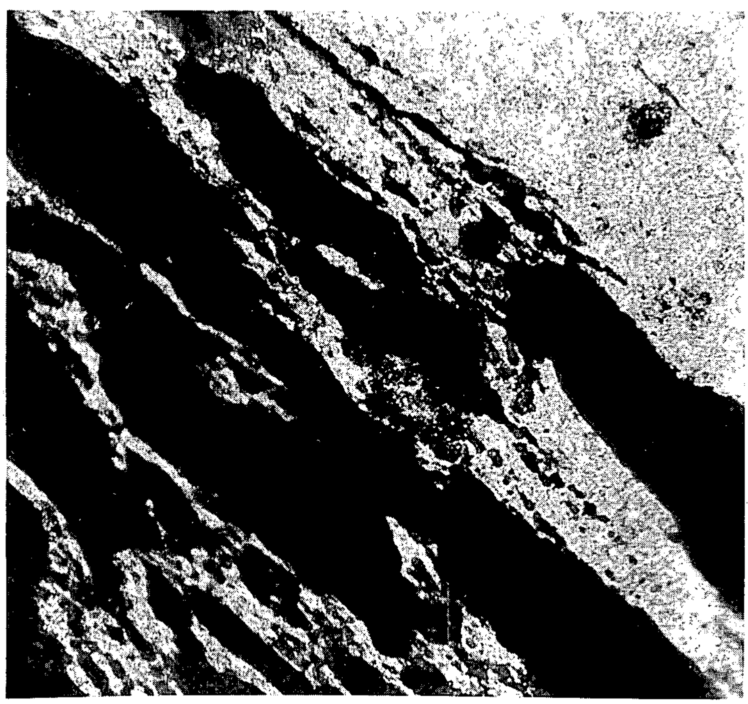

Figure I-53b, Internal Corrosion on Boron Strip #11, Fuel Element 60, 2 Inches from the Bottom. Note the Laminated appearance with apparent good material enclosed by corrosion. 500x Longitudinal Section. 0.5% HF etch.

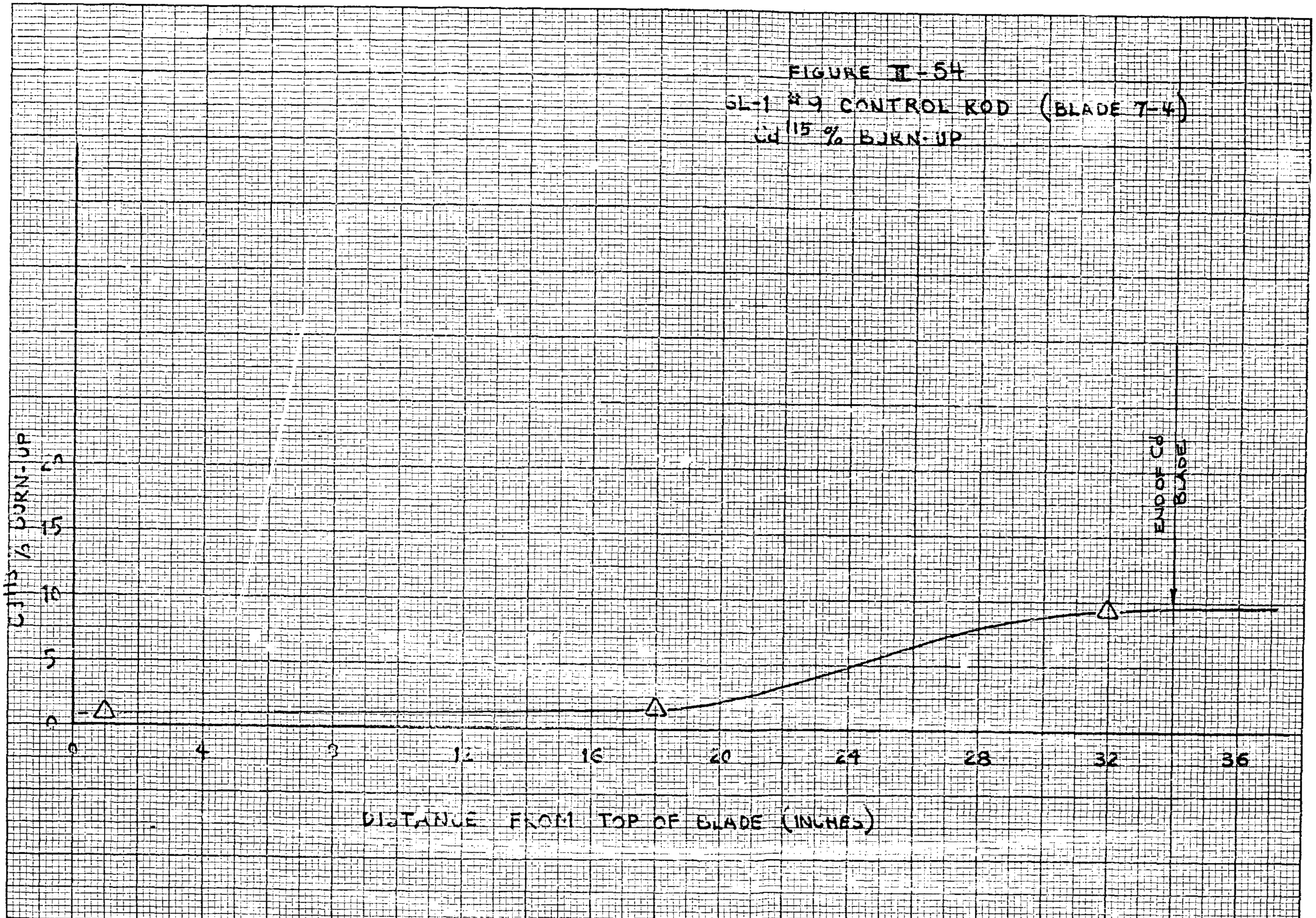
FIGURE I-54
CONTROL ROD (BLADE 7-4)
% BURN-UP
% BURN-UP
15
10
0
4
16
20
24
28
32
36
DISTANCE FROM TOP OF BLADE (INCHES)
END OF Cd BLADE

Figure I-54

T SECTION CONTROL BLADE *6

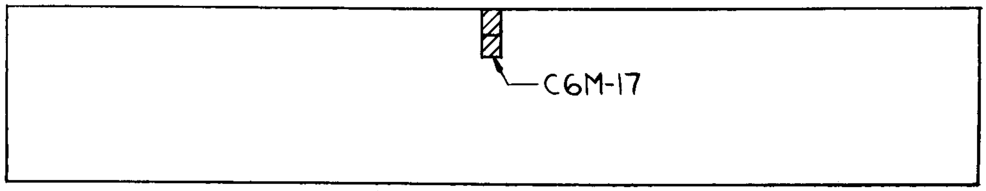

STRIPS 60, 58 & 58-60 ALL CUT SIMILAR

CONTROL BLADE * 7 - SECTION 52-47

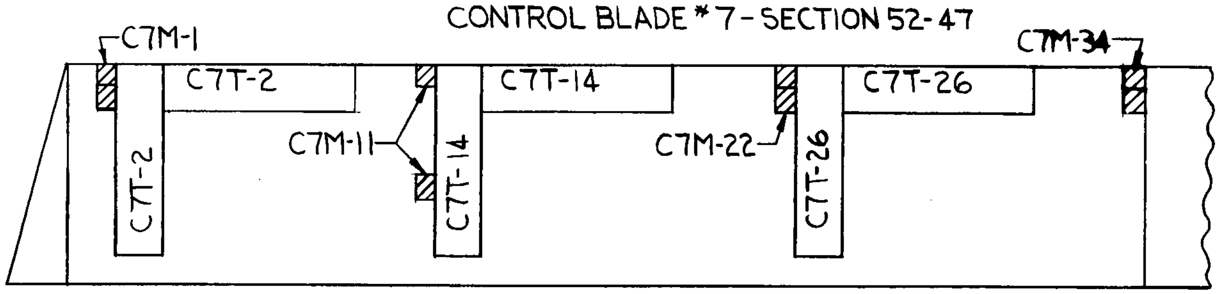

CONTROL BLADE * 9 - SECTION 10-41

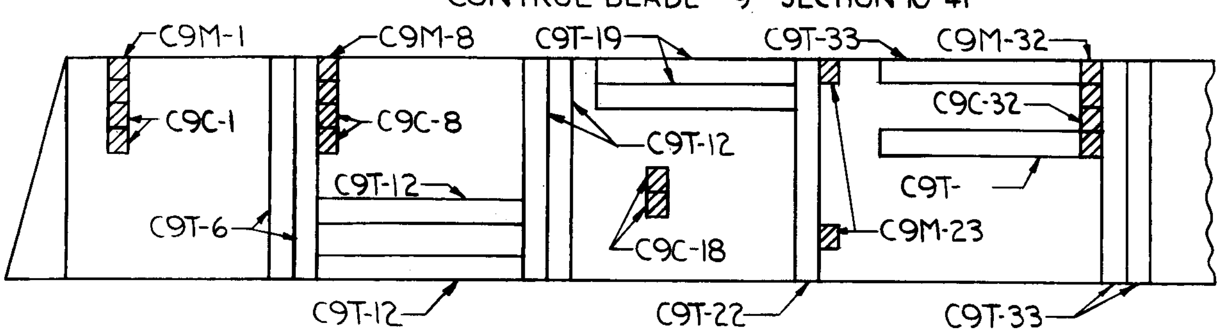

FIG. NO. I-55
SL-1 CONTROL BLADE
SPECIMEN LOCATION

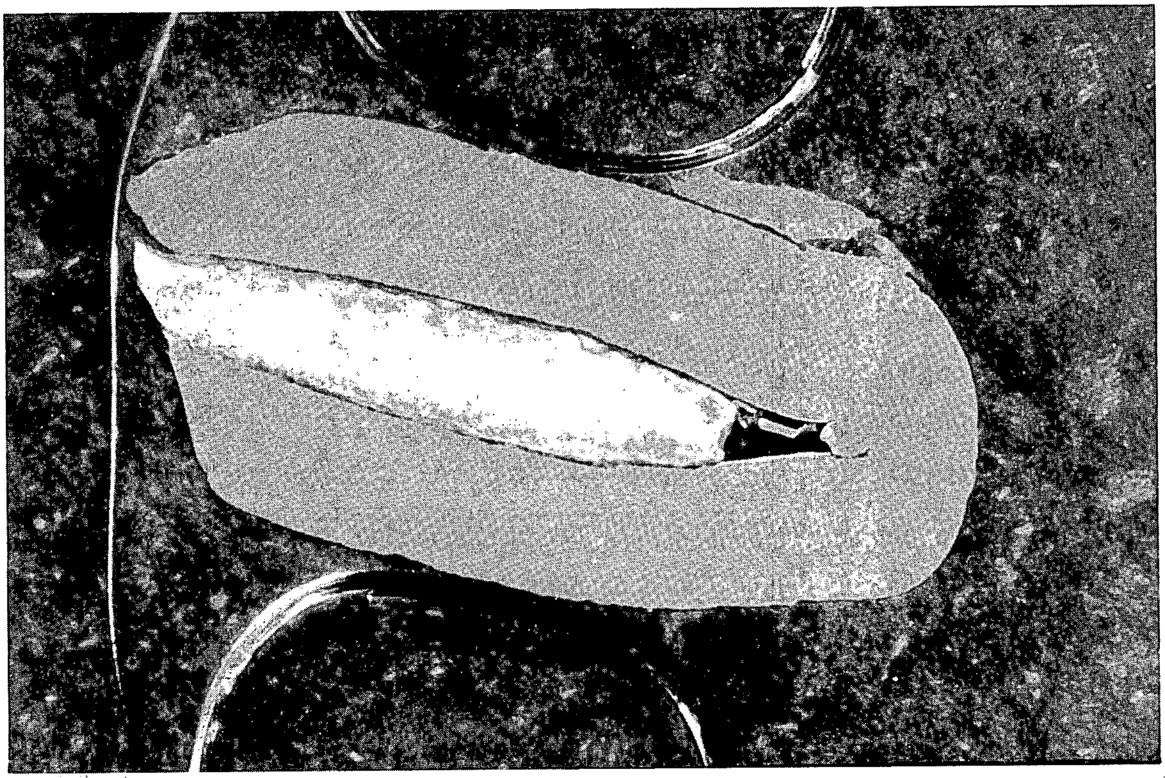

Figure I-56, Top of #9 Control Blade Weld Edge. Note poor weld penetration.

U-5174-21

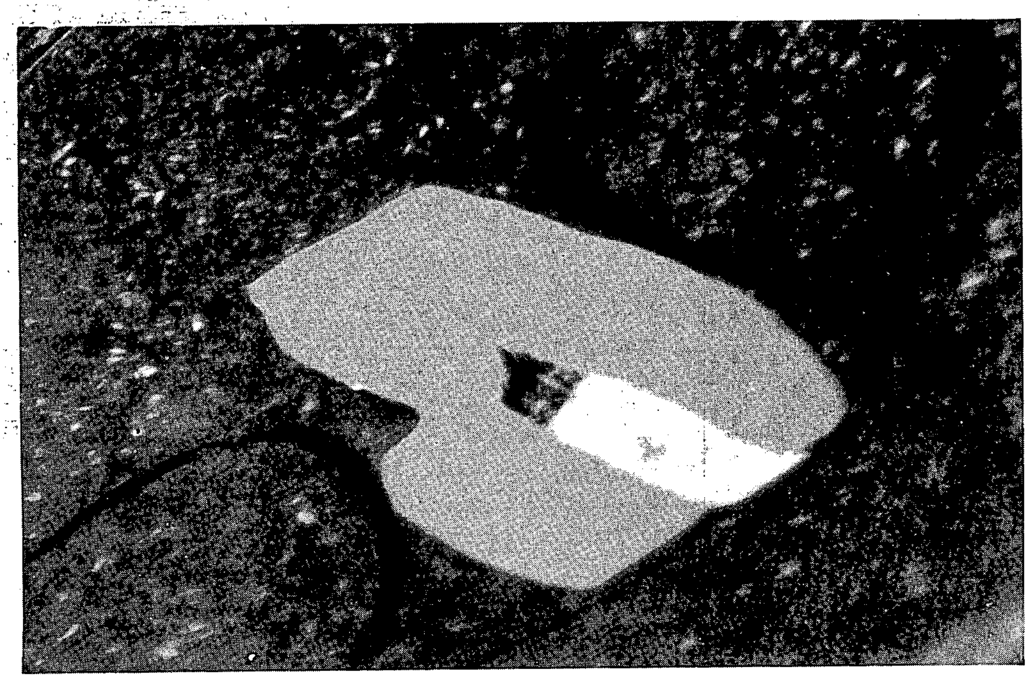

Figure I-57, Spot Weld 23 Inches from the Top of #9 Control Blade.

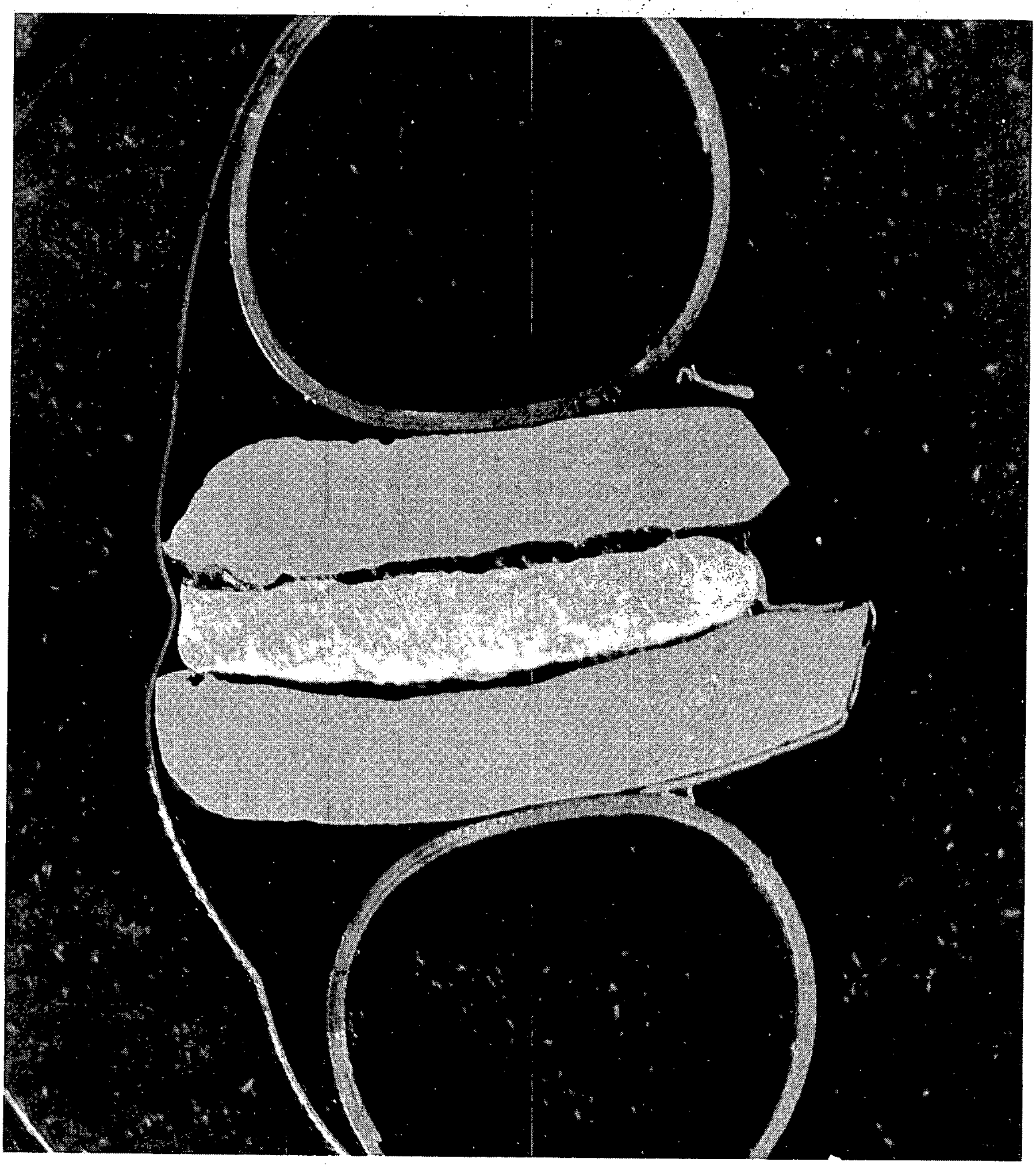

Figure I-58, Longitudinal Section 11 Inches from Top of #3 Control Blade.

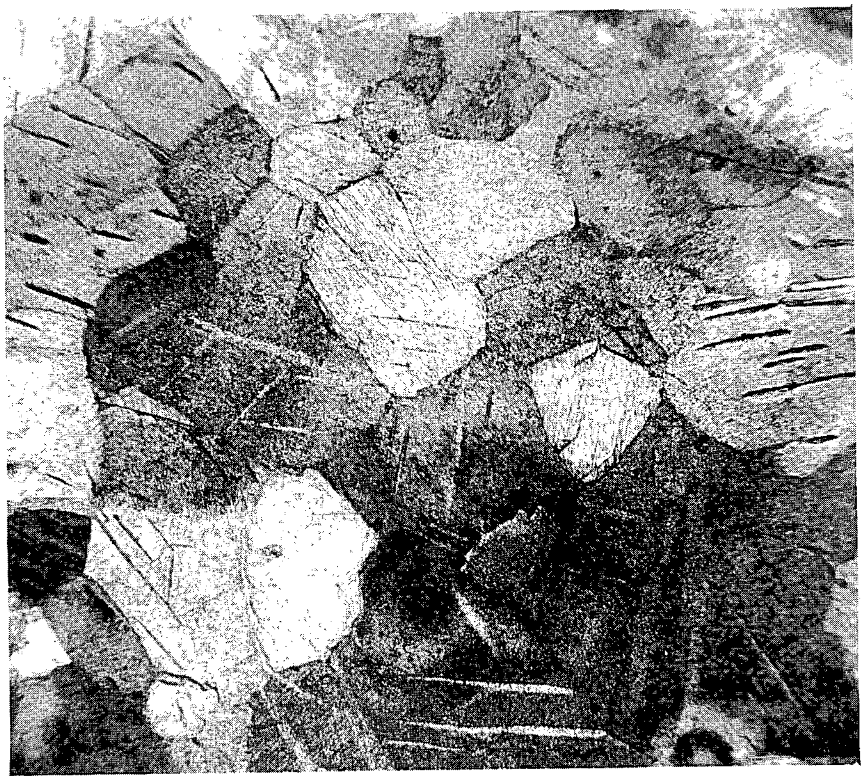

Figure I-59a, Structure of Cadmium 11 Inches from Top of #1 Control Blade. Longitudinal, 265x. Aqua Regia etch.

U-5175-437A

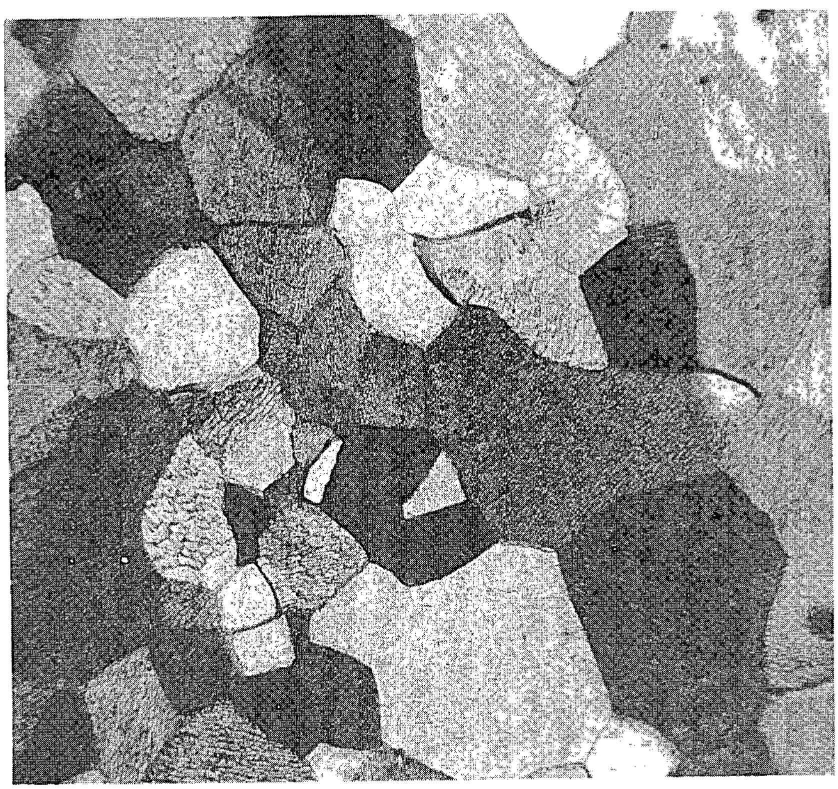

Figure I-59b, Structure of Cadmium 32 Inches from Top of #9 Control Blade. Longitudinal, 265x. Aqua Regia etch.

Figure I-60, Weld Edge 11 Inches from Top of Control Blade #1.

U-5175-444G

Figure I-61a, Structure of Cadmium at Top of Control Blade #1 Away from Weld. Transverse, 265x. Aqua Regia etch.

U-5175-444F

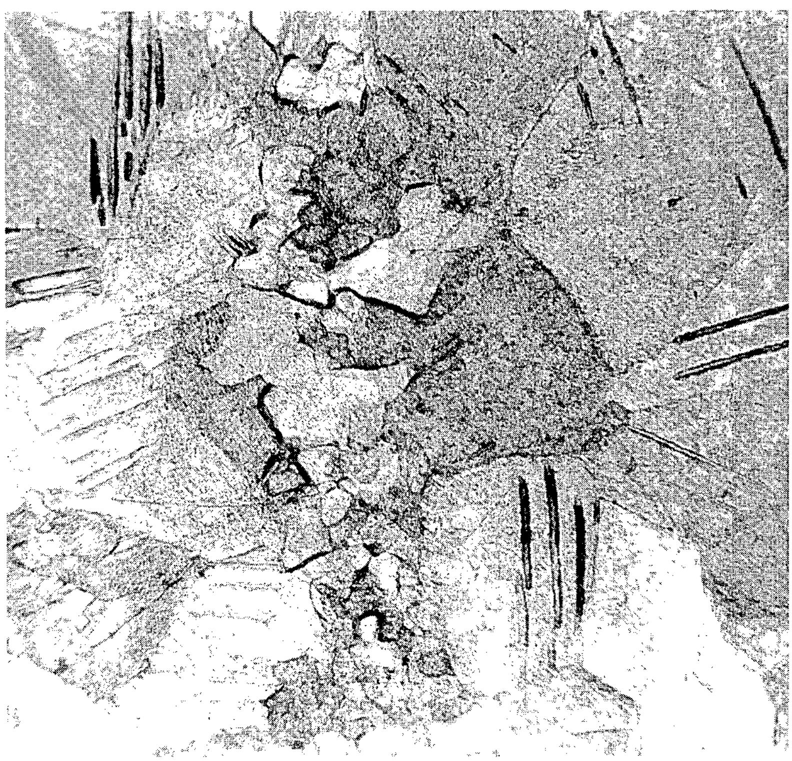

Figure I-61b, Structure of Cadmium at Top of #1 Control Blade Near Weld. Transverse, 265x. HF etch.

Figure I-62, Portion of Unirradiated Blade with the Cadmium in Place. Only one of the four spot welds was holding.

Figure I-63, Portion of Unirradiated Blade with Cadmium Removed from Clad. Note melted upper edge and corrosion.

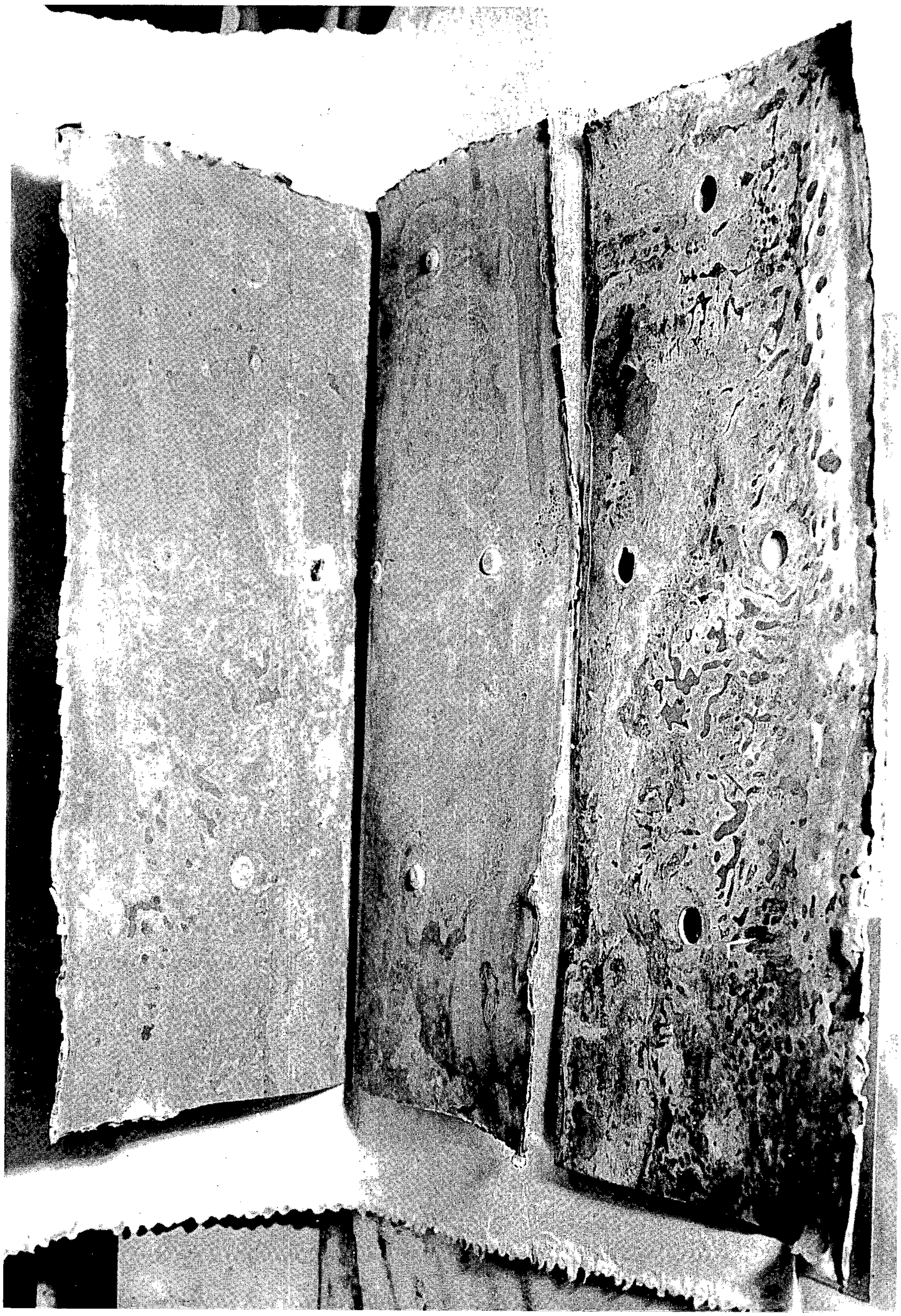

Figure I-64, Portion of Unirradiated Blade with Cadmium and Clad Separated to Show Opposite Side.

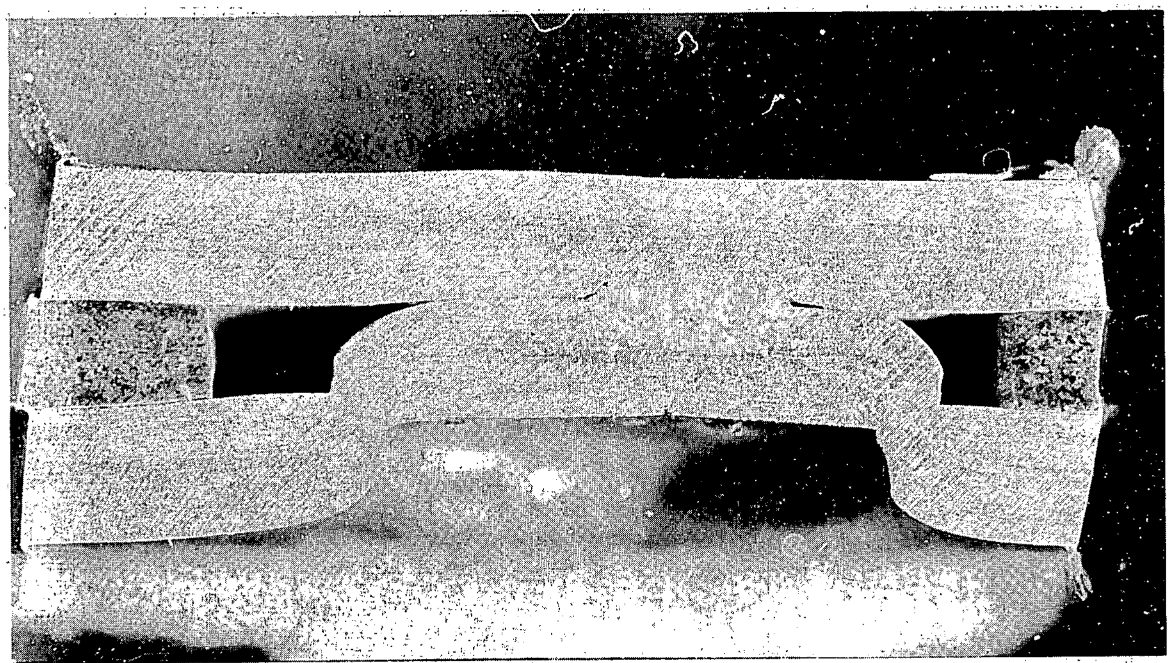

Figure I-65a, Spot Weld of Clad of Unirradiated Control Blade.

U-5001-386

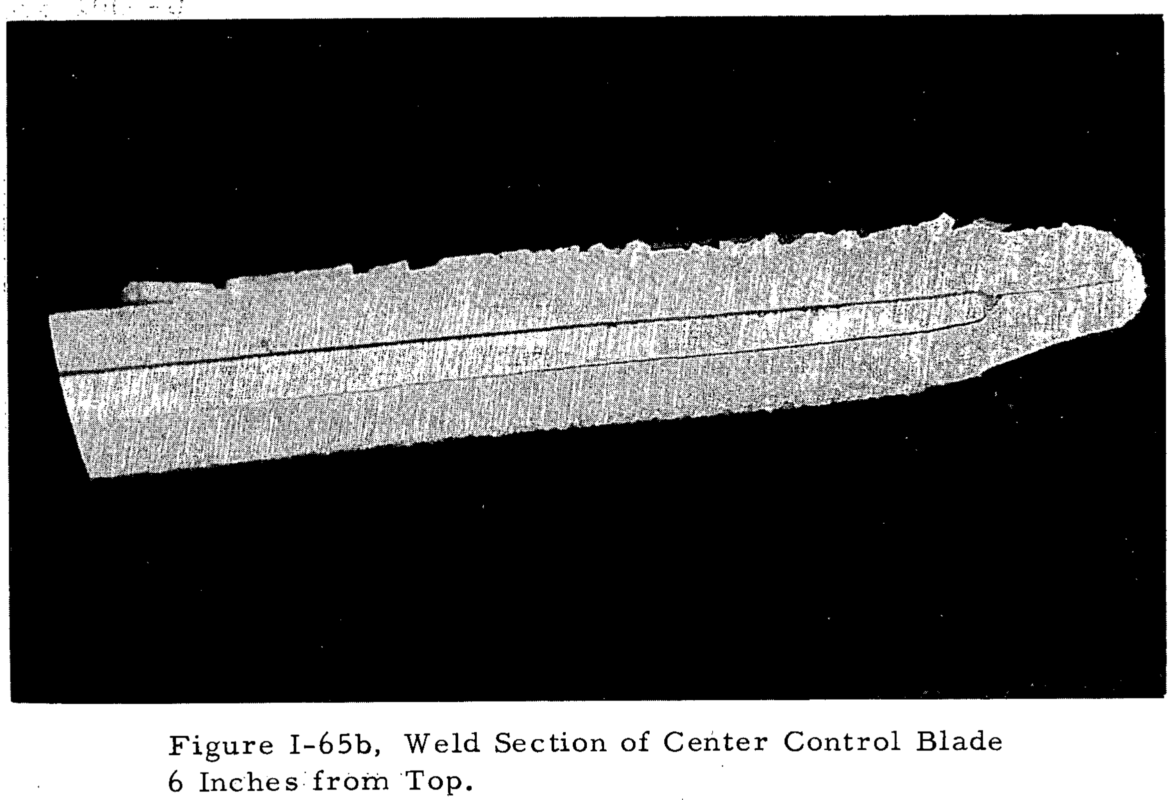

Figure I-65b, Weld Section of Center Control Blade 6 Inches from Top.

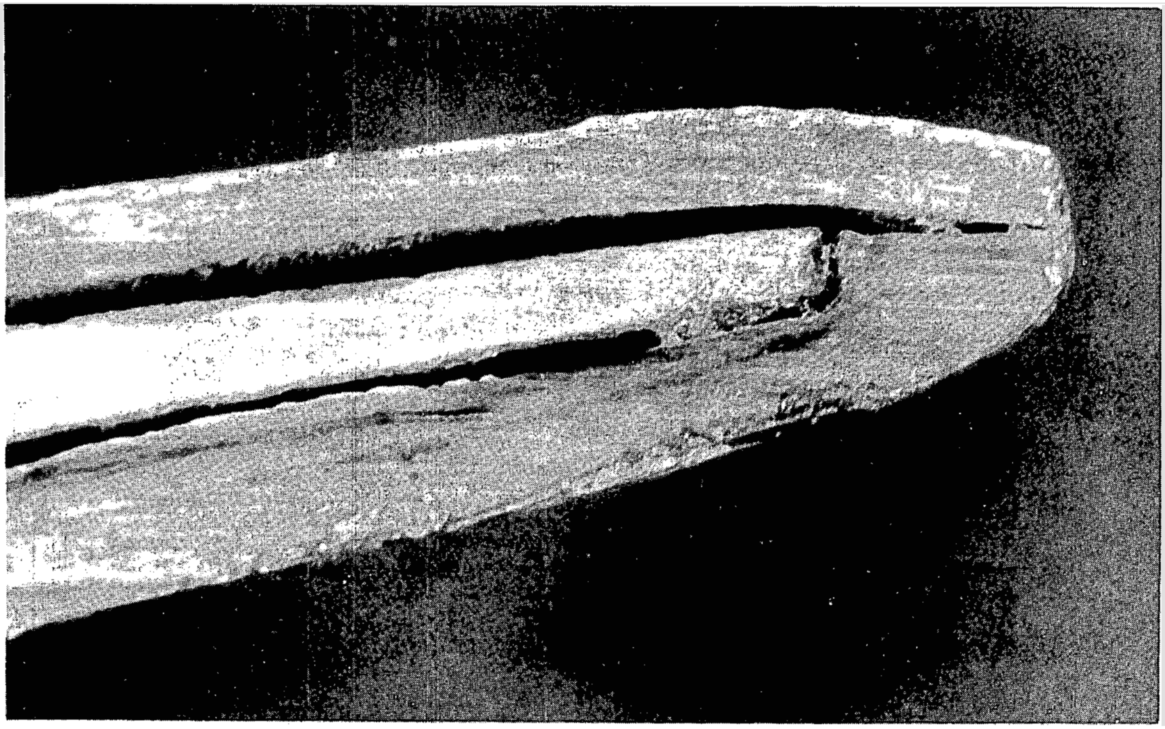

Figure I-66a, Weld Section of Center Control Blade 8 Inches from Top.

U-5001-396

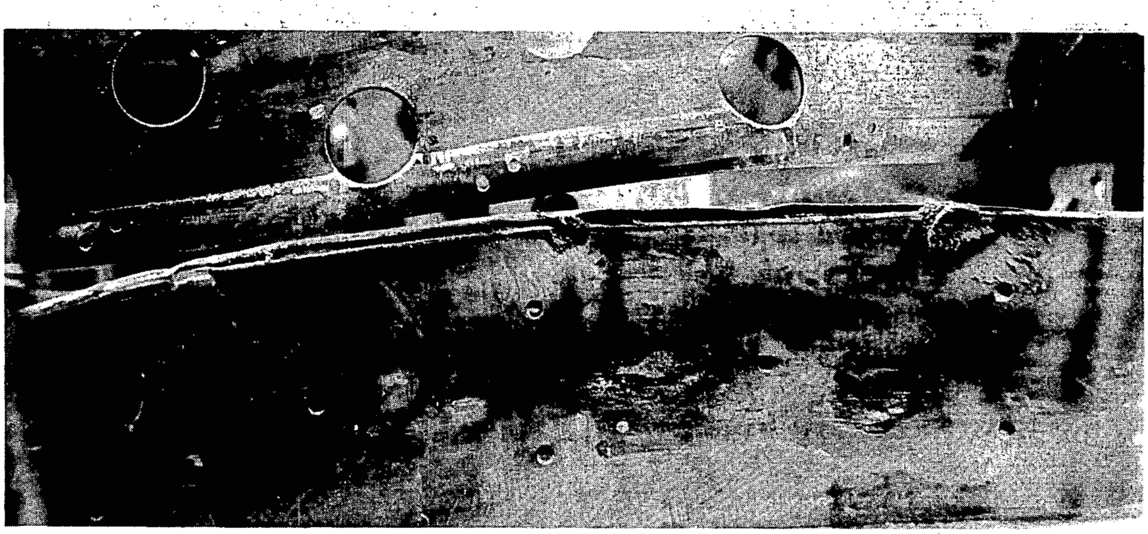

Figure I-66b, #3 Control Blade Showing Broken Weld Edge.

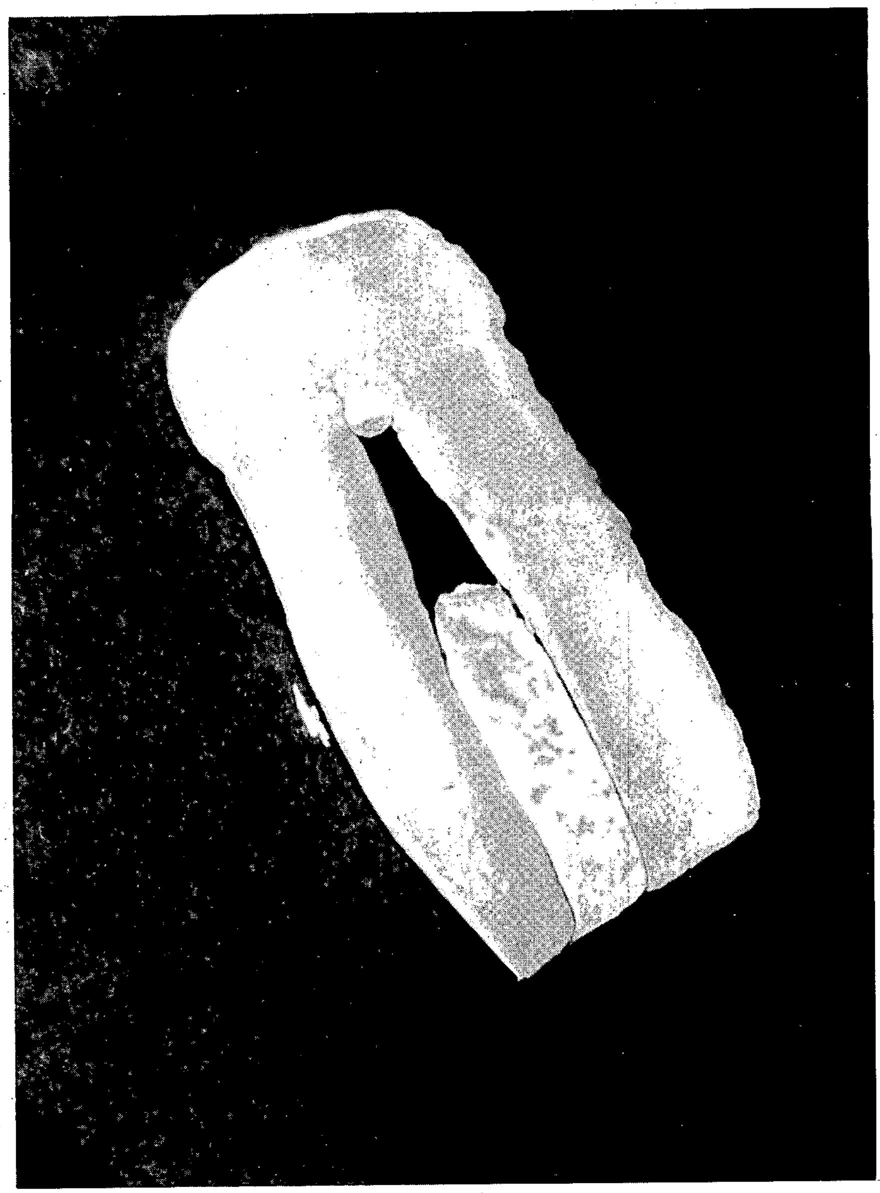

Figure I-67, Weld Edge 1 Inch from Top of #9 Control Blade.

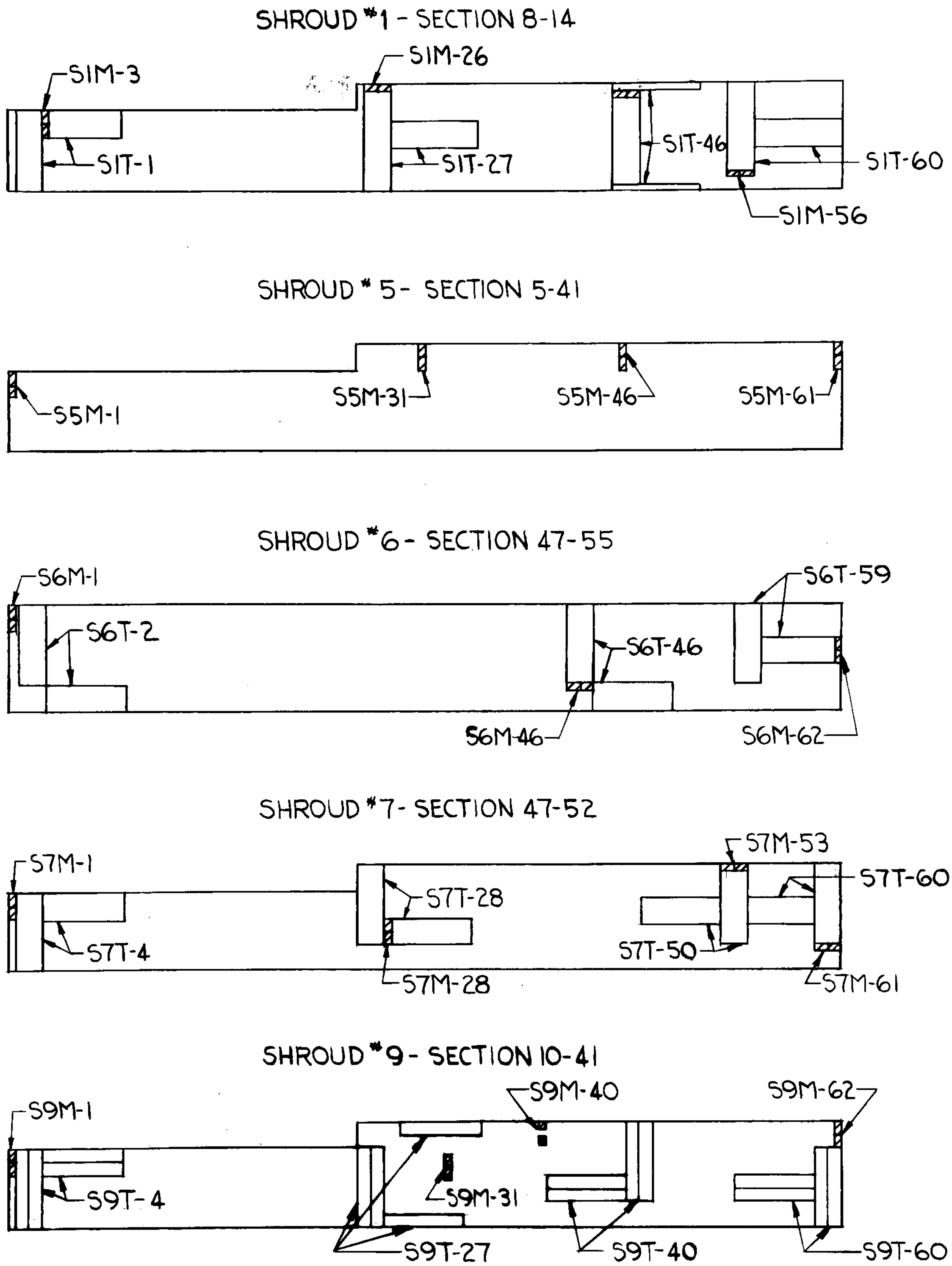

FIG. I68
SL-I SHROUD MATERIAL
SPECIMEN LOCATION

U-5174-20

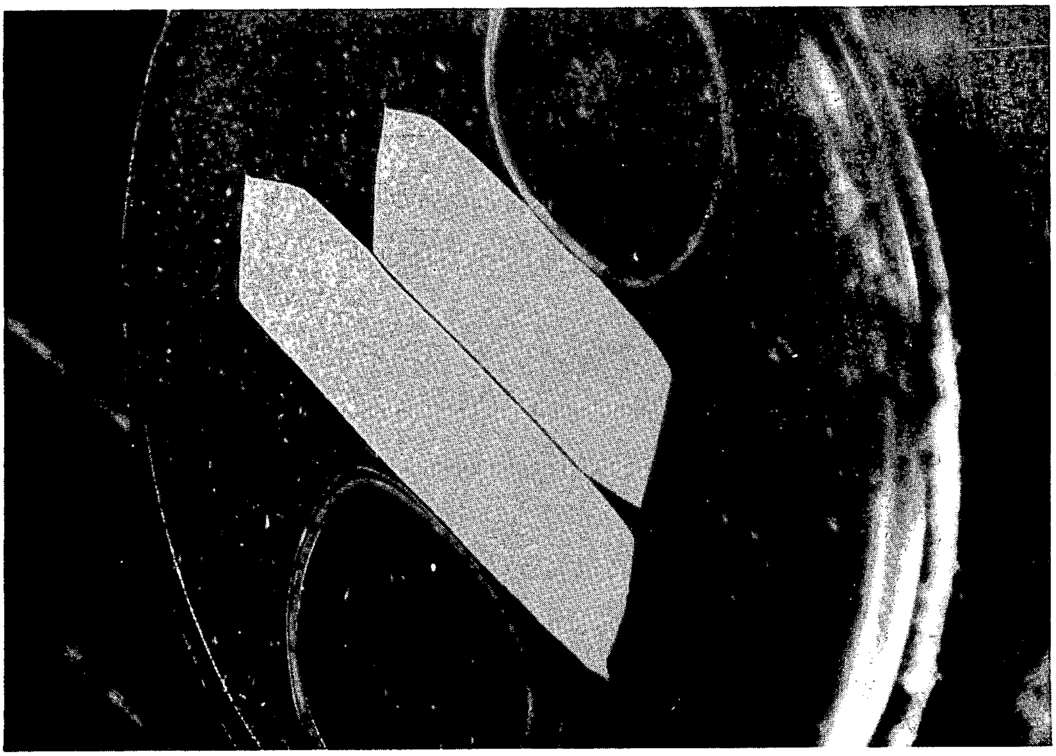

Figure I-69, Longitudinal and Transverse Sections from Section 4 of #9 Shroud, 31 Inches from Top.

U-5174-38

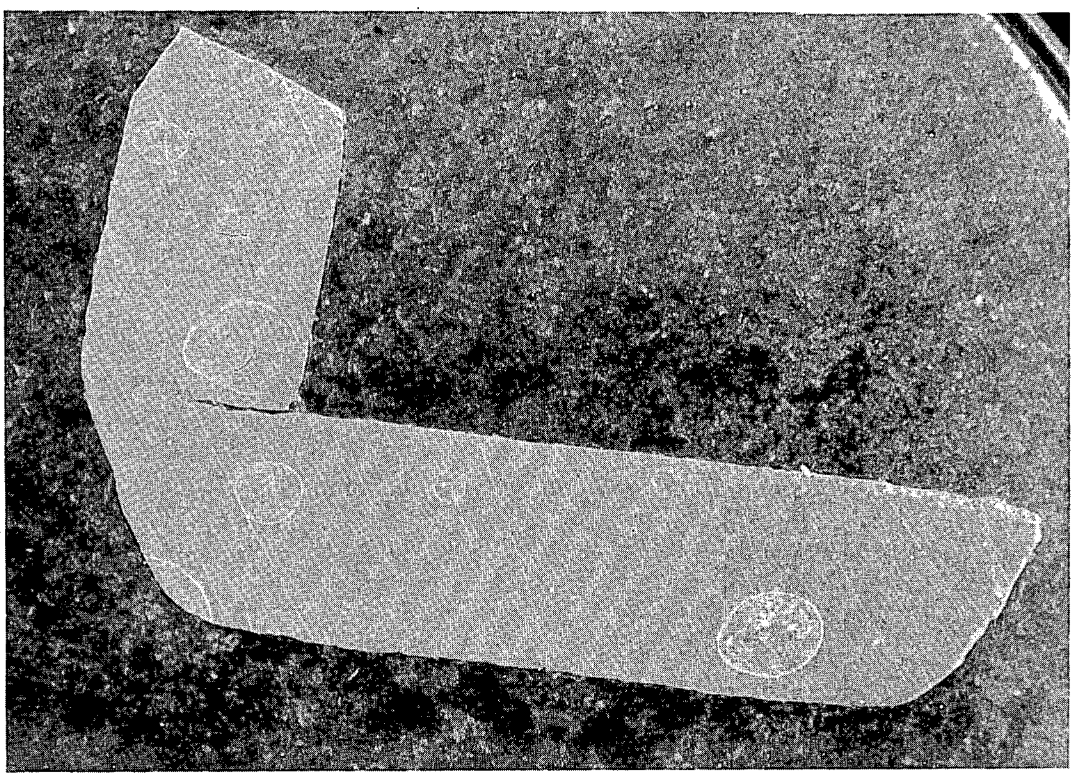

Figure I-70, Weld Section from Section 1-8 of #1 Shroud, 3 Inches from Top.

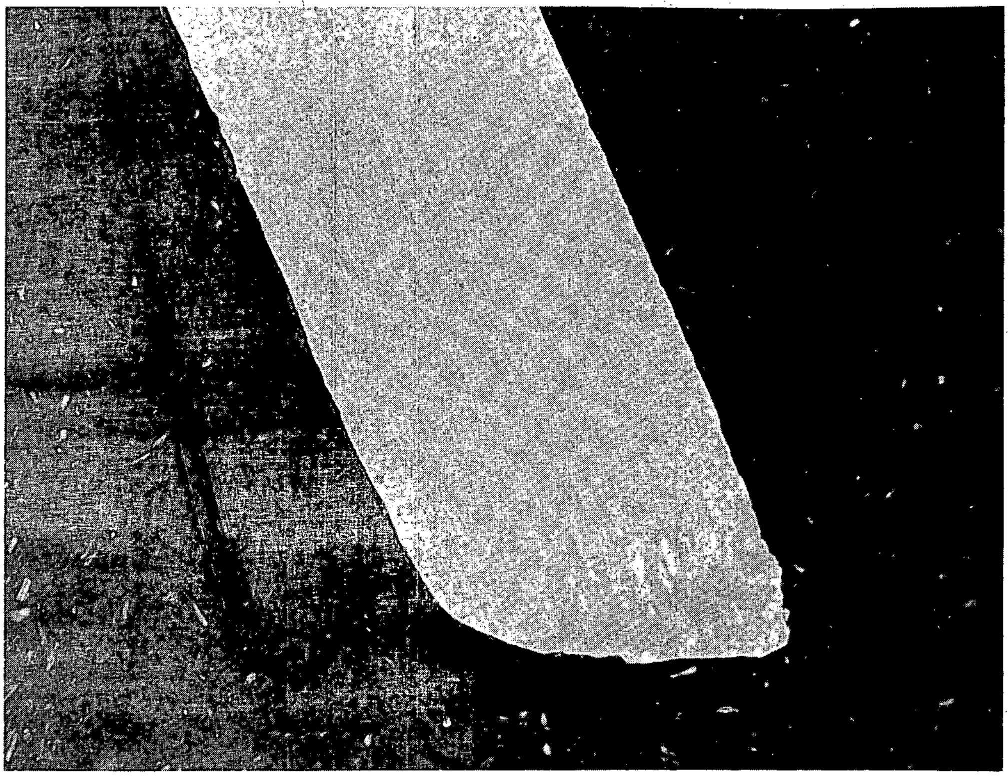

Figure 1-71a, Macrophotograph of the Failed Weld of Shroud #1, 3 Inches from Top.

U-5093-446A

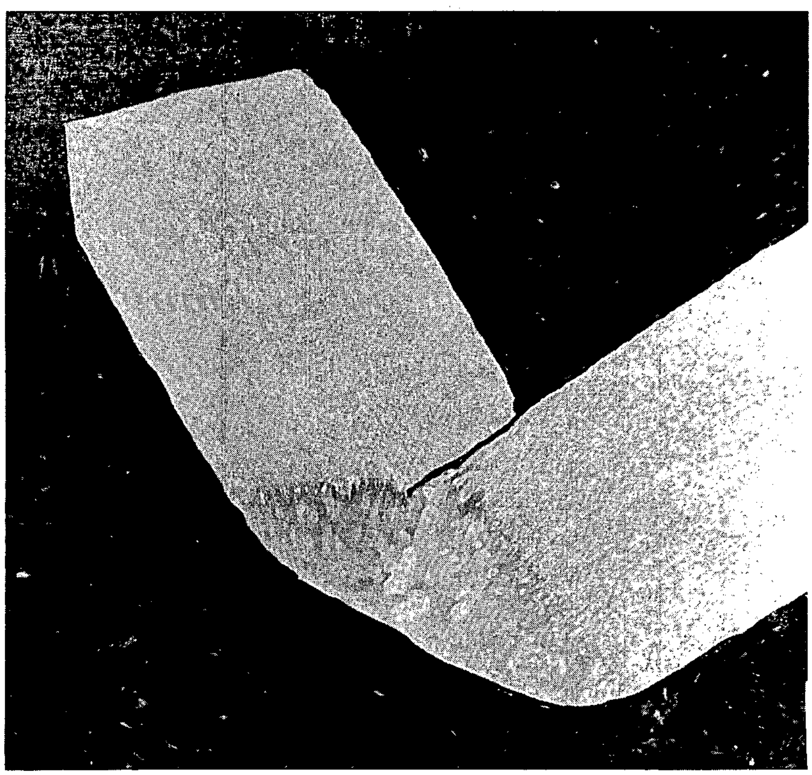

Figure I-71b, Macrophotograph of the Weld of Shroud #1, 3 Inches from Top, in Region of No Failure. Note lack of weld penetration.

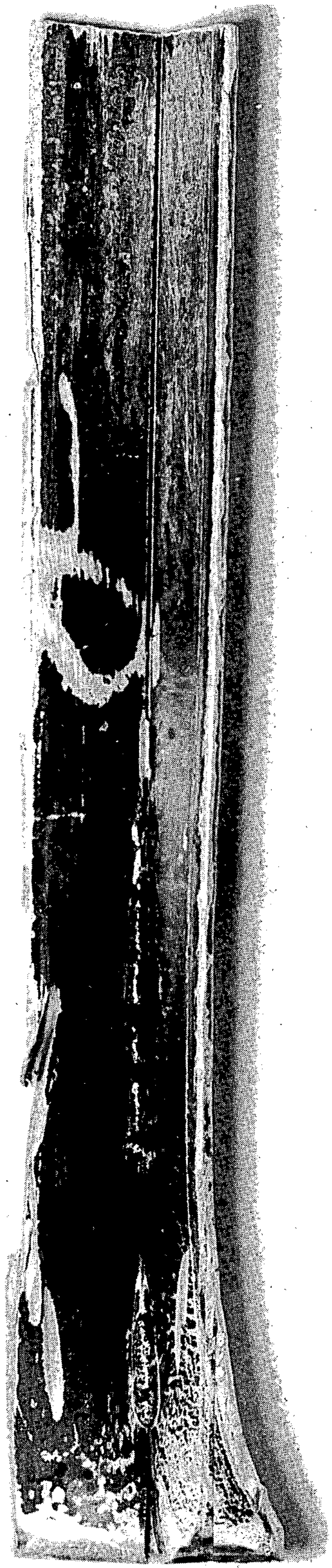

Figure I-72, Inside of Weld Seam Showing Variation in Weld Penetration.

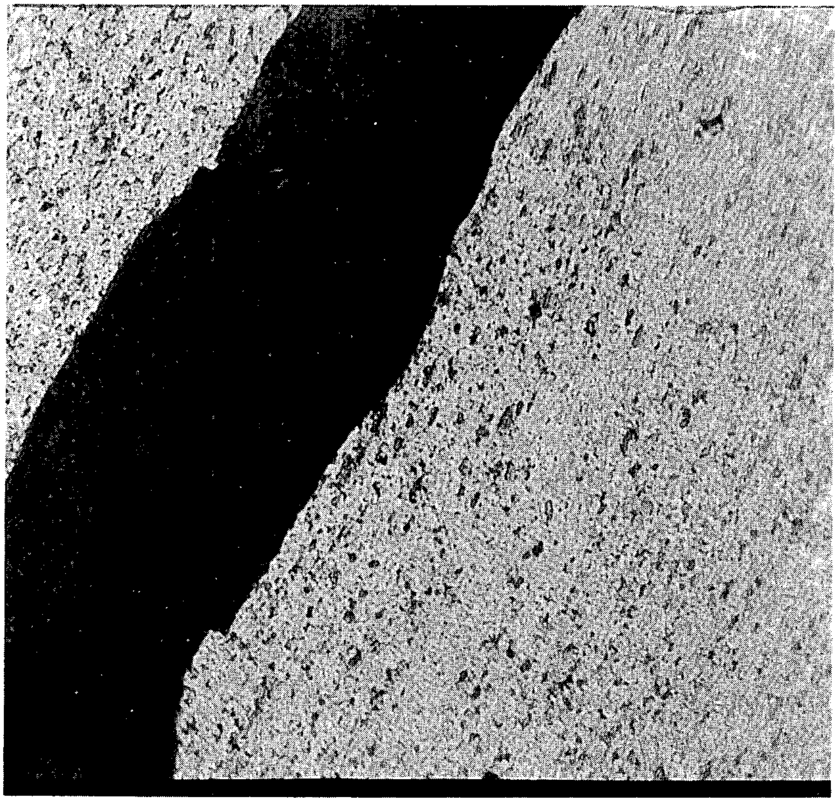

Figure I-73a, Section 4 of #9 Shroud, 31 Inches from the Top. Corrosion on Edge of Longitudinal and Transverse Sections. 500x. 0.5% HF etch.

U-5175-446D

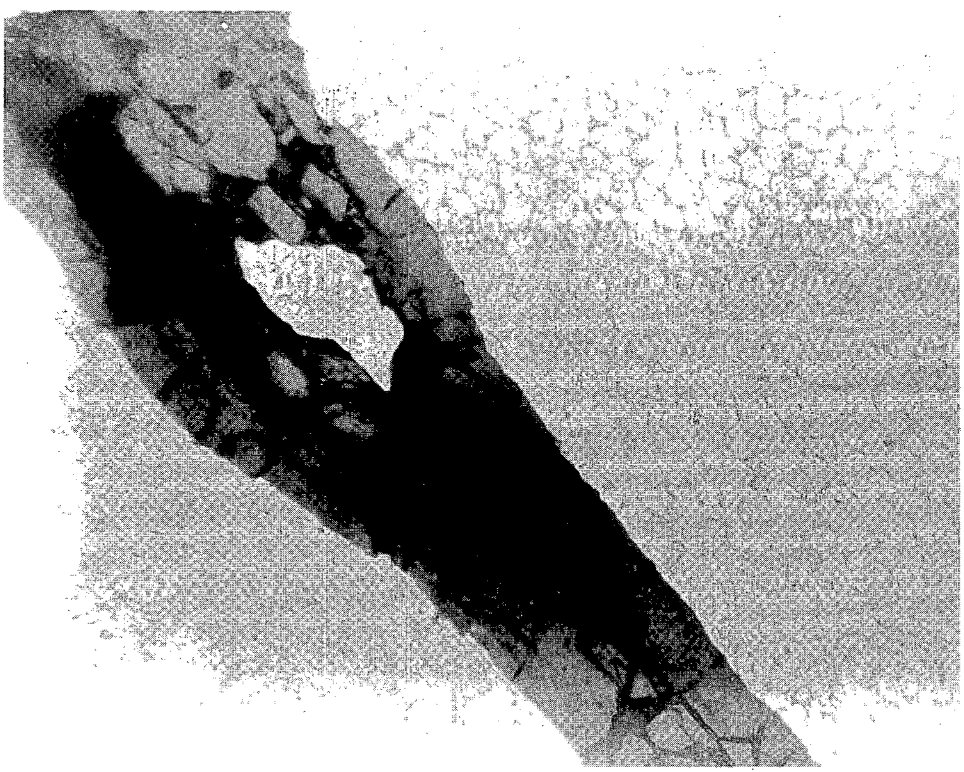

Figure I-73b, Section 1-8 of #1 Shroud, 3 Inches from Top Weld Joint, Showing Corrosion and Lack of Fusion. 500x. 0.5% HF etch.

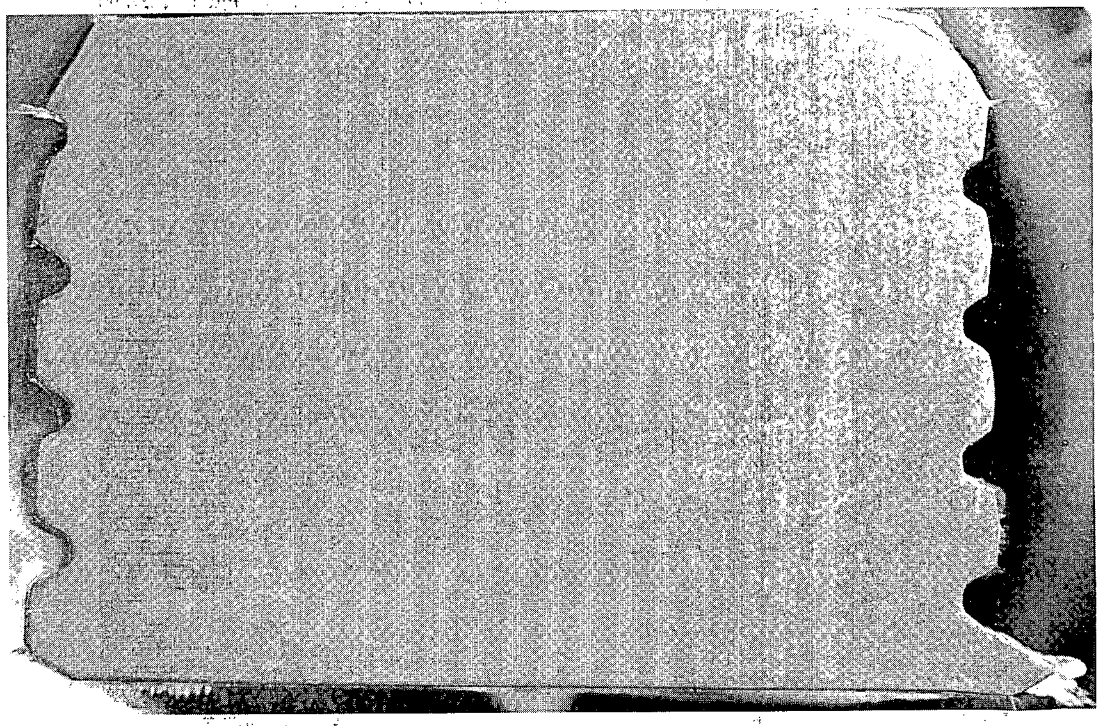

Figure I-74, Macrophotograph Showing Sheared Threads on Shield Plug Flange Stud.

U-4290-3

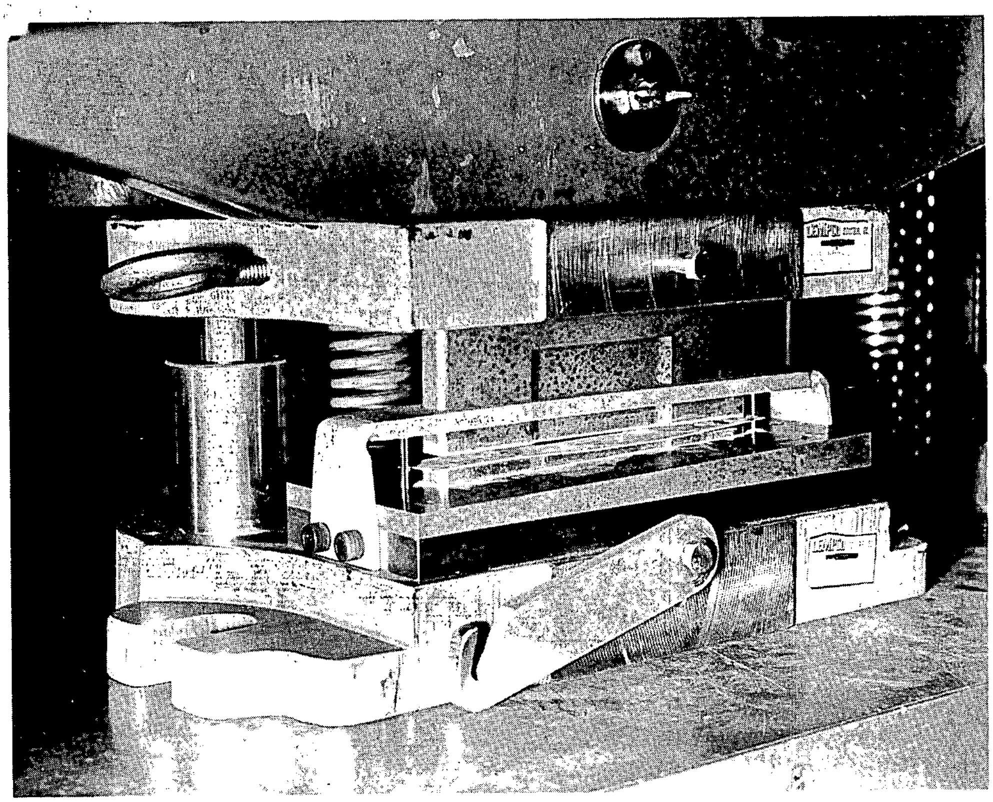

Figure I-75, 6 x 3/4 Inch Blank Ready for Shearing in Tensile Specimen Punch. Note pins holding blank in position.

U-4290-7

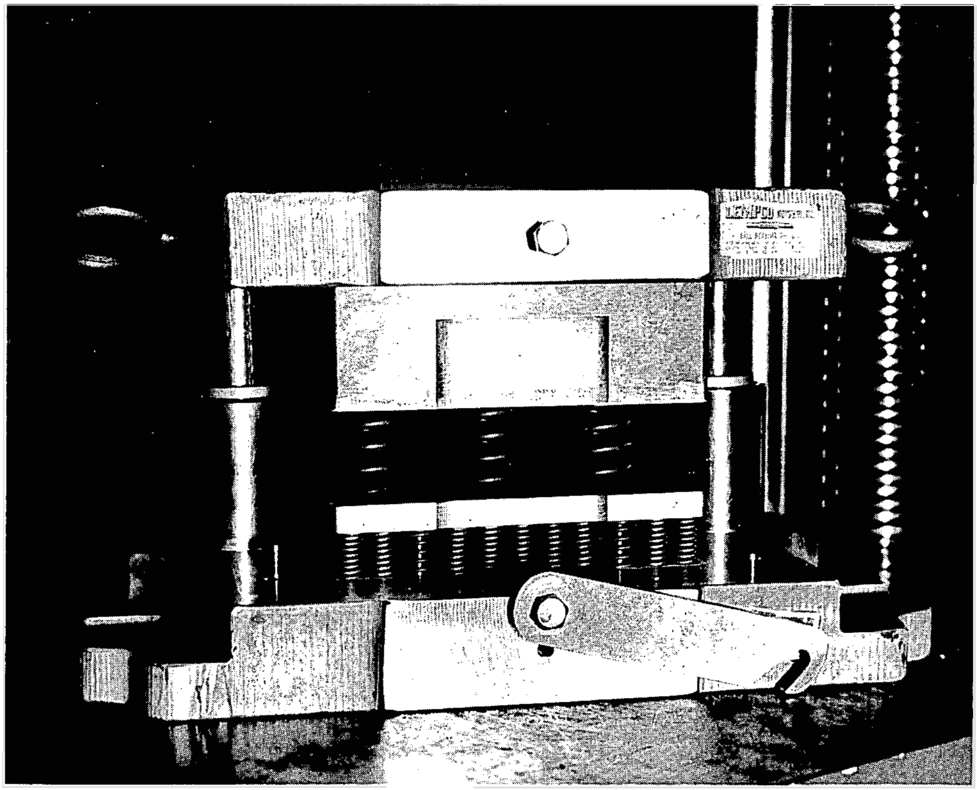

Figure I-76, Die Removed from Tensile Specimen Punch to Show Die Stripper and Die Stripper Springs.

U-4290-6

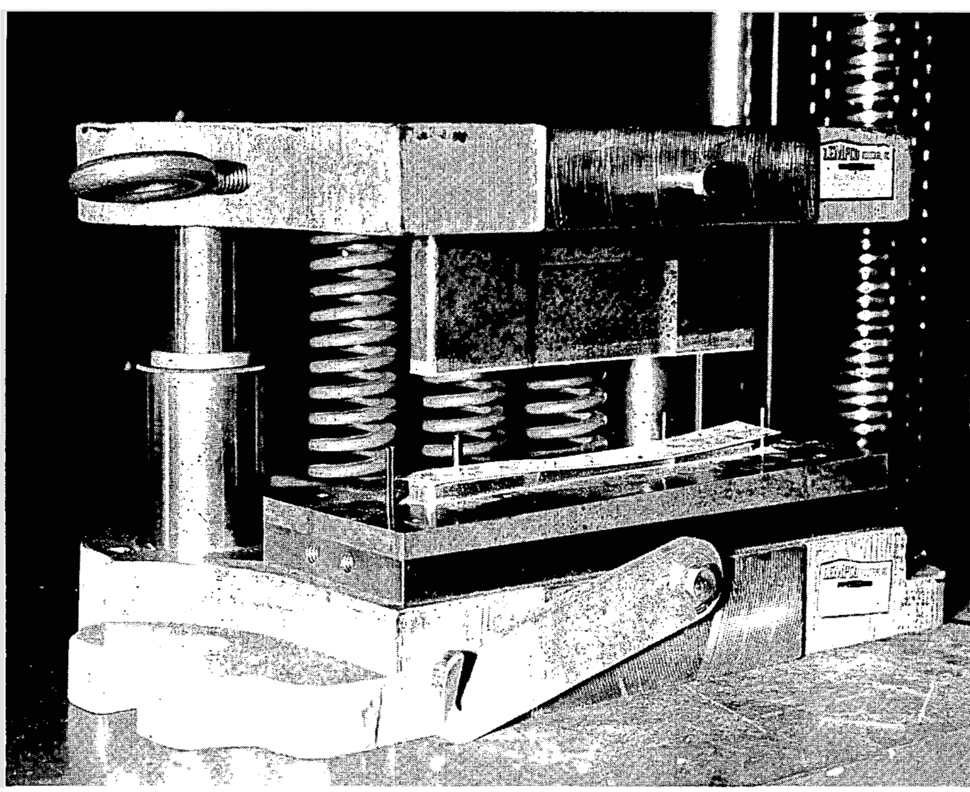

Figure I-77, Punch Stripper Removed to Show Specimen Locating Pins and 3 Die Opening Springs.

U-4290-1

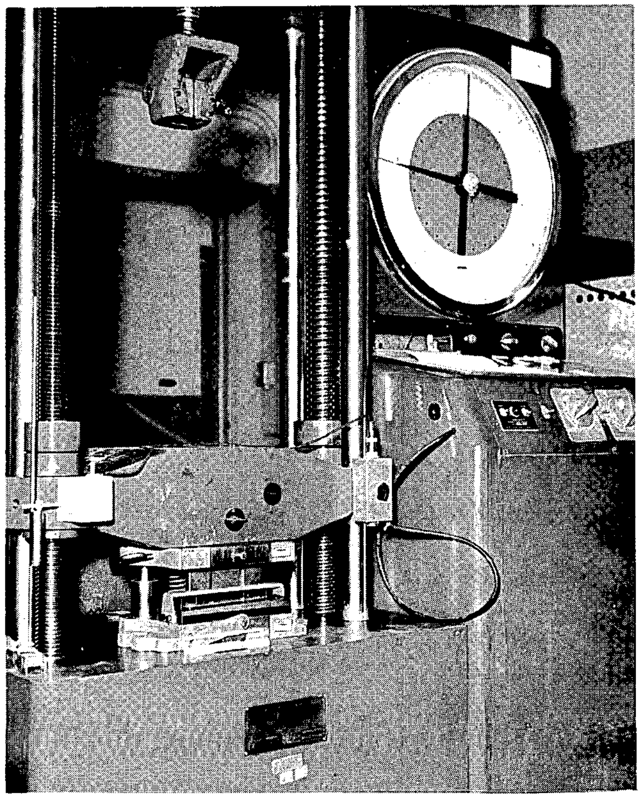

Figure I-78, Tensile Specimen Shear in Position in Tensile Testing Machine.

U-4290-5

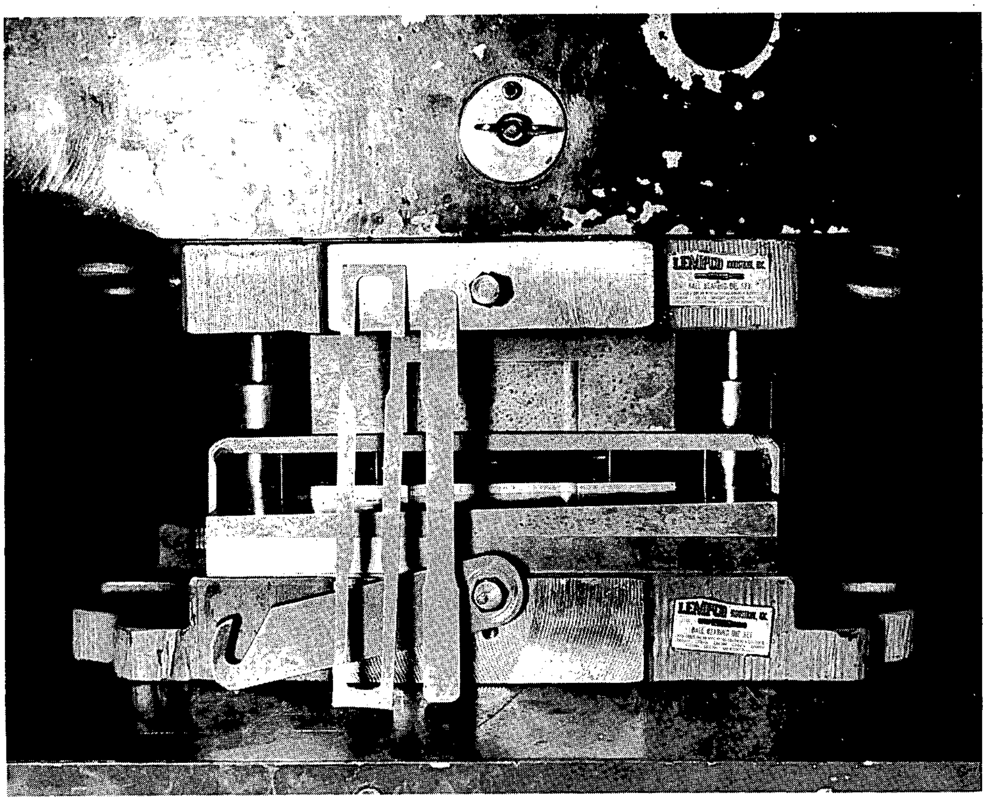

Figure I-79, Specimen and Trim with Shear in Open Position. Note shear angle of 1.3° on die.

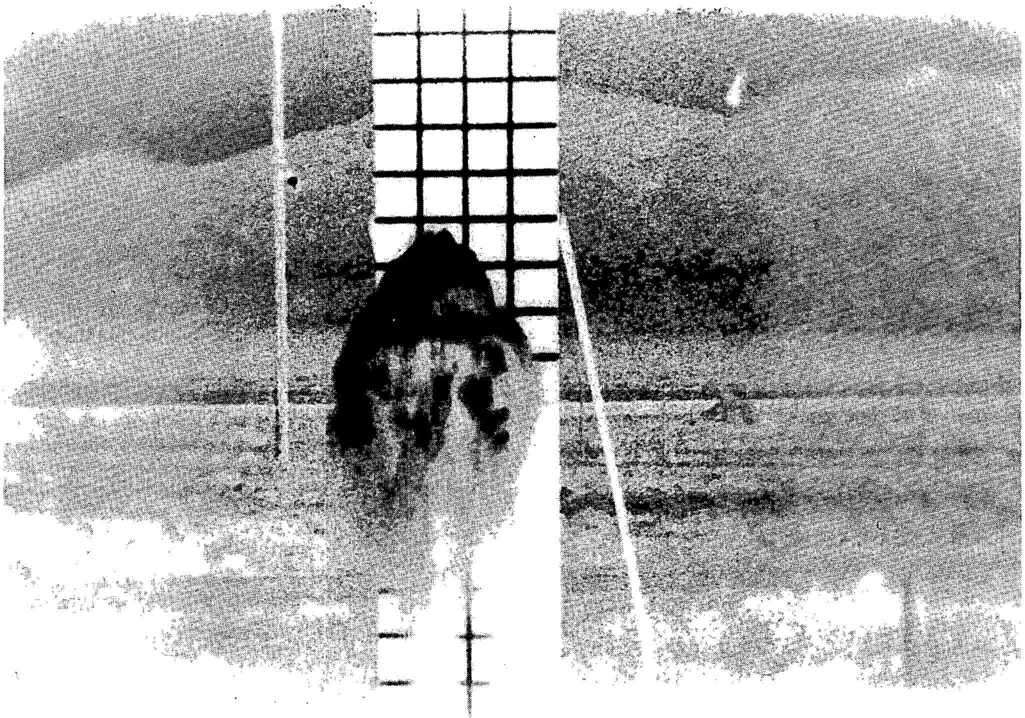

Figure I-80, Water Ejection from Vessel During Open Head Test.

U-5185-2

Figure I-81, Hole in Vessel Wall Just Above Thermal Shield Created by Shock Wave from Explosive Charge.

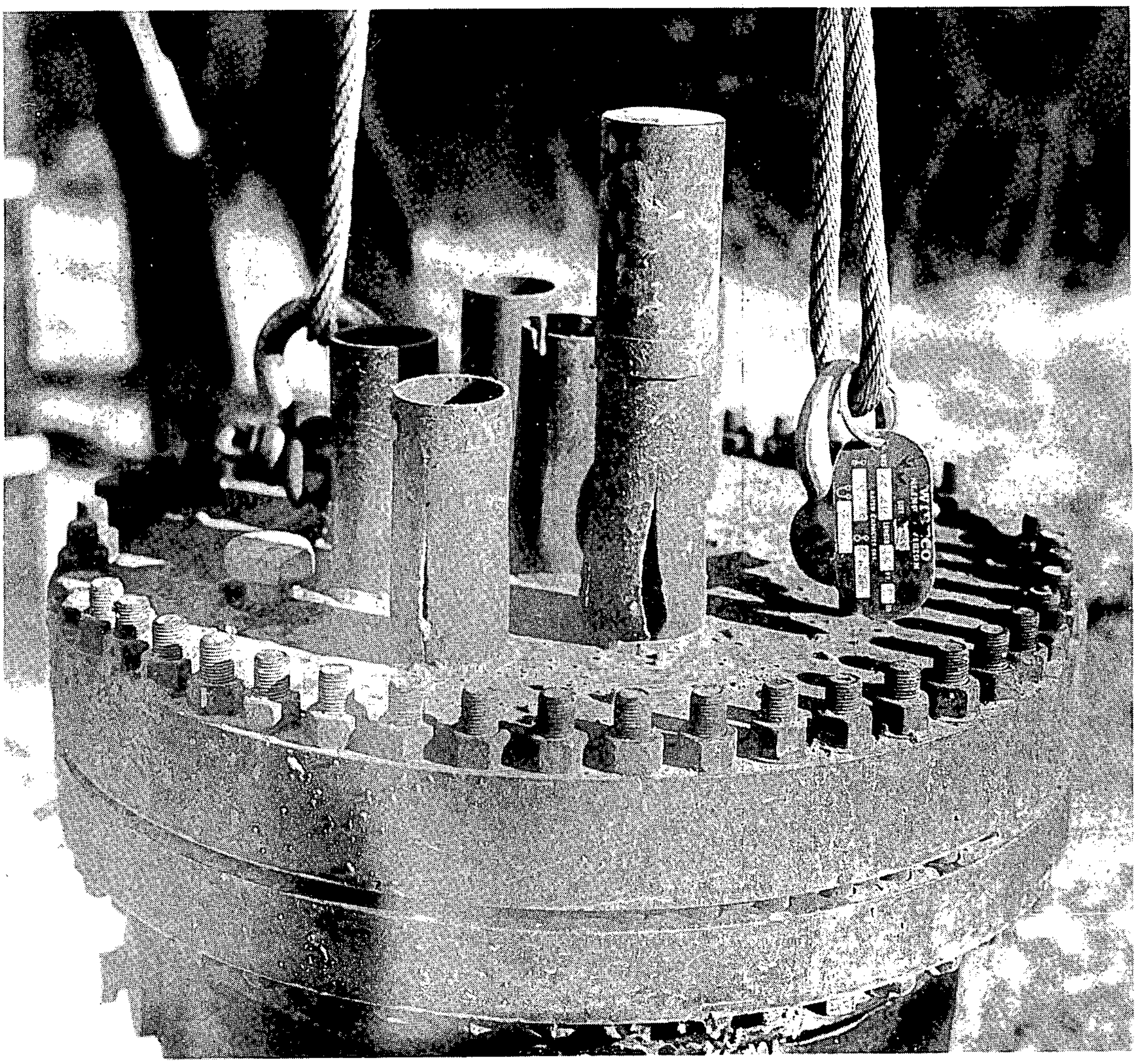

Figure I-82, Bulged and Broken Nozzles, the Results of Water Hammer Against Vessel Head.

II. SUPPLEMENTAL ANALYSIS OF POST-INCIDENT DATA

1. The Nuclear Excursion

The excess reactivity inserted by the original motion of the central control rod and the total nuclear energy release of the excursion were reported in IDO-19311 to be 2.4 ± 0.3% ΔK and 130 ± 10 Mw-sec. Subsequent evaluation and analysis has created no reason to significantly alter these values.

1.1 Energy

The supplementary flux wire data reported in Appendix E indicates that the energy release was 80 Mw-sec in the center 16 elements (78 Mw-sec reported in IDO 19311), and 53 Mw-sec (50 Mw-sec previously) in the outer 24 elements, for a total nuclear energy release of 133 Mw-sec. The estimated standard deviation of this value is approximately ± 10 Mw-sec, assuming spectral changes during the excursion were not such that a significant fraction of the fissions occurred in the resonance region.

1.2 Regions of Melt

The photomicrograph studies of heat-affected fuel plates revealed very definite zones. Figures I-28 and I-30 show cross sections of two fuel plates in which a zone of limited melt is just visible at the very center of the meat. This zone probably just reached the melting temperature of 640°C but did not receive enough additional heat to completely melt the metal. Figures I-32 and I-35b show, under different magnification, the same plate in which there is not only a zone of limited melt but, at the center of the meat, a zone of "complete" melt as well. The temperature of this central zone probably exceeded 640°C after complete melting occurred.

The identification of the heat input in the center of the fuel plates in various regions of the reactor, coupled with the flux wire information from the same regions, permits an independent estimate of the effective period of the reactor, i. e., the period, just prior to the beginning of the major shutdown mechanism. The flux wire information enables one to predict the maximum temperature that the center section of the plate will reach for an excursion of a given period and burst shape. The burst shape and temperature distributions given in IDO-19311, Section IV-1.4 are believed to describe the SL-1 burst relatively well for an effective period in the neighborhood of 4 m sec. Table II-1 compares the temperatures calculated from the flux wire data for several different periods with the temperatures it is believed the plates in question reached at their centers. In this table an "equivalent temperature" is used for convenience in the calculations, defined as the temperature which would have been reached if the fuel had not melted.

TABLE II-1

Maximum Temperatures (end of excursion) in Center of Fuel Meat

A) "Limited" Melt Region - Effective Temperature at end of excursion = 640°C

Thermal flux in moderator	$(2.0 \pm 0.3) \times 10^{14}$ n/cm^2
4 m sec period	(775 ± 120)°C
5 m sec period	(730 ± 110)°C
3 m sec period	(860 ± 130)°C

B) "Complete" Melt Region - Equivalent effective temperature at end of excursion = 640 ± 310 (heat of fusion) = 950°C

Thermal flux in moderator	$(2.5 \pm 0.5) \times 10^{14}$ n/cm^2
4 m sec period	(945 ± 190)°C
5 m sec period	(890 ± 180)°C
3 m sec period	(1050 ± 210)°C

Table II-1 indicates that an effective period between 5 m sec and 4 m sec gives the best correlation with the zones of melt. However, a flatter and/or more symmetrical burst shape than that assumed would result in lower maximum temperatures at the center of the plate. It should be noted that the errors due to experimental uncertainties are large, causing the ranges of predicted temperatures to overlap for the three different periods. The 4 m sec period certainly gives acceptable agreement within the standard deviations, but the 3 m sec period is considerably less credible. The initial reactivities of effective 3, 4, and 5 m sec period, allowing for about -0.13% $\Delta K/K$ for plate and moderator expansion effects, are 2.9, 2.4, and 2.05% ΔK, respectively. Thus, the correlation of the zones of melt with the flux wire information essentially agrees with the estimated $(2.4 \pm 0.3)\%$ ΔK initial reactivity estimate based on the central control rod position and the limited applicable critical-experiment data.

1.3 Theoretical Excursion Model

The mathematical model for predicting nuclear energy release from an excursion (see Section III-6 and 7) correlates satisfactorily to the 130 Mw-sec energy with the 2.4% ΔK initial reactivity of the SL-1. This model is probably not capable of accuracy better than ±30%, and therefore cannot effectively correlate the energy and reactivity to even as close an accuracy as the errors affixed to these values by other considerations cited above.

Therefore, within the ±10 to 15% uncertainty placed on these values, the initial reactivity was about 2.4% ΔK creating a 3.6 m sec period. The effective period at the time steam formation commenced was 4 m sec, the total nuclear energy release was 133 Mw-sec, and peak power was 16,000 to 19,000 Mw, depending on the burst shape.

2. Fission Product Release

The release of fission products to the reactor operating room and to the outside of the building was affected by the containment provided by the pressure vessel and building at the time of the accident. The release of fission products from the fuel was dominated by the disintegration or complete melting of a portion of the reactor (about 20%) and the release of virtually all the fission products from these regions. Most of the water above the core was expelled during the incident, but it is not known how well the released fission products mixed with this water, or how many drifted out afterwards through the five open ports of the vessel. The building shell was not airtight, but nevertheless provided quite adequate containment, probably because the incident produced essentially no positive pressure differential to drive the products out of the building. Less than 1/2% of the iodine -131 and a negligible fraction of the non-volatile fission product inventory was found on the desert.

2.1 Radiation Levels

Estimates (IDO-19311, Section III-4.3) based on measured radiation levels on the operating floor and of the debris removed from the building indicated that 3 to 5% of the fission product inventory (based on the Way-Wigner formula) escaped from the pressure vessel. This is more likely to be an underestimate rather than an overestimate.

2.2 Fuel Inventory

85% of the core was accounted for by weighing identifiable pieces of fuel, and much of the remainder was found in the debris on the bottom of the vessel. Following the statistical sampling of the debris at ITS (IDO-19311, Table III-5), this material was sent to the Idaho Chemical Processing Plant, where 1177 grams of uranium were recovered. Allowing for the samples withdrawn previously for analysis, about 1200 grams of uranium was in the debris. This amount, if it originated from a 16% burnup region, contained 1100 grams of U-235. Table II-2 gives the apparent disposition of the core as a result of the incident.

If the unrecovered portion of the core material had twice the average burnup of the core, then it should have contained 11% of the fission product inventory. Some of this "missing" 11% may have been lost into the Hot Shop during the removal of the material from the core and some of it may have been deposited on the walls of the vessel, core, and core structure, and therefore not have escaped into the building. These effects probably would have accounted for at least 10 to 20% of the missing fission products. Therefore, the results of the fuel inventory indicate that perhaps as much as 10% of the fission product inventory escaped from the reactor vessel.

TABLE II-2

Fission Product Inventory Deduced from Uranium Analysis

15% of core plate material* was not recovered in identifiable plate form. This missing portion of the core, having been in the high flux region, should have contained approximately 30% of the total fission product inventory, and 1790 grams of U-235.

1104 grams of U-235 were recovered from the debris.

Thus:

5.7% of the fuel inventory is unaccounted for, containing 11% of the total fission product inventory.

*Note that 20% of the plate area was destroyed by melting or vaporization but about one fourth of this re-solidified onto the intact portions of plates.

2.3 Fission Product Analysis

The debris in the bottom of the vessel was analyzed for representative long-lived fission products by three methods:

a. The soluble portion of the total debris sent to ICPP for analysis. This result will not include those fission products in the insoluble residue.

b. The soluble portion of representative samples taken at ITS. The absence of information from the insoluble residue plus statistical sampling errors will both effect this result.

c. Fusion samples from representative sampling of the debris at ITS. The fusion process leaves no residue, but will boil away any highly volatile fission products. Its main disadvantage is the statistical sampling errors.

Table II-3 summarizes the above three results, basing the conclusions on the assumption that 30% of the core fission product inventory is unaccounted for from identifiable fuel plate material.

TABLE II-3

Fission Product Inventory in Debris

		Nature of Data	% of Total Fission Products
1.	ICPP Data*	Soluble + Material Only. Cs-137, Ce-144, Sr-90, Ru-106	12 ± 2
2.	ITS Solution	Soluble + Material Only. Cs-137. Random sampling.	23 ± 8
3.	ITS Fusion	Random sampling. Cs-137.	14 ± 6

* See Table I-VIII
\+ Soluble in HCL and HNO_3

Items (1) and (2) in the table represent lower limits of the fission product inventory in the debris because the results do not include any of the fission products in the insoluble residue, which was radioactively very hot. The large errors in the ITS data are statistical sampling errors derived from the spread in the data obtained on uranium inventory (IDO-19311, Table III-5) by a similar sampling procedure. It is estimated from the data in Table II-3, that about (18 ± 3)% of the fission product inventory was in the debris. Approximately 70% of the fission product inventory was accounted for in identifiable fuel plate material. Therefore, (12 ± 3)% of the total inventory remains unaccounted for. Some of this was lost during operations in the Hot Shop, and some was scattered upon surfaces throughout the pressure vessel and core. Thus, the unaccounted fission product inventory represents an upper limit to the amount which escaped from the vessel.

In summary, the radiation levels on the operating floor can account for approximately 5% of the fission products being outside of the vessel (essentially a lower limit) while the unaccounted for fission products and fuel indicated that as much as 10% of the fission products may have escaped from the vessel.

3. Heat and Mechanical Effects

3.1 Energy to Form Steam

The energy that was deposited in the water in a time short compared to the acceleration time of the water slug was estimated in IDO-19311 (Section IV-3.2) to be:

50 Mw-sec from the nuclear energy release
24 Mw-sec from the aluminum-water reaction.

The metal-water reaction energy release was based on certain preliminary data which has since been confirmed. First, the statistics on the quantities of various particle sizes were improved (Table I-IX). Second, the fraction of the α-Al_2O_3 that would not be found in the debris was estimated to be 40%. Approximately 1.5 Kg of the metal-water reaction product was found in the debris; and the unaccounted for uranium, which would mostly be in a fine particulate form, is 38% of the total uranium not found in or on fuel plates (Section II-2). Since it is reasonable to expect that the fraction of particulate uranium that escaped from the vessel would be similar to the fraction of α-Al_2O_3 that escaped, the total amount of α-Al_2O_3 that was formed is about 2.5 Kg, representing 24 Mw-sec of chemical energy (±30%).

The energy released from a 1/2-pound charge of Pentolite is 1.16 Mw-sec, which produced water hammer damage during the Aberdeen scale model tests equivalent to that in the SL-1 incident. When scaled upwards by a factor of 64, the appropriate volume scaling factor for the 1/4 scale model, this also gives 74 Mw-sec for the energy used to accelerate the water in the SL-1. The very close agreement between the scale model tests and the estimates produced from the incident evidence is somewhat fortuitous, considering the net uncertainties in these estimates. However, the close agreement does add credence to the understanding of the excursion and the usefulness of the scale model tests. From a consideration of the period and temperature distribution in the SL-1, one can calculate the expected total nuclear energy release (see Section III). From this, the expected disintegration and melting can be deduced (P. IV-12 of IDO-19311). The additional chemical energy from the resulting metal-water reaction can be estimated. Thus, the total energy quickly deposited in the water is known. Scale model tests using explosives of this equivalent energy can then be used to produce water hammer effects similar to those that the incident would create. A major limitation of this technique is that it does not produce the equivalent damage to those components which are subject to severe shock waves from the explosive, shock waves which the incident itself would not produce. See, for instance, Figure I-81.

3.2 Water and Plug Velocities

The velocity of the expelled water from the open-head scale model tests was 225 ± 25 ft/sec, significantly larger than the estimated 160 ft/sec impact velocity to produce a 10,000 psi peak water hammer. The water slug measured in the open-head test, however, had no air cushioning effect as did the water impinging against the closed head of the SL-1. This cushioning effect will reduce the ultimate velocity by about 10%. Furthermore, the acceleration geometry in the open head tests was somewhat different from that in the actual vessel. The column of water was presumably accelerated for a longer time over a greater distance in the open-head tests, until the effective piston of water was free from the walls of the vessel and the pressure below it was relieved. However, the upper portion of the piston, once it left the confines of the pressure vessel, spread outward and reduced the effectiveness of the acceleration from below. The extra acceleration was, therefore, substantially reduced from what would be expected from a solid slug. It is difficult to assess whether the 225 ft/sec measured under open-head conditions is equivalent to 160 ft/sec impact velocity with the head closed. The difference is considerable, and one would be inclined to conclude that the actual impact velocity was slightly greater than the estimated 160 ft/sec, and that the peak water hammer pressures were proportionately greater than the estimated 10,000 psi.

The velocity of the ejected plugs, during the somewhat aborted closed-head test, was measured to be 70 ± 10 ft/sec, whereas 85 ft/sec had been estimated. The bursting of the vessel during this test undoubtedly substantially reduced the water hammer effect, and the water expulsion velocity through the nozzles. The plug velocities were, therefore, considerably lower than they would have been had the vessel wall not burst. It is concluded that the estimated 85 ft/sec might also be slightly low, in view of the nebulous results from the closed head test.

The damage incurred at the head indicates, on one hand, that the water hammer effect was insufficient (guide tubes unaffected), and on the other hand, that it was sufficient (bulged and split nozzles) to reproduce the effects of the SL-1. Therefore, it seems that the scale model tests essentially confirm that the water and plug velocities of 160 and 85 ft/sec, respectively, and that the peak water hammer pressures of 10,000 psi probably can be relied upon to within the ± 25% estimated uncertainty associated with the calculations of these transient phenomena.

4. Radiation and Burnup Effects

4.1 Boron Strips

The boron-aluminum strips (originally 0.42% boron, 93% enriched) that were recovered were examined metallurgically for the type of radiation damage and corrosion that occurred and chemically for the boron -10 burnup and the total boron content. The results of the chemical analyses given in Table I-XI show relatively poor correlation between the total boron loss from the samples and the % B-10 burnup. The method by which the samples were prepared prior to the chemical analysis (the corrosion was removed by buffing), however, probably affected the composition of the original sample so as to alter the expected ratio of boron to aluminum. The forces imparted to the surfaces of these strips during the incident also could be expected to have disturbed the surface corrosion layer.

The corrosion effects to the boron strips were of two types:

a. Normal corrosion of the surface, independent of the radiation exposure.

b. Corrosion resulting from or induced by radiation damage, and generally proceeding from the surface inward. This type of corrosion is characterized by a cracking and swelling of the matrix. It is surmised that the corrosion that attacks the regions affected by the helium gas formation (product of n,α reaction on boron) readily opens up fissures in the matrix, thus allowing the corrosion to penetrate deeper into the surface.

The degree of corrosion-radiation damage to the boron-aluminum strips vs. the boron burnup and the thermal flux have been considered. At the temperature at which the SL-1 normally operated, the effective cross section of B-10 is 2620 barns. A 50% burnup will occur after an exposure of 2.6×10^{20} nvt thermal neutrons (at 220°C). The isotopic ratios in samples taken from the edge of deteriorated strips (i.e. maximum deterioration prior to disintegration) show burnup of (67 ± 12)%. However, the thermal flux data (C. W. Luke, unpublished data) indicates that these regions received, throughout the operation of the SL-1, $(2.1 \pm 0.6) \times 10^{20}$ n/cm^2. These two results do differ, but not by more than the spread in the errors. It has therefore been concluded that the boron strips disintegrated after a burnup of about 50% and an exposure greater than 2.5×10^{20} n/cm^2 thermal flux at 220°C. The strips show essentially no deterioration for burnup of less than 30% (or less than 1×10^{20} nvt, thermal).

4.2 Pressure Vessel Radiation Levels

It has been previously discussed in the text that the upper section of the pressure vessel had radiation levels in the 300 to 700 mr/hr range at contact; whereas, the lower section was approximately 5 R/hr at 5 feet. Since decontamination processes had not proven successful for the lower portion of the vessel, it was expected that these radiation levels were more a function of activation products than fission products impregnated in the rough inner surface. Representative disintegration rates due to the activation products of Mn-54 (in the iron) and Co-60 (in the stainless steel) were computed for a typical area which a "Cutie Pie" radiation monitor might survey. The results were a level of 250 mr/hr at 1 foot for the upper 9-1/2 feet of vessel and 6 R/hr at 1 foot for the lower 4-1/2 feet, which adequately account for the observed levels without the inclusion of fission product contamination.

The pressure vessel activation shown in Figure I-4 presents a phenomenon in which the ratio of thermal to fast flux (measured by Mn-54 and Co-60) changes significantly as one moves away from the core. Horizontally opposite the core, the thermal flux is 5 times the fast flux, while near the top of the vessel the ratio is between 20 and 30. In moving away from the core toward the bottom of the vessel, the ratio of thermal to fast flux also increases to approximately 10. The bottom of the support cylinder has a boron shield which would attenuate any thermal neutron flux being reflected back into the vessel.

To account for the apparent reduction in the thermal to fast flux ratio near the active core, consideration is given to the 3/4-inch thick stainless steel thermal shield located just inside the pressure vessel wall at approximately the same longitudinal position as the core. This structural member is a slow neutron absorber, attenuating the thermal flux by nearly 40% while not significantly affecting the fast neutron environment. However, the structural material external to the pressure vessel, the carbon steel jacket, and the uncertainties in the composition of the thermal shield all induce uncertainties into the interpretation of the results.

III THE PREDICTION OF REACTOR EXCURSIONS

1. Introduction and General Remarks about SL-1 Excursion

The analysis of the physics of the SL-1 excursion was undertaken to: (1) indicate what design parameters were most pertinent to explaining the severity of the accident; (2) define the shutdown mechanism; (3) attempt to derive a model that would, with reasonable accuracy, define the reactor transients and other reactor systems. To obtain a better insight into the excursion, the analog computer approach was considered most feasible, particularly because of its flexibility in permitting program changes, thus allowing the investigator to observe the results and to gain a better understanding of the system characteristics.

The results of the SL-1 incident investigation[(1)] yielded information about the nuclear power transient which clearly showed that the events contributing to the termination of the transient were significantly different from those that have occurred in the non-destructive SPERT tests. The destruction in the center section of the SL-1 core was such that the high flux regions of the fuel elements were completely destroyed, comprising approximately 20% of the core. The nature of this destruction left the recoverable portions of these destroyed regions largely in a fine particulate state, confirming the fact that portions of these elements reached vaporization temperatures and violently destroyed themselves. The peak flux region reached vaporization temperature at about the time that 70% of the total 130 Mw-sec of nuclear energy had been developed. Though surface temperatures were well above the saturation temperature of water (at one atmosphere) at this time, the extent of steam formation from heat conducted to the water was insufficient to terminate the nuclear excursion, before the termination was brought about by the vaporization and explosion of fuel plates.

A list of the most significant features of the SL-1 excursion is given in Table III-I, while Table III-2 contains the significant features of the SL-1 core.

(1) IDO 19311; SL-1 Final Report, General Electric Co.

TABLE III-I SL-1 EXCURSION

Initial excess reactivity	$2.4 \pm 0.3\% \Delta k$
Initial period	3.6 ± 0.5 m sec
Effective period at time of major feedback initiation	3.9 ± 0.5 millisec.
Total nuclear energy released	133 ± 10 Mw-sec
Peak/average energy density ratio	2.9 ± 0.3
Fraction of core destroyed	20%
Threshold of destruction (thermal flux) of fuel plate	$3.7 \pm 0.4 \times 10^{14}$ n/cm^2

TABLE III-2 SL-1 CORE CHARACTERISTICS

Number of Elements	40
Initial loading of U^{235} per element	350 gms
Average burnup at time of incident	8%
Peak burnup at time of incident	20%
Number of plates per element	9
Fuel "meat" thickness (Al-U)	50 mils
Cladding thickness (Al-2% Ni)	35 mils
Water channel width	310 mils
Active area per plate	25.8 x 3.5 inches^2
Moderator void coefficient (average)	$1 \times 10^{-4}\% \Delta k/cm^3$
(maximum)	$5 \times 10^{-4}\% \Delta k/cm^3$
Moderator flux/fuel flux ratio	1.1
Total active plate area	3.6×10^5 cm^2

The boron poison strips still in the active section of the core at the time of the incident did not contribute directly to the initiation of the incident. Their major effect was to distort the normally expected flux distribution. The flux wire monitors contained in the core during the excursion have made it unnecessary to give consideration to the boron strips, for the flux wires yielded the energy distribution directly.

The significant difference between the SPERT-BORAX plate-type cores and the SL-1 core was in the fuel plate thickness (60 mils total vs. 120 mils for SL-1) and the fuel plate area (nominally twice that of the SL-1 per unit core volume). The thicker fuel plate cladding of the SL-1, though composed of aluminum, effectively insulated the water from the fuel for excursions of short duration, in the shorter than 10 millisecond period range. The smaller plate area of the SL-1 reduces the rate of void formation by conduction of heat to the water from the plates. These effects, coupled with the small void coefficient of the SL-1, delayed the shutdown of the reactor due to normal steam formation and thereby permitted the SL-1 to attain higher power and greater energy release for a given initial period.

2. Shutdown Mechanisms

The basic shutdown mechanism in a light water reactor is the removal of moderator from the active core lattice, thus increasing the migration length and the leakage from the core. The loss of water can be produced by:

1. The expansion of fuel plates and of the water itself due to heating of these components.

2. Production of steam in the water channels.

3. A violent explosion and destruction of hot fuel plates, giving rise to a rapid displacement of water from the core and the production of steam. Some fuel loss will also occur, simultaneously.

2.1 Plate and Moderator Expansion

Each of these three mechanisms is of greater order violence than the preceding one, and each one predominates as the shutdown mode in certain regions of the period spectrum. The plate and moderator expansion effect is adequate to limit excursions of periods in the 100 millisecond range. If steam forms after the peak of the power burst, it will merely shut off the excursion on a faster, negative period.

The amount of reactivity that can be compensated by expansion without boiling any of the moderator is determined by the amount of heat stored in the plates and the amount that can be transferred to the water before the plate surface temperature much exceeds the saturation temperature. The temperature distribution between plates and moderator is strongly influenced by the rate at which the power or heat production rate is increasing. The very fast reactor periods bring about considerable accumulation of energy in the meat before the cladding surface reaches saturation temperature, while the very slow periods permit the transfer of more than a negligible fraction of the total energy to the moderator. The flux profile also influences the total energy that can be accumulated before boiling is initiated in the peak flux region. The higher the peak to average flux ratio, the less total energy is developed before the peak flux regions begin to boil.

To determine the effectiveness of expansion of the plates and moderator before boiling occurs, the contributions to the compensated reactivity from the plates and the moderator at the time the average plate surface temperature reaches 40°C above ambient are shown in Table III-3 for various reactor periods of the SL-1. An average 40°C temperature rise represents a temperature rise in the peak flux regions of about 115°C, or approximately 35°C above the assumed saturation temperature. This amount of overshoot is approximately the average expected throughout the period region of interest before boiling commences, though of course, the faster periods will have a much larger overshoot. It has further been assumed, for purposes of comparison of the periods, that the reactor approaches the average 40°C (ΔT) plate surface temperature condition on the stated asymptotic period. This is less valid an approximation for the longer periods in which even a small reactivity compensation noticeably affects the period.

TABLE III-3 REACTIVITY COMPENSATION

Due to Expansion of SL-1 Fuel and Moderator when Average Plate Surface Temperature is 40°C above Ambient

Period, Milli-seconds	Inverse Period, Sec^{-1}	Inserted Reactivity $\%\Delta k/k$	Compensated $\%\Delta k/k$ in Metal Expansion	Compensated $\%\Delta k/k$ in Conduction to Water	Compensated $\%\Delta k/k$ in Water by Neutron Heating	Total of Listed Compensated Reactivities, $\%\Delta k/k$
2	500	3.6	0.080	0.002	0.016	0.098
4	250	2.2	0.042	0.002	0.008	0.052
5	200	1.89	0.038	0.002	0.008	0.048
10	100	1.29	0.028	0.003	0.006	0.037
20	50	1.01	0.024	0.005	0.005	0.034
40	25	0.85	0.021	0.007	0.004	0.032
50	20	0.82	0.021	0.008	0.004	0.033
70	15	0.79	0.020	0.009	0.004	0.033
80	12.5	0.77	0.020	0.009	0.004	0.033
100	10	0.75	0.020	0.011	0.004	0.035
150	6.7	0.73	0.020	0.013	0.004	0.037
200	5	0.72	0.020	0.014	0.004	0.038

The delayed neutron fraction of the SL-1 is 0.70%. Thus, for periods as fast as about 125 m sec, plate and moderator expansion is adequate to limit the prompt rise of the excursion, as can be deduced from Table III-3. Steam may ultimately form while the reactor is at or near its peak power, but steam itself does not contribute to the limiting of the excursion (termination of prompt rise) except for periods shorter than about 125 m sec. In the case of the SPERT 1-A reactor, the surface area and void coefficient were much larger than for SL-1 and permitted more compensation of reactivity by water expansion. Therefore, the SPERT 1-A excursions that could be controlled without steam formation were for periods longer than 50 to 100 m sec(2).

2.2 Steam Formation from Plates (smooth surfaces)

If plate and moderator expansion are not adequate to limit the excursion, steam will eventually form on the plate surfaces, resulting in considerably more rapid moderator displacement and quick control of the excursion, relative to the effects observed with plate and moderator expansion alone.

Steam can only form after the plate surface temperature has exceeded the saturation temperature. The empirical information available on the occurrence of steam void relative to the time that the plate surface attains saturation temperature is presented in Figures III-1 and III-2 (from references 3, 4, and 5). These figures present the temperature overshoot above saturation and the time delay, respectively, before steam forms. The fact that, under transient conditions, steam does not begin to form at the instant the plate surface reaches saturation is probably a combination of two effects:

1. The thermal resistance at the interface between the cladding surface and the water. The nature of the surface and the motion of the water both influence the value of the resistance: It may also be affected by the rate of change of the temperature difference and thus have a period dependence.

2. The amount of superheating above the saturation temperature and the duration that such a condition can exist in the water. This latter effect is strongly dependent upon the water motion and upon the presence of any nucleation centers such as might be produced by the dilation of adsorbed air on the plates, by dissolved air or other impurities in the water, or by the radiolytic formation of nucleation centers.

(2) IDO 16512 - Phillips Petroleum Company, SPERT Quarterly Progress Report, July-September 1958, P. 47.

The first effect of the thermal resistance amounts to essentially a temperature differential, while the superheating effect amounts to a time delay before boiling commences. One would expect that the temperature differential effect would predominate for long period transients, while the time delay effect of superheating would be the limiting factor governing the commencement of boiling for extremely short transients.

The major out-of-pile work that has attempted to determine experimentally the amount of surface temperature overshoot under transient conditions of a steady period has been performed at Berkeley, California [3, 4]. The plots of Figures III-1 and III-2 were made primarily from this data, but also included are a few in-pile points obtained during SPERT transient tests[5]. Despite the scatter in the data, it does appear for very short periods, that boiling commences after a time delay of about 3 to 5 milliseconds after the plate surface reaches saturation. In the long period region, it appears from the data that boiling commences when the plate surface temperature exceeds saturation temperature by about 20 to 40°C. The overshoot condition appears to be the dominating factor for periods longer than 10 m sec ($\alpha = 100$), while the time delay appears to be the determining criterion in the short period region.

The above rough conclusions concerning the temperature overshoot are drawn for excursions originating from an ambient temperature of about 20°C, and this ambient temperature will be assumed (unless otherwise specified) throughout this report. Unless significant discontinuities in heat transfer occur (such as the sudden commencing of boiling) or unless the reactor power rise departs from a steady period, all temperatures will increase exponentially with the period of the reactor, i. e.

$$T - T_{ambient} = f(x)e^{\alpha t}$$

where f(x) is a function of the location in the fuel plate or moderator. For ambient temperatures near saturation, the rate of rise when the surface temperature passes through the saturation point will be much less than the corresponding rate of rise for a 20°C ambient condition. Therefore, it would be expected that, for excursions originating near the saturation temperature, the factor governing the initiation of steam formation would be the amount of temperature overshoot on the plate surface rather than the time delay, even in the short period region.

(3) V.E. Schrock et al, Univ. of Calif., Berkeley, Series #163, Issue #2, Jan. 1961
(4) V.E. Schrock et al, Univ. of Calif., Berkeley, Series #163, Issue #2, Nov. 1961
(5) R.W. Miller, G.F. Brockett, E.Feinauer, Phillips Petroluem Co. private communication

Once it begins, steam formation is initially a rather sudden process resulting in significant quantities of steam in a very short time interval. For relatively long reactor periods (small prompt excess reactivity), the initial steam formation is sufficient to create a step insertion of negative reactivity which quickly terminates the power rise and drives the power back to zero. The out-of-pile data of reference 2 generally show that almost immediately after the first detectable steam formation, the void volume reaches about 0.1 mm^3 per mm^2 of plate area, and that an additional increase of about a factor of 10, to 1 mm^3 per mm^2 of plate area, occurs during the subsequent 0.6 period. Recent work by S.M. Zivi (Trans. of Amer. Nuc. Soc., Vol. 5, #1, P. 161), indicate that the initial formation of steam may actually be a dilation of adsorbed gas bubbles on the plate surfaces.

To examine the effectiveness of the initial, virtually instantaneous formation of steam, consider the SPERT 1-A core on a 20 millisecond period. The prompt excess reactivity is 0.25% Δk, most of which must be compensated by steam in order to limit the excursion. With a void coefficient of $6 \times 10^{-4}\%\Delta k/cm^3$, 400 cm^3 of steam will be needed. Using the smaller value of 0.1 mm^3/mm^2 as a virtual instantaneous void area density, 400 cm^3 of steam will need to be developed over 40,000 cm^2 of plate area, which is less than 10% of the total plate area. Since so little plate area is required, there is little variation of flux over this region, and steam is produced throughout this small region almost simultaneously.

In the case of the SL-1, with a much smaller void coefficient, consider the steam and plate area, over which the steam must form, to compensate for a 4 millisecond period. The amount of prompt excess reactivity to be compensated by steam is about 1.4%Δk (about 0.1%Δk should be compensated by expansion). With a void coefficient of $1 \times 10^{-4}\%\Delta k/cm^3$, 1.4×10^4 cm^3 of steam will be required. At the "initial" surface steam void density of 0.1 mm^3/mm^2 of plate area, 1.4×10^6 cm^2 of plate area is required. The SL-1 only has 4.2×10^5 cm^2 of plate area. However, after about 0.6 period (assume 4 milliseconds), those areas that first produced steam will then have a surface steam density of 1 mm^3 per mm^2 of plate area. This void density over one-third of the core will produce the required void. However, because of the peaked nature of the SL-1's flux profile, there is almost a one period delay after the peak flux region reaches a given temperature until one-third of the core has reached this same temperature. This fact, plus the approximate 0.6 period delay until the development of 1 mm^3/mm^2 of steam void, results in at least a 6 millisecond delay until sufficient steam is developed to terminate the excursion. Also the excursion period is gradually being lengthened while the steam is being produced, thus further lengthening the time until adequate compensation by steam can occur. In fact, the delay is sufficient to permit vaporization temperatures to be reached in the center of the plates in the peak flux region before normal steam formation (from intact plates) is adequate to limit the excursion.

2.3 Bursting of Fuel Plates

As in the case of the SL-1 excursion, the formation of adequate steam to control an excursion may be delayed sufficiently, in a fast-period transient, to permit the center portion of the fuel plates to reach vaporization temperatures. Such temperatures, it is expected, would create very high internal pressures in the fuel plate of sufficient magnitude to explode the fuel plate. The rate at which pressure due to vaporization develops in the plate, and the rapidity with which this pressure can explode the plate is probably extremely fast, such that the process will occur in a fraction of a millisecond. Information concerning the time scale of the vaporization and explosion process would be most useful in calculating the very destructive, short period transients. For very short period transients in the one millisecond and less range, the time delay involved in the bursting of plates can be extremely important, for during this time considerable additional energy will be generated. However, for longer periods such as that of the SL-1 (4 milliseconds), the time delay involved in the bursting of the plates is small compared to the period, so that the total energy of the excursion would not be significantly greater than if the bursting process were instantaneous.

The reactor period, under which a particular fuel plate can be expected to reach vaporization temperatures, is governed largely by the thickness of the cladding and its thermal conductivity. Certainly vaporization will occur for all periods shorter than that which permits the plate center temperature to reach vaporization (2040°C) before the surface temperature has exceeded saturation for more than the 3 to 5 millisecond delay that occurs in the short-period transient boiling process. (All temperatures are in degrees above ambient, which is assumed to be 20°C, except where otherwise noted. Saturation temperature is, therefore, approximately 80°C. The equivalent temperature difference of the heat of fusion is 310°C.)

Appendix F contains a derivation of the solutions to the temperature diffusion equation for plate type elements undergoing an exponential increase in power. These equations can be utilized for a power burst shape consisting of a combination of exponentials, as employed in IDO 19311, SL-1 Report.

The ratio of center to surface temperature vs. reactor period has been plotted in Figure III-4, for the SL-1 fuel plates, and in Figure III-5, for the SPERT-BORAX type of fuel plates. Interpreting from the graph of Figure III-4, it will be observed that, at a period of 3.0 milliseconds, the vaporization temperature is reached in the center of the plates when the surface tempersture is 420°C, which occurs 5 milliseconds after the surface tempersture reaches saturation (ΔT = 80°C). At the time of vaporization of the plates, essentially no steam has had a chance to form, and plate explosion would result and be the major shutdown mechanism. Because of the small void coefficient and rather peaked flux in the SL-1, the apparent 3.6 millisecond initial period (compensated to about 3.9 milliseconds by plate and moderator expansion) was short enough that plate-explosion was still probably the major shutdown mechanism. The center of the plates actually would have reached vaporization 7.5 milliseconds after the surface attained saturation temperature on a continuing 3.9 milliseconds exponential. Though some steam was formed by this time, it was probably inadequate to terminate the power increase or to reduce its rate of rise significantly.

In the case of SPERT or BORAX plates, the period at which plate vaporization occurs before significant steam formation is 2.0 milliseconds, as can be interpreted from Figure III-5. When vaporization occurs, the plate surface temperature is 970°C, which is equivalent to a 5 millisecond delay after the saturation temperature was reached. The region in which plate-explosion is a major feedback mechanism extends back to somewhat longer period excursions, probably nearly as far as to the 2.6 m sec. excursion of the BORAX destructive test. In this test there would have occurred a 7 millisecond delay, on a continuing exponential, after the plate surface reached saturation and until the center of the plate vaporized. However, normal steam formation is felt to have occurred by that time in sufficient quantities to terminate the BORAX power rise before plate vaporization actually occurred (unlike the case of the SL-1). The destruction in the BORAX primarily occurred when the rather thin plates, heated to temperatures above melting throughout their thickness, lost their mechanical integrity and disintegrated. Note that the temperature ratio between center and surface of the plate is relative to the ambient temperature base. Raising the ambient temperature closer to saturation requires that much higher temperature ratios (shorter periods) be achieved in order to explode the plates before significant quantities of steam have been formed. This fact offers some justification for attempting to maintain reactor conditions as near as possible to the saturation temperature, either by reducing the latter, i.e. by depressurizing the system, or by heating the reactor, thus minimizing the possibility of plate-explosion in an excursion. This consideration is more pertinent for reactors having thickly cladded fuel plates or pins.

3. Power Burst Shapes

If an amount of negative reactivity is inserted (via feedback mechanisms) to compensate for the prompt excess-reactivity, the power increase will be terminated and the point of peak power will be established. Though it is difficult enough to define the burst to its peak, the description of the burst shape beyond the peak involves the specification of the rate at which quite large amounts of compensating reactivity are added to the system.

Drawing on a large mass of empirical data obtained from SPERT and BORAX tests, certain general conclusions can be drawn. The burst shapes are generally asymmetrical, with more energy being accumulated up to peak power than is accumulated after peak power. The asymmetry of the bursts seem to vary with the initial reactor period, with the tendency being for the bursts to become more symmetrical as the period becomes shorter in the region in which steam is the major shutdown mechanism[6, 7].

A further characteristic of the burst shape is its sharpness, characterized by the rate at which the power trace departs from the continuing positive exponential. SPERT[8] has employed a two-term exponential which can be varied to account for the relative sharpness of the burst. This representation,

$$\phi = \phi_o \left[e^{\alpha t} - \frac{r-1}{r} e^{\left(\frac{r}{r-1}\right)\alpha t} \right] ,$$

offers little variation in the symmetry of the burst, however, giving 75 to 80 percent of the energy before the peak for all values of the parameter r between about 1.25 and 10. Nevertheless, this functional representation does give a fair approximation to most SPERT I type bursts in the 10 to 50 millisecond range, and is particularly valuable because it permits analytical solutions to be obtained for the temperature diffusion equation in the plates (see Appendix F).

3.1 Rate of Development of Shutdown Mechanism

A reactivity feedback mechanism proportional to energy will result in a perfectly symmetrical burst[9]. A mechanism proportional to higher powers of energy will create more and more asymmetrical bursts. The plate-moderator expansion mechanism for compensating for reactivity is proportional to energy, and should, therefore, yield a symmetrical burst so long as it is the only feedback mechanism. Steam void formation, however, from a given plate area accumulates more rapidly, immediately after the threshold, than does the energy generated by that section of plate[3, 4]. Thus most excursions compensated by steam would be asymmetrical. Though the data in references 3 and 4 does not extend to large amounts of void, it can be expected that once an effective blanketing of the plates with steam occurs, the void growth rate will be rapidly reduced. One would then assume that continued void growth throughout the reactor would be governed by the growth in the amount of plate area over which boiling has developed, a rate depending on the flux distribution in the reactor. For most reactors, with peak to average flux ratios of 2.5 or greater, the plate area above a certain threshold temperature increases slowly

(6) AECD 3840, BORAX Experiments, 1953.
(7) IDO 16790 - SPERT I Destructive Test Program Safety Analysis, June 15, 1962.
(8) IDO 16512 - SPERT Quarterly Progress Report, July-September 1958.
(9) Fuchs; Efficiency for Very Slow Assembly, LA 596 (August 2, 1946).
IDO 16393, a specialization on the above treatment, is more pertinent.

at first, but the rate of increase rises rapidly as the main portion of the core passes this threshold. This aspect would also generally contribute to the asymmetry of the burst.

The expulsion of moderator due to the explosion of the plates is a very rapid mechanism once it begins. If large areas of fuel plate reach destruction, as for extremely short periods, the development of compensated reactivity would undergo the same general behavior as that of steam formation in less serious excursions. The burst shapes, in general, would be asymmetrical for excursions in which only a small amount of plate area is needed to reach vaporization in order to terminate the excursion. The asymmetrical shape would alter, becoming more symmetrical, as more and more plate area is required.

3.2 Burst Shape Variation Throughout the Period Domain

From the arguments in the preceding section, certain general conclusions can be drawn concerning the change in burst shape with change in period.

In the region where expansion effects alone can compensate for the prompt excess reactivity, the burst shape would be expected to be symmetrical (except as the delayed neutrons might alter it) until the threshold of steam formation occurred. Steam production, being a much greater and more rapid reactivity feedback mechanism, would rapidly chop off the burst, creating an asymmetrical burst shape.

Even in the region where steam is required for prompt excess reactivity compensation prior to reaching the peak, the sudden production of steam in the high flux regions of the reactor occurs at a rate faster than the first power of the energy. This results in a rapid termination of these long-period bursts, resulting in an asymmetrical burst with a rather sharp shape. However, as the period shortens, the sudden burst of steam associated with the peak flux regions is inadequate by itself to turn over the burst and to introduce further negative reactivity to drive the power down. Steam will be required from other than the peak flux regions of the reactor. Since the rate at which plate area passes the threshold of boiling depends upon the flux distribution of the reactor, the resulting reactivity compensation rate will be different in different reactors. This rate will probably be proportional, initially, to a much lower power of the energy, in fact perhaps as low as the first power in the case of flux distributions that are quite peaked. The burst shape then becomes more broad and tends to be more symmetrical. However, as long as threshold feedback mechanisms play a significant part, and if these thresholds occur at a significant fraction of the peak power, true symmetry in the burst can never be obtained.

In considering shorter and shorter periods in the region in which steam is the important feedback mechanism, eventually energy densities sufficient to explode the plates will be attained. Once this new threshold is reached, the resulting reactivity compensation becomes considerably greater and more rapid (proportional once again to a high power of the energy) than that associated with ordinary steam formation. The burst shape is rather quickly chopped off and again becomes quite unsymmetrical. Continued shortening of the period throughout this region would result in a return to the burst shape behavior typical of that occurring as the period is reduced through the steam shutdown region, i.e. the burst shapes would probably become more symmetrical.

4. Analog Computer Analysis of Excursions

The analog computer studies were undertaken to evaluate some of the conclusions stated in the previous section. The 10 decade analog simulation is described in Appendix C. The analog circuit is shown in Figure III-6. Amplifiers 1, 3, 9, 11, 13, 14, 23, 25, and 34 simulate the reactor kinetics. Their arrangement is such that $\alpha = 1/\tau$ is produced as the output of amplifier 14. This is then integrated and inverted by amplifier 23 to produce ln ϕ (ϕ = flux or power). This arrangement produces, with reasonable accuracy, ten decade variation in the flux. Amplifiers 10, 12, and 26 make up the log-to-linear conversion, which is set to produce two decades of linear flux. Any two desired decades can be selected by potentiometer P-7. The circuit parameters were adjusted so that 1 second of computer time was equal to 10 milliseconds of real time.

Since the expulsion of moderator, which leads to reactivity feedback, consists of three major mechanisms; fuel plate and moderator expansion, normal steam formation, and explosion of the fuel plates, a method of simulating each of these was incorporated in the model. The fuel plate and moderator expansion were combined into a common feedback loop, that was made directly proportional to the energy by integrating the output of amplifier 17. The required energy, ($\int \phi dt$), with proper scaling, produces -0.667% Δk feedback, full scale. The output of amplifier 17 is also used to create delayed feedback. Since the integrator, #17, operates from the beginning of the excursion, it represents the total energy. However it is not used to insert feedback until the time the multiplier at the output is turned on. The magnitude of this feedback can then be established by the feedback resistor. Because this feedback is delayed, when it is inserted, it is proportional to all of the accumulated energy. Therefore, it resembles an explosive transfer of energy to the moderator. Its insertion was timed to coincide with the time that the fuel-plate center-temperature reaches vaporization in the highest flux region of the core. In order to mock up the SL-1 excursion corresponding to the measured energy release, the feedback resistance was adjusted to produce the 130 megawatt seconds measured by the flux wires.

The normal steam void formation was simulated by integrator 6 and its associated switching circuit. The integrator was shut off until the plate surface temperature had exceeded the saturation temperature for a specified time delay (3 to 5 milliseconds for short period transients). The resulting feedback was then proportional to the energy generated after the specified delay. The scaling factor for the feedback was determined by the feedback resistor, which could be varied so as to simulate various magnitudes of the steam void feedback mechanism. The other major portion of the analog circuit was the simulation of the temperature distribution in the plate. The temperatures throughout a half thickness of the plate were simulated by a five-region mockup, three of these regions in the meat and the other two in the cladding. The surface temperature and center temperature outputs were then used as trigger points for the reactivity feedbacks corresponding to steam formation and plate explosion, respectively.

5. Analog Computer Results

The analog circuit used (Figure III-6) incorporates no flow simulation of steam from the core, and hence has no means of releasing compensated reactivity from the system; therefore, it describes only a single power excursion. The evidence for only a single power burst in the SL-1 incident is quite conclusive, as discussed in IDO 19311 (ref. 1). It is very difficult to establish an absolute calibration between the various outputs, for analog results based on logarithmic simulation. In the case in question, the temperature output was used to calibrate the energy and power at an early point in the excursion before significant feedback had occurred and while the temperature diffusion equation for exponentially increasing energy is valid.

Typical results of the study are shown in Figures III-7, 8, 11 (a, b, and c), and 12 which show some of the parameters recorded for each simulated excursion. Of particular interest are summation of Δk, reciprocal period ($^1/_\tau$), linear power, and total energy. These particular plots define the nuclear behavior of the system and suitably illustrate the significant differences between various excursions. The temperature system defines the physical effects which create the transient feedback mechanisms.

The linear energy feedback due to moderator and plate expansion was derived directly from the energy output, without the use of the temperature distribution equations. Because the magnitude of this feedback mechanism was small, no attempt was made to vary it. Full scale on the energy amplifier (which was seldom reached on any of the runs) was equal to -0.667% Δk feedback, the maximum to be expected by expansion for a 130 Mw-sec transient (using the peak void coefficient).

The insertion of feedback proportional to energy accumulated after a certain trip point, i.e. the steam void feedback, was triggered by T_4, the surface temperature, usually at 10% of full scale on the temperature output amplifier. From this trigger point and the desired temperature of the trigger, both the energy and temperature curves were calibrated (except for excursions in which the feedback from plate explosion was the main feedback).

The first effect of the thermal resistance amounts to essentially a temperature differential, while the superheating effect amounts to a time delay before boiling commences. One would expect that the temperature differential effect would predominate for long period transients, while the time delay effect of superheating would be the limiting factor governing the commencement of boiling for extremely short transients.

The major out-of-pile work that has attempted to determine experimentally the amount of surface temperature overshoot under transient conditions of a steady period has been performed at Berkeley, California [3, 4]. The plots of Figures III-1 and III-2 were made primarily from this data, but also included are a few in-pile points obtained during SPERT transient tests[5]. Despite the scatter in the data, it does appear for very short periods, that boiling commences after a time delay of about 3 to 5 milliseconds after the plate surface reaches saturation. In the long period region, it appears from the data that boiling commences when the plate surface temperature exceeds saturation temperature by about 20 to 40°C. The overshoot condition appears to be the dominating factor for periods longer than 10 m sec (α = 100), while the time delay appears to be the determining criterion in the short period region.

The above rough conclusions concerning the temperature overshoot are drawn for excursions originating from an ambient temperature of about 20°C, and this ambient temperature will be assumed (unless otherwise specified) throughout this report. Unless significant discontinuities in heat transfer occur (such as the sudden commencing of boiling) or unless the reactor power rise departs from a steady period, all temperatures will increase exponentially with the period of the reactor, i. e.

$$T - T_{ambient} = f(x)e^{\alpha t}$$

where f(x) is a function of the location in the fuel plate or moderator. For ambient temperatures near saturation, the rate of rise when the surface temperature passes through the saturation point will be much less than the corresponding rate of rise for a 20°C ambient condition. Therefore, it would be expected that, for excursions originating near the saturation temperature, the factor governing the initiation of steam formation would be the amount of temperature overshoot on the plate surface rather than the time delay, even in the short period region.

(3) V.E. Schrock et al, Univ. of Calif., Berkeley, Series #163, Issue #2, Jan. 1961
(4) V.E. Schrock et al, Univ. of Calif., Berkeley, Series #163, Issue #2, Nov. 1961
(5) R.W. Miller, G.F. Brockett, E.Feinauer, Phillips Petroluem Co. private communication

Once it begins, steam formation is initially a rather sudden process resulting in significant quantities of steam in a very short time interval. For relatively long reactor periods (small prompt excess reactivity), the initial steam formation is sufficient to create a step insertion of negative reactivity which quickly terminates the power rise and drives the power back to zero. The out-of-pile data of reference 2 generally show that almost immediately after the first detectable steam formation, the void volume reaches about 0.1 mm^3 per mm^2 of plate area, and that an additional increase of about a factor of 10, to 1 mm^3 per mm^2 of plate area, occurs during the subsequent 0.6 period. Recent work by S.M. Zivi (Trans. of Amer. Nuc. Soc., Vol. 5, #1, P. 161), indicate that the initial formation of steam may actually be a dilation of adsorbed gas bubbles on the plate surfaces.

To examine the effectiveness of the initial, virtually instantaneous formation of steam, consider the SPERT 1-A core on a 20 millisecond period. The prompt excess reactivity is 0.25% Δk, most of which must be compensated by steam in order to limit the excursion. With a void coefficient of $6 \times 10^{-4}\% \Delta k/cm^3$, 400 cm^3 of steam will be needed. Using the smaller value of 0.1 mm^3/mm^2 as a virtual instantaneous void area density, 400 cm^3 of steam will need to be developed over 40,000 cm^2 of plate area, which is less than 10% of the total plate area. Since so little plate area is required, there is little variation of flux over this region, and steam is produced throughout this small region almost simultaneously.

In the case of the SL-1, with a much smaller void coefficient, consider the steam and plate area, over which the steam must form, to compensate for a 4 millisecond period. The amount of prompt excess reactivity to be compensated by steam is about 1.4%Δk (about 0.1%Δk should be compensated by expansion). With a void coefficient of $1 \times 10^{-4}\% \Delta k/cm^3$, 1.4×10^4 cm^3 of steam will be required. At the "initial" surface steam void density of 0.1 mm^3/mm^2 of plate area, 1.4×10^6 cm^2 of plate area is required. The SL-1 only has 4.2×10^5 cm^2 of plate area. However, after about 0.6 period (assume 4 milliseconds), those areas that first produced steam will then have a surface steam density of 1 mm^3 per mm^2 of plate area. This void density over one-third of the core will produce the required void. However, because of the peaked nature of the SL-1's flux profile, there is almost a one period delay after the peak flux region reaches a given temperature until one-third of the core has reached this same temperature. This fact, plus the approximate 0.6 period delay until the development of 1 mm^3/mm^2 of steam void, results in at least a 6 millisecond delay until sufficient steam is developed to terminate the excursion. Also the excursion period is gradually being lengthened while the steam is being produced, thus further lengthening the time until adequate compensation by steam can occur. In fact, the delay is sufficient to permit vaporization temperatures to be reached in the center of the plates in the peak flux region before normal steam formation (from intact plates) is adequate to limit the excursion.

2.3 Bursting of Fuel Plates

As in the case of the SL-1 excursion, the formation of adequate steam to control an excursion may be delayed sufficiently, in a fast-period transient, to permit the center portion of the fuel plates to reach vaporization temperatures. Such temperatures, it is expected, would create very high internal pressures in the fuel plate of sufficient magnitude to explode the fuel plate. The rate at which pressure due to vaporization develops in the plate, and the rapidity with which this pressure can explode the plate is probably extremely fast, such that the process will occur in a fraction of a millisecond. Information concerning the time scale of the vaporization and explosion process would be most useful in calculating the very destructive, short period transients. For very short period transients in the one millisecond and less range, the time delay involved in the bursting of plates can be extremely important, for during this time considerable additional energy will be generated. However, for longer periods such as that of the SL-1 (4 milliseconds), the time delay involved in the bursting of the plates is small compared to the period, so that the total energy of the excursion would not be significantly greater than if the bursting process were instantaneous.

The reactor period, under which a particular fuel plate can be expected to reach vaporization temperatures, is governed largely by the thickness of the cladding and its thermal conductivity. Certainly vaporization will occur for all periods shorter than that which permits the plate center temperature to reach vaporization (2040°C) before the surface temperature has exceeded saturation for more than the 3 to 5 millisecond delay that occurs in the short-period transient boiling process. (All temperatures are in degrees above ambient, which is assumed to be 20°C, except where otherwise noted. Saturation temperature is, therefore, approximately 80°C. The equivalent temperature difference of the heat of fusion is 310°C.)

Appendix F contains a derivation of the solutions to the temperature diffusion equation for plate type elements undergoing an exponential increase in power. These equations can be utilized for a power burst shape consisting of a combination of exponentials, as employed in IDO 19311, SL-1 Report.

The ratio of center to surface temperature vs. reactor period has been plotted in Figure III-4, for the SL-1 fuel plates, and in Figure III-5, for the SPERT-BORAX type of fuel plates. Interpreting from the graph of Figure III-4, it will be observed that, at a period of 3.0 milliseconds, the vaporization temperature is reached in the center of the plates when the surface tempersture is 420°C, which occurs 5 milliseconds after the surface tempersture reaches saturation (ΔT = 80°C). At the time of vaporization of the plates, essentially no steam has had a chance to form, and plate explosion would result and be the major shutdown mechanism. Because of the small void coefficient and rather peaked flux in the SL-1, the apparent 3.6 millisecond initial period (compensated to about 3.9 milliseconds by plate and moderator expansion) was short enough that plate-explosion was still probably the major shutdown mechanism. The center of the plates actually would have reached vaporization 7.5 milliseconds after the surface attained saturation temperature on a continuing 3.9 milliseconds exponential. Though some steam was formed by this time, it was probably inadequate to terminate the power increase or to reduce its rate of rise significantly.

In the case of SPERT or BORAX plates, the period at which plate vaporization occurs before significant steam formation is 2.0 milliseconds, as can be interpreted from Figure III-5. When vaporization occurs, the plate surface temperature is 970°C, which is equivalent to a 5 millisecond delay after the saturation temperature was reached. The region in which plate-explosion is a major feedback mechanism extends back to somewhat longer period excursions, probably nearly as far as to the 2.6 m sec. excursion of the BORAX destructive test. In this test there would have occurred a 7 millisecond delay, on a continuing exponential, after the plate surface reached saturation and until the center of the plate vaporized. However, normal steam formation is felt to have occurred by that time in sufficient quantities to terminate the BORAX power rise before plate vaporization actually occurred (unlike the case of the SL-1). The destruction in the BORAX primarily occurred when the rather thin plates, heated to temperatures above melting throughout their thickness, lost their mechanical integrity and disintegrated. Note that the temperature ratio between center and surface of the plate is relative to the ambient temperature base. Raising the ambient temperature closer to saturation requires that much higher temperature ratios (shorter periods) be achieved in order to explode the plates before significant quantities of steam have been formed. This fact offers some justification for attempting to maintain reactor conditions as near as possible to the saturation temperature, either by reducing the latter, i.e. by depressurizing the system, or by heating the reactor, thus minimizing the possibility of plate-explosion in an excursion. This consideration is more pertinent for reactors having thickly cladded fuel plates or pins.

3. Power Burst Shapes

If an amount of negative reactivity is inserted (via feedback mechanisms) to compensate for the prompt excess-reactivity, the power increase will be terminated and the point of peak power will be established. Though it is difficult enough to define the burst to its peak, the description of the burst shape beyond the peak involves the specification of the rate at which quite large amounts of compensating reactivity are added to the system.

Drawing on a large mass of empirical data obtained from SPERT and BORAX tests, certain general conclusions can be drawn. The burst shapes are generally asymmetrical, with more energy being accumulated up to peak power than is accumulated after peak power. The asymmetry of the bursts seem to vary with the initial reactor period, with the tendency being for the bursts to become more symmetrical as the period becomes shorter in the region in which steam is the major shutdown mechanism[6, 7].

A further characteristic of the burst shape is its sharpness, characterized by the rate at which the power trace departs from the continuing positive exponential. SPERT[8] has employed a two-term exponential which can be varied to account for the relative sharpness of the burst. This representation,

$$\phi = \phi_o \left[e^{\alpha t} - \frac{r-1}{r} e^{\left(\frac{r}{r-1}\right) \alpha t} \right],$$

offers little variation in the symmetry of the burst, however, giving 75 to 80 percent of the energy before the peak for all values of the parameter r between about 1.25 and 10. Nevertheless, this functional representation does give a fair approximation to most SPERT I type bursts in the 10 to 50 millisecond range, and is particularly valuable because it permits analytical solutions to be obtained for the temperature diffusion equation in the plates (see Appendix F).

3.1 Rate of Development of Shutdown Mechanism

A reactivity feedback mechanism proportional to energy will result in a perfectly symmetrical burst[9]. A mechanism proportional to higher powers of energy will create more and more asymmetrical bursts. The plate-moderator expansion mechanism for compensating for reactivity is proportional to energy, and should, therefore, yield a symmetrical burst so long as it is the only feedback mechanism. Steam void formation, however, from a given plate area accumulates more rapidly, immediately after the threshold, than does the energy generated by that section of plate[3, 4]. Thus most excursions compensated by steam would be asymmetrical. Though the data in references 3 and 4 does not extend to large amounts of void, it can be expected that once an effective blanketing of the plates with steam occurs, the void growth rate will be rapidly reduced. One would then assume that continued void growth throughout the reactor would be governed by the growth in the amount of plate area over which boiling has developed, a rate depending on the flux distribution in the reactor. For most reactors, with peak to average flux ratios of 2.5 or greater, the plate area above a certain threshold temperature increases slowly

(6) AECD 3840, BORAX Experiments, 1953.
(7) IDO 16790 - SPERT I Destructive Test Program Safety Analysis, June 15, 1962.
(8) IDO 16512 - SPERT Quarterly Progress Report, July-September 1958.
(9) Fuchs; Efficiency for Very Slow Assembly, LA 596 (August 2, 1946). IDO 16393, a specialization on the above treatment, is more pertinent.

at first, but the rate of increase rises rapidly as the main portion of the core passes this threshold. This aspect would also generally contribute to the asymmetry of the burst.

The expulsion of moderator due to the explosion of the plates is a very rapid mechanism once it begins. If large areas of fuel plate reach destruction, as for extremely short periods, the development of compensated reactivity would undergo the same general behavior as that of steam formation in less serious excursions. The burst shapes, in general, would be asymmetrical for excursions in which only a small amount of plate area is needed to reach vaporization in order to terminate the excursion. The asymmetrical shape would alter, becoming more symmetrical, as more and more plate area is required.

3.2 Burst Shape Variation Throughout the Period Domain

From the arguments in the preceding section, certain general conclusions can be drawn concerning the change in burst shape with change in period.

In the region where expansion effects alone can compensate for the prompt excess reactivity, the burst shape would be expected to be symmetrical (except as the delayed neutrons might alter it) until the threshold of steam formation occurred. Steam production, being a much greater and more rapid reactivity feedback mechanism, would rapidly chop off the burst, creating an asymmetrical burst shape.

Even in the region where steam is required for prompt excess reactivity compensation prior to reaching the peak, the sudden production of steam in the high flux regions of the reactor occurs at a rate faster than the first power of the energy. This results in a rapid termination of these long-period bursts, resulting in an asymmetrical burst with a rather sharp shape. However, as the period shortens, the sudden burst of steam associated with the peak flux regions is inadequate by itself to turn over the burst and to introduce further negative reactivity to drive the power down. Steam will be required from other than the peak flux regions of the reactor. Since the rate at which plate area passes the threshold of boiling depends upon the flux distribution of the reactor, the resulting reactivity compensation rate will be different in different reactors. This rate will probably be proportional, initially, to a much lower power of the energy, in fact perhaps as low as the first power in the case of flux distributions that are quite peaked. The burst shape then becomes more broad and tends to be more symmetrical. However, as long as threshold feedback mechanisms play a significant part, and if these thresholds occur at a significant fraction of the peak power, true symmetry in the burst can never be obtained.

In considering shorter and shorter periods in the region in which steam is the important feedback mechanism, eventually energy densities sufficient to explode the plates will be attained. Once this new threshold is reached, the resulting reactivity compensation becomes considerably greater and more rapid (proportional once again to a high power of the energy) than that associated with ordinary steam formation. The burst shape is rather quickly chopped off and again becomes quite unsymmetrical. Continued shortening of the period throughout this region would result in a return to the burst shape behavior typical of that occurring as the period is reduced through the steam shutdown region, i.e. the burst shapes would probably become more symmetrical.

4. Analog Computer Analysis of Excursions

The analog computer studies were undertaken to evaluate some of the conclusions stated in the previous section. The 10 decade analog simulation is described in Appendix C. The analog circuit is shown in Figure III-6. Amplifiers 1, 3, 9, 11, 13, 14, 23, 25, and 34 simulate the reactor kinetics. Their arrangement is such that $\alpha = 1/\tau$ is produced as the output of amplifier 14. This is then integrated and inverted by amplifier 23 to produce ln ϕ (ϕ = flux or power). This arrangement produces, with reasonable accuracy, ten decade variation in the flux. Amplifiers 10, 12, and 26 make up the log-to-linear conversion, which is set to produce two decades of linear flux. Any two desired decades can be selected by potentiometer P-7. The circuit parameters were adjusted so that 1 second of computer time was equal to 10 milliseconds of real time.

Since the expulsion of moderator, which leads to reactivity feedback, consists of three major mechanisms; fuel plate and moderator expansion, normal steam formation, and explosion of the fuel plates, a method of simulating each of these was incorporated in the model. The fuel plate and moderator expansion were combined into a common feedback loop, that was made directly proportional to the energy by integrating the output of amplifier 17. The required energy, ($\int \phi dt$), with proper scaling, produces -0.667% Δk feedback, full scale. The output of amplifier 17 is also used to create delayed feedback. Since the integrator, #17, operates from the beginning of the excursion, it represents the total energy. However it is not used to insert feedback until the time the multiplier at the output is turned on. The magnitude of this feedback can then be established by the feedback resistor. Because this feedback is delayed, when it is inserted, it is proportional to all of the accumulated energy. Therefore, it resembles an explosive transfer of energy to the moderator. Its insertion was timed to coincide with the time that the fuel-plate center-temperature reaches vaporization in the highest flux region of the core. In order to mock up the SL-1 excursion corresponding to the measured energy release, the feedback resistance was adjusted to produce the 130 megawatt seconds measured by the flux wires.

The normal steam void formation was simulated by integrator 6 and its associated switching circuit. The integrator was shut off until the plate surface temperature had exceeded the saturation temperature for a specified time delay (3 to 5 milliseconds for short period transients). The resulting feedback was then proportional to the energy generated after the specified delay. The scaling factor for the feedback was determined by the feedback resistor, which could be varied so as to simulate various magnitudes of the steam void feedback mechanism. The other major portion of the analog circuit was the simulation of the temperature distribution in the plate. The temperatures throughout a half thickness of the plate were simulated by a five-region mockup, three of these regions in the meat and the other two in the cladding. The surface temperature and center temperature outputs were then used as trigger points for the reactivity feedbacks corresponding to steam formation and plate explosion, respectively.

5. Analog Computer Results

The analog circuit used (Figure III-6) incorporates no flow simulation of steam from the core, and hence has no means of releasing compensated reactivity from the system; therefore, it describes only a single power excursion. The evidence for only a single power burst in the SL-1 incident is quite conclusive, as discussed in IDO 19311 (ref. 1). It is very difficult to establish an absolute calibration between the various outputs, for analog results based on logarithmic simulation. In the case in question, the temperature output was used to calibrate the energy and power at an early point in the excursion before significant feedback had occurred and while the temperature diffusion equation for exponentially increasing energy is valid.

Typical results of the study are shown in Figures III-7, 8, 11 (a, b, and c), and 12 which show some of the parameters recorded for each simulated excursion. Of particular interest are summation of Δk, reciprocal period ($1/\tau$), linear power, and total energy. These particular plots define the nuclear behavior of the system and suitably illustrate the significant differences between various excursions. The temperature system defines the physical effects which create the transient feedback mechanisms.

The linear energy feedback due to moderator and plate expansion was derived directly from the energy output, without the use of the temperature distribution equations. Because the magnitude of this feedback mechanism was small, no attempt was made to vary it. Full scale on the energy amplifier (which was seldom reached on any of the runs) was equal to -0.667% Δk feedback, the maximum to be expected by expansion for a 130 Mw-sec transient (using the peak void coefficient).

The insertion of feedback proportional to energy accumulated after a certain trip point, i.e. the steam void feedback, was triggered by T_4, the surface temperature, usually at 10% of full scale on the temperature output amplifier. From this trigger point and the desired temperature of the trigger, both the energy and temperature curves were calibrated (except for excursions in which the feedback from plate explosion was the main feedback).

The insertion of feedback proportional to the total accumulated energy, i.e. corresponding to plate explosion, was triggered by T_o, the center temperature in the fuel plate, usually at full scale on the temperature amplifier. Where this temperature had significance for the particular excursion, such as to represent the vaporization temperature, full scale deflection was used to establish the temperature scale. Then the excursion energy was calibrated, usually in the low temperature region of the surface temperature plot, at a point prior to the time of insertion of any significant amount of feedback.

Table III-4 shows the results of some of the typical excursions run on the analog computer using various combinations of feedback. In the A series, only steam formation feedback was used (plus the small expansion effect). The table indicates a trend away from symmetry as the delay is increased between the time that plate temperature reaches saturation and the time of application of the linear feedback. However, this departure from symmetry is not significant, and the burst shape is not too unsymmetrical for all cases of linear energy feedback in the period range where the feedback delay is as long or longer than the initial period. In fact, it has been shown theoretically that linear energy feedback throughout the excursion leads to a symmetrical burst(9).

When the feedback mechanism is changed to a step input proportional to all the accrued energy and inserted when fuel plate temperature reaches a specified amount, the departure from symmetry is pronounced. This is shown in the B series of runs in Table III-4. In each case the feedback was adjusted so as to cause the total energy of the excursion to be equal to 130 Mw sec. Not only does shutdown occur more rapidly, but the amount of reactivity necessary to produce shutdown becomes greater as the trigger temperature is set higher and higher. This is of course to be expected, since as greater amounts of energy are accumulated before the trigger temperature, the negative period required to stay within the energy constraints of the SL-1 excursion becomes much greater. In the case in which the trigger temperature was set several hundred degrees above the saturation temperature (corresponding to a brief 1/2 millisecond delay), the reactivity had to be inserted extremely rapidly and had to be of considerable magnitude, so as to make the reactor highly subcritical, almost immediately. When the trigger temperature for the step reactivity insertion was set at the normal vaporization temperature, the plate surface temperature at that time is over 500°C. This is far too large an overshoot (in time or temperature) to be consistent with an assumption of no steam formation. Thus, a combination of steam-void and plate-explosion reactivity compensating mechanisms was probably present at the peak of the burst.

The above two shutdown mechanisms were combined in various manners to produce the results tabulated in Table III-4, Series C. These runs were for a 4 millisecond period and combination of T_o and T_4 feedback. Each run represents approximately 130 megawatt seconds. The energy-at-peak to total energy ratio indicates a non-symmetric burst with the drop from peak power being faster than the rise to peak power. This is, of course, due to the rather large step insertion from the plate center temperature trip. The center temperature trigger level for this series was actually 1950°C, slightly below the vaporization temperature of 2040°C. (discovered following accurate calibration of the output traces). This difference is probably within the overall accuracy of the analog simulation and will not significantly effect the results of the simulation. In each case the surface temperature at the time of the step reactivity insertion was sufficiently late for steam formation to be occurring. But the feedback from steam was not adequate to terminate the excursion. Probably any one of these curves could well suit the SL-1 incident, since they are all within the experimental uncertainty of the energy. The peak power varies from 17,000 to 19,500 megawatts. Power burst shapes for runs #C-2 and C-6 are shown in Figure III-7. These curves have approximately the same shape with a ratio of energy-at-peak to total energy of 0.56. While the burst shapes are similar the summation Δk curves show a considerable difference. Figure III-8 shows the variation in the summation Δk. The obvious step insertion of reactivity for run C-2 is unusually large and is intended to correspond to the very rapid formation of void from a very large heat transfer area, (as from an exploded plate). The summation Δk curve for C-6 shows a much smaller step-reactivity insertion. For the C-2 case, the step magnitude was 2.1% and the C-6 curve 0.4%. When data on the rate of void growth[3, 4] is considered, curve C-6 (the smaller step insertion) is probably the more realistic simulation of the excursion.

The D and E series of transient runs show the difficulty of fitting the SL-1 excursion to a period greatly different than approximately 4 milliseconds. In the case of the D series (5 millisecond period), run D-1 employs linear energy feedback (plus the plate-moderator expansion effect) with a 4.4 millisecond delay between the plate surface reaching saturation temperature and the application of the feedback. When the magnitude of this feedback was decreased, and the delay shortened (as in runs D-3 and D-4) to permit vaporization and its feedback to occur, the total burst energy could not be reduced sufficiently to meet the 130 megawatt second constraint, unless the T_o feedback was very strong, as in run D-5. The primary consideration is that vaporization was attained only after the accumulation of too much energy. The 5 m sec period can be made to give a good fit, except for the fact that it then does not allow center temperatures to rise sufficiently throughout enough of the core to account for the vaporization that apparently occurred and the large step reactivity that would then be required. Two major factors contributed to the elimination of the 2.4 millisec period as a possible excursion period for the accident. First, the rod withdrawal rate required, as discussed in the SL-1 final report (IDO-19311), would be extremely fast. Second, the amount of feedback reactivity needed to stay within the energy constraint is quite large. With the energy constraint of 130 Mw sec, the burst shape for any given initial reactor period is defined within limits. In other words, the simulated feedback mechanism must be defined so that it will compensate for the original reactivity as well as determine the rate of power reduction so as to keep the total energy within the 130 megawatt second constraint. Inspection of both the D-5 (a 5 millisecond transient with much plate destruction) and E-3 analog computer runs show that the total negative reactivity insertion is about 7.5% and 10%, respectively. The reactivity thus inserted defines not only the period but the amount of energy developed on the back side of the burst. Furthermore, about 6% and 5% Δk reactivity is inserted by the initial step insertion for runs D-5 and E-3, respectively. All of these

TABLE III-4

Results of Typical Analog Computer Simulated Excursions - Ambient Temperature = 26°C

Run Number	A-1	A-2	A-3	A-4	A-5	A-6	A-7	B-1	B-2	B-3	E-1	E-2	E-3
Initial Period, Milliseconds	3.6	3.6	3.6	3.6	3.6	3.6	3.6	3.6	3.6	3.6	2.4	2.4	2.4
Type of Feedback*	S	S	S	S	S	S	S	V	V	V	S, V	S, V	S, V
Delay of T_4 Feedback, Milliseconds	3.8	2.6	2.1	4.4	6	0	0	---	---	---	2.3	1.4	2.3
Plate Surface Temp. at Trigger, °C	168	132	118	210	314	70	70	---	---	---	175	125	175
Feedback from Steam at End, %Δk	3.8	3.5	3.3	4.0	5.0	3.0	3.1	---	---	---	1.2	2.7	2.3
Center Temp. at T_o Trip, °C†	---	---	---	---	---	---	---	1950	2100	2700	3000	2000	3000
Step Feedback Initially, %Δk	---	---	---	---	---	---	---	3.4	3.9	6.5	4.8	1.0	1.2
T_o Feedback at End, %Δk	---	---	---	---	---	---	---	4.2	5.7	8.0	7.6	2.9	4.8
E(peak)/E(total), %	50	51	52	56	59	50	50	56	66	78	64	50	50
Power at Peak, 1000 Mw	13.2	10.0	9.5	13.9	15.4	8.4	7.7	18.5	21.3	26.4	39.1	39.4	39.6
Total Energy, Mw-sec	130	130	130	130	130	130	130	130	130	130	130	205	191

*S ≡ Steam Triggered by T_4

*V ≡ Vaporization Triggered by T_o

† All temperatures include correction for heat of fusion equivalent and are therefore actual temperatures.

TABLE III-4 (Cont'd)

Run Number	C-1	C-2	C-3	C-4	C-5	C-6	D-1	D-2	D-3	D-4	D-5	G-1	G-2	G-3
Initial Period, Milliseconds	3.6	3.6	3.6	3.6	3.6	3.6	5	5	5	5	5	3.6	3.6	3.6
Type of Feedback	S, V	S, V	S, V	S, V	S, V	S, V	S	S, V	S, V	S, V	S, V	S	S	S
Delay of T_4 Feedback, Milliseconds	4.7	3.8	5.0	5.0	2.3	3.4	4.4	3.6	3.5	3.5	3.8	5	0.5	3.2
Plate Surface Temp. at Trigger, °C	240	185	250	250	128	160	170	145	140	140	150	250	80	155
Feedback from Steam at End, %Δk	0.6	0.8	2.8	2.3	2.3	3.7	2.8	1.5	1.0	0.8	0.9	4.8	3.5	9.6
Center Temp. at T_o Trip, °C	1950	1950	1950	1950	1950	1950	---	2100	2100	2100	2100	---	---	---
Step Feedback, Initially %Δk	2.1	2.8	1.2	1.1	1.0	0.3	---	0.6	0.6	1.4	6.0	---	---	---
T_o Feedback at End, %Δk	3.8	4.7	1.8	1.9	1.8	0.5	---	1.0	1.3	2.5	6.6	---	---	---
E(peak)/E(total), %	54	56	58.	58	59	56	57	60	46	56	88	56	61	70
Power at Peak, 1000 Mw	17.4	17.2	17.8	19.4	19.0	17.2	11.7	12.1	11.6	10.2	10.7	18.2	19.8	22.4
Total Energy, Mw-sec	129	123	123	134	129	123	144	150	185	150	107	130	130	130

values seem to be extremely large and not generally consistent with the highly peaked flux and small void coefficient of the SL-1.

Basically, the long period transient (5 milliseconds) does not permit the vaporization temperature to be reached soon enough over a large enough portion of the core (the temperature distribution is too flat); while the short period excursion (2.4 milliseconds) accumulates too much energy by virtue of the fact that an extremely large step insertion of reactivity is required to shut the reactor down rapidly enough. However, without knowing more about the plate-explosion process, the elimination from consideration of such a large reactivity insertion cannot be positively made.

Further consideration was given to the shape of the burst as a function of the type of feedback. Feedback proportional to the square of the energy and the fourth power of the energy, accumulated following the trigger temperature, were employed. These results are shown in Table III-4, Series G, in which it is apparent that the stronger the exponent for the energy feedback, the more unsymmetrical the burst becomes. See Figure III-12. From the data on development of void formation (references 3 and 4), it is apparent that the void from a unit area of plate initially grows much faster than the first power of the energy. This rapid growth soon abates, and the void volume eventually approaches saturation. Consideration must then be given to the rate at which area in the reactor attains sufficient energy density to produce steam. The latter effect, required when large steam void is needed for shutdown, amounts to feedback that develops more nearly proportional tothe first power of the energy. Therefore, in the case of the SL-1 on a 4 millisecond period, for which large quantities of steam must be produced for reactivity compensation, the approximation of steam void growing as the first power of the energy is not implausible.* However, for longer period excursions, the small steam void growth proportional to a higher power of energy, resulting in a rather unsymmetrical burst shape. And as one progresses through the steam void shutdown region toward shorter periods, the burst shape becomes more symmetrical.

6. Model for Excursions in Water Cooled Reactors Having Plate-Type Fuel Elements**

From the considerations previously discussed, a mathematical model for a single reactor transient has been developed. It attempts to determine the total energy, approximate burst shape, and the peak power of an excursion of a specified initial period. The information required for a particular reactor are its static characteristics, primarily the flux

*The limitations of the number of analog computer components available actually prevented incorporating a feedback proportional to a power of energy greater than 1 along with the T_0 feedback proportional to accumulated energy.

**Though only plate-type reactors have been considered, the extension to pin-type cores is straightforward. The only major modification is the conversion of the temperature distribution equations from one dimensional geometry to cylindrical geometry.

distribution and void coefficient, plus its general physical characteristics such as plate thickness, spacing, and material composition. Empirical transient information on the reactor in question is not required for the model.

6.1 Computation of Energy up to point at which Steam Formation Begins

a. For long period transients, the surface temperature of the peak flux region must exceed a specified temperature overshoot, which is caused by the thermal resistance at the interface of the fuel plate and water. See Figure III-1.

b. For short period transients, steam formation is delayed after the surface temperature reaches saturation, partly by the thermal resistances at the interface, but primarily by a necessary superheat delay until bubble formation commences. The delay amounts to approximately 3 to 5 milliseconds. See Figure III-2. Up to the point of steam formation, power and energy rise approximately exponentially, with the rate at the commencement of steam formation being that of the initial period, with some slight compensation for plate expansion and moderator heating effects.

The energy to this point is approximately that computed for the average temperature of the plates in the entire core. Heat conduction to the moderator can generally be neglected except for very long period transients.

(1) $$T_{ave} = \left[T_{peak\ surface}\right] \left[\frac{T_{ave}}{T_{surface}}\right]_{\alpha} \left[\frac{\phi_{ave}}{\phi_{peak}}\right]$$

$T_{peak\ surface}$ is the surface temperature in the peak flux region when steam formation first occurs.

$\left.\frac{T_{ave}}{T_{surface}}\right]_{\alpha}$ = is the ratio characterized by the temperature distribution in the plates, which, for a given fuel plate, is a function of the reciprocal period, $1/\tau$. (See Figures III-4 and 5)

$\frac{\phi_{ave}}{\phi_{peak}}$ = is the reciprocal of the peak to average flux ratio in the core.

The total nuclear energy generated to this point in the excursion is:

(2) $$E = \frac{1}{0.86} \left[T_{ave}\right] \times \left[m_{plates}\right] \times \left[C_p\right]$$

where m_{plates} is the total mass of the fuel plates and C_p is their specific heat (average of meat and clad), and 1/0.86 is the ratio of total nuclear energy to that promptly deposited in the plates. For long period transients, the heat deposited in the water due to conduction may be significant and will require that an additional factor slightly greater than 1.0 be included in equation (2).

The power at the time steam formation commences will be approximately

$$P = E \alpha'$$

where α' is the effective reciprocal period at that time. It is the initial reciprocal period less that amount of compensation for expansion of fuel plate and moderator heating. This compensated reactivity should be computed from the average void coefficient and the change in volume of the fuel plates for their average temperature rise plus the expansion of the water due to that portion of energy which contributes to the nuclear heating of the water. For long period transients, the heating of the water due to conduction and its resulting expansion and effect on void formation must also be included.

6.2 Computation of Energy from the Time Steam Formation Commences to the Time of Peak Power

Once steam formation commences in the peak flux region, reactivity compensation progresses quite rapidly. The exact rate at which steam forms throughout the core depends both on the continued rate of void growth, where steam has already appeared, and on the flux distribution which determines the rate at which plate surface area attains the conditions necessary for the production of void. Where a complete specification of the flux profile is not available or too cumbersome, it may be assumed that the net effect of the above two contributions to the steam production rate approximates a linear feedback of reactivity with respect to time.

The following semi-empirical criteria are suggested for computing the length of time required to develop a specified amount of steam void. (The empirical information is derived from references 3 and 4.)

a. The initial steam formation, following the required delay or temperature overshoot amounts to

10^{-1} mm^3/mm^2 of plate-surface area.

b. In the ensuing time duration of approximately 0.6 periods, the steam void increases to

$10^0 = 1$ mm^3/mm^2 of plate-surface area.

c. The time duration between when the peak flux region attains initial boiling and when a region of lower flux attains boiling can be computed by using a representative average period for the reactor during this time and the flux profile for the core (i.e. Figure III-3).

By balancing considerations (a), (b), and (c) above, a time duration from the commencement of steam formation in the peak flux region until sufficient steam is produced to compensate for the prompt excess reactivity may be ascertained.

By assuming a linear feedback of the prompt excess reactivity over the estimated time interval, one can write

$$(3) \qquad \frac{dn}{dt'} = n \frac{kx}{\mathcal{l}} \left[1 - \frac{t'}{T} \right]$$

where kx is the excess prompt reactivity when steam formation commences.

T is the time required to compensate for this prompt excess reactivity.

$\mathcal{l}$ is the reactor generation time.

t' is real time.

By making the transformation,

$$t = T - t', \; dt = -dt'$$

equation (3) becomes

$$(4) \qquad \frac{dn}{dt} = -n \frac{kx}{\mathcal{l}} \quad \frac{t}{T}$$

The solution, integrating from 0 to t, is:

$$(5) \qquad n = n_o \; e^{-\frac{kx}{2\mathcal{l}} \cdot \frac{t^2}{T}}$$

and

$$(5a) \qquad n\;(T) = n_o \; e^{-\frac{kx}{2\mathcal{l}} T} \quad \text{at } t = T.$$

Equation (5) is a Gaussian, and the transformation from equation (3) to equation (4) merely switched the time variable symmetrically from one side of the "bell shaped curve" to the other.

n_o represents the peak power of the excursion, at the moment the prompt excess reactivity is exactly equal to zero.

n (T) is the power at the time steam formation commences.

The integral of equation (5) gives the energy accumulated from the time steam formation begins until peak power is reached.

$$E = \int_o^T ndt = \int_o^T n_o\, e^{-\left(\frac{kx}{2\ell T}\ \frac{t^2}{2}\right)} dt$$

Let $U = \sqrt{\frac{kx}{\ell T}}\ t,$ then

$$(6) \quad E = n_o \frac{T}{kx} \int_o^{\sqrt{\frac{kxT}{\ell}}} e^{-\frac{U^2}{2}} dU = n_o \sqrt{\frac{2\pi \ell T}{kx}} \left[\operatorname{erf} \sqrt{\frac{kxT}{\ell}} \right]$$

where the erf X is defined as

$$(7) \quad \operatorname{erf} X = \frac{1}{\sqrt{2\pi}} \int_o^x e^{-\frac{U^2}{2}} dU$$

The (erfX) is the integral of the normal error function F, from o (corresponding to peak power) to that argument corresponding to the power when steam formation begins, i.e.

from the argument where $F = \frac{1}{\sqrt{2\pi}} = .399$

to the argument where $F = \frac{n(T)}{n_o} \cdot \frac{1}{\sqrt{2\pi}}$

6.3 Computation of Energy Following Peak of Excursion

The energy accumulated after the peak of the excursion is not significant from consideration of the overall magnitude of the excursion Under most of the experimental power burst shapes obtained for SPERT and BORAX, the energy accumulated before the peak of the excursion is at least half and usually 75% of the total energy of the entire excursion.

The approximation employed in obtaining the energy from the commencement of steam formation to the peak of the burst can be extended to the continuation of the burst beyond its peak. In general, this extension will be even more crude, since it will be necessary to specify the time rate of change of rather large voids. One rough treatment would be to assume symmetry around the peak and to extend the integral in equation (6) from zero time (peak) to infinity (end of burst). However, some consideration should be given to the changing rate of void formation, and the resulting change in rate of insertion of compensating reactivity, and to derive an average rate for the significant duration of time after the peak of the burst.

From the data in reference 4, it appears that on the continuing exponential power rise, the steam void of 1 mm^3/mm^2 will double in approximately 0.3 periods. The average power (for reference 4 data) during this factor of two increase in steam void (0.3 periods) is 1.17 of the initial power, P_o. However, in the case of an excursion, once P_o is attained the power decreases. Presumably the continuation of steam formation will be governed somewhat by the average power during this time interval. Assuming that the power burst shape following that peak is approximately a Gaussian, then the power at the point where half the energy following the peak has been developed will be at 0.63 P_o. Thus, the doubling of the steam void might be expected to require approximately (1.17/0.63) (0.3 initial periods) or about 0.6 initial periods. This steam growth rate is still faster than is required for the total accumulated energy to double, which would require a time of about one initial period at steady peak power level. Thus, the time required following the peak of the burst to insert an additional amount of reactivity, equal to that compensated already by steam at the peak, will be shorter than the time required to double the energy. The steam doubling time will be about 0.6 initial periods for that void which, at the peak, amounted to about 1 mm^3/mm^2. Adjustment of this time to a smaller value would be appropriate if the void density was smaller at the peak of the burst, (such as for excursions requiring only a small portion of steam to compensate for reactivity at the peak), since void growth up to 1 mm^3/mm^2 is more rapid than the continued growth. A reduction in the value of this time to double the steam void also results from the spread of steam to other surfaces of the plates, as their energy density becomes sufficiently high for them to contribute to the overall void.

The energy generated on the back side of the burst will then be:

$$(8) \quad E_{back} = n_o \sqrt{\frac{T'}{kx}} \int_0^{\infty} e^{-\frac{U^2}{2}} dU = n_o \frac{1}{2} \sqrt{\frac{2\pi \ell T'}{kx}}$$

where n_o is the peak power

T' is the time after peak power required to add an additional amount of reactivity kx.

kx is the initial prompt excess reactivity

This treatment of the energy following the peak of the burst fails somewhat in accurately describing the observed and theorized ratio of total energy to energy at the peak of the excursion. However, it does give a representative approximation to the back side of the excursion. Inasmuch as the energy developed after the peak power is not quite as important in determining the destructive aspects of the excursion as that developed up to peak power, the approximation is probably satisfactory for most applications.

7. Conclusions Concerning the Prediction of Energy Release

The model described in the previous section has been used to calculate roughly the peak powers and energies of excursions of various periods for the SL-1, BORAX, and SPERT-I DU-12/25 cores. These predicted values are shown as the curves in Figures III-9 and 10, with the experimental points shown for those reactor transients for which data exists. Some of the specific predicted values are listed in Table III-5. The calculations were performed without any high degree of sophistication and without having available the needed data on the flux distributions in the BORAX or SPERT cores (the BORAX peak to average flux ratio was assumed to be 2.1).

Figures III-9 and 10 show that in the range above 2 Mw-sec, the excursion model does predict the relative differences in excursion magnitude between the various cores, and succeeds in predicting the absolute energies and peak powers within about ±25%, a considerably smaller variation than exists in the relative differences between the reactors. For excursions of the same initial period, the energy release from an SL-1 excursion is predicted to be 3 to 4 times larger than the energy release from the BORAX, which in turn is about 3 times larger than the energy release to the peak of the excursion for the SPERT I DU-12/25, (or about 2 times larger than the total DU-12/25 energy release). Furthermore, the relative agreement or disagreement between the predicted and experimental values is predicated by the uncertainties in the above model and the uncertainties in the experimental data from each reactor transient (about ± 20%).

No pretense is made that the calculations using this model are precise and accurate. The use of a digital computer to calculate reactivity changes with energy precisely, using the flux profile and steam growth rates, would enhance the credibility of the results. However, the simple model and simple desk calculations employed can apparently predict the energy release and peak powers much better than within an uncertainty of a factor of two. Improvement in the accuracy and consistency of the void growth data and empirical information pertaining to the explosion and/or disintegration of fuel plates at or near the vaporization temperature would certainly ameliorate the mathematical approximations of the excursion model.

TABLE III-5

Summary of Predicted Excursion Energies Peak Powers vs. Initial Period for SL-1 SPERT and BORAX all from Assumed 80°C Subcooled Condition

SL-1

T	E_{total}	E_{peak}	P_{max}	Measured Energy
125 M sec	11 Mw sec	8 Mw sec	63 Mw	
50	21	15	227	
20	33	23	869	
10	43	27	1840	
3.6	156*	116	18,900*	130 ± 15 ref. (1)
2	410	300	130,000	

SPERT DU 12/25 (energy to peak only)

T	E_{total}	E_{peak}	P_{max}	Measured Energy
75	2.6	2.2	46	1.7 (peak) (7)
50	4.1	2.7	54	2.3 (peak) (7)
20	6.5	4.0	173	4 (peak) (7)
10	9.9	5.7	450	6 (peak) (7)
5	17.5	10.5	1510	8 (peak) (7)
2.6	52	31	7,700	
2	70	52	18,200	

BORAX

T	E_{total}	E_{peak}	P_{max}	Measured Energy
2.6	117†	69	18,100	135 ± 25 (10)

* 60° C subcooled (similar to incident) gives total energy of 141 Mw-sec. and peak power of 16400 Mw.

† At 72° C subcooled, total energy is 105 Mw-sec.

In terms of information useful in improving the accuracy of the model, the results of the SPERT I destructive tests, currently in progress, will certainly be of interest to compare with the upper portions of the curves of Figures III-9 and 10. However, these tests can no more than corroborate or cast doubt upon the model. Of nearly as much interest would be an extension of the work of Johnson, Schrock, and associates at the University of California on the transient conditions during void formation and growth. It is from this data that much of the reliability of the excursion model depends. The present data is quite scattered and uncertain, and the above investigators no doubt are continuing their work. However, enough data does exist from which the rough conclusions used in constructing the excursion model have been drawn. (Note that these conclusions are those of the authors of this report and do not necessarily represent those of Johnson, Schrock, and associates.) For the very short period, highly destructive excursions, steam formation from intact plates fades into insignificance. It is then that the exact nature of the destruction of the plates becomes extremely important in establishing the magnitude of the excursion. In this realm essentially no empirical information exists (except perhaps for that deduced from the SL-1 and BORAX analyses) and the process virtually defies theoretical analysis. It appears that out-of-pile tests of fuel plates in the destructive region are of paramount importance if the severe reactor transients are to be accurately predicted.

The mere fact that the excursion energy or peak power can be predicted does not a priori enable the prediction of the destruction external to the reactor core. The fission product release to the surroundings, water expulsion, missile impact damage, and explosive forces generated all depend on the reactor system design and structure. Though a prediction of excursion energy can lead to an estimate of reactor damage and the amount of steam formed within a short time of the nuclear transient (within a fraction of a second), such as was done in the SL-1 final report, (IDO-19311), the ultimate damage depends on the ability of the reactor plant to withstand the pressures produced. The latter evaluation is greatly simplified by scale model destructive tests. But to perform these properly, the explosive release of energy to the water and surroundings must conform to that expected from the nuclear excursion. (Witness the unwanted damage results of the scale model destructive tests of the SL-1, Figure I-81.)

Though the nuclear excursion model developed in this report is only accurate to about ±30%, it is probably quite adequate for hazards analyses which require the introduction of considerations having much larger uncertainties before the ultimate damage can be predicted. It is felt that the major problems remaining in hazard analysis of water cooled and moderated reactors are not in the nuclear physics of the excursion, but in the prediction of the ultimate damage to the reactor plant and surroundings.

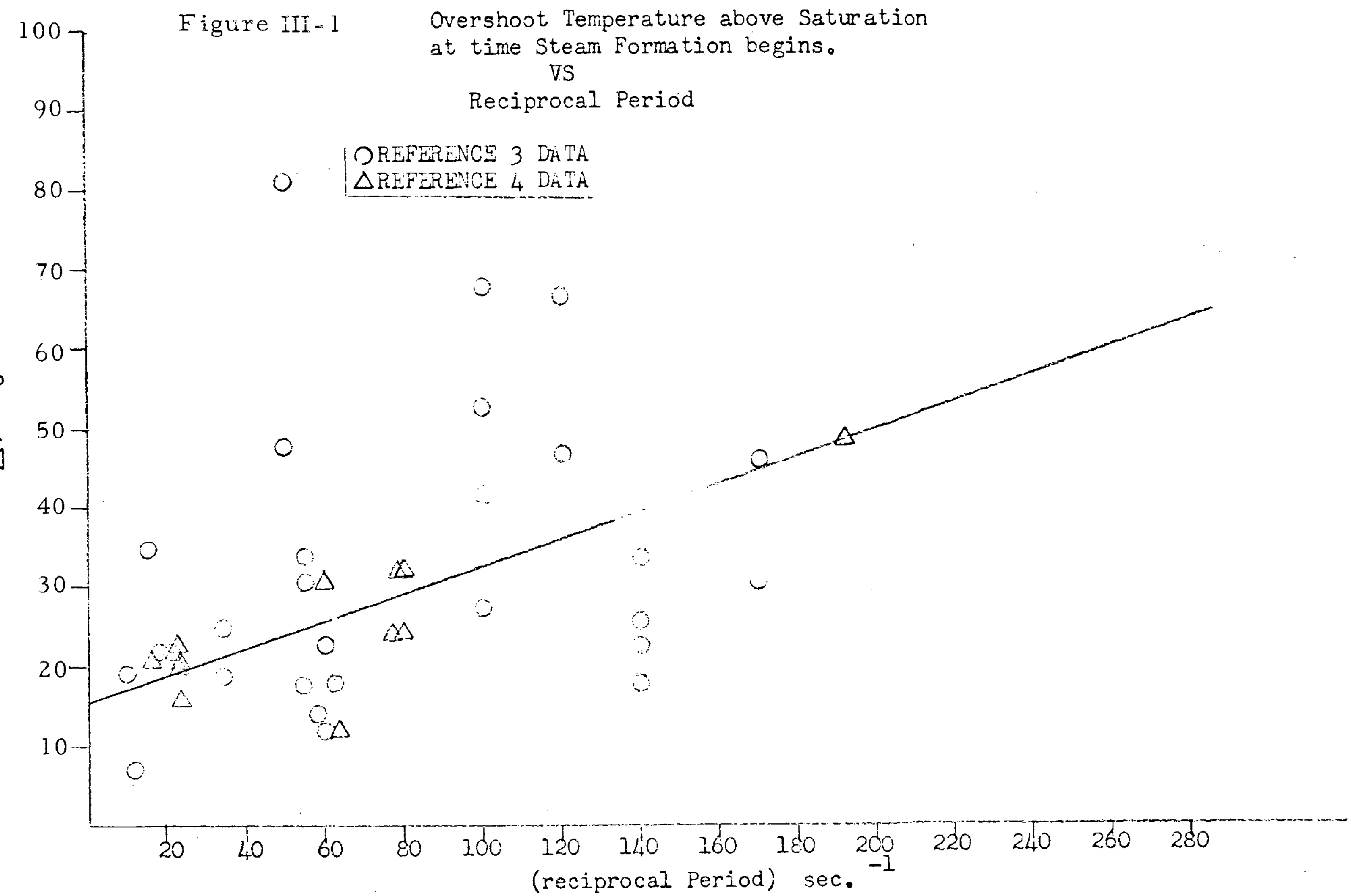

Figure III-1 Overshoot Temperature above Saturation at time Steam Formation begins. VS Reciprocal Period

Figure III-2 Delay time after plate surface reaches saturation until significant steam formation occurs

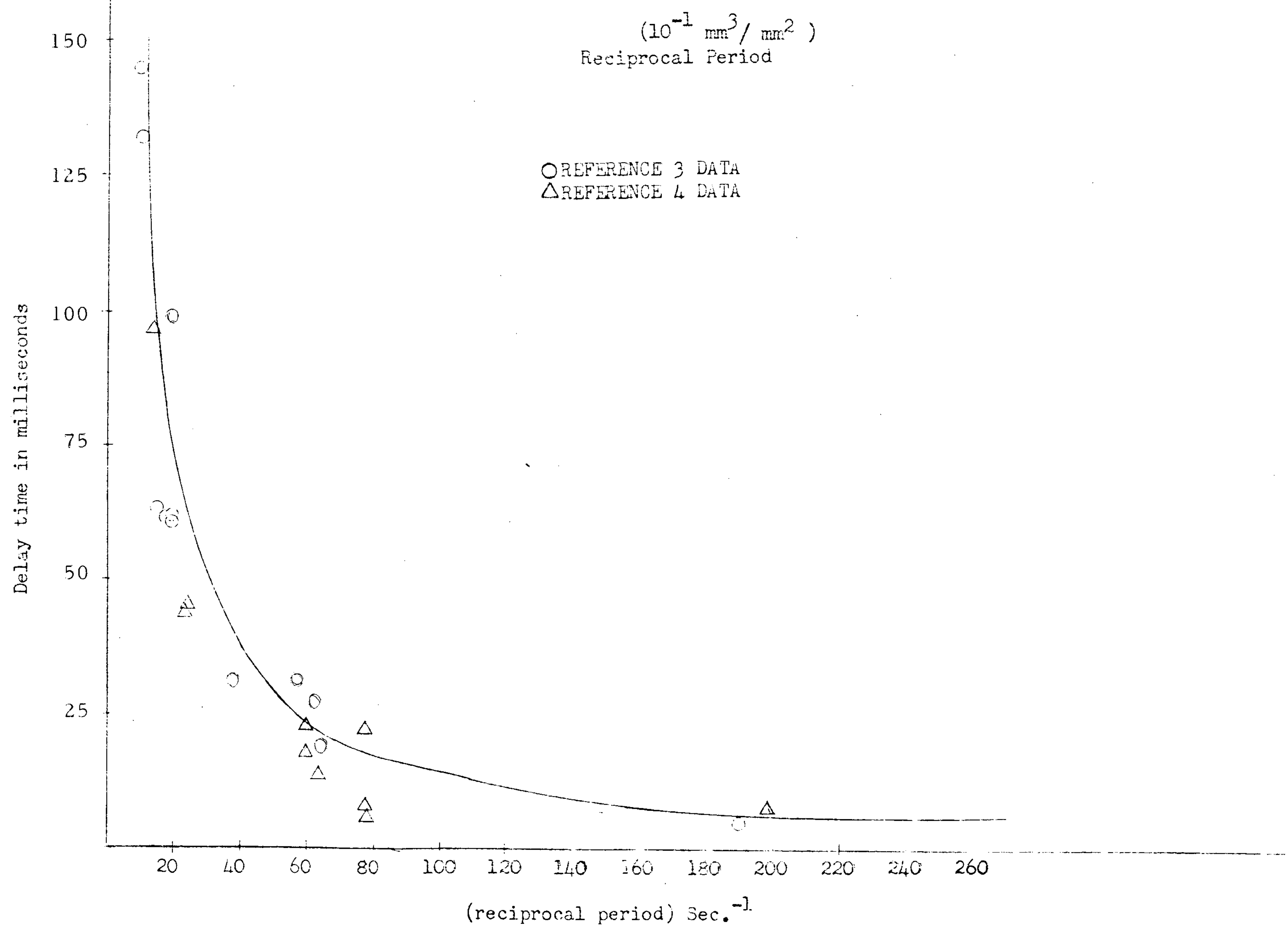

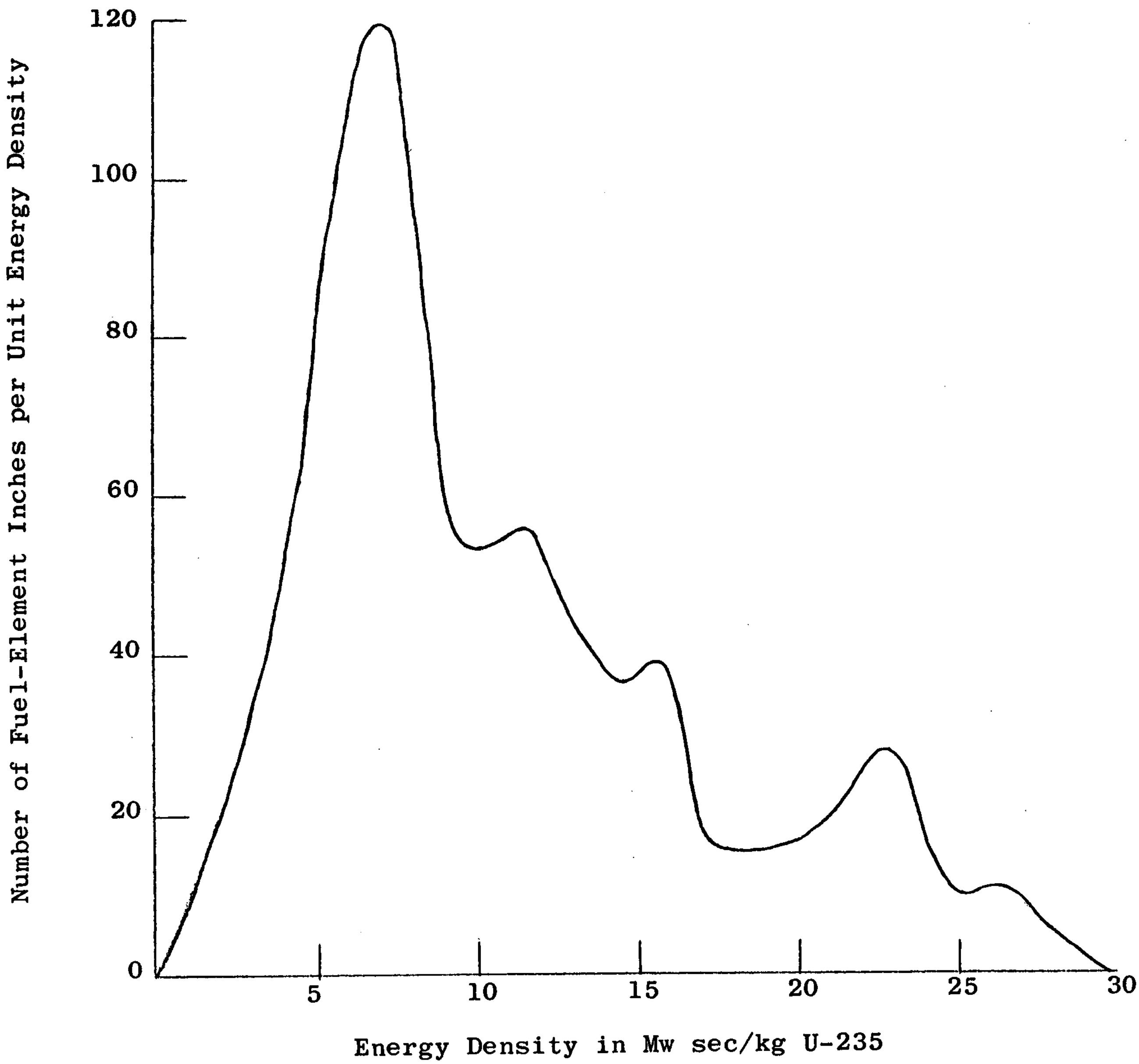

Figure III-3. Flux profile of SL-1 excursion, showing the number of fuel-element inches (longitudinal) that attained a specified unit energy density. (From Table I-XVI).

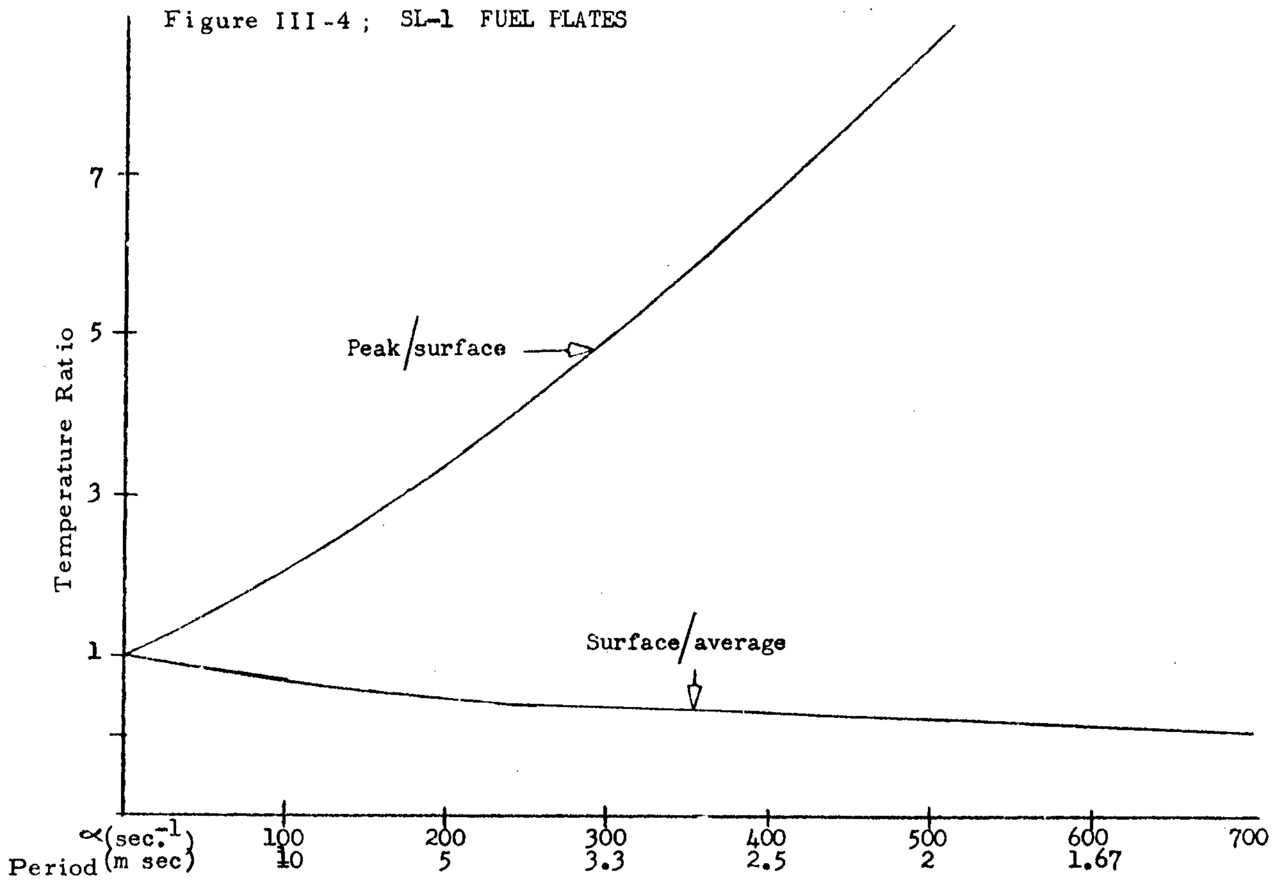
Figure III-4 ; SL-1 FUEL PLATES
Temperature Ratio
7
5
3
1
Peak/surface
Surface/average
∝(sec.⁻¹)
Period (m sec)
100
10
200
5
300
3.3
400
2.5
500
2
600
1.67
700

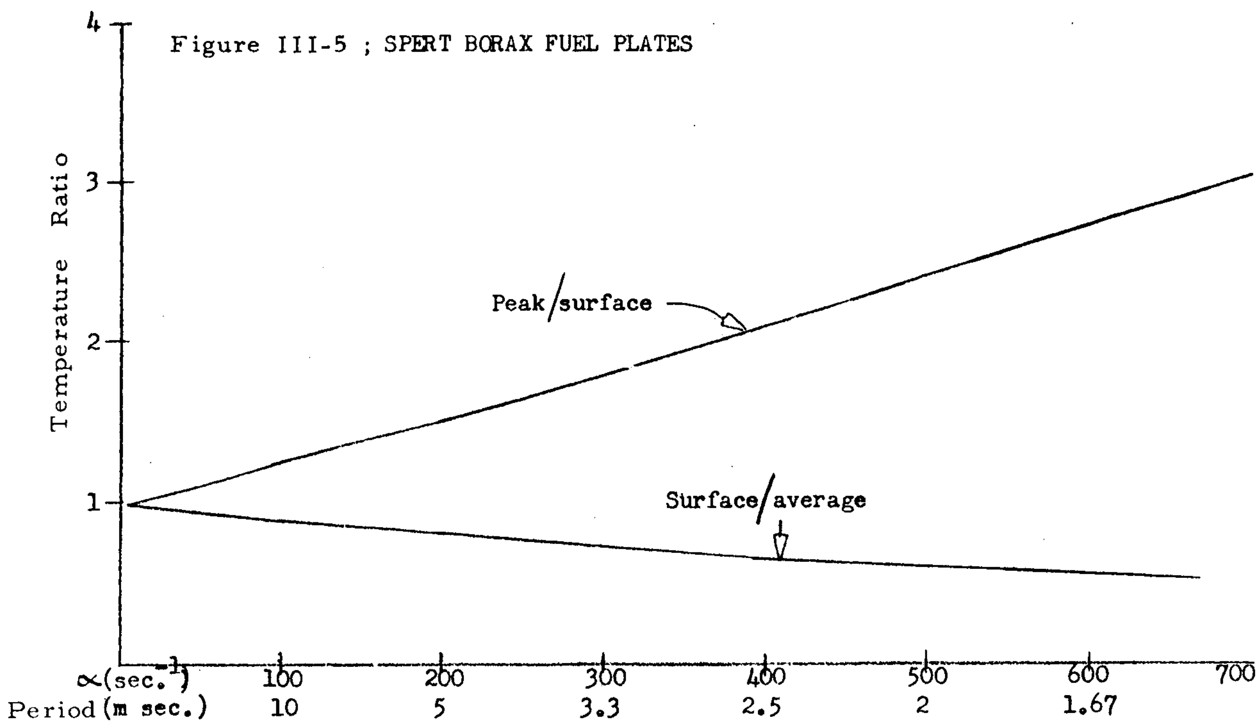
Figure III-5 ; SPERT BORAX FUEL PLATES
Temperature Ratio
4
3
2
1
Peak/surface
Surface/average
∝(sec.⁻¹)
Period (m sec.)
100
10
200
5
300
3.3
400
2.5
500
2
600
1.67
700

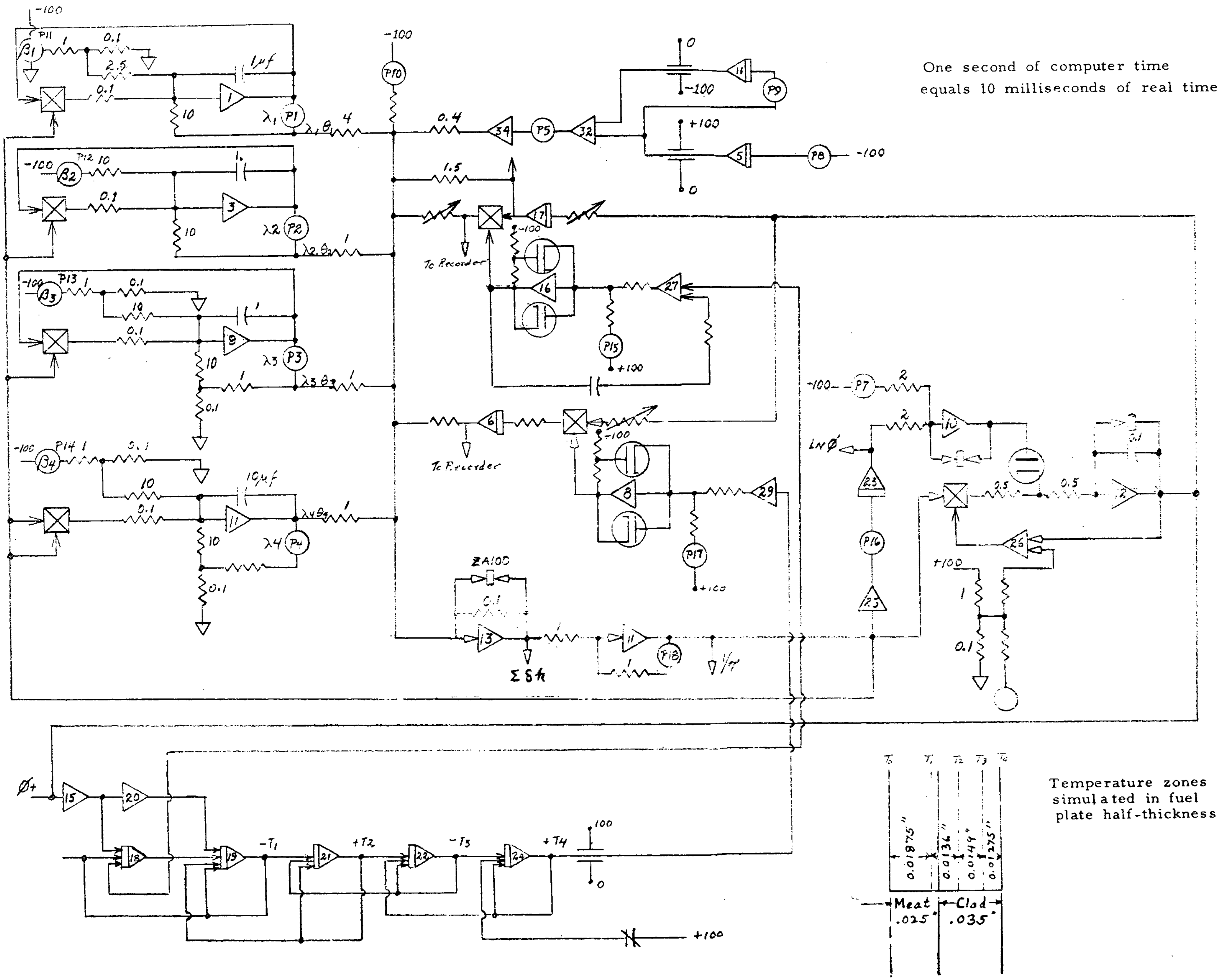

Figure III-6 Analog Computer Circuit for Logarithmic Simulation of Reactor Transients

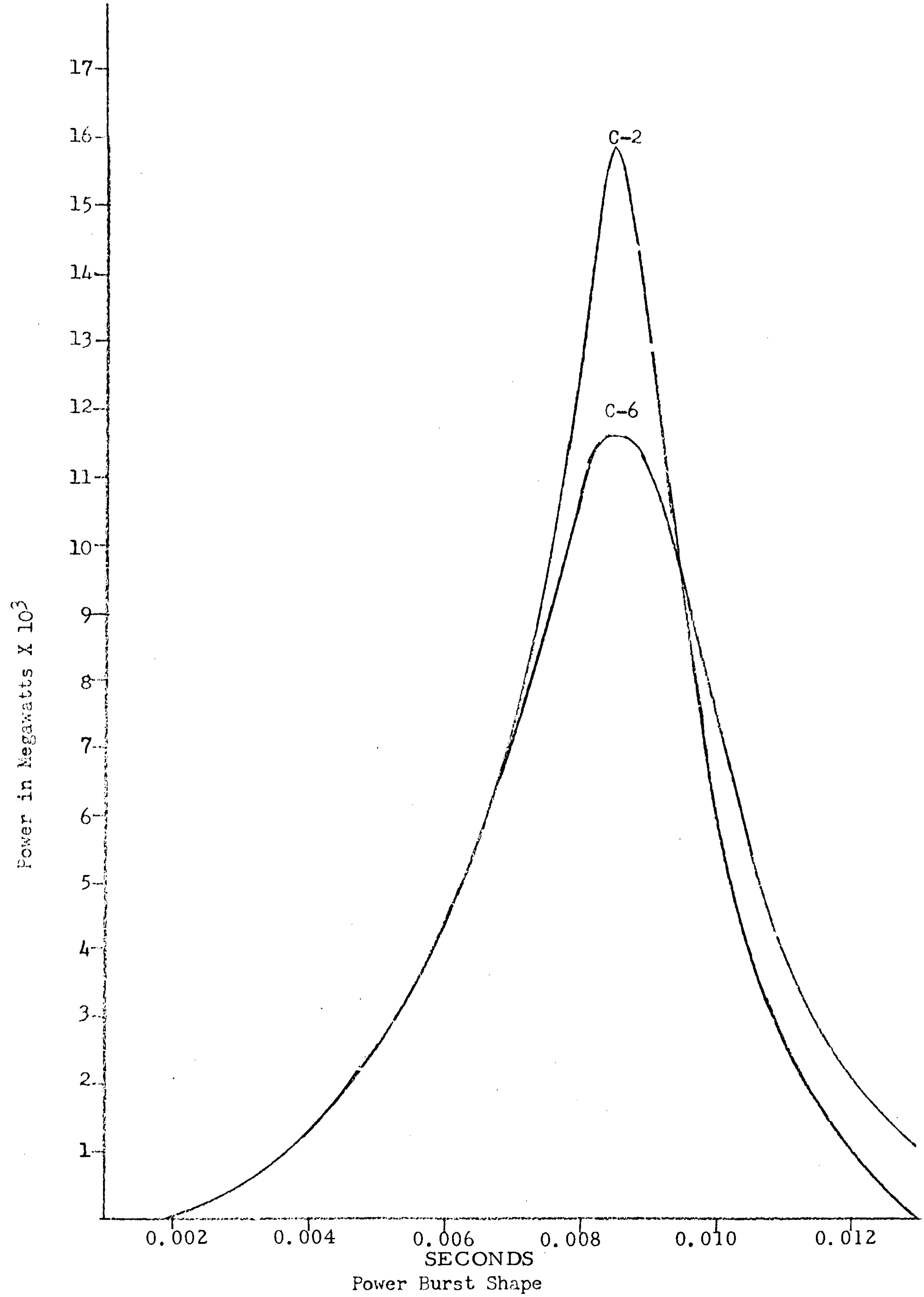

Figure III-7 Comparison of Power Burst Shapes from Analog Computer

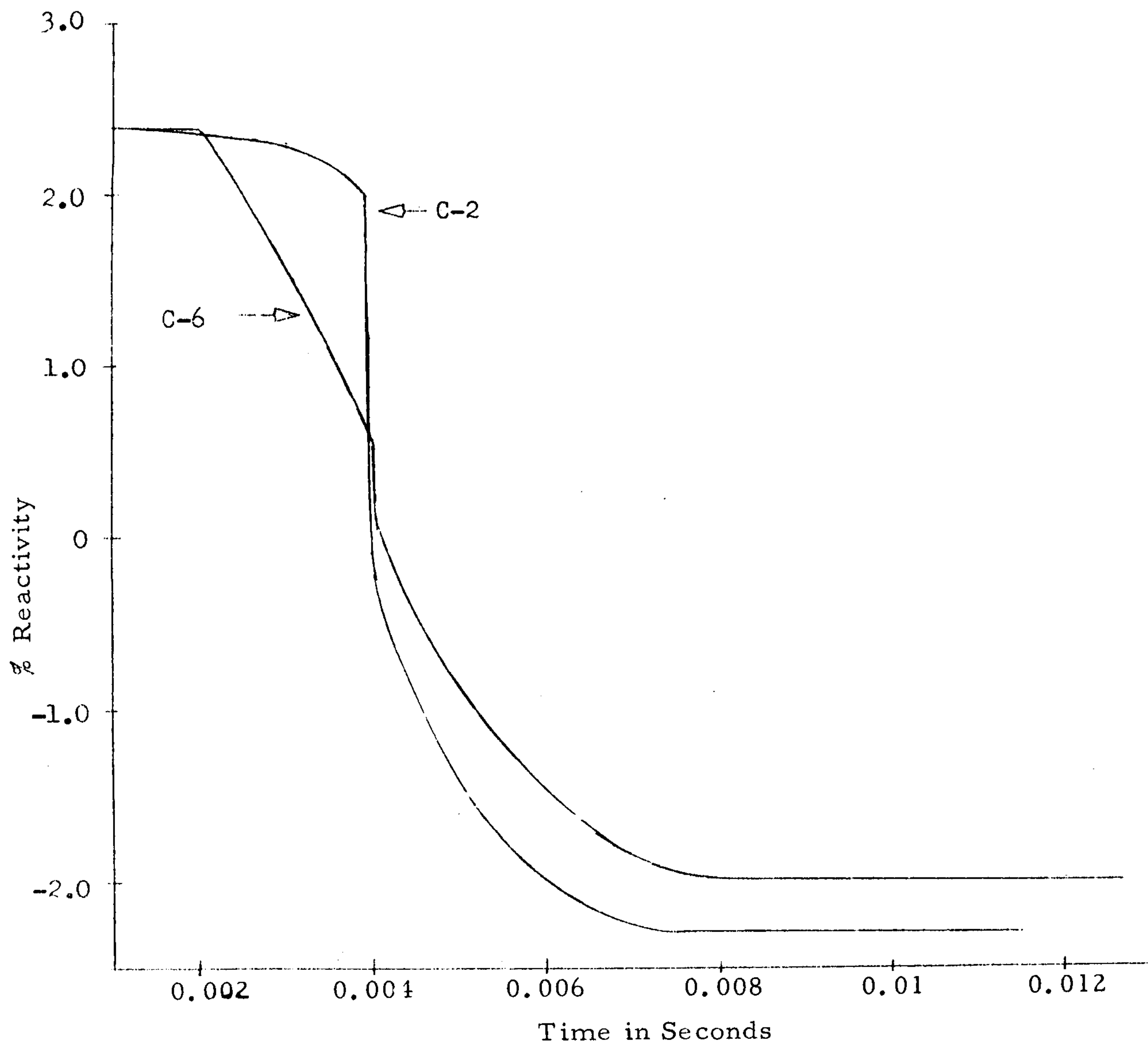

Figure III-8 Total Reactivity for Analog Computer "Excursions"

Predicted and Measured
Nuclear Energy Release vs. Period

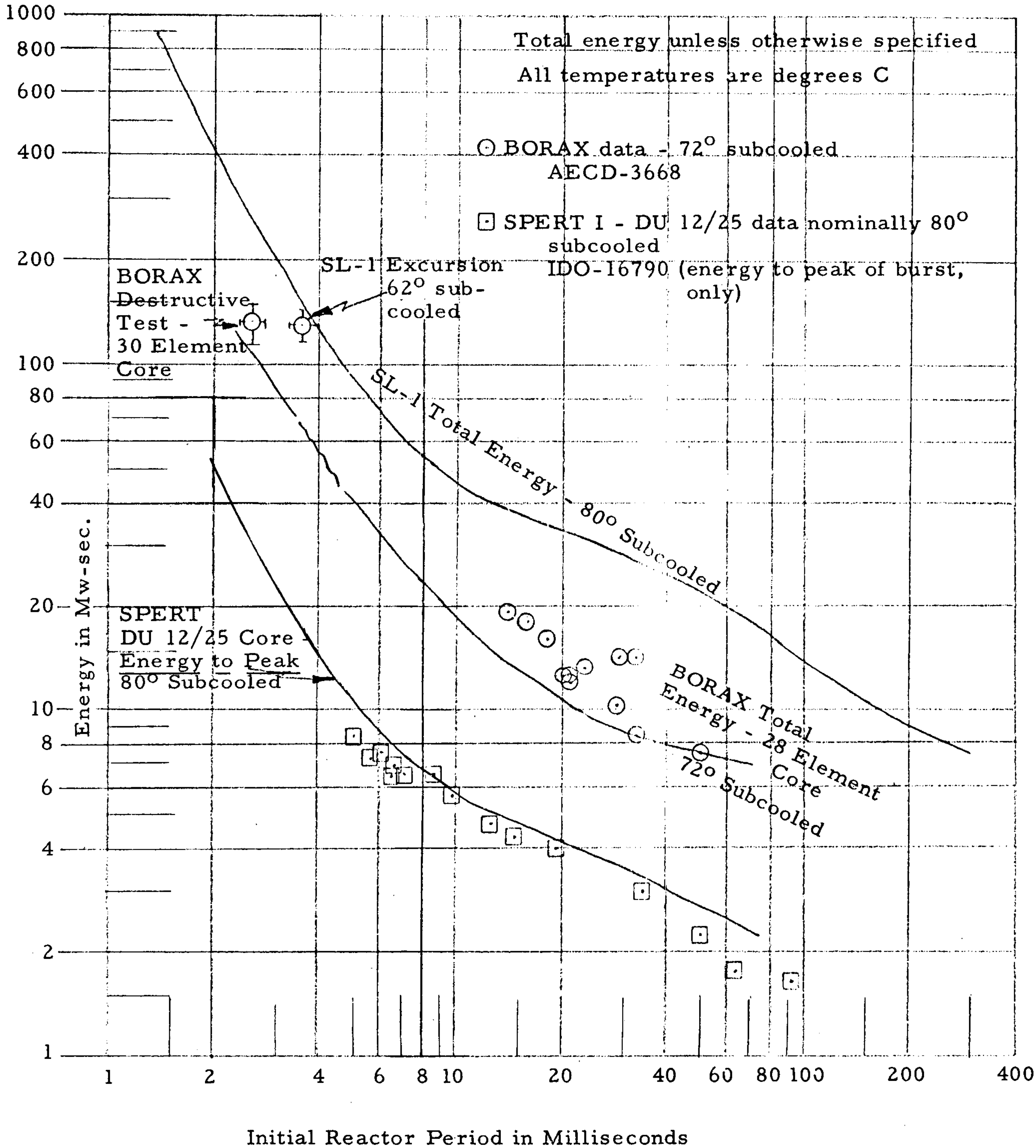

Figure III-9(a)

Predicted and Measured
Nuclear Energy Release vs. Period

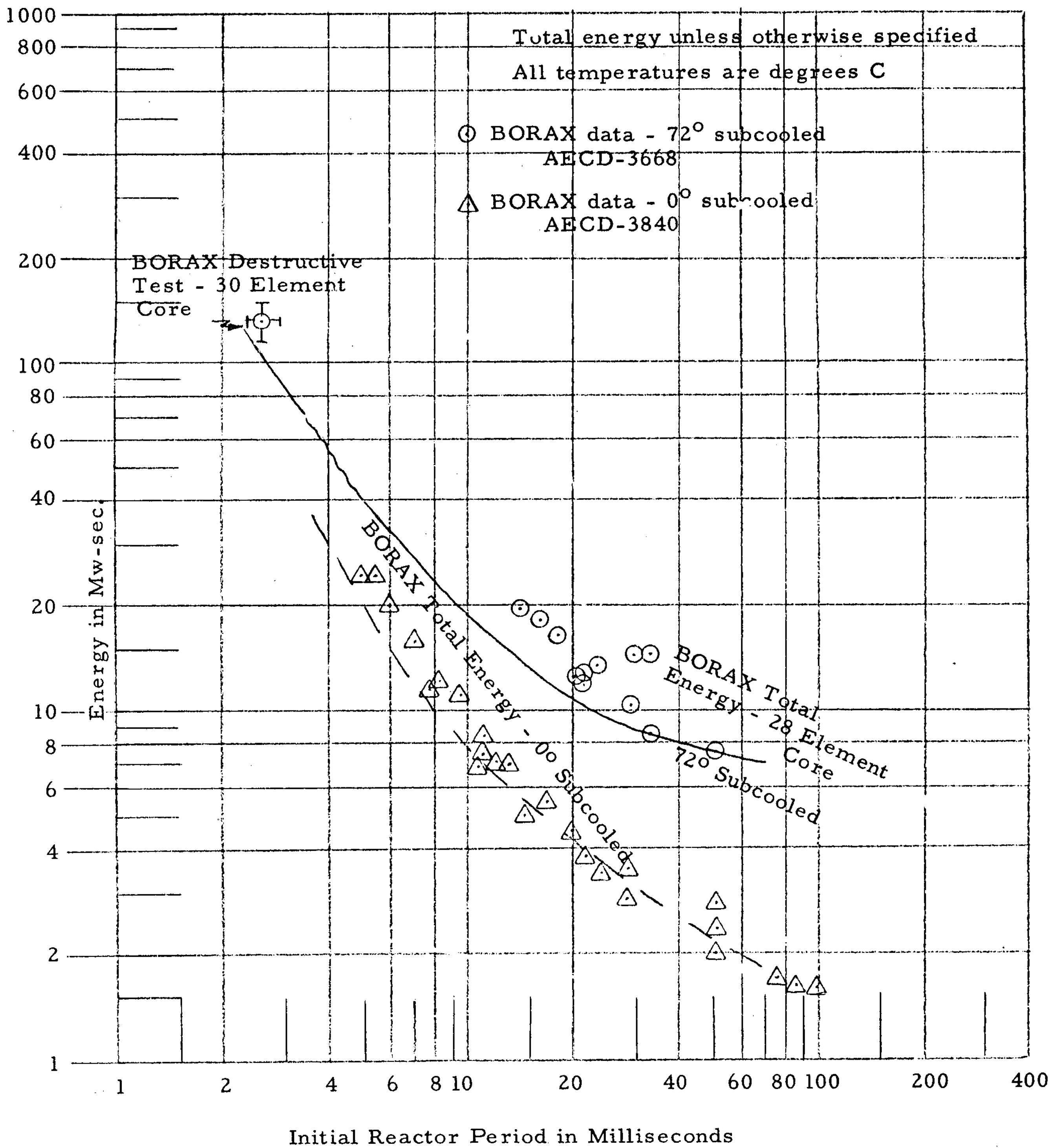

Figure III-9(b)

Predicted and Measured
Peak Power vs. Reactor Period

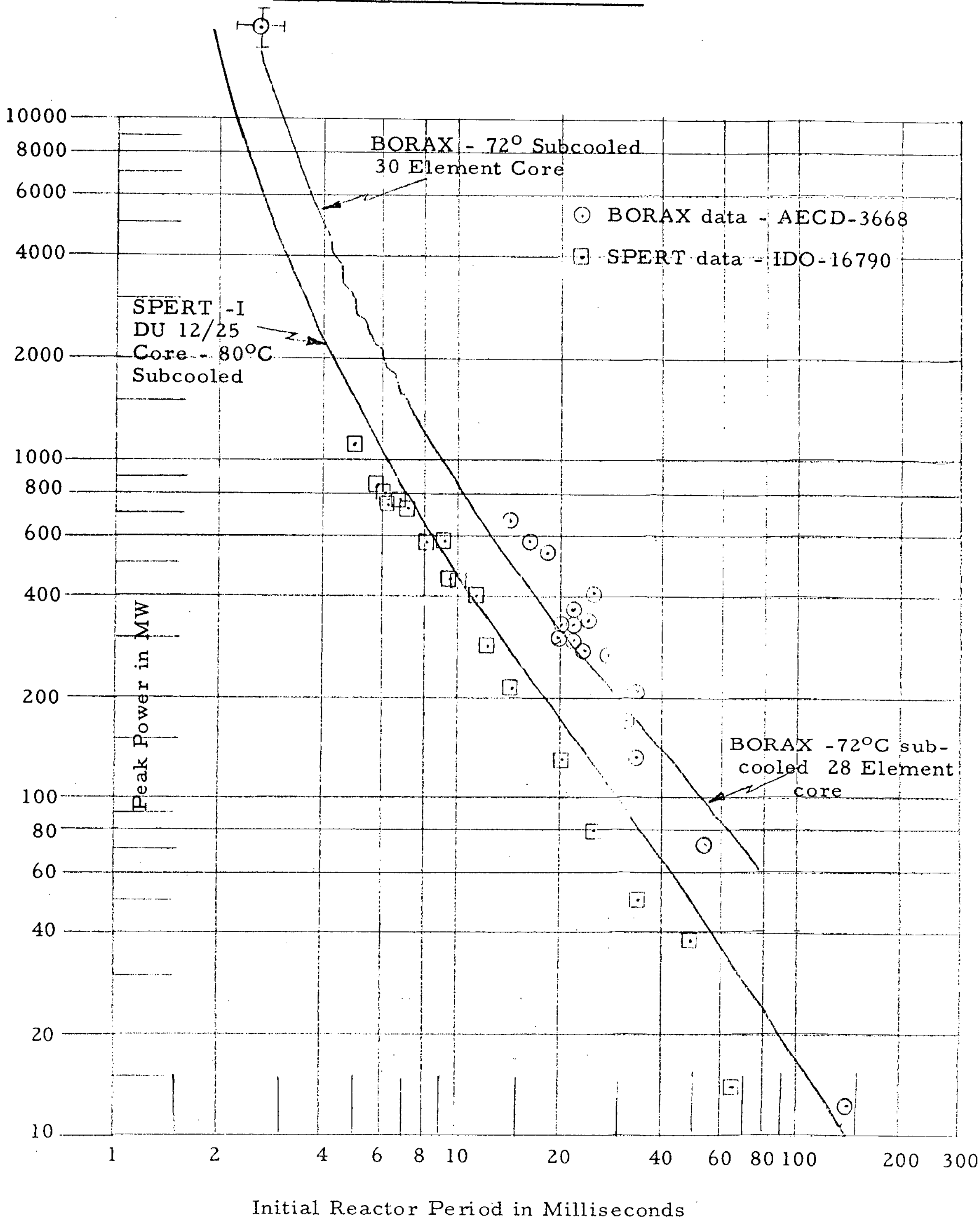

Figure III -10

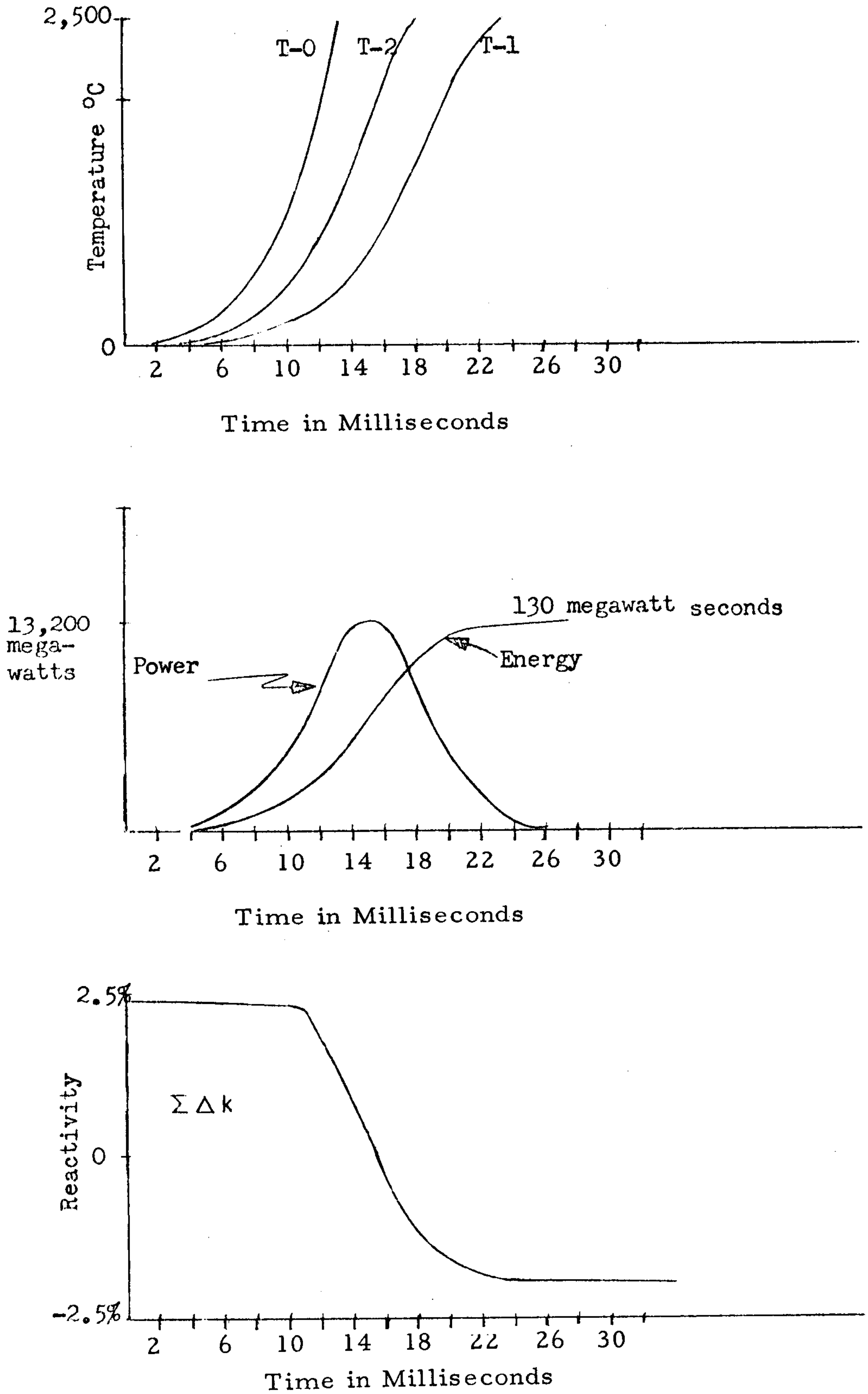

ANALOGUE TRANSIENT
RUN # A-1

Figure III-11(a) Typical Analog Computer Excursion Output
(See Table III-4)

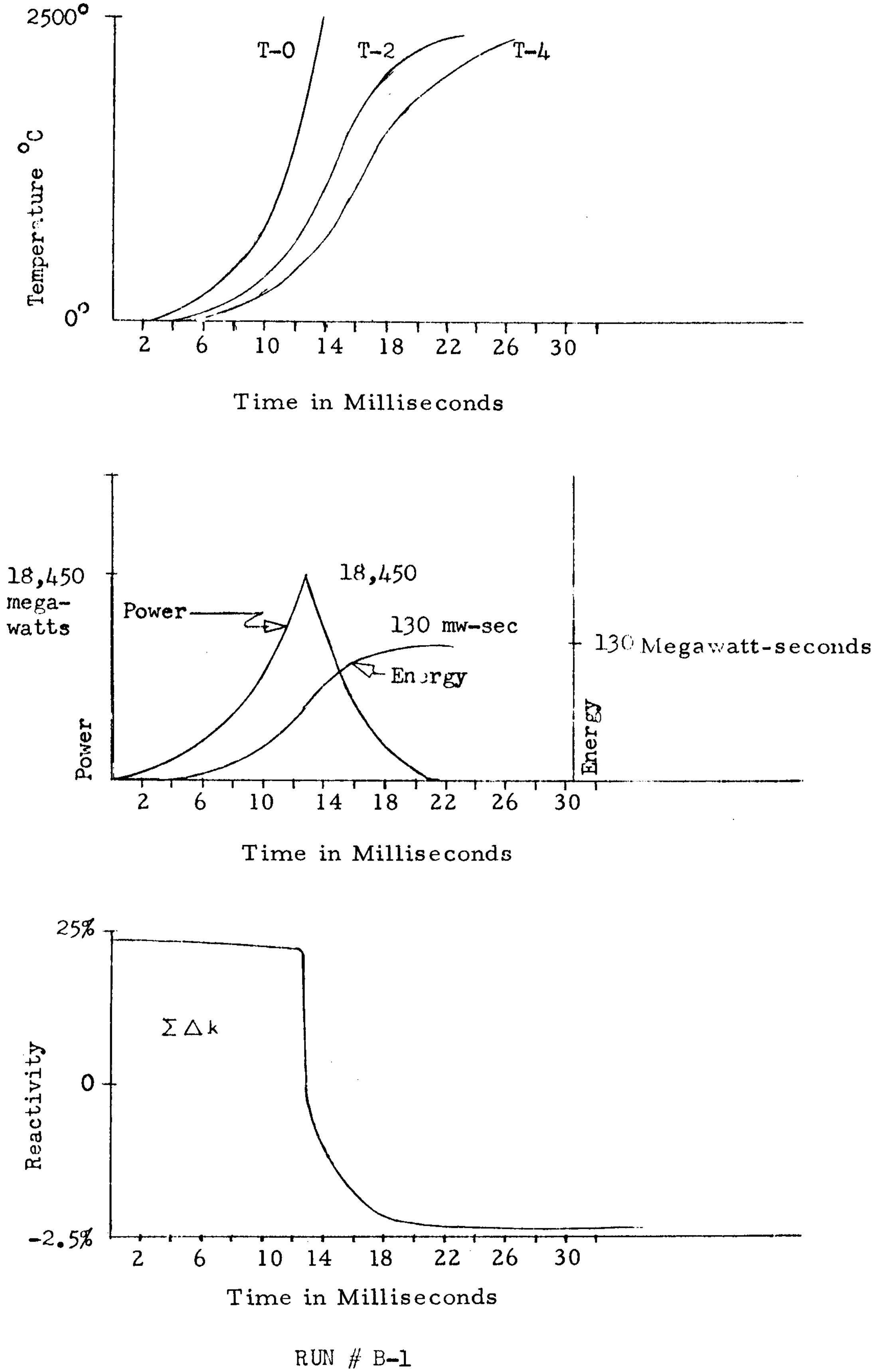

Figure III-11(b) Typical Analog Computer Excursion Output (See Table III-4)

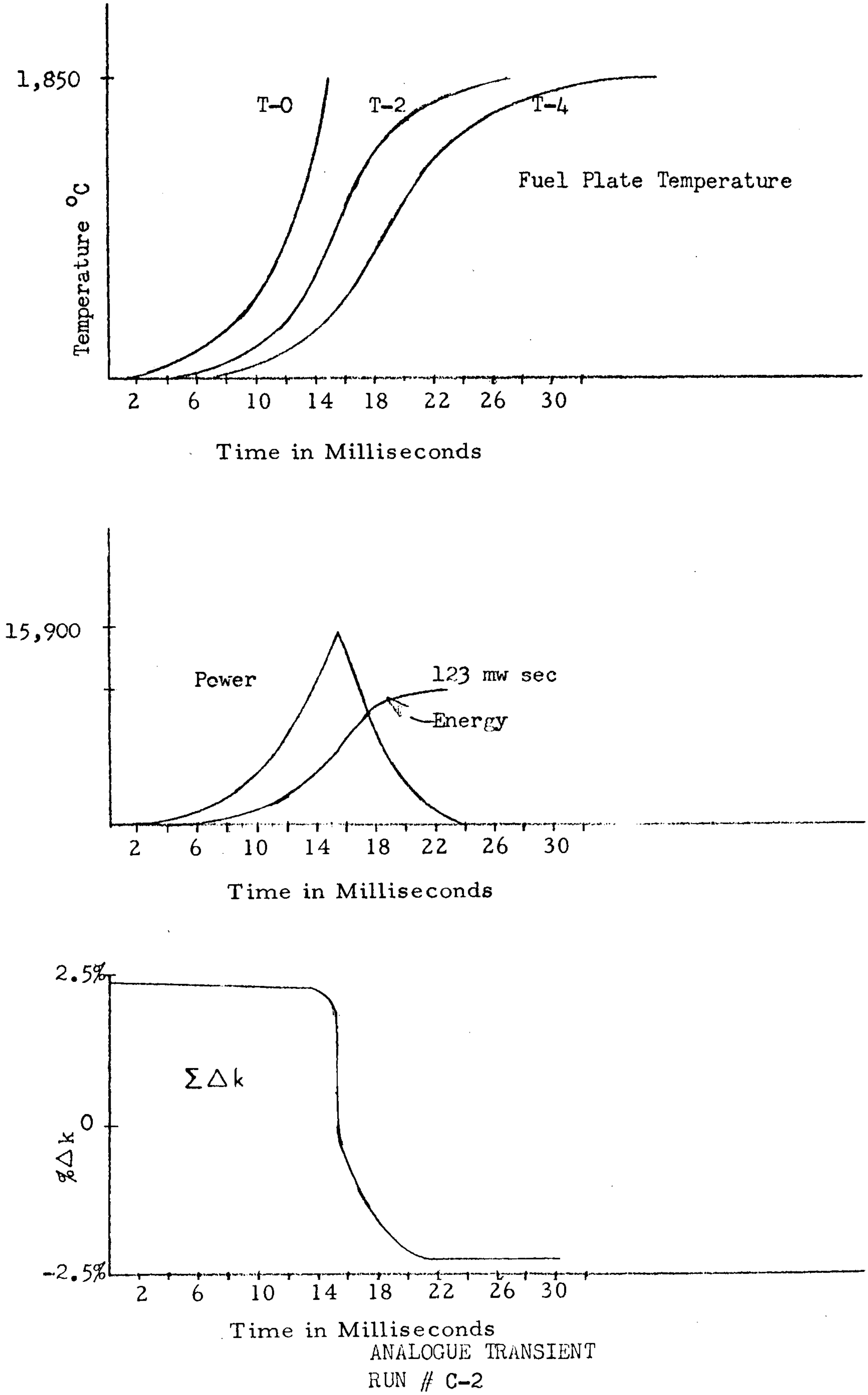

Figure III-11(c) Typical Analog Computer Excursion Output
(See Table III-4)

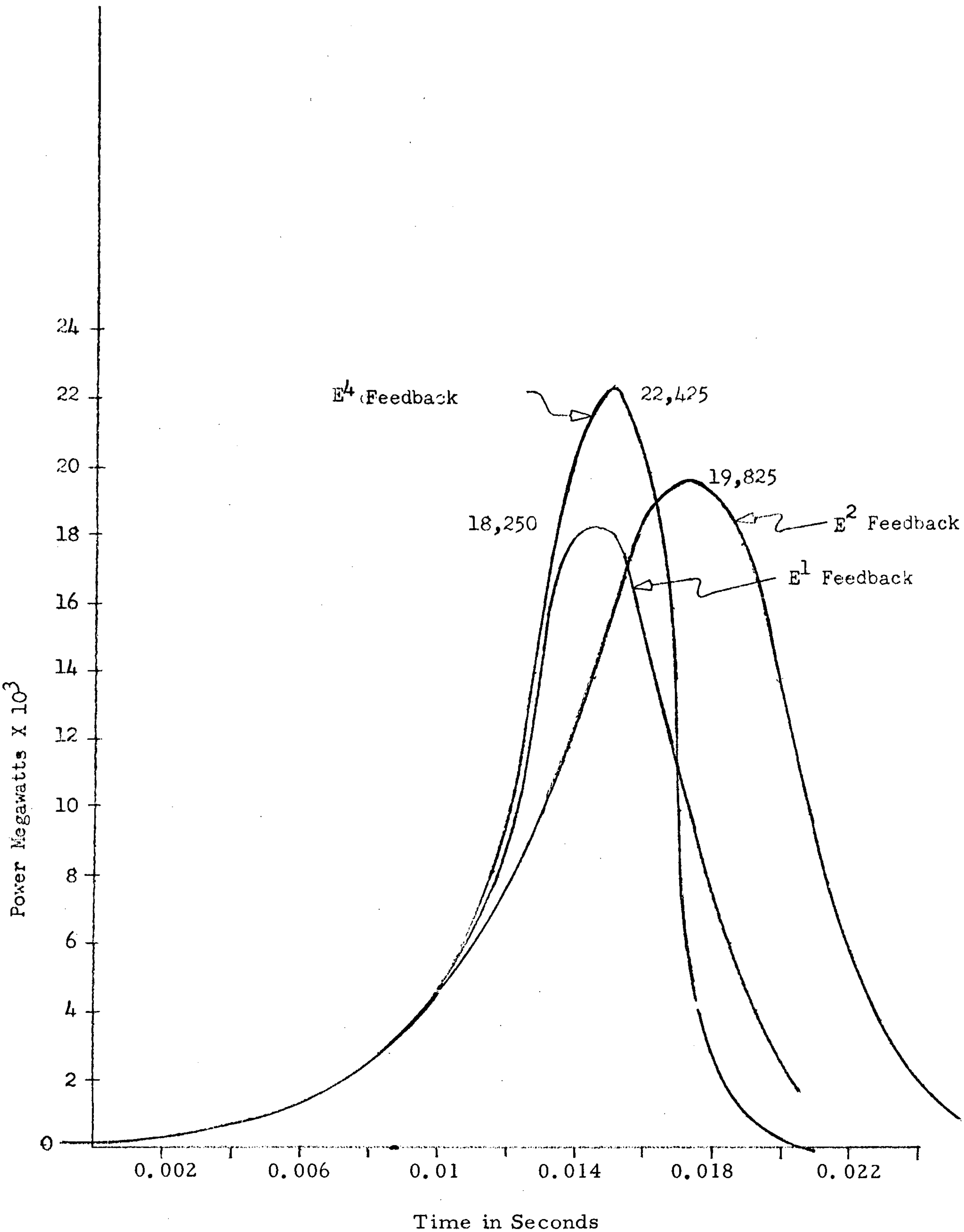

Figure III-12 Comparison of Burst Shapes for E, E^2, and E^4 Feedback

IV. IMPLICATIONS OF THE SL-1 INCIDENT ON FUTURE REACTOR PLANT DESIGN AND OPERATION

During the course of the SL-1 investigation, several areas of plant design and operation were recognized as significant contributors to either the incident itself or to the magnitude of the resulting damage. In addition, certain conditions were observed, which while not directly associated with the accident, seem worthy of comment. Although it is recognized that generalizations of this sort are frequently misleading or even dangerous, they may be of some benefit if used with discretion. This section presents a list of selected subjects for consideration together with a brief discussion of their relevancy to the SL-1.

1. Reactor Design

1.1 Single Rod Worth

Conclusive evidence revealed that the SL-1 excursion was caused by the partial withdrawal of the central control rod. The reactivity associated with the 20 inch withdrawal of this one rod has been estimated to be 2.4% $\Delta k/k$ which was sufficient to induce prompt criticality and place the reactor on a 4 millisecond period.

Except where unusual requirements preclude resonable alternatives, reactor designs should not permit criticality as the result of the movement of a single control mechanism, with all other controls in their least reactive position. When this cannot reasonably be done, justification for the design, and special operating procedures and safeguards should be prepared.

1.2 Manual Control Rod Movement

Normal maintenance of the SL-1 control rod drive systems necessitated manual movement of the control rod blades at two times during the disconnection and reconnection of the drive mechanisms. It was during the reconnection phase that the disastrous rod movement occurred. Although there was no proof that the rod movement resulted from manual force, subsequent tests established the feasibility of such an act and no evidence was seen which would suggest anything to the contrary.

To preclude the possibility of human error from becoming paramount, reactor designs should provide for mechanical restraints to manual control rod movements during normal maintanance operations. Manual movement of control rods cannot realistically be prevented throughout the life of any reactor. However, such movements should not be a part of routine maintenance. If they become necessary, operating procedures should be prepared incorporating safety precautions, strict supervision, and management approval.

1.3 Fuel Cladding

The thickness of the cladding of the SL-1 fuel elements had an important effect on the magnitude of the excursion. Because of the extremely short period, this 0.035 inch cladding became an effective thermal insulator and impeded the flow of heat to the reactor water where it could initiate shutdown of the reactor. A thinner cladding would have greatly reduced the maximum power level. Thus the effect of cladding thickness should be considered in the design of the fuel elements and in the estimation of the hazards of operation. Unfortunately, a quantitative relationship between cladding thickness and the magnitude of the excursion has not been determined at this time.

1.4 Pressure Vessel Support

The SL-1 pressure vessel is believed to have moved vertically some 9 feet during the incident. This movement resulted in the severance of all facility piping and promoted the spread of contamination. The loss of the facility piping precluded use of the boron solution injection system which was available as a backup reactivity control. Had this system been operable, and especially if it had operated automatically, it would have positively prevented any multiple or recurrent reactivity excursions. Loss of the piping connections also resulted in the loss of capability to supply water for removing after-heat, which could be extremely serious in a higher-powered reactor. Because of these effects, it is important to give serious consideration to adequate structural anchors if the possibility of a water hammer is foreseen.

1.5 Core Material Integrity

The burnable boron poison used in the SL-1 was applied in the form of boron-aluminum strips which were spot welded to the fuel elements. Prior to the accident, these strips were observed to have buckled in several areas, causing fuel element sticking, and to have corroded and otherwise deteriorated, as evidenced by core reactivity changes and direct examination. Metallographic examination of the core materials also revealed many areas of faulty welds and excessive corrosion. Although none of these problems are presumed to have had any influence on the incident itself, the progressively decreasing shutdown margin which resulted from corrosion and other losses of the poison is not in the best interests of safety. Furthermore, the buckled fuel strips and poor welds are not conducive to satisfactory reactor operation.

All materials considered for use in the core of reactors should undergo rigid quality control both during their selection and subsequent fabrication. In addition, long term environmental tests prior to reactor operation are frequently appropriate. In cases where such environmental tests are not deemed necessary to the development program, reactor materials should be periodically examined during the operating phase to reconfirm their suitability.

2. Plant Design

2.1 Plant Accessibility

SL-1 recovery operations were seriously hampered by the very limited access to the reactor floor and to the fan room located above the reactor floor. The reactor floor was located 21 feet above ground level and access consisted of one freight door and two spiral stairways. Optimum accessibility should be a standard design consideration for any future reactor plant.

2.2 Decontamination

Recovery operations at the SL-1 were continually impeded by geometries which were difficult to decontaminate. Reactor water laden with fission products was ejected from the reactor vessel during the incident and this water spread throughout the reactor building, even into the gravel used as shielding below the reactor room operating floor. Removal of radiation sources within the gravel was not completed until reactor building teardown by which time more than 15,000 cubic feet of this gravel had been removed and buried.

Consideration for adequate drains, smoothly contoured and painted surfaces, and adequate seals for inaccessible areas should not be overlooked in any reactor plant design.

2.3 Audible Warning

Because of the extremely short period of the excursion, no timely warning could have been provided for the operators. However, it is possible that the events preceding the excursion may have resulted in a somewhat gradual increase in reactivity and this would often be true in the general case. Instrumentation to provide an audible warning to nearby personnel of any increase in reactivity during all maintenance operations would be a valuable and inexpensive safeguard.

2.4 Fission Product Containment

Reactors are normally provided with several methods of fission product containment by their design. The primary device is often the cladding on the fuel elements, the secondary device is the reactor vessel and the third is a specially designed containment vessel which sometimes serves as the building structure. The SL-1 initially provided with two of these devices in the form of fuel element cladding and a reactor vessel. However, at the time of the incident, the top of the reactor vessel was partially open so that it was not very effective in retaining fission products once the fuel plates had lost their integrity.

In designing for containment, therefore, the possibility of accidents occurring during maintenance operations under incomplete containment should be considered. Similarly, hazards studies should include consideration of such situations.

Evaluation of the SL-1 accident revealed that between 5 and 15% of the fission product inventory was ejected from the reactor vessel during the excursion and yet only a fraction of 1% escaped from the reactor building. As the SL-1 reactor building was not designed as a containment vessel, it is interesting to note its effectiveness in this regard. With minor changes, its capabilities for this purpose might have been further improved. It is suggested that the plant designers might well take advantage of this observation, and consider making inexpensive improvements to conventional building structures in lieu of designing more costly total containment systems.

2.5 Emergency Plans

The need for adequate emergency supplies, records, and procedures was highlighted by the SL-1 incident. During the first few hectic hours and days following the accident, an NRTS disaster plan was in effect. The objectives of this plan were to determine the magnitude of the accident, to recover the casualties and to determine the status of the reactor with respect to future excursions. Efforts to effect these plans were initially hampered by the lack of readily available plant records and health physics supplies at the SL-1 site. For example, the first few attempts at personnel entry into the reactor building were repulsed due to lack of radiation measuring instruments of sufficient range. Also such things as clean shoe covers, coveralls, respirators and face masks were not readily available.

Reactor plants should include an emergency supply cache in the plant vicinity that is sufficiently remote from the reactor building to survive the maximum credible accident. This building should contain at least a minimum of emergency supplies such as high range radiation instruments, health physics clothing, respirators and up-to-date drawings, pictures and procedures relevant to any anticipated emergency operation.

3. Plant Operations

3.1 Reactor Operating Consoles

At the time of the SL-1 incident, three operating personnel were at the plant. All three were working near the reactor top head and were fatally injured by the blast. The reactor operating console was unmanned and very few channels of recording instrumentation were in operation. Because little is known about the time sequence of events as the reactor approached criticality, it is impossible to say whether an operator at an active operating console could have prevented the incident; probably not. However, his knowledge, together with the charts from the operating recorders would have been invaluable during the subsequent incident evaluation.

A manned reactor operating console with active nuclear and process instrumentation recorders should be considered as highly desirable during all periods of reactor maintance which involve potential changes of core reactivity, regardless of their magnitude.

3.2 Partially Filled Vessels

The water level in the SL-1 vessel was approximately 2-1/2 feet below the top head prior to the accident. This space provided room for the water piston to accelerate before it contacted the top head and manifested its energy in the form of water hammer with attendant pressures of perhaps 10,000 psi.

Had the vessel been completely filled with water at the time of the accident, it is improbable that the vessel would have been ejected upward, thereby reducing damage severity. Keeping the vessel filled with water would have also provided maximum personnel shielding and, in this case, would have been an extremely inexpensive safety precaution.

3.3 Projectile Potential

During the SL-1 incident, the five shield plugs for the control rod access nozzles were in place but not bolted down. Each of these plugs was ejected as a potentially fatal projectile. One of the plugs impaled one of the operators and the other four plugs inflicted considerable damage to the ceiling above the reactor and to equipment in the fan room. Had there been a containment vessel, the plugs might well have ruptured it and thus compromised the safety characteristics designed into the plant.

Operational procedures requiring that pressure vessel openings be covered and secured sequentially would have prevented all but one of these plugs from being ejected. Such a procedure should not be a serious operational burden and could provide an additional measure of safety. For many classes of accidents, flying objects may constitute a greater hazard to human life than the radiation.

3.4 Flux Detectors

Invaluable evidence regarding maximum power generation and power distribution within the SL-1 core was obtained from newly installed flux wires. With very little expense, similar flux monitors could be provided initially and replaced regularly in all operating reactors. Such monitors should contain materials having a fairly wide range of half lives to be fully effective.

3.5 Shutdown Conditions

Water temperatures in the SL-1 vessel were 90 to 100°F prior to the incident. Before the formation of steam could be effective as a shutdown mechanism, sufficient heat had to be transferred from the fuel elements to the water to achieve saturation temperatures in the water. The delay involved with this heat transfer is large when compared to times associated with a reactor on a 4 millisecond period, and this delay allowed extremely high fuel element temperatures - in this case sufficiently high to cause fuel vaporization. Had the core temperatures been at the water saturation condition immediately prior to the incident, the peak power attained during the excursion would probably have been reduced by a factor of ten. It is suggested that in water moderated and cooled reactors the water be maintained at nearly saturation conditions whenever other conditions permit.

3.6 Abnormal Conditions

The SL-1 had experienced a history of boron loss, fuel element sticking, and control rod sticking which were of concern to the operators of the plant and which were undergoing active investigation. Though these problems had no direct relation on the SL-1 accident, it appears in retrospect that they may have warranted plant shutdown, and that continued operation may have indicated unwise emphasis on achieving operational goals.

APPENDIX A

Sampling Procedure and Sample Designation and Identification

Fuel Plate

Samples of fuel plate were remotely cut on an air-powered shear, except in a few areas where the material was so badly burned that only a few broken fragments could be obtained. Shaded parts of the plates indicate areas of melt as seen in visual examination.

Sample designations are:

First letter, "F", indicates fuel sample
Second letter indicates type or disposition of sample, i.e.,

M - metallurgical
C - chemistry
T - tensile specimen
ANL - Argonne National Laboratories
ORNL - Oak Ridge National Laboratories

First numeral (or pair of numerals) indicates the fuel element number from which the sample was taken.
Second numeral (or pair of numerals) indicates the approximate distance in inches from the top of the fuel plate.

Example: Sample number FM52-27 designates a sample from fueled material to be mounted for metallurgical examination. The sample was cut from one of the fuel element plates 52, about 27 inches from the top of the plate.

Burnable Boron Poison Strip

All boron strip samples were cut with an air-powered shear.

Sample designations are:

First letter, "B" indicates boron sample.
Second letter indicates type, or purpose of the sample, i.e.,

M - metallurgical
C - chemistry
T - tensile specimen

First numeral is the number of the boron strip, as etched on the strip itself.
Second numeral indicates the approximate distance in inches from the top of the strip to the mid-point of the sample.

Example: Sample BM 11-3 is a boron sample cut from strip 11 for metallurgical sample preparation. The mid-point of the sample is about 3 inches from the top of the strip.

Special Fuel Plate Tensile Specimen Punch

A special shear was designed and fabricated to shear tensile specimens from aluminum shroud, fuel plate, boron strip and cadmium blades with a minimum expenditure of hot cell man hours and minimum contamination.

A ball bearing die set with 4x8 inch die space, 1-1/4 and 1-1/2 inch thick punch and die holder respectively, and 1 inch posts, was used to mount the punch and die as shown in Figure I-75. The main features of the shear are as follows:

1. Spring loaded die ejector to keep specimen flat during shearing and eject sheared specimen from die, Figures I-75 and I-76.

2. Shear angle of die of 1/8 inch in 5-1/2 inch, Figure I-79.

3. Die opening action and punch stripping force is provided by springs in the die set, Figure I-77.

4. Designed so that any press or tensile testing machine can be used to provide shearing force on die set, Figure I-78.

5. Punch to die clearance of .007 inches for use up to 1/8 inch thick aluminum base metal samples.

6. Dowel pin alignment permits disassembly of individual components, sharpening of punch and die, and replacement of parts as required.

The tensile specimen shear performed satisfactorily in all aspects. Punch to die clearance of .010 inches was found to be excessive during operation in that a heavy flash was generated which prevented ejection of the sheared specimen. For aluminum type specimens up to 1/8 inch thick clearance of .005 inches is recommended.

Force required for shearing 1/8 inch thick aluminum fuel plate was about 15,000 pounds. This includes the force to compress all the springs in the shear (about 1600 pounds).

Cadmium Control Blades

The control blade samples were generally cut into strips with a large abrasive wheel, using water coolant. Metallurgical and chemical samples were then cut from the strips with an air-powered shear. Each pair of metallurgical samples was cut so that one sample included either an edge weld or a center spot-weld.

Sample designations are:

First letter, "C", indicates cadmium sample.
First numeral indicates the number of the control blade from which the sample was taken.
Second letter indicates type (or purpose) of sample, i.e.,

M - metallurgical
C - chemistry
T - tensile specimen

Second numeral indicates the approximate distance in inches from the top of the cadmium strip to the mid-point of the sample.

Example: Sample C9C-18 is a cadmium sample cut from control blade 9 for chemical determination of cadmium burnup. The midpoint of the sample was 18 inches from the upper edge of the cadmium strip.

Sections of control blade are designated by the numbers of the fuel elements on each side of the control blade section. Section 10-41 lies between cartridges 10 and 41.

Aluminum Shroud

Sampling the shrouds at the exact positions outlined in the schedule was not possible because of the location of the weep-holes. Sample designations are:

First letter, "S", indicates shroud material.
First numeral indicates the number of the shroud from which the sample was taken.
Second letter indicates the type, or purpose, of the sample, i.e.,

M - metallurgical
C - chemistry
T - tensile specimen

Second numeral indicates the approximate distance in inches from the top of the shroud to the midpoint of the sample.

Sections of shroud are designated by hyphenated numbers of fuel cartridges between which the shroud section was sandwiched.

Example: Section 47-52 of shroud 7 is that section of shroud which lay between cartridges 47 and 52 in the reactor.

APPENDIX B

SL-1 Reactor Debris Chemicals for Fusion Samples

Samples of the SL-1 reactor debris were extremely difficult to dissolve. Three fusion fluxes were tried each on about 10 gram samples of fine screenings:

1.	$K_2S_2O_8$	5:1	at	1000° C.
2.	Na_2CO_3	3:1	at	1200° C.
3.	NaOH	3:1	at	500° C.

The above conditions were tried on samples of medium and coarse screening samples with better results than on fine samples. The best flux proved to be NaOH.

Samples were reacted with fused NaOH at about 500° C for 15-30 minutes in platinum dishes. The melt was cooled, dissolved in water or dilute HCl and made up to a standard volume of 1000 ml or 2000 ml. with dilute HCl.

Aliquots of these solutions were taken for further dilution and fission product separations.

APPENDIX C

Logarithmic Simulation of Reactor Transient

The simulation used for the SL-1 reactor was developed* as shown below. The differential equations defining the time behavior of a reactor are given in equation (1) and (2) below. (The symbols are those used in Shultz, M.N. - Control of Nuclear Reactor Power Plants.)

(1) $$\frac{dn}{dt} = \left(\frac{\delta k - \beta}{\ell}\right) n + \sum_i \lambda_i C_i + S$$

(2) $$\frac{dC_i}{dt} = \frac{\beta_i n}{\ell} - \lambda_i C_i$$

Dividing both (1) and (2) by n produces:

(3) $$\frac{1}{n} \frac{dn}{dt} = \frac{\delta k - \beta}{\ell} + \sum_i \frac{\lambda_i C_i}{n} + \frac{S}{n}$$

(4) $$\frac{1}{n} \frac{dC_i}{dt} = \frac{\beta_i}{\ell} - \frac{\lambda_i C_i}{n}$$

If the following change in variables is used:

$$\alpha = \text{inverse period} = \frac{1}{n} \frac{dn}{dt}$$

$$\theta_i = \frac{C_i}{n}$$

and

$$S^1 = \frac{S}{n}$$

equation (3) becomes:

(5) $$\alpha = \frac{\delta k - \beta}{\ell} + \sum_i \lambda_i \theta_i + S^1$$

* Private communication from G. E. Gorker, General Electric Co., Cincinnati, Ohio

Furthermore,

(6) $$\frac{1}{n}\frac{dC_i}{dt} = \frac{d}{dt}\left(\frac{C_i}{n}\right) + \frac{C_i}{n}\left(\frac{1}{n}\frac{dn}{dt}\right) = \frac{d\Theta_i}{dt} + \frac{\Theta_i}{\tau}$$

Equating the right hand members of equations (4) and (6) and rearranging terms produces:

(6a) $$\frac{d\Theta_i}{dt} = \frac{\beta i}{\ell} - \Theta_i(\alpha + \lambda_i)$$

The last consideration is the source term.

Since $\frac{dS^1}{dt} = S\frac{d(\frac{1}{n})}{dt}$ for a constant source.

Then

(7) $$\frac{dS^1}{dt} = -\alpha S^1$$

and $\alpha = \frac{1}{n}\frac{dn}{dt} = \frac{d(\ln n)}{dt}$, or

(8) $$\ln\frac{n}{n_o} = \int \alpha\, dt$$

where n_o = initial power level.

Multiplying equation (5) and (6a) through by ℓ produces equations (9) and (10) which are used to program the analog simulator.

(9) $$\alpha\ell = \delta k - \beta + \sum \ell\lambda_i\Theta_i + \ell S^1$$

(10) $$\frac{d(\ell\Theta_i)}{dt} = \beta i - \ell\Theta_i(\lambda_i + \alpha)$$

APPENDIX D

Sample Calculations of Excursion Energy

This appendix contains some sample calculations of excursion energy for certain typical excursions of SL-1, SPERT, and BORAX. The results of similar calculations over the entire spectrum of initial period are shown in Figures III-9 and III-10. The equations referred to are in Section III-6.

(A) SPERT DU 12/25, 5 m sec period, 80°C subcooled

$$K \text{ excess} = 1.87\% \ \Delta K$$

$$\frac{\text{Average plate temperature}}{\text{Plate surface temperature}} = 1.22$$

$$\frac{\text{Peak flux}}{\text{Average flux}} = 2.4$$

(1) Energy to commencement of steam formation:

4 millisecond overshoot for peak flux region surface temperature gives:

$80 \, e^{4/5} = 178\,°C$ peak surface temperature

ΔT (average for reactor plates) $= \dfrac{178}{2.4} \times 1.22 = 90.5\,°C$.

When boiling commences:

Energy in plates = 4.5 Mw-sec; Total energy $= \dfrac{4.5}{0.86} = 5.2$ Mw-sec

Power $\approx \dfrac{5.2}{5 \times 10^{-3}} = 1040$ Mw

(2) Energy from time steam begins to form to peak of excursion:

Initial prompt K excess = 1.17% ΔK,

of which about 0.12% will be compensated by expansion at 1040 Mw (5.2 Mw-sec), leaving 1.05% ΔK to be compensated by steam.

For average void coefficient $6 \times 10^{-4}\%/cm^3$ for this large quantity of steam,

$$\frac{1.05\%}{6 \times 10^{-4}\%/cm^3} \times \frac{10^3 \ mm^3/cm^3}{10^{-1} \ mm^3/mm^2} = 18 \times 10^6 \ mm^2$$

of plate area must have steam at density of $10^{-1} \ mm^3/mm^2$.

This is 66% of reactor area. This amount of reactor plate area would be producing steam about 5 to 8 m sec after initial steam formation. But, 6.6% of reactor area would be producing steam about 1 m sec after initial steam, and this would grow to a density of $1 \ mm^3/mm^2$ in about 3 m sec, to give the required steam void.

Thus, with a total approximate time delay of 4 m sec to the peak of the burst, equation (5a) gives

$$1040 \text{ Mw} = n_o \exp^{-}\left[\frac{1.05 \times 10^{-2} \times 4 \times 10^{-3}}{2 \times 5.7 \times 10^{-5}}\right] = n_o e^{-0.47} = 0.69 \ n_o$$

$$n_o = 1510 \text{ Mw}$$

Equation (6) gives, for the energy

$$E = 1510\sqrt{\frac{2\pi \times 5.7 \times 10^{-5} \times 4 \times 10^{-3}}{1.05 \times 10^{-2}}} \left[\text{erf}X\right]$$

where erfX = 0.305, giving

$$E = 5.3 \text{ Mw-sec}$$

Summing the results of (1) and (2) gives the energy to the peak of the burst of 10.5 Mw-sec, with a peak power of 1510 Mw.

(3) Energy after peak of burst.

Doubling the amount of steam will take a little less than 0.3 initial-periods, or about 2.5 m sec.

Using equation (8),

$$E_{back} = 1510 \times 1/2\sqrt{\frac{2\pi \times 5.7 \times 10^{-5} \times 2.5 \times 10^{-3}}{1.05 \times 10^{-2}}}$$

$$= 1510 \times 1/2 \times 9.23 \times 10^{-3} = 7.0 \text{ Mw-sec.}$$

Thus, the total energy of the excursion is 17.5 Mw-sec, and the

$$\frac{\text{Energy at peak}}{\text{Total Energy}} = 0.60$$

(B) BORAX 2.6 m sec excursion, 30 element core, 80°C subcooled.

K excess = 3.20% ΔK

$$\frac{\text{Average plate temperature}}{\text{Plate surface temperature}} = 1.47$$

$$\frac{\text{Plate center temperature}}{\text{Plate surface temperature}} = 2.06$$

$$\frac{\text{Peak flux}}{\text{Average flux}} = 2.1 \text{ (assumed)}$$

(1) Energy until steam formation begins:

4 m sec overshoot gives peak surface temperature of

$80\ e^{(4/2.6)} = 372°C$

and average plate temperature of $\frac{372}{2.1}\ 1.47 = 260°C$

Energy in plates = 25.5 Mw sec. Total energy = 29.7 Mw sec.

$$\text{Power} = \frac{29.7}{2.6 \times 10^{-3}} = 11,400 \text{ Mw}.$$

(2) Energy to peak of excursion

Initial prompt K excess = 2.5% ΔK, of which about 2.3% ΔK must be compensated by steam.

With a void coefficient of $4 \times 10^{-4}\% \ \Delta K/cm^3$ and a void density of $10^{-1}\ mm^3/mm^2$, $60 \times 10^4\ cm^2$ or 120% of the core plate area must be covered with steam.

However, only 12% of the core at a steam density of 1 mm^3/mm^2 is required.

It will require about 1.0 m sec after initial steam formation until 12% of the core is producing steam, and an additional 1.6 m sec for the steam to develop to 1 mm^3/mm^2 density.

With a 2.6 m sec delay, the peak power is (equation (3))

$$11,400 = n_o \exp -\frac{2.3 \times 10^{-2} \times 2.6 \times 10^{-3}}{2 \times 6.5 \times 10^{-5}} = n_o\ e^{-0.46} = 0.631\ n_o$$

n_o = 18,100 Mw

Energy from commencement of steam formation to the peak of the excursion:

$$E = 18,100\sqrt{\frac{2\pi \times 6.5 \times 10^{-5} \times 2.6 \times 10^{-3}}{2.3 \times 10^{-2}}} \quad \text{erf}X$$

where erfX = 0.317

E = 39.0 Mw sec

Total energy to peak of excursion = 69 Mw sec

(Note: Had the energy increase continued on a 2.6 m sec exponential, the peak temperatures in the center of the plates would have been 1810°C, well below the effective vaporization temperature of 2040 + 310°C.)

(3) Energy after peak of burst

About 0.6 initial periods, or 1.6 m sec will elapse while the steam void is doubling.

$$E_{back} = 18,100 \times 1/2\sqrt{\frac{2\pi \times 6.5 \times 10^{-5} \times 1.6 \times 10^{-3}}{2.3 \times 10^{-2}}} = 48 \text{ Mw sec}$$

Total energy of excursion = 117 Mw sec with a peak power of 18,100 Mw. The 72° subcooled case yields 105 Mw sec.

(C) SL-1 3.6 m sec initial excursion, 2.4% ΔK, 1.7% ΔK prompt excess, 80°C subcooled, incident core

$$\frac{\text{Average Plate Temperature}}{\text{Plate Surface Temperature}} = 2.6$$

$$\frac{\text{Plate Center Temperature}}{\text{Plate Surface Temperature}} = 4.6$$

$$\frac{\text{Peak Flux}}{\text{Average Flux}} = 2.9$$

4 m sec overshoot beyond saturation temperature for peak plate surface temperature yields 243°C at peak flux region on the surface and 1118°C at the center of the plate. The average plate temperature throughout the core is 218°C.

Energy deposited in plates is 36.2 Mw sec giving a total energy of 42.1 Mw sec of nuclear energy at a power of 11,300 Mw.

This energy creates plate and water expansion which compensates for about 0.13% ΔK leaving the reactor on a 3.9 m sec period.

1.57% ΔK must be compensated by steam formation (or plate explosion), requiring

$$\frac{1.57\%}{1 \times 10^{-4}\%/\text{cm}^3} \times \frac{10^3\ \text{mm}^3/\text{cm}^3}{10^{-1}\ \text{mm}^3/\text{mm}^2} = 1.57 \times 10^8\ \text{mm}^2 \text{ which is four}$$

times the actual core area.

Refering to Figure III-3, it can be observed that even at 1 mm^3/mm^2, 42% of the core area must be covered with steam, which will occur after about 4 m sec (for steam to occur over 42% of the core) plus 2.4 m sec (for the initial steam to develop to the density of 1 mm^3/mm^2). Thus approximately 6 m sec delay will occur before sufficient steam is formed to terminate the excursion.

But, on a continuing 3.9 m sec exponential, vaporization (2040 + 310°C) will be reached in 2.9 m sec. Even with the compensation due to steam, vaporization should be attained in about 4 m sec, at which time the power rise will be terminated.

From equation (3), for a 4 m sec delay to the peak of the burst:

$$n = 11,300\ \text{Mw} = n_o\, e^{-\frac{1.57 \times 10^{-2}}{6.1 \times 10^{-5} \times 2}\ 4 \times 10^{-3}} = n_o\, e^{-.515}$$

n_o = Peak power = 18,900 Mw

$$E = 18,900 \sqrt{\frac{2\pi \times 6.1 \times 10^{-5} \times 4 \times 10^{-3}}{1.57 \times 10^{-2}}}\ \left[\text{erf}X\right] = 64.0\ \text{Mw sec}$$

where erfX = 0.344

Total energy to peak of burst = 108 Mw sec.

Energy on back side of burst:

Once vaporization occurs, the shutdown process becomes quite rapid, probably such that an additional 1.5% ΔK is added in about 1 m sec.

$$E_{back} = 1/2 \times 18,900 \sqrt{\frac{2\pi \times 6.1 \times 10^{-5} \times 10^{-3}}{1.5 \times 10^{-2}}} = 47.7 \text{ Mw sec}$$

$$E_{total} = 156 \text{ Mw sec}: \quad \frac{\text{Energy to peak}}{\text{Total Energy}} = 0.69$$

(D) SL-1, 3.6 m sec, same as preceding calculation except 60°C subcooled, about the condition just before the incident.

4 m sec overshoot beyond saturation temperature for the peak plate surface temperature, yields 182°C at peak flux region on the surface and 838°C at the center.
The average plate temperature = 164°C throughout core.
Energy in plates = 27.2 Mw sec.
Total energy of 31.6 Mw sec at 8500 Mw.
On continuing exponential, it would take 1.1 m sec longer to reach vaporization temperature than in the 80°C subcooled case.
Thus, 1.57% Δk is inserted in about 5.1 m sec (relative to the 80°C subcooled calculation).

$$\text{Peak Power} = \frac{8500}{0.518} = 16,400 \text{ Mw}$$

E = 68.4 Mw sec

where erfX = 0.374

Total energy to peak of burst = 100 Mw sec

Energy on back side = 41.4 Mw sec

Total energy = 141 Mw sec

(Measured value was 133 ± 10 Mw sec)

(E) BORAX excursion from ambient condition of saturation temperature:

In calculating excursions originating from saturation temperature, the temperature overshoot until boiling commences is the major determining factor. Time delay does not have the significance for these excursions as it did for the short period, subcooled transients. It is difficult to derive any reliable conclusions from the temperature overshoot data of references 3 and 4, even for those tests originating from saturation temperature. (Possibly the experimental method of simulating the exponential rise is too gross of an approximation for the 0° subcooled tests.) Appropriate guesses of the amount of temperature overshoot (from 0° subcooled conditions) were made from considerations of the overshoot and time delay used in the 80°C subcooled calculations. These values, used in calculating the BORAX 0° subcooled transients, are listed below.

Period	Temperature Overshoot (0° Subcooled)
50 m sec	30°C
20 m sec	35°C
10 m sec	50°C
5 m sec	90°C

As can be seen from Figure III-9(b), the excursion energies calculated using the above overshoots are consistently lower, by about 30%, than the energies measured in the BORAX tests for periods shorter than 20 milliseconds. However, the same discrepancy is observed for the 72° subcooled tests compared to the predicted energies, which in the shorter-than-20 m sec range employ a time delay rather than an overshoot in the calculation. It is felt that these discrepancies are due to some reactor characteristics not being properly considered in the calculations rather than grossly incorrect values of the overshoot or time delay.

APPENDIX E

Supplement to Appendix E of IDO 19311 - Tabulation of Flux Measured by Each Co-Al Pellet

Element Number	Wire Number	Position Between Plates	Position From Top of Fuel Plate Inches	Thermal Flux $n/cm^2 \times (10^{-14})$
8	1435	B	0.5	1.53
			3.5	1.54
			6.5	2.67
			9.5	3.36
			12.5	4.21
			15.5	4.39
			18.5	4.54
39	2013	B	6.5	1.02
			9.5	2.48
			12.5	3.93
			15.5	4.60
			18.5	4.65
			21.5	3.93
			24.5	3.08
			27.0	2.86
41	1249	G	0.5	1.44
			3.5	3.29
			6.5	2.65
41	1433	B	0.5	2.65
			3.5	2.72
			6.5	3.45
			9.5	3.61
			12.5	4.39
			15.5	4.79
47	1526*	G	0.5	0.59
			3.5	0.94
			6.5	1.30
			9.5	1.66
			12.5	1.86
			15.5	1.63
			18.5	1.17
			21.5	1.06
51	1272	B	0.5	0.77
			3.5	0.82
			6.5	0.84
			9.5	0.92
			12.5	1.92
			15.5	2.60
			18.5	1.92
			21.5	1.53
			24.5	1.23
			27.0	1.14

*Identification Not Positive

Element Number	Wire Number	Position Between Plates	Position From Top of Fuel Plate Inches	Thermal Flux $n/cm^2 \times (10^{-14})$
55	1201	E	3.5	0.96
			6.5	1.63
			9.5	2.62
			12.5	2.93
			15.5	3.18
			18.5	2.95
			21.5	2.41
			24.5	2.05
			27.0	1.59
60	1766*	D	-5.5	.122
			-2.5	.135
			0.5	.195
			3.5	.339
			6.5	.283
			9.5	.695
			12.5	.872
			15.5	1.04
			18.5	1.46
			21.5	1.31
			24.5	.926
			27.0	1.07

Following wires or parts thereof were not recovered.

2	1368	B	
2	1403	G	
11	1972	G	Sheath recovered but no contents
62	1546	E	Contaminated during analysis

*Identification Not Positive

APPENDIX F

Temperature Distribution Equations in Fuel Plates & Moderator

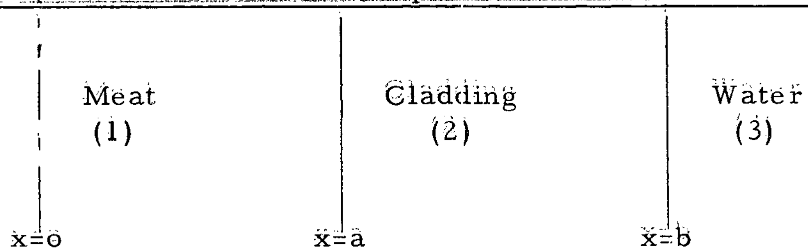

The differential equations of heat conduction in each of the three mediums, during a reactor excursion, are:

(1) $\rho_1 c_1 \dfrac{\partial \theta_1}{\partial t} = k_1 \nabla^2 \theta_1 + Q_o e^{\alpha t}$

(2) $\rho_2 c_2 \dfrac{\partial \theta_2}{\partial t} = k_2 \nabla^2 \theta_2$

(3) $\rho_3 c_3 \dfrac{\partial \theta_3}{\partial t} = k_3 \nabla^2 \theta_3$

where the meat source term is $Q_o e^{\alpha t} \dfrac{\text{energy units}}{\text{sec cm}^3}$
θ is the temperature above ambient
ρ is the density in gm/cm^3
c is the specific heat in energy units/gm C°
k is the thermal conductivity in energy units/sec cm C°
α is the inverse period of the excursion

Letting $\mu^2 = \dfrac{\alpha \rho c}{k}$; one obtains the following general solutions to the equations:

$$\theta_1 = A e^{\alpha t} \cosh \mu_1 x + \frac{Q_o}{\alpha \rho c} e^{\alpha t}$$

$$\theta_2 = B e^{\alpha t} \left[\cosh \mu_2 (x-a) + D \sinh \mu_2 (x-a)\right]$$

$$\theta_3 = E e^{\alpha t} \left[\cosh \mu_3 (x-b) - \sinh \mu_3 (x-b)\right]$$

Certain boundary conditions have already been applied to these equations, specifically symmetry of temperature in the meat and zero temperature far out in the moderator. The simplification that the moderator gap is infinite is essentially accurate for all but the very long periods, greater than several hundred milliseconds. The further boundary conditions of temperature and heat-current continuity at the boundary of meat-clad and of clad-water are to be used. The continuity condition of temperature is quite valid at the meat-clad interface where the metallurgical bond is essentially a solid solution. At the clad-water interface, the temperature is not continuous, due to the thermal resistance of the boundary. However, it will be shown in the difference between infinite resistance and zero resistance at this boundary has an insignificant effect on the temperature distributions, except for the long period excursions.

In applying the above boundary conditions on obtains the solutions:

$$\theta_1 = \frac{Q_o}{\alpha \rho c} \quad e^{\alpha t} \left[1 - \frac{D\cosh \mu_1 x}{D\cosh \mu_1 a + \dfrac{k_1 \mu_1}{k_2 \mu_2} \sinh \mu_1 a} \right]$$

$$\theta_2 = \frac{k_1 \mu_1}{k_2 \mu_2} \quad \frac{Q_o e^{\alpha t}}{\alpha \rho c} \qquad \frac{\sinh \mu_1 a \left[\cosh \mu_2 (x-a) - D\sinh \mu_2 (x-a) \right]}{D\cosh \mu_1 a + \dfrac{k_1 \mu_1}{k_2 \mu_2} \sinh \mu_1 a}$$

$$\theta_3 = \frac{k_1 \mu_1}{k_2 \mu_2} \; \frac{Q_o e^{\alpha t}}{\alpha \rho c} \; \frac{\sinh \mu_1 a \left[\cosh \mu_2 (b-a) - D \sinh \mu_2 (b-a) \right]}{D \cosh \mu_1 a \quad \dfrac{k_1 \mu_1}{k_2 \mu_2} \sinh \mu_1 a}$$

$$\times \left[\cosh \mu_3 (x-b) - \sinh \mu_3 (x-b) \right]$$

$$\text{where} \quad D = \frac{\sinh \mu_2 (b-a) + \dfrac{k_3 \mu_3}{k_2 \mu_2} \cosh \mu_2 (b-a)}{\cosh \mu_2 (b-a) + \dfrac{k_3 \mu_3}{k_2 \mu_2} \sinh \mu_2 (b-a)}$$

For infinite resistance at the water boundary, the equation for D becomes:

$$D = \frac{\sinh \mu_2 (b-a)}{\cosh \mu_2 (b-a)}$$

Comparing the difference between the two extreme conditions, the difference in the clad surface temperature for infinite resistance compared to zero resistance is only 4% for the SL-1 fuel plates in a 20 millisecond transient (also for SPERT-BORAX) plates in a 7 millisecond transient). Thus, the type of boundary condition employed at the clad-water interface is of little consequence in the results of calculated temperature distributions for any but "long" period transients.

The source term Q_o/α is equal to the total energy generated per cm^3 of meat up to the time $t = 0$ in the excursion (i.e., $e^{\alpha t} = 1$). This calibration is of course valid only as long as the reactor remains on the initial exponential period, $1/\alpha$. For a complete power burst approximated by a series of exponentials, the temperature equations are a series of expressions similar to those used in calculating temperature distributions for the assumed burst shape for the SL-1 (reference 1, IDO-19311, page IV-7).

LIST OF MAJOR REFERENCES

1. IDO 19311 - SL-1 Final Report , General Electric Co., August, 1962
2. IDO 16512 - Phillips Petroleum Co., Spert Quarterly Progress Report, July-September, 1958
3. V.E. Schrock et al, Univ. of Calif. Berkeley, Series #163, Issue #2, January, 1961
4. V.E. Schrock et al, Univ. of Calif., Series #163, Issue #2, November, 1961
5. R.W. Miller, G.F. Brockett, E. Feinauer, Phillips Petroleum Co., Private Communication
6. AECD 3840, Transient and Steady State Characteristics of Boiling Reactor. BORAX Experiments, 1953, Dietrich and Layman
7. IDO 16790, SPERT I Destructive Test Program Safety Analysis, June 15, 1962, Spano and Miller
8. IDO 16512, SPERT Quarterly Progress Report, July-September, 1958
9. Fuchs, Efficiency for Very Slow Assembly, LA 956 (August 2, 1946) IDO 16393, a specialization on the linear energy feedback kinetics is a more pertinent treatment
10. AECD-3668, BORAX-I Experiments, 1954, J. R. Dietrich